

INVESTIGATION OF THE MECHANICAL PROPERTIES OF ALUMINUM
TITANATE (Al_2TIO_5) DOPED NI-YSZ SOLID OXIDE FUEL CELL ANODES

by

Madisen Wynn McCleary

A dissertation submitted in partial fulfillment
of the requirements for the degree

of

Doctor of Philosophy

in

Materials Science

MONTANA STATE UNIVERSITY
Bozeman, Montana

May 2019

©COPYRIGHT

by

Madisen Wynn McCleary

2019

All Rights Reserved

DEDICATION

To Josh, for your continued support of me and my dreams.

ACKNOWLEDGEMENTS

My greatest appreciation and thanks to my advisor, Dr. Roberta Amendola for her unwavering support of me. I cannot even begin to express my gratitude for her support even when times were rough. I would not be at this point, writing my dissertation, if it was not for her. She has always put me and my dreams on the forefront. We have worked hard to get to this point, and I could not imagine trying to do this without the continuous support from her. I hope that as we both continue in our careers that we help each other to continue to grow and support each other both in research and in our lives.

There are many people who have made an impact on my life and helped me get to this point. My love and thanks to my parents for pushing me to be the best that I can be. I would not have made it to this point without their love and support of my dreams. Thanks to the rest of my family and friends for supporting me through their prayers and encouragement. I have big ambitions for my career, but they would not be possible without the support of those around me. I hope that through my career I can give back to those who have helped me and give hope to those wanting to follow in my footsteps. I strive to be an encouragement and role model to the future of women in the field of Materials Science, but I could not do that without my support team. To Mr. Mark Porter and Dr. Khalid Khan for their encouragement to pursue the fields of engineering and Materials Science and showing me where my true passions lie.

I would also like to thank my committee members: Dr. Robert Walker, Dr. Stephen Sofie, Dr. Paul Gannon and Dr. Jack Skinner for their support and guidance throughout my dissertation research.

TABLE OF CONTENTS

1. INTRODUCTION	1
Solid Oxide Fuel Cell.....	1
Fracture Mechanics of Ceramics	6
Weibull Statistical Analyses	11
Motivation and Objectives	15
References.....	18
2. EFFECT OF ALUMINUM TITANATE (AL ₂ TIO ₅) DOPING ON THE MECHANICAL PERFORMANCE OF SOLID OXIDE FUEL CELL NI-YSZ ANODE	27
Contribution of Authors and Co-Authors	27
Manuscript Information Page	28
Abstract	29
Introduction.....	30
Experimental.....	32
Results and Discussion	33
Mechanical properties.....	33
Microstructural analyses	38
Conclusions.....	45
Acknowledgements.....	46
References.....	47
3. INVESTIGATION OF THE KINETICS OF THE SOLID-STATE REDUCTION PROCESS OF UNDOPED AND ALUMINUM TITANATE (AL ₂ TIO ₅) DOPED NIO-YSZ ANODES FOR SOLID OXIDE FUEL CELLS.....	50
Contribution of Authors and Co-Authors	50
Manuscript Information Page	51
Abstract	52
Introduction.....	53
Methods.....	55
Experimental.....	55
Kinetic models	57
Results and discussion	58
Conclusions.....	70
Acknowledgements.....	70
References.....	71

TABLE OF CONTENTS - CONTINUED

4. ANALYSIS OF THE MECHANICAL STRENGTH AND FAILURE MODE OF UNDOPED AND ALUMINUM TITANATE (Al_2TiO_5 , ALT) DOPED NI-YSZ SOLID OXIDE FUEL CELL ANODES UNDER UNIAXIAL AND BIAXIAL STRENGTH TESTING CONDITIONS.....	77
Contribution of Authors and Co-Authors	77
Manuscript Information Page	78
Abstract	79
Introduction.....	80
Experimental	83
Results and Discussion	85
Mechanical Properties.....	85
Advanced Statistical Analysis to Identify Presences of Multiple Fractographic Populations	91
Finite Mixture Modeling and Assessing Evidence for Multiple Strength Distributions	92
Microstructural Analyses	96
Conclusions.....	102
Acknowledgements.....	103
References.....	104
5. EFFECT OF REDOX CYCLING ON THE MECHANICAL PERFORMANCE OF UNDOPED AND ALUMINUM TITANATE (Al_2TiO_5 , ALT) DOPED NIO-YSZ SOLID OXIDE FUEL CELL ANODES	109
Contribution of Authors and Co-Authors	109
Manuscript Information Page	110
Abstract	111
Introduction.....	112
Methods.....	114
Results and Discussion	117
Mechanical Properties.....	117
Microstructural Analyses	125
Conclusion	136
Acknowledgements.....	137
References.....	138

TABLE OF CONTENTS - CONTINUED

6. MECHANICAL PERFORMANCE OF ALUMINUM TITANATE (Al_2TiO_5 , ALT) DOPED NiO-YSZ SOFC HALF CELLS	145
Contribution of Authors and Co-Authors	145
Manuscript Information Page	146
Abstract	147
Introduction.....	147
Methods.....	150
Results and Discussion	151
Mechanical Properties.....	151
Microstructural Analysis.....	155
Conclusions.....	160
References.....	162
7. CONCLUSIONS.....	167
Summary of Work.....	167
Final Remarks	171
8. REFERENCES CITED.....	173
9. APPENDICES	191
APPENDIX A: Effect of Particle Size on the Mechanical Performance of Undoped and Aluminum Titanate (Al_2TiO_5) Doped Ni-YSZ Solid Oxide Fuel Cell Anodes.....	191
APPENDIX B: Effect of Hydrogen Concentration on the Mechanical Properties of Reduced Aluminum Titanate (Al_2TiO_5) Doped Ni-YSZ Solid Oxide Fuel Cell Anodes	218
APPENDIX C: Effect of Doping Method on the Mechanical Properties of Aluminum Titanate (Al_2TiO_5) Doped Ni-YSZ Solid Oxide Fuel Cell Anodes	239

LIST OF TABLES

Table 2.1: Weibull modulus of anode material.....	34
Table 2.2: Mechanical properties of anode material.....	34
Table 2.3: Porosity of anode material	34
Table 3.1: NiO reduction kinetic model selection based on the Hancock-Sharp method.....	59
Table 3.2: NiO reduction kinetic model description and corresponding integral expressions	59
Table 3.3: Comparison between the residual sum of squares (RSS) of models predicted with the Hancock-Sharp method and the Avrami-Erofe'ev model for fitting experimental data for the reduction of undoped and 1–10 wt% ALT doped NiO-YSZ at 800 °C, by 5% H ₂ -95% N ₂ gas	63
Table 3.4: Avrami-Erofe'ev exponent “n” and times needed to convert 97 wt% of NiO into metallic Ni, in the undoped and 1–10 wt% ALT doped NiO-YSZ system, at 800 °C when 5% H ₂ -95% N ₂ gas and pure hydrogen are used	64
Table 4.1: Mechanical properties and porosity of uniaxial (TPB) and biaxial (ROR) strength testing samples.....	87
Table 4.2: BIC values for model selection.....	95
Table 5.1: Mechanical properties of ALT doped Ni-YSZ anodes after undergoing 1, 2 or 5 redox cycles	118
Table 5.2: Weibull modulus and 90% confidence interval for ALT doped NiO-YSZ anodes after undergoing 1, 2 or 5 redox cycles	120
Table 5.3: Porosity measurements for ALT doped NiO-YSZ anodes after undergoing 1, 2 or 5 redox cycles	125
Table 6.1: Mechanical properties of anode/electrolyte assembly	152

LIST OF FIGURES

Figure 1.1: Anode Supported SOFC Schematic [10].....	2
Figure 1.2: Example of transgranular (a and c) and intergranular (b and d) [84].....	8
Figure 1.3: Diagram of three-point bending test setup	9
Figure 1.4: Diagram of ring on ring testing apparatus.....	10
Figure 2.1: Weibull plots of NiO-YSZ (oxidized) and Ni-YSZ (reduced) samples.....	35
Figure 2.2: FE-SEM cross sectional image of NiO-YSZ + (a) 0 wt%, (b) 1 wt%, (c) 5 wt%, and (d) 10 wt%	39
Figure 2.3: FE-SEM cross sectional image of Ni-YSZ + (a) 0 wt%, (b) 1 wt%, (c) 5 wt%, and (d) 10 wt% ALT	39
Figure 2.4: FE-SEM surface image of NiO-YSZ + (a) 0 wt%, (b) 1 wt%, (c) 5 wt%, and (d) 10 wt% ALT	40
Figure 2.5: FE-SEM surface image of Ni-YSZ + (a) 0 wt%, (b) 1 wt%, (c) 5 wt%, and (d) 10 wt% ALT.....	41
Figure 2.6: Auger elemental map of Ni-YSZ + 10 wt% ALT sample surface: (a) details of mapped areas, (b) Nickel-Blue, Titanium-Red, Aluminum-Green, and (c) Zirconium-Blue, Titanium-Red, Aluminum-Green.....	41
Figure 3.1: Plot of the Hancock and Sharp method for the reduction of undoped and 1-10 wt.% ALT doped NiO-YSZ at 800°C by 5% H ₂ -95% N ₂ gas (a) and pure hydrogen (b)	58
Figure 3.2: Comparison between the experimental data points and models (solid lines) predicted for the reduction of undoped and 1-10 wt% ALT doped NiO-YSZ at 800°C, by 5% H ₂ -95% N ₂ gas	60
Figure 3.3: Comparison between the experimental data points and models (solid lines) predicted for the reduction of undoped and 1-10 wt.% ALT doped NiO-YSZ at 800°C, by pure hydrogen	61

LIST OF FIGURES - CONTINUED

Figure 3.4: Comparison between the experimental data (markers) and AEn models (solid lines) for the reduction of undoped and 1-10 wt.% ALT doped NiO-YSZ at 800°C, by 5% H ₂ -95% N ₂ gas (a) and pure hydrogen (b)	62
Figure 3.5: FE-SEM surface image of NiO-YSZ + (a) 0 wt%, (b) 1 wt%, (c) 5 wt%, and (d) 10 wt% ALT reduced by 5% H ₂ -95% N ₂ gas.....	68
Figure 3.6: FE-SEM surface image of NiO-YSZ + (a) 0 wt%, (b) 1 wt%, (c) 5 wt%, and (d) 10 wt% ALT reduced by 100% H ₂ gas.....	68
Figure 4.1: Weibull plots of uniaxial (TPB) and biaxial (ROR) strength testing.....	86
Figure 4.2: Histograms and Probability Density Estimates for the TPB and ROR sample data, 0-10% ALT.....	94
Figure 4.3: Probability Density with Fitted Weibull Mixture Distribution (left) and Model Responsibilities for Each Specimen (right)	96
Figure 4.4: FE-SEM surface morphology of uniaxial (TPB) and biaxial (ROR) strength testing samples with a) 0 wt% ALT, b) 1 wt% ALT, c) 5 wt% ALT and d) 10 wt% ALT	97
Figure 4.5: Weibull plots with populations denoted for uniaxial (TPB) and biaxial (ROR) strength testing	98
Figure 4.6: Fracture surface of undoped sample batches with a) TPB and b) ROR testing methods.....	99
Figure 4.7: Fracture surfaces of a,c) 5% and b,d) 10% ALT doped sample batches fractured with a,b) TPB and c,d) ROR testing methods	99
Figure 4.8: Fracture Surface Morphology of 1% ALT doped Ni-YSZ after a) TPB and b) ROR testing	102
Figure 5.1: Weibull plots of ALT doped NiO-YSZ anodes after undergoing a) 1, b) 2 or c) 5 redox cycles	121

LIST OF FIGURES - CONTINUED

Figure 5.2: FE-SEM surface morphology of a) 0 wt% ALT, b) 1 wt% ALT, c) 5 wt% ALT and d) 10 wt% ALT doped NiO-YSZ anode material after undergoing 1 redox cycle.....	126
Figure 5.3: FE-SEM surface morphology of a) 0 wt% ALT, b) 1 wt% ALT, c) 5 wt% ALT and d) 10 wt% ALT doped NiO-YSZ anode material after undergoing 2 redox cycles	127
Figure 5.4: FE-SEM surface morphology of a) 0 wt% ALT, b) 1 wt% ALT, c) 5 wt% ALT and d) 10 wt% ALT doped NiO-YSZ anode material after undergoing 5 redox cycles	127
Figure 5.5: FE-SEM fracture surface morphology of a) 0 wt% ALT, b) 1 wt% ALT, c) 5 wt% ALT and d) 10 wt% ALT doped NiO-YSZ anode material after undergoing 1 redox cycle	133
Figure 5.6: FE-SEM fracture surface morphology of a) 0 wt% ALT, b) 1 wt% ALT, c) 5 wt% ALT and d) 10 wt% ALT doped NiO-YSZ anode material after undergoing 2 redox cycles.....	133
Figure 5.7: FE-SEM fracture surface morphology of a) 0 wt% ALT, b) 1 wt% ALT, c) 5 wt% ALT and d) 10 wt% ALT doped NiO-YSZ anode material after undergoing 5 redox cycles.....	134
Figure 6.1: Weibull plot of anode/electrolyte assembly	154
Figure 6.2: FE-SEM surface morphology of anode side of 5 wt% ALT doped sample with a) max strength, b) median strength and c) minimum strength	156
Figure 6.3: FE-SEM surface morphology of electrolyte side of sample with a) max strength, b) median strength and c) minimum strength.....	156
Figure 6.4: FE-SEM fracture surface morphology of anode side of 5 wt% ALT doped sample with a) max strength, b) median strength and c) minimum strength	157
Figure 6.5: FE-SEM fracture surface morphology of anode-electrolyte interface of sample with a) max strength, b) median strength and c) minimum strength	159

LIST OF FIGURES - CONTINUED

Figure 6.6: FE-SEM fracture surface morphology of anode-electrolyte interface of sample with a) max strength, b) median strength and c) minimum strength 160

ABSTRACT

Recently, there has been growing interest in anode supported Solid Oxide Fuel Cells (SOFCs) because of improved single cell performance. In these systems, the anode layer is the thickest and provides the mechanical strength of the stack. Nickel-yttria stabilized zirconia (Ni-YSZ) composites are widely used as anode material but, in contrast to the vast amount of data available on their electrochemical properties, little data on the mechanical performance exists. This dissertation work focuses on the use of secondary materials added to traditional Ni-YSZ anodes to enhance SOFC anode mechanical performance. Small amounts of, aluminum titanate (Al_2TiO_5 , ALT), added to the NiO-YSZ system during the manufacturing process, results in a material that is over 50% stronger than the native Ni-YSZ.

Samples with different geometries have been fabricated and tested in uniaxial and biaxial strength testing apparatuses. Advanced microscopy techniques and Weibull statistical analyses have been used to properly characterize the mechanical performance, the failure mechanism and to elucidate chemical compositions.

This work has found that the enhanced strength resulting from ALT is related to the development of secondary phases: Al_2O_3 reacts with NiO to form NiAl_2O_4 while TiO_2 preferentially reacts with YSZ to form a solid YSZ framework defined as the “rough phase” that add stiffness to the system and persists upon reduction. The mechanical behavior of reduced samples has been related to the partial reduction of NiAl_2O_4 which results in the formation of Ni nanoparticles within an Al_2O_3 matrix (“small particle phase”). This phase is characterized by a high strength interface while adding ductility and crack deflection ability to the system. ALT was also found responsible for changing the Ni-YSZ system failure mechanism from an intergranular to a transgranular fashion indicating the material toughness increased.

During cyclic operational testing, ALT has potential for mechanical stabilization through porosity development with secondary phase formation. Testing of ALT anodes with YSZ electrolyte material showed increased strength over similar native assemblies.

This dissertation work lays the foundation for future research into the effects of ALT doping on the SOFC system and how this material could be tailored for even further increases in strength.

CHAPTER ONE

INTRODUCTION

Solid Oxide Fuel Cell

As society faces the global energy crisis there is a necessity for a reliable and robust renewable energy system to replace the use of fossil fuels. Solid Oxide Fuel Cells (SOFCs) are one such system with promise for wide commercialization. A SOFC produces power by electrochemically oxidizing a fuel in order to produce electrical power with the only by-products of water vapor and heat. One of the major advantages to SOFCs is the ability for fuel flexibility [1–9]. Fuels such as alcohol, methane, short chain hydrocarbons and syngas can be used to power the SOFC. Typically, SOFCs operate with hydrogen gas as the fuel because it is clean and does not require extra processing to clean off carbon from the electrodes. Current research is exploring the use of SOFCs in civil and military applications as auxiliary power units (APUs) and is focusing on improving performance to ensure SOFCs' competitiveness in the market.

A single SOFC has three components: an anode, an electrolyte, and a cathode. For power production, air is supplied to the cathode and fuel (hydrogen or hydrocarbons) on the anode. At the cathode, oxygen reacts to form oxygen ions following Equation 1. Oxygen ions then diffuse through the electrolyte to react with hydrogen at the anode and

form water vapor and electrons (Equation 2). These electrons are then recycled to the cathode where they can subsequently react with oxygen.



There are different types of SOFCs dependent on temperature and support component. Each component of the cell is typically a ceramic material. Basing on the operating temperatures SOFC can be classified as; low temperature SOFCs operating temperatures are less than 600°C [10–12], intermediate temperatures between 600 and 800°C [13–15], and high temperatures at 800°C or above [16–18]. Also, SOFCs can be identified based on the support component (anode, electrolyte or cathode supported) which carries the mechanical strength of the SOFC. Such component will be the thickest layer as demonstrated in Figure 1 for the anode (green) [19].

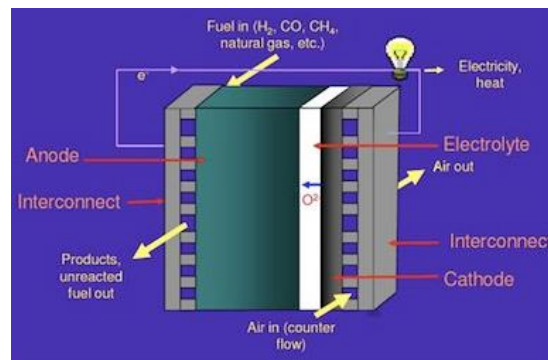


Figure 1.1: Anode Supported SOFC Schematic [10]

Each of the components of the SOFC is composed of ceramic or cermet (ceramic-metal) materials. Common materials for the anode are nickel oxide (NiO) and yttria stabilized zirconia (YSZ) [20–22]. For the cathode, lanthanum strontium manganite

(LSM) is used [23–25] and YSZ is typically used for the electrolyte [26–29]. These materials have been selected because of their similar coefficients of thermal expansion which is crucial to avoid cracking between the components - lowering or even halting power output. Research is ongoing into the use of different materials for each of the components in order to maximize the power output. As SOFCs continue to be used in the market, there is an increasing challenge for researchers to find materials that offer high performance, low degradation and low manufacturing cost.

One of the main drawbacks for SOFCs, currently, is the low single cell (anode, electrolyte and cathode assembly) power output. Research is ongoing into increasing power from single SOFCs by the use of different materials, but promising candidates are costly for marketability [30–36]. Low power output has been solved by stacking single SOFC units with a connecting component called the interconnect. Originally the interconnect was a ceramic material, but due to cost restrictions and difficulties in the manufacturing process, these components have been replaced by metallic materials [37–39].

To maximize the power output from the stack, the contact area between adjacent cells must be as high as possible. To accomplish this, the stack is subjected to high clamping pressures on the order of 65-70 kPa [40,41]. Due to the extreme operating conditions, the stack is under stresses both from mechanical loading and thermal cycling. Therefore, it is important to investigate the thermo-mechanical properties of the individual SOFC components before implementation into the larger SOFC stack. Due to the inherent brittleness of ceramic materials, the reliability and longevity of SOFCs

depends on the mechanical strength and fracture characteristics of the components. These include the coefficient of thermal expansion, elastic behavior (Young's modulus) and the fracture characteristics. In contrast to the wide array of research on the electrochemical performance of SOFC materials [42–47], little fundamental data is available for the mechanical properties of SOFC materials and especially so for new anode compositions [48–50]. Therefore, it is crucial to investigate the mechanical performance of SOFC materials before implementation into the SOFC stack.

The body of research in this dissertation will focus on the anode material of an anode supported design. Anode supported SOFCs have advantages for lower temperature operation as there are lesser ohmic losses and better interface contacts. Research has been focused on increasing power output from single anode supported SOFCs but there is still a necessity for stacking in anode supported SOFCs at this time. As stated previously, this component is typically composed of NiO and YSZ. This material composition has been found to have adequate power production for the low cost of materials and manufacturing [51–54]. The anode is the fuel side component of the SOFC. During operation, NiO in the anode will react with hydrogen in the fuel to form water vapor and create Ni metal as shown in Equation 3.



Ceramic materials are extremely sensitive to changes in chemical composition and manufacturing process. The reduction reaction above causes microstructure changes in the material that effect its mechanical performance. Specifically, for NiO-YSZ based anode materials, after reduction of the NiO to metallic nickel at high temperatures, the Ni

grains will begin to grow in what is termed Ostwald ripening or nickel coarsening. Nickel coarsening is thermodynamically favorable and results in the loss of triple phase boundaries (TPB) in the anode material [22,55–59]. TPBs are the locations at which the reaction to produce electrons takes place (Equation 2). With a loss of TPBs, there is a loss of power output from the SOFC.

Due to Ni coarsening, researchers have been investigating new materials that can either replace NiO-YSZ anodes or doping materials that can be added to the existing anode to decrease Ni coarsening and stabilize the microstructure. Several new promising anode material compositions are under investigation but much more research is needed before implementation into the SOFC [48,49,60–66]. Researchers have found that the introduction of secondary phases that do not compromise the electrochemical performance can also have benefits of increasing mechanical strength by manipulation of the microstructure [35,36,67,68].

The addition of these secondary phases can be accomplished using different manufacturing processes. One common method of doping is by mechanical mixing. During this process, dopant powder is added to the other ceramic components during initial mixing. Mechanical mixing will then homogeneously disperse the dopant material. The advantage of using mechanical mixing is that it can be easily implemented into a manufacturing procedure and can be used for a variety of ceramics processing techniques including tape casting and isostatic pressing. Another common method that is used commonly to increase electrochemical performance is infiltration. During this process, the doping material is infiltrated through the porosity after a tape casting or pressing

procedure. More about the influence of pores on the mechanical properties will be discussed in the “Fracture Mechanics of Ceramics” section. One of the drawbacks of infiltration is that the process is time consuming and may not be easily implemented into a manufacturing plant.

Previous work has found that the introduction of Al_2O_3 to YSZ electrolytes improves sintering behavior along with the electrical and mechanical properties of the material [35,67,69–71]. Also, TiO_2 addition has found similar benefits [36,72–76]. Previous research has found that the addition of aluminum titanate, Al_2TiO_5 , (ALT) helps to stabilize the microstructure of NiO-YSZ anodes allowing for slower degradation rates and high power output [77–80]. There is little fundamental data on the mechanical strength and fracture mechanics of ALT doped anode material. This body of work seeks to complement the research on the electrochemical benefits with investigation into the mechanical performance of ALT doped NiO-YSZ anode material.

Fracture Mechanics of Ceramics

As previously discussed, the SOFC stack is under mechanical stresses such as clamping pressures, thermal expansion and the weight of the cells in the stack. This body of research focuses on the mechanical properties of ALT doped NiO-YSZ anode material in an anode supported SOFC at high temperatures (800°C). Ceramic materials are brittle materials which possess high strength but low ductility (strains at less than 0.1% before failure). Due to this characteristic, brittle materials have unpredictable and catastrophic failures.

The strength of a brittle material is dependent on its ability to resist crack propagation and on the size, distribution and severity of flaws. Flaws in a brittle material can include cracks (either surface or bulk), pores, or irregular grain shape. These flaws are variable and randomly distributed throughout the material. Flaws are usually introduced during the manufacturing process. Pores, in particular, are one major flaw in ceramic materials. Depending on the size, shape and distribution of pores throughout the ceramic material, the mechanical strength will be affected. Research has been conducted on pore morphology and how pores influence the mechanical properties of brittle materials [53,81–83]. In general, higher porosity will result in lower strength. Flaws within the ceramic structure act like stress concentrators and may potentially lead to catastrophic crack propagation.

Crack propagation can be transgranular (cleavage) or intergranular and it occurs by the successive and repeated breaking of atomic bonds along specific planes when the fracture path propagates through the grains or between the grains, respectively (Figure 2) [84]. For transgranular fracture to occur, the amount of energy required for crack propagation is higher when compared to the intergranular. Grain boundaries are locations with high flaw concentration and usually exhibit less than ideal mechanical properties. Transgranular fracture in brittle materials is preferable as it is an indicator of higher strength.

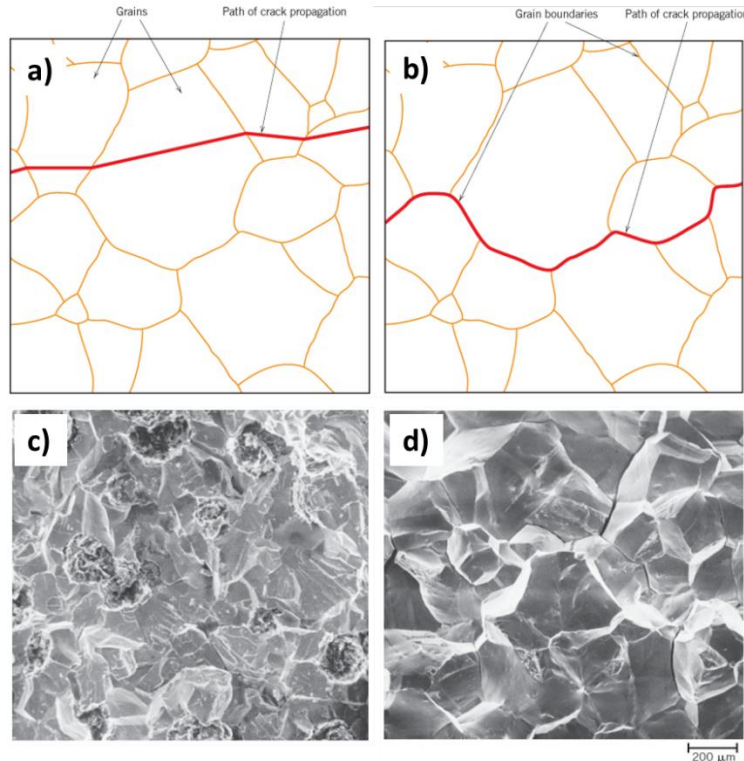


Figure 1.2: Example of transgranular (a and c) and intergranular (b and d) [84]

This body of research involves mechanical testing on the ALT doped NiO/YSZ anode material. Due to the ceramic sensitivity to the presence of flaws within the material, care must be taken when evaluating the mechanical strength. Common materials testing systems for brittle materials are three or four-point bending (uniaxial loading), ring on ring (equibiaxial loading) and ball on three balls (equibiaxial loading). These and many other testing systems have been qualified for testing of brittle materials by the American Society for Testing and Materials. A variety of testing standards are used and referenced in this body of research.

Three-point bending and ring on ring testing will be used for this research. ASTM C1161-13 (Standard Test Method for Flexural Strength of Advanced Ceramics at

Ambient Temperature) [85] is the standard used for three-point bending. For this testing, samples are loaded at three distinct locations along the length of a rectangular bar. A diagram of the testing setup can be found in Figure 3 [85]. The length, L , is determined by the ASTM Standard depending on the overall length of the samples. Under this loading configuration, the samples are subjected to a uniaxial load in the middle of the test specimen.

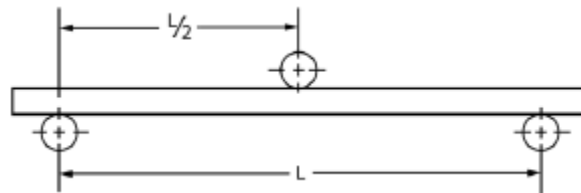


Figure 1.3: Diagram of three-point bending test setup

The ASTM C1499-15 (Standard Test Method for Monotonic Equibiaxial Flexural Strength of Advanced Ceramics at Ambient Temperature) [86] is the standard used for ring on ring testing. For this testing, a circular sample is manufactured and tested with the sample loaded between concentric rings. As the sample is loaded on a ring, the testing distributes the loading and is considered equibiaxial testing. Figure 4 [86] shows a diagram of the ring on ring testing apparatus. These two testing methods are commonly used to have a reliable evaluation of a ceramic material strength [87–92]. For both these testing methods, the sample dimensions, dimensions of the testing system and force at failure are recorded for calculations of the mechanical strength.

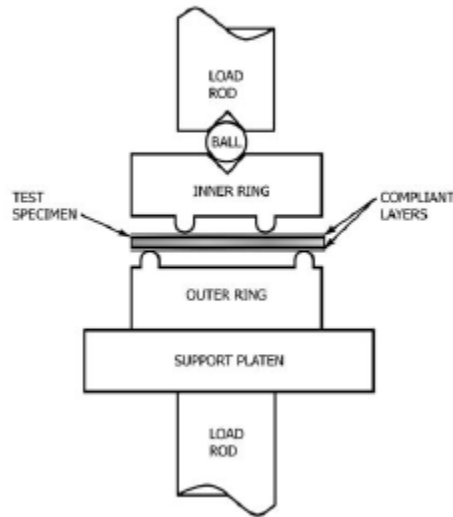


Figure 1.4: Diagram of ring on ring testing apparatus

During uniaxial flexural tests, such as three- or four-point bending, the maximum stress goes from tensile to compressive through the sample thickness and is experienced at the surface. Such measurement may; however, provide only a partial characterization of the material load bearing capacity due to the sample's geometry that introduces low curvature radius defects (sample edges) acting like stress concentrators. Also, advanced engineering ceramic components fail often due to multiaxial stress conditions. Biaxial flexural tests on disc-shaped specimens like ring-on-ring or ball-on-ring are particularly favored because the maximum tensile stress occurs at the center of the surface opposite to load application and, consequently, edge flaws do not influence the results.

Due to the unpredictable nature of brittle fracture, testing of these materials requires statistical approach. ASTM standards state that at least 30 samples per batch must be tested to conduct the required statistical evaluation. The flexural strength or

modulus of rupture (MOR) of the material, is calculated after fracture as per Equation 4 (Three point bending) Equation 5 (ring on ring) [85,86].

$$\sigma_f = \frac{3FL}{2bh^2} \quad (4)$$

$$\sigma_f = \frac{3F}{2\pi h^2} \left[(1 - \nu) \frac{D_S^2 - D_L^2}{2D^2} + (1 + \nu) \ln \frac{D_S}{D_L} \right] \quad (5)$$

Where σ_f is the flexural strength (Pa), F is the force at fracture (N), L is the length between bottom supports (m), b is the width of the sample (m), h is the height is the sample (m), ν is the Poisson's ratio for the material (assumed at 0.3), D_S is the diameter of the support ring (m), D_L is the diameter of the loading ring (m), and D is the diameter of the sample (m). The flexural strength values are then used for Weibull statistics.

Weibull Statistical Analyses

As previously discussed, due to the sensitivity of ceramics to random flaw distribution, there is a necessity to evaluate the mechanical properties using statistical methods. The most common and widely used approach is the Weibull distribution [49,90,92–95]. The Weibull statistics are based off the weakest link theory where failure of the material occurs when the weakest flaw under tension fails. The standard used for Weibull statistical evaluation is ASTM 1239-13 (Standard Practice for Reporting Uniaxial Strength Data and Estimating Weibull Distribution Parameters for Advanced Ceramics) [96]. The type of Weibull statistics used for this body of research is the two-parameter method that estimates the Weibull modulus and characteristic strength. These values are used to determine both the strength and the reliability of the tested material.

The equation used for evaluation of these parameters is the cumulative distribution function for the Weibull distribution (Equation 6).

$$P_f = 1 - \exp \left[- \left(\frac{\sigma}{\sigma_0} \right)^m \right] \quad (6)$$

Where P_f is the probability of failure, σ is the modulus of rupture (flexural strength) for each sample, σ_0 is the characteristic strength, m is the Weibull modulus. In order to calculate the characteristic strength and the Weibull modulus, the following steps must be taken as outline below in accordance with ASTM Standard 1239-13 [96]. After calculation of each sample's flexural strength using equations 4 or 5 above, sort them in ascending order and assign them to a specific probability of failure. The probability of failure (P_f) is determined by Equation 7.

$$P_f(\sigma_i) = \frac{i-0.5}{N} \quad (7)$$

Where $P_f(\sigma_i)$ is the probability of failure for a specific sample in the data set, i indicates the sample index and N is the total number of samples in the data set. This will assign each sample with a specified probability of failure. The sample with the lowest strength will have the lowest probability of failure; whereas, the highest strength sample will be assigned the highest probability of failure. This seems contradictory but these probabilities are distributed in this manner because if another sample was tested it would have a high probability of failing before the highest strength observed for the batch and have a low probability to fail before the lowest strength sample. Once the probability of failure values have been associated to a specific strength value, they need to be plotted to determine the characteristic strength and Weibull modulus. The plot should display

$\ln(\ln(1/(1-P_f)))$ versus $\ln(\sigma)$. These equations are determined by converting Equation 6 into a straight-line formula where the Weibull modulus will be calculated as the slope of the line. The characteristic strength is calculated at a probability of failure of 63.2% which will give a value of zero for $\ln(\ln(1/(1-P_f)))$.

Once the Weibull modulus and characteristic strength have been determined for the sample batch then analyses of these values and their influence on fracture properties can be conducted. The Weibull modulus indicates the nature, severity and dispersion of flaws within the material. A low Weibull modulus would be indicative of non-homogeneous dispersion of flaws within the material which leads to more unpredictable failures. A low Weibull modulus is correlated with wide spread in the flexural strength calculated from the batch. In contrast, a high Weibull modulus indicates a homogeneous flaw distribution leading to a more reliable material. This is a result of low spread in the flexural strength data showing consistent failure strength.

Typical Weibull modulus values for NiO-YSZ anode materials are between 5 and 7 [97]. For SOFC components, the characteristic strength should be as high as possible without significantly decreasing the Weibull modulus. Typical strengths for NiO-YSZ anode materials is between 80 and 130 MPa [49,94]. After calculation of the Weibull modulus and characteristic strength, fractography must be implemented to determine fracture mechanisms. This includes imaging of the fracture surface to determine fracture mode and fracture initiation. Fractography is then compared to mechanical strength values to assess fracture mechanics of the material.

As stated previously, the Weibull approach considers the weakest link theory where the weakest spot under tension determines the strength of the sample. If the volume under tension is large, then there is a higher probability of encountering a flaw; thus, the apparent strength will be lower. In contrast, if the tested volume is small, then the strength will be apparently high. Due to this phenomenon, the volume under tension or the effective volume (V_{eff}) must be taken into account for each sample tested [89,90,98–100]. Equations 8 and 9 are used to calculate the effective volume for the three-point bending and ring on ring methods, respectively.

$$V_{eff} = \frac{lwh}{2(m+1)^2} \quad (8)$$

$$V_{eff} = \left\{ \frac{\pi}{2} D_L^2 \right\} \left\{ 1 + \left[\frac{44(1+\nu)}{3(1+m)} \right] \left[\frac{5+m}{2+m} \right] \left(\frac{D_S - D_L}{D_S D} \right)^2 \left[\frac{2D^2(1+\nu) + (D_S - D_L)^2(1-\nu)}{(3+\nu)(1+3\nu)} \right] \right\} \left\{ \frac{h}{2(m+1)} \right\} \quad (9)$$

Where l is the distance between the support points (mm), w is the width of the sample (mm), h is the height of the sample (mm), m is the Weibull modulus, D_L is the diameter of the loading ring (mm), D_S is the diameter of the support ring (mm), D is the diameter of the sample (mm), ν is the Poisson's ratio (assumed to be 0.3). After calculation of the effective volume for each sample, the average effective volume for the batch can be calculated. Using the effective volume, the characteristic strength can be scaled to the same effective volume (1 mm^3). The scaled characteristic strength is calculated using Equation 10.

$$\sigma'_0 = \sigma_0 \left(\frac{V_{eff}}{1 \text{ mm}^3} \right)^{\frac{1}{m}} \quad (10)$$

Where σ_0' is the scaled characteristic strength (MPa), σ_0 is the characteristic strength (MPa), V_{eff} is the effective volume (mm^3), and m is the Weibull modulus. Using the scaled characteristic strength allows for equal comparison between sample batches of different effective volumes.

Motivation and Objectives

Due to the unpredictable fracture behavior of ceramic materials, it is critical to fully investigate the thermo-mechanical properties. This is of utmost importance for SOFC materials as the components must be able to withstand large multiaxial stresses during the harsh operating conditions. It is assumed for this dissertation work that the SOFC is operating at high temperatures (around 800°C) and that the individual cells are combined into a stack configuration. It is also assumed that the SOFC will be in an anode supported design leading to the anode material carrying the mechanical load of the cell. Given these conditions, stress from thermal expansion along with clamping pressures can induce large stress on the material, especially the cells close to the bottom of the stack due to the weight of the cells above.

This research is motivated by a necessity to characterize the mechanical properties of anode materials due to the lack of research in this area. Much research can be found for the electrochemical properties of anode supported SOFCs, but little fundamental data exists on the mechanical properties. Some research has been done on undoped Ni/YSZ anodes but there is not a consistent method for mechanical property testing. Differences in testing methodology can lead to vast changes in mechanical strength due to stress distribution during testing; therefore, comparison of data between

multiple research papers is difficult. The aim of this body of work is to add to the growing knowledge base for Ni/YSZ based anodes' fracture mechanics and mechanical strength in reference to undoped and doped anodes with secondary phases.

The addition of ALT was studied due to the vast improvement in electrochemical properties. Previous work has shown the advantages of ALT doping in terms of anchoring of the nickel catalyst. This addition aids in increased power output and decreased degradation rates. The improvements in electrochemical properties give promise of this material being used in commercially produced SOFCs. Before use of these ALT doped Ni/YSZ anodes in commercial cells, thorough testing must be conducted on the mechanical performance. For stack operation, mechanical strength is of importance for increased longevity of the SOFC stack. Mechanical failure of the individual SOFCs could lead to power loss and possible explosions; therefore, care must be taken in choosing materials that have high strength and higher electrochemical properties.

For this research, in-depth studies of ALT doped Ni/YSZ anodes were conducted. Chapter 2 discusses the initial mechanical testing of bulk ALT doped Ni/YSZ anodes. This study led to the discovery of secondary phases that are believed to influence material behavior. Chapter 3 discusses the mechanisms of ALT doped Ni/YSZ anodes reduction due to a noticed increased reduction time with ALT doping. The mechanisms for reduction have been used to elucidate secondary phase formations within the doped anode. Chapter 4 studied the effects of testing conditions on material's strength. This study allowed for elucidation of the fracture mechanism due to the differences in loading

configuration. After discovery of the basic fracture mechanisms for the ALT doped anode, Chapters 5 and 6 build on the previous studies to test the material in simulated operating conditions. From all these studies, an understanding of the mechanical strength improvement and fracture mechanisms has been discovered for this ALT doped anode material. Using this knowledge, it is the goal of this dissertation work to apply this knowledge for commercialization of this doped anode material and increase the base knowledge for fracture mechanics and mechanical properties of anode materials.

References

- [1] A. Lanzini, P. Leone, Experimental investigation of direct internal reforming of biogas in solid oxide fuel cells, *Int. J. Hydrogen Energy*. 35 (2010) 2463–2476. doi:10.1016/j.ijhydene.2009.12.146.
- [2] A. Lanzini, P. Leone, M. Pieroni, M. Santarelli, D. Beretta, S. Ginocchio, Experimental investigations and modeling of direct internal reforming of biogases in tubular solid oxide fuel cells, *Fuel Cells*. 11 (2011) 697–710. doi:10.1002/fuce.201000173.
- [3] C.J. Laycock, J.Z. Staniforth, R.M. Ormerod, Biogas as a fuel for solid oxide fuel cells and synthesis gas production: effects of ceria-doping and hydrogen sulfide on the performance of nickel-based anode materials., *Dalton Trans.* 40 (2011) 5494–5504. doi:10.1039/c0dt01373k.
- [4] P. Piroonlerkgul, S. Assabumrungrat, N. Laosiripojana, A.A. Adesina, Selection of appropriate fuel processor for biogas-fuelled SOFC system, *Chem. Eng. J.* 140 (2008) 341–351. doi:10.1016/j.cej.2007.10.007.
- [5] Y. Shiratori, T. Oshima, K. Sasaki, Feasibility of direct-biogas SOFC, *Int. J. Hydrogen Energy*. 33 (2008) 6316–6321. doi:10.1016/j.ijhydene.2008.07.101.
- [6] Y. Shiratori, T. Ijichi, T. Oshima, K. Sasaki, Internal reforming SOFC running on biogas, *Int. J. Hydrogen Energy*. 35 (2010) 7905–7912. doi:10.1016/j.ijhydene.2010.05.064.
- [7] J. Staniforth, R.M. Ormerod, Implications for using biogas as a fuel source for solid oxide fuel cells: Internal dry reforming in a small tubular solid oxide fuel cell, *Catal. Letters*. 81 (2002) 19–23. doi:10.1023/A:1016000519280.
- [8] I. Wheeldon, C. Caners, K. Karan, B. Peppley, Utilization of Biogas Generated from Ontario Wastewater Treatment Plants in Solid Oxide Fuel Cell Systems: A Process Modeling Study, *Int. J. Green Energy*. 4 (2007) 221–231. doi:10.1080/15435070601015585.
- [9] I. V. Yentekakis, Open- and closed-circuit study of an intermediate temperature SOFC directly fueled with simulated biogas mixtures, *J. Power Sources*. 160 (2006) 422–425. doi:10.1016/j.jpowsour.2005.12.069.
- [10] C.-C. Yu, J.D. Baek, C.-H. Su, L. Fan, J. Wei, Y.-C. Liao, P.-C. Su, Inkjet-printed Porous Silver Thin Film as a Cathode for Low-Temperature Solid Oxide Fuel Cell, *ACS Appl. Mater. Interfaces*. (2016) acsami.6b01943. doi:10.1021/acsami.6b01943.
- [11] A. V. Call, J.G. Railsback, H. Wang, S.A. Barnett, Degradation of nano-scale cathodes: a new paradigm for selecting low-temperature solid oxide cell materials, *Phys. Chem. Chem. Phys.* 18 (2016) 13216–13222. doi:10.1039/C6CP02590K.

- [12] K.C. Neoh, G.D. Han, M. Kim, J.W. Kim, H.J. Choi, S.W. Park, J.H. Shim, Nanoporous silver cathode surface treated by atomic layer deposition of CeO_x for low-temperature solid oxide fuel cells., *Nanotechnology*. 27 (2016) 185403. doi:10.1088/0957-4484/27/18/185403.
- [13] F. Ye, Q. Zhou, K. Xu, Z. Zhang, X. Han, L. Yang, J. Xu, H. Xu, K. Wu, Y. Guan, Phase stability and electrochemical performance of $\text{Y}_{0.5}\text{Ca}_{0.5-x}\text{In}_x\text{BaCo}_{3.2}\text{Ga}_{0.8}\text{O}_{7+??}$ ($x = 0$ and 0.1) as cathodes for intermediate temperature solid oxide fuel cells, *J. Alloys Compd.* 680 (2016) 163–168. doi:10.1016/j.jallcom.2016.04.028.
- [14] Y. Zhu, W. Zhou, Y. Chen, Z. Shao, An Aurivillius Oxide Based Cathode with Excellent CO_2 Tolerance for Intermediate-Temperature Solid Oxide Fuel Cells, *Angew. Chemie Int. Ed.* 6845 (2016) 8988–8993. doi:10.1002/anie.201604160.
- [15] X. Lv, X. Liu, C. Gu, Y. Weng, Determination of safe operation zone for an intermediate-temperature solid oxide fuel cell and gas turbine hybrid system, *Energy*. 99 (2016) 91–102. doi:10.1016/j.energy.2016.01.047.
- [16] a Atkinson, S. Barnett, R.J. Gorte, J.T.S. Irvine, a J. McEvoy, M. Mogensen, S.C. Singhal, J. Vohs, Advanced anodes for high-temperature fuel cells., *Nat. Mater.* 3 (2004) 17–27. doi:10.1038/nmat1040.
- [17] M. Irshad, K. Siraj, R. Raza, A. Ali, P. Tiwari, B. Zhu, A. Rafique, A. Ali, M. Kaleem Ullah, A. Usman, A Brief Description of High Temperature Solid Oxide Fuel Cell's Operation, Materials, Design, Fabrication Technologies and Performance, *Appl. Sci.* 6 (2016) 75. doi:10.3390/app6030075.
- [18] R. Irankhah, B. Raissi, A. Maghsoudipour, A. Irankhah, S. Ghashghai, NiFe_2O_4 Spinel Protection Coating for High-Temperature Solid Oxide Fuel Cell Interconnect Application, *J. Mater. Eng. Perform.* 25 (2016) 1515–1525. doi:10.1007/s11665-016-1949-z.
- [19] E. De Guire, NexTech's SOFC interconnect coating surpasses one-year mark, (2012). <http://ceramics.org/ceramic-tech-today/nextechs-sofc-interconnect-coating-surpasses-one-year-mark> (accessed August 9, 2016).
- [20] A.N. Busawon, D. Sarantaridis, A. Atkinson, Ni infiltration as a possible solution to the redox problem of SOFC anodes, *Electrochem. Solid-State Lett.* 11 (2008) B186–B189. doi:10.1149/1.2959078.
- [21] G.B. Johnson, P. Hjalmarsson, K. Norrman, U.S. Ozkan, A. Hagen, Biogas Catalytic Reforming Studies on Nickel-Based Solid Oxide Fuel Cell Anodes, *Fuel Cells*. 16 (2016) 219–234. doi:10.1002/fuce.201500179.
- [22] D. Kennouche, Y. -c. K. Chen-Wiegart, J.S. Cronin, J. Wang, S. a. Barnett, Three-Dimensional Microstructural Evolution of Ni- Ytria-Stabilized Zirconia Solid Oxide Fuel Cell Anodes At Elevated Temperatures, *J. Electrochem. Soc.* 160 (2013) F1293–F1304. doi:10.1149/2.084311jes.

- [23] T.P. Holme, C. Lee, F.B. Prinz, Atomic layer deposition of LSM cathodes for solid oxide fuel cells, *Solid State Ionics*. 179 (2008) 1540–1544. doi:10.1016/j.ssi.2007.12.100.
- [24] L. Dos Santos-Gomez, E.R. Losilla, F. Martin, J.R. Ramos-Barrado, D. Marrero-Lopez, Novel microstructural strategies to enhance the electrochemical performance of La_{0.8}Sr_{0.2}MnO₃-d cathodes, *ACS Appl. Mater. Interfaces*. 7 (2015) 7197–7205. doi:10.1021/acsami.5b00255.
- [25] X. Fan, C.Y. You, J.L. Zhu, L. Chen, C.R. Xia, Fabrication of LSM-SDC composite cathodes for intermediate-temperature solid oxide fuel cells, *Ionics (Kiel)*. 21 (2015) 2253–2258. doi:10.1007/s11581-015-1396-0.
- [26] T. Park, G.Y. Cho, Y.H. Lee, W.H. Tanveer, W. Yu, Y. Lee, Y. Kim, J. An, S.W. Cha, Effect of anode morphology on the performance of thin film solid oxide fuel cell with PEALD YSZ electrolyte, *Int. J. Hydrogen Energy*. 41 (2016) 2–7. doi:10.1016/j.ijhydene.2016.04.092.
- [27] C.N. Ginestra, R. Sreenivasan, A. Karthikeyan, S. Ramanathan, P.C. McIntyre, Atomic Layer Deposition of Y₂O₃/ZrO₂ Nanolaminates: A Route to Ultrathin Solid-State Electrolyte Membranes, *Electrochem. Solid-State Lett.* 10 (2007) B161. doi:10.1149/1.2759606.
- [28] D.Y. Jang, H.K. Kim, J.W. Kim, K. Bae, M.V.F. Schlupp, S.W. Park, M. Prestat, J.H. Shim, Low-temperature performance of yttria-stabilized zirconia prepared by atomic layer deposition, *J. Power Sources*. 274 (2015) 611–618. doi:10.1016/j.jpowsour.2014.10.022.
- [29] J.H. Shim, S. Kang, S.W. Cha, W. Lee, Y.B. Kim, J.S. Park, T.M. Gur, F.B. Prinz, C.C. Chao, J.W. An, Atomic layer deposition of thin-film ceramic electrolytes for high-performance fuel cells, *J. Mater. Chem. A*. 1 (2013) 12695–12705. doi:10.1039/c3ta11399j.
- [30] F. Zhao, A. V. Virkar, Dependence of polarization in anode-supported solid oxide fuel cells on various cell parameters, *J. Power Sources*. 141 (2005) 79–95. doi:10.1016/j.jpowsour.2004.08.057.
- [31] A.C. Müller, D. Herbsttritt, E. Ivers-Tiffée, Development of a multilayer anode for solid oxide fuel cells, *Solid State Ionics*. 152–153 (2002) 537–542. doi:10.1016/S0167-2738(02)00357-0.
- [32] Z.R. Wang, J.Q. Qian, S.R. Wang, J.D. Cao, T.L. Wen, Improvement of anode-supported solid oxide fuel cells, *Solid State Ionics*. 179 (2008) 1593–1596. doi:10.1016/j.ssi.2008.03.022.
- [33] T. Setoguchi, K. Okamoto, K. Eguchi, H. Arai, Effects of anode material and fuel on anodic reaction of solid oxide fuel cells, *J. Electrochem. Soc.* 139 (1992) 2875–2880. doi:10.1149/1.2068998.

- [34] M. Kleitz, F. Petitbon, Optimized SOFC electrode microstructure, *Solid State Ionics*. 92 (1996) 65–74. doi:10.1016/S0167-2738(96)00464-X.
- [35] C.R. He, W.G. Wang, Alumina Doped Ni/YSZ Anode Materials for Solid Oxide Fuel Cells, *Fuel Cells*. 9 (2009) 630–635. doi:10.1002/fuce.200800152.
- [36] M. Mori, Y. Hiei, H. Itoh, G.A. Tompsett, N.M. Sammes, Evaluation of Ni and Ti-doped Y₂O₃ stabilized ZrO₂ cermet as an anode in high-temperature solid oxide fuel cells, *Solid State Ionics*. 160 (2003) 1–14. doi:10.1016/S0167-2738(03)00144-9.
- [37] J.E. Hammer, S.J. Laney, R.W. Jackson, K. Coyne, F.S. Pettit, G.H. Meier, The oxidation of ferritic stainless steels in simulated solid-oxide fuel-cell atmospheres, *Oxid. Met.* 67 (2007) 1–38. doi:10.1007/s11085-006-9041-y.
- [38] R. Amendola, P. Gannon, B. Ellingwood, K. Hoyt, P. Piccardo, P. Genocchio, Oxidation behavior of coated and preoxidized ferritic steel in single and dual atmosphere exposures at 800°C, *Surf. Coatings Technol.* 206 (2012) 2173–2180. doi:10.1016/j.surfcoat.2011.09.054.
- [39] J. Rufner, P. Gannon, P. White, M. Deibert, S. Teintze, R. Smith, H. Chen, Oxidation behavior of stainless steel 430 and 441 at 800 C in single (air/air) and dual atmosphere (air/hydrogen) exposures, *Int. J. Hydrogen Energy*. 33 (2008) 1392–1398. doi:10.1016/j.ijhydene.2007.12.067.
- [40] T. Dey, D. Singdeo, M. Bose, R.N. Basu, P.C. Ghosh, Study of contact resistance at the electrode-interconnect interfaces in planar type Solid Oxide Fuel Cells, *J. Power Sources*. 233 (2013) 290–298. doi:10.1016/j.jpowsour.2013.01.111.
- [41] T. Dey, A. Dey, P.C. Ghosh, M. Bose, A.K. Mukhopadhyay, R.N. Basu, Influence of microstructure on nano-mechanical properties of single planar solid oxide fuel cell in pre- and post-reduced conditions, *Mater. Des.* (2014). doi:10.1016/j.matdes.2013.06.052.
- [42] D. Klotz, A. Leonide, A. Weber, E. Ivers-Tiffée, Electrochemical model for SOFC and SOEC mode predicting performance and efficiency, *Int. J. Hydrogen Energy*. 39 (2014) 20844–20849. doi:10.1016/j.ijhydene.2014.08.139.
- [43] C. Jiang, J.T.S. Irvine, Catalysis and oxidation of carbon in a hybrid direct carbon fuel cell, *J. Power Sources*. 196 (2011) 7318–7322. doi:10.1016/j.jpowsour.2010.11.066.
- [44] M.R. Somalu, V. Yufit, N.P. Brandon, The effect of solids loading on the screen-printing and properties of nickel/scandia-stabilized-zirconia anodes for solid oxide fuel cells, *Int. J. Hydrogen Energy*. 38 (2013) 9500–9510. doi:10.1016/j.ijhydene.2012.06.061.
- [45] T. Shimura, Z. Jiao, S. Hara, N. Shikazono, Quantitative analysis of solid oxide fuel cell anode microstructure change during redox cycles, *J. Power Sources*. 267 (2014) 58–68. doi:10.1016/j.jpowsour.2014.04.152.

- [46] A. Bertei, E. Ruiz-Trejo, K. Kareh, V. Yufit, X. Wang, F. Tariq, N.P. Brandon, The fractal nature of the three-phase boundary: A heuristic approach to the degradation of nanostructured solid oxide fuel cell anodes, *Nano Energy*. (2017). doi:10.1016/j.nanoen.2017.06.028.
- [47] J. Kong, K. Sun, D. Zhou, N. Zhang, J. Mu, J. Qiao, Ni-YSZ gradient anodes for anode-supported SOFCs, *J. Power Sources*. 166 (2007) 337–342. doi:10.1016/j.jpowsour.2006.12.042.
- [48] M. Radovic, E. Lara-curzio, Elastic Properties of Nickel-Based Anodes for Solid Oxide Fuel Cells as a Function of the Fraction of Reduced NiO, *J. Am. Ceram. Soc.* 87 (2004) 2242–2247. doi:10.1111/j.1151-2916.2004.tb07499.x.
- [49] M. Radovic, E. Lara-Curzio, Mechanical properties of tape cast nickel-based anode materials for solid oxide fuel cells before and after reduction in hydrogen, *Acta Mater.* 52 (2004) 5747–5756. doi:10.1016/j.actamat.2004.08.023.
- [50] J. Wei, T. Osipova, J. Malzbender, M. Krüger, Mechanical characterization of SOFC/SOEC cells, *Ceram. Int.* 44 (2018) 11094–11100. doi:10.1016/j.ceramint.2018.03.103.
- [51] J.R. Wilson, S. a. Barnett, Solid Oxide Fuel Cell Ni–YSZ Anodes: Effect of Composition on Microstructure and Performance, *Electrochem. Solid-State Lett.* 11 (2008) B181. doi:10.1149/1.2960528.
- [52] W.Z. Zhu, S.C. Deevi, A review on the status of anode materials for solid oxide fuel cells, *Mater. Sci. Eng. A*. 362 (2003) 228–239. doi:10.1016/S0921-5093(03)00620-8.
- [53] M. Pihlatie, A. Kaiser, M. Mogensen, Mechanical properties of NiO/Ni–YSZ composites depending on temperature, porosity and redox cycling, *J. Eur. Ceram. Soc.* 29 (2009) 1657–1664. doi:10.1016/j.jeurceramsoc.2008.10.017.
- [54] N. Mahato, A. Banerjee, A. Gupta, S. Omar, K. Balani, Progress in material selection for solid oxide fuel cell technology: A review, *Prog. Mater. Sci.* 72 (2015) 141–337. doi:10.1016/j.pmatsci.2015.01.001.
- [55] L. Holzer, B. Iwanschitz, T. Hocker, B. M??nch, M. Prestat, D. Wiedenmann, U. Vogt, P. Holtappels, J. Sfeir, A. Mai, T. Graule, Microstructure degradation of cermet anodes for solid oxide fuel cells: Quantification of nickel grain growth in dry and in humid atmospheres, *J. Power Sources*. 196 (2011) 1279–1294. doi:10.1016/j.jpowsour.2010.08.017.
- [56] Z. Jiao, N. Shikazono, N. Kasagi, Quantitative Characterization of SOFC Nickel-YSZ Anode Microstructure Degradation Based on Focused-Ion-Beam 3D-Reconstruction Technique, *J. Electrochem. Soc.* 159 (2012) B285. doi:10.1149/2.045203jes.

- [57] S. Kim, H. Moon, S. Hyun, J. Moon, J. Kim, H. Lee, Performance and durability of Ni-coated YSZ anodes for intermediate temperature solid oxide fuel cells, *Solid State Ionics*. 177 (2006) 931–938. doi:10.1016/j.ssi.2006.02.007.
- [58] G.J. Nelson, K.N. Grew, J.R. Izzo, J.J. Lombardo, W.M. Harris, A. Faes, A. Hessler-Wyser, J. Van Herle, S. Wang, Y.S. Chu, A. V. Virkar, W.K.S. Chiu, Three-dimensional microstructural changes in the Ni-YSZ solid oxide fuel cell anode during operation, *Acta Mater.* 60 (2012) 3491–3500. doi:10.1016/j.actamat.2012.02.041.
- [59] D. Simwonis, F. Tietz, D. Stover, Nickel coarsening in annealed Ni / 8YSZ anode substrates for solid oxide fuel cells, *Solid State Ionics*. 132 (2000) 241–251. doi:10.1016/S0167-2738(00)00650-0.
- [60] J. Wei, G. Pećanac, J. Malzbender, Review of mechanical characterization methods for ceramics used in energy technologies, *Ceram. Int.* 40 (2014) 15371–15380. doi:10.1016/j.ceramint.2014.07.089.
- [61] G. Pećanac, S. Baumann, J. Malzbender, Mechanical properties and lifetime predictions for Ba_{0.5}Sr_{0.5}Co_{0.8}Fe_{0.2}O_{3-δ} membrane material, *J. Memb. Sci.* 385–386 (2011) 263–268. doi:10.1016/j.memsci.2011.10.005.
- [62] G. Pećanac, L. Kiesel, R. Kriegel, J. Malzbender, Comparison of thermo-mechanical characteristics of non-doped and 3 mol% B-site Zr-doped Ba_{0.5}Sr_{0.5}Co_{0.8}Fe_{0.2}O_{3-??}, *Ceram. Int.* 40 (2014) 1843–1850. doi:10.1016/j.ceramint.2013.07.086.
- [63] A. Atkinson, A. Selçuk, Mechanical behaviour of ceramic oxygen ion-conducting membranes, *Solid State Ionics*. 134 (2000) 59–66. doi:10.1016/S0167-2738(00)00714-1.
- [64] M. Lipińska-Chwałek, L. Kiesel, J. Malzbender, Mechanical properties of porous MgO substrates for membrane applications, *J. Eur. Ceram. Soc.* 34 (2014) 2519–2524. doi:10.1016/j.jeurceramsoc.2014.03.009.
- [65] B.X. Huang, V. Vasechko, Q.L. Ma, J. Malzbender, Thermo-mechanical properties of (Sr,Y)TiO₃ as anode material for solid oxide fuel cells, *J. Power Sources*. 206 (2012) 204–209. doi:10.1016/j.jpowsour.2012.01.137.
- [66] S. Giraud, J. Canel, Young's modulus of some SOFCs materials as a function of temperature, *J. Eur. Ceram. Soc.* 28 (2008) 77–83. doi:10.1016/j.jeurceramsoc.2007.05.009.
- [67] Y. Ye, J. Li, H. Zhou, J. Chen, Microstructure and mechanical properties of yttria-stabilized ZrO₂/Al₂O₃ nanocomposite ceramics, *Ceram. Int.* 34 (2008) 1797–1803. doi:10.1016/j.ceramint.2007.06.005.
- [68] R. Kubrin, G. Blugan, J. Kuebler, Influence of cerium doping on mechanical properties of tetragonal scandium-stabilized zirconia, *J. Eur. Ceram. Soc.* 37 (2017) 1651–1656. doi:10.1016/j.jeurceramsoc.2016.11.038.
- [69] S. Tekeli, The flexural strength, fracture toughness, hardness and densification behaviour of various amount of Al₂O₃-doped 8YSCZ/Al₂O₃ composites used as an

electrolyte for solid oxide fuel cell, *Mater. Des.* 27 (2006) 230–235.
doi:10.1016/j.matdes.2004.10.011.

[70] J.S. Lee, K.H. Choi, B.K. Ryu, B.C. Shin, I.S. Kim, Effects of gallia additions on sintering behavior of gadolinia-doped ceria, *Ceram. Int.* 39 (2004) 807–812.
doi:10.1016/j.materresbull.2004.07.022.

[71] H. Xu, H. Yan, Z. Chen, The flexural strength and densification behavior of Al₂O₃-doped Ce_{0.8}Y_{0.2}O_{1.9} electrolyte composites, *Mater. Sci. Eng. A.* 447 (2007) 222–226. doi:10.1016/j.msea.2006.10.027.

[72] N. Matsui, D. Kagaku, No Title, *J. Electrochem. Soc. Japan.* 58 (1990) 716.

[73] S.S. Lion, W.L. Worrell, Electrical properties of novel mixed-conducting oxides, *Appl. Phys. A Solids Surfaces.* 49 (1989) 25–31. doi:10.1007/BF00615461.

[74] Y.I. Kiyoshi Kobayashi, Yukiharu Kai, Shu Yamaguchi, Norihiko Fukatsu, Tsuyoshi Kawashima, K. Kobayashi, Y. Kai, S. Yamaguchi, N. Fukatsu, T. Kawashima, Y. Iguchi, Electronic conductivity measurements of 5 mol% TiO₂-doped YSZ by a d.c.-polarization technique, *Solid State Ionics.* 93 (1997) 193–199. doi:10.1016/S0167-2738(96)00534-6.

[75] K. Kobayashi, K. Kato, T. Kawashima, S. Yamaguchi, Y. Iguchi, Total Electrical Conductivity Measurements of TiO₂ Doped YSZ Ceramics, *J. Ceram. Soc. Japan.* 106 (1998) 1073.

[76] K. Swider, W. Worrell, Electronic Conduction Mechanism in Ytria- Stabilized Zirconia-Titania under Reducing Atmospheres, *J. Electrochem. Soc.* 143 (1996) 3706–3711. <http://jes.ecsdl.org/content/143/11/3706.short>.

[77] M. Nagano, S. Nagashima, H. Maeda, A. Kato, Sintering behavior of Al₂TiO₅ base ceramics and their thermal properties, *Ceram. Int.* 25 (1999) 681–687.
doi:10.1016/S0272-8842(98)00083-2.

[78] S.W. Sofie, D.R. Taylor, Controlled Thermal Expansion Anode Compositions with Improved Strength for Use in Anode Supported SOFCs, *Adv. Solid Oxide Fuel Cells III.* (2008) 215–223.

[79] C.H. Law, S.W. Sofie, Anchoring of Infiltrated Nickel Electro-Catalyst by Addition of Aluminum Titanate, *J. Electrochem. Soc.* 158 (2011) B1137–B1141.
doi:10.1149/1.3610226.

[80] D.R. Driscoll, M.D. McIntyre, M.M. Welander, S.W. Sofie, R.A. Walker, Enhancement of high temperature metallic catalysts: Aluminum titanate in the nickel-zirconia system, *Appl. Catal. A Gen.* 527 (2016) 36–44.
doi:10.1016/j.apcata.2016.08.020.

[81] D.N. Boccaccini, H.L. Frandsen, S. Soprani, M. Cannio, T. Klemensø, V. Gil, P.V. Hendriksen, Influence of porosity on mechanical properties of tetragonal stabilized zirconia, *J. Eur. Ceram. Soc.* (2018). doi:10.1016/j.jeurceramsoc.2017.09.029.

- [82] Z. Cui, Y. Huang, H. Liu, Predicting the mechanical properties of brittle porous materials with various porosity and pore sizes, *J. Mech. Behav. Biomed. Mater.* 71 (2017) 10–22. doi:10.1016/j.jmbbm.2017.02.014.
- [83] A. Bertei, C. Nicoletta, Percolation theory in SOFC composite electrodes: Effects of porosity and particle size distribution on effective properties, *J. Power Sources.* 196 (2011) 9429–9436. doi:10.1016/j.jpowsour.2011.06.087.
- [84] W.D. Callister, D.G. Rethwisch, *Fundamentals of Materials Science and Engineering: An Integrated Approach*, 5th Editio, Wiley, 2015.
- [85] ASTM C1161-13, Standard Test Method for Flexural Strength of Advanced Ceramics at Ambient Temperature, *ASTM Int.* (2013) 1–19. doi:10.1520/C1161-13.2.
- [86] ASTM C1499-15, Standard Test Method for Monotonic Equibiaxial Flexural Strength of Advanced Ceramics at Ambient Temperature, *ASTM Int.* (2015) 1–19. doi:10.1017/CBO9781107415324.004.
- [87] B. Timurkutluk, M.D. Mat, Effects of anode fabrication parameters on the performance and redox behavior of solid oxide fuel cells, *J. Power Sources.* 258 (2014) 108–116. doi:10.1016/j.jpowsour.2014.02.023.
- [88] H.L. Frandsen, M. Makowska, F. Greco, C. Chatzichristodoulou, D.W. Ni, D.J. Curran, M. Strobl, L.T. Kuhn, P. V. Hendriksen, Accelerated creep in solid oxide fuel cell anode supports during reduction, *J. Power Sources.* 323 (2016) 78–89. doi:10.1016/j.jpowsour.2016.04.097.
- [89] H. Fischer, W. Rentzsch, R. Marx, A modified size effect model for brittle nonmetallic materials, *Eng. Fract. Mech.* 69 (2002) 781–791. doi:10.1016/S0013-7944(01)00126-6.
- [90] B. Charlas, D.W. Ni, H.L. Frandsen, K. Brodersen, M. Chen, Mechanical Properties of Supports and Half-Cells for Solid Oxide Electrolysis Influenced by Alumina-Zirconia Composites, *Fuel Cells.* 17 (2017) 132–143. doi:10.1002/fuce.201600036.
- [91] D.-W. Ni, B. Charlas, K. Kwok, T.T. Molla, P.V. Hendriksen, H.L. Frandsen, Influence of temperature and atmosphere on the strength and elastic modulus of solid oxide fuel cell anode supports, *J. Power Sources.* 311 (2016) 1–12. doi:10.1016/j.jpowsour.2016.02.027.
- [92] B. Charlas, H.L. Frandsen, K. Brodersen, P.V. Henriksen, M. Chen, Residual stresses and strength of multilayer tape cast solid oxide fuel and electrolysis half-cells, *J. Power Sources.* 288 (2015) 243–252. doi:10.1016/j.jpowsour.2015.04.105.
- [93] H.L. Frandsen, T. Ramos, A. Faes, M. Pihlatie, K. Brodersen, Optimization of the strength of SOFC anode supports, *J. Eur. Ceram. Soc.* (2012). doi:10.1016/j.jeurceramsoc.2011.11.015.

- [94] A. Nakajo, J. Kuebler, A. Faes, U.F. Vogt, H.J. Schindler, L.K. Chiang, S. Modena, J. Van Herle, T. Hocker, Compilation of mechanical properties for the structural analysis of solid oxide fuel cell stacks. Constitutive materials of anode-supported cells, *Ceram. Int.* 38 (2012) 3907–3927. doi:10.1016/j.ceramint.2012.01.043.
- [95] M. Radovic, E. Lara-curzio, B. Armstrong, C. Walls, Elastic properties, biaxial strength and fracture toughness of nickel-based anode materials for solid oxide fuel cells, in: *Dev. SOLid Oxide Fuel Cells Lithium Ion Batter.*, 2005: pp. 31–40.
- [96] ASTM C1239-13, Standard Practice for Reporting Uniaxial Strength Data and Estimating Weibull Distribution Parameters for Advanced Ceramics, *ASTM Int.* (2013) 1–9. doi:10.1520/C1239-13.Scope.
- [97] J. Laurencin, G. Delette, F. Lefebvre-Joud, M. Dupeux, A numerical tool to estimate SOFC mechanical degradation: Case of the planar cell configuration, *J. Eur. Ceram. Soc.* 28 (2008) 1857–1869. doi:10.1016/j.jeurceramsoc.2007.12.025.
- [98] A. Nakajo, J. Kuebler, A. Faes, U.F. Vogt, H.J. Schindler, L.K. Chiang, S. Modena, J. Van Herle, T. Hocker, Compilation of mechanical properties for the structural analysis of solid oxide fuel cell stacks. Constitutive materials of anode-supported cells, *Ceram. Int.* 38 (2012) 3907–3927. doi:10.1016/j.ceramint.2012.01.043.
- [99] H.L. Frandsen, T. Ramos, A. Faes, M. Pihlatie, K. Brodersen, Optimization of the strength of SOFC anode supports, *J. Eur. Ceram. Soc.* 32 (2012) 1041–1052. doi:10.1016/j.jeurceramsoc.2011.11.015.
- [100] F. Baratta, W. Matthews, Errors Associated with Flexure Testing of Brittle Materials, *U.S. Army Mater. Technol. Lab.* (1987) 16, 41–42.

CHAPTER TWO

EFFECT OF ALUMINUM TITANATE (Al_2TiO_5) DOPING ON THE MECHANICAL
PERFORMANCE OF SOLID OXIDE FUEL CELL NI-YSZ ANODE

Contribution of Authors and Co-Authors

Author: Madisen McCleary

Contributions: Prepared and mechanically tested samples, compiled and analyzed numerical data, performed fractographic analyzes, generated figures/tables and wrote manuscript.

Co-author: Roberta Amendola

Contributions: Provided insight on experimental design and implementation. Aided in manuscript editing and preparation.

Manuscript Information Page

Madisen McCleary, Roberta Amendola

Status of Manuscript:

- Prepared for submission to a peer-reviewed journal
- Officially submitted to a peer-review journal
- Accepted by a peer-reviewed journal
- Published in a peer-reviewed journal

Published by Fuel Cells (DOI: 10.1002/fuce.201700073)

EFFECT OF ALUMINUM TITANATE (Al_2TlO_5) DOPING ON THE MECHANICAL PERFORMANCE OF SOLID OXIDE FUEL CELL NI-YSZ ANODE

Madisen McCleary, Roberta Amendola*

Montana State University, Mechanical Engineering, 220 Roberts Hall, Bozeman, MT

59717, United States

[*] Corresponding author, Roberta.amendola@montana.edu

Keywords: Ceramics, Doping, Electron Microscopy, Mechanical Properties, Solid State Reactions

Abstract

The mechanical behavior of un-doped and 1-10 wt% aluminum titanate doped NiO-YSZ anodes was evaluated in the oxidized and reduced state of the material. Sample bars 25x5x2 mm were fabricated and tested in a three-point bending apparatus and statistical analyses of the collected data were performed. A remarkable enhancement of the flexural strength was found both for the reduced and oxidized state of the material when compared to the un-doped samples. In both cases, the development of a secondary phase was observed proportional to the doping amount of aluminum titanate. Morphological analyses along with preliminary phase identification and suspected mechanisms for strength enhancement are presented and discussed.

Introduction

A solid oxide fuel cell (SOFC) is an energy conversion device that electrochemically oxidizes a fuel in order to produce electrical power and heat. For several decades, research effort focused on improving the performance of SOFCs to justify its existence and competitiveness within the renewable energy market. With SOFC technology becoming mature, materials selection is an increasingly significant challenge due to the need to find candidates able to offer high performance and durability under operative conditions, while maintaining cost effectiveness and ease of fabrication. In comparison with the electrolyte supported design, anode supported SOFC design is better suited for operation at lower temperatures because lesser ohmic loss and better interface contact can be realized. Recently, there has been growing interest in anode supported SOFCs with excellent single cell performance [1–7]; however, to produce significant power, planar SOFC units must be stacked in electrical series. To maximize the contact between adjacent single cell units, stacks are subjected to high clamping pressures e.g., 65–70 kPa [8,9]. For anode-supported cell, the anode substrate provides the mechanical strength of the stack but in contrast to the vast amount of data available on their electrochemical properties, little fundamental data on the mechanical performance of these systems exist. Due to the inherent brittleness of the dense ion-conducting ceramic membranes, the reliability and robustness of SOFCs depends critically on the thermo-mechanical properties of their components such as coefficient of thermal expansion, elastic behavior and fracture characteristics.

Therefore, it is fundamental to address their mechanical integrity before any stack operation can be undertaken. Despite active search for alternatives, Ni–YSZ composites are widely used as anode components [10,11]. For this reason, a strong YSZ framework able to support the mechanical load under operative conditions is necessary. Several promising substrate materials have been well studied so far [12–20]; however, new compositions require further investigations. The mechanical properties of ceramics are strongly sensitive to variations in materials chemistry and processing methods. The introduction of a second phase, which does not compromise the sintering and electrochemical performance of the anode, has been proven as a successful approach to manipulate the material microstructure enhancing its mechanical performance [6,7,21,22]. A common ceramic manufacturing technique is mechanical mixing of precursor powders with selected particle size followed by an appropriate sintering process. This process easily allows for production of customized formulations, namely the introduction of second phase constituents, without requiring any additional processing.

Previous research reported that appropriate doping level of Al_2O_3 shows a beneficial effect on the sintering behavior as well as on the electrical and mechanical properties of YSZ electrolytes [6,21,23–25]. TiO_2 addition was found to have a similar effect [7,26–30]. Previous research [31–34] has observed that the addition of aluminum titanate Al_2TiO_5 , (ALT) to the Ni/YSZ system stabilizes SOFC performance in terms of slow degradation rates and high power output. Since there is little fundamental data on the mechanical strength and fracture mechanism of ALT doped systems, this study aims

to complement the electrochemical benefits offered by Al_2TiO_5 doping investigating its effect on the mechanical performance of NiO/YSZ and Ni/YSZ anodes.

Experimental

Nickel Oxide (NiO) powder (4 μm , Alfa Aesar) and 8 mol% Yttrium Stabilized Zirconium (8YSZ), powder (300 nm, Tosoh) and Aluminum Titanate (ALT) powder (25 nm, Sigma Aldrich) were used for sample manufacturing. Powders, in the ratio of 34 wt% YSZ, 66 wt% NiO and 0-10 wt% ALT, were mechanically mixed for 24 hours with binder (5 wt% Polyethylene Glycol, Alfa Aesar) and deionized water and subsequently placed in a freeze drier under a vacuum for at least 48 hours to allow sublimation of the water.

Rectangular 25 x 5 x 2 mm samples were manufactured pressing 1.5 grams of powder in a uniaxial hydraulic press under a force of 22 kN for 1 minute. This procedure was developed to produce defect-free samples required for reliable mechanical testing. Thermolysis of pressed samples was performed for 2 hours in ambient air heating at 2°C/min up to 450°C in a box furnace (Thermolyne, 1300). Sintering was conducted with a heating/cooling rate of 5°C/min up to 1400°C and a dwell time of 5 hours (Zircar, Hot Spot 110). Reduction was performed in a tube furnace (Thermo Scientific, Lindberg Blue M) flowing 5% H_2 and 95% N_2 gas, at 800°C for a time sufficient to convert 97 wt% of NiO into metallic nickel. The percentage reduction was evaluated with a Radwag XA 82/220.R2 microscale. Time required for the reduction process varied proportionally to the doping amount of ALT.

Un-doped and 1, 5 and 10 wt% ALT doped batches of 30 oxidized and reduced samples were loaded at a rate of 0.2 mm/min in a three-point bending apparatus (Pasco Scientific 8236) as per ASTM C1161-13 standard. Fracture strength, effective volume V_{eff} , scaled characteristic strength σ_0' , Weibull modulus (m) with normalized upper and lower bounds, and porosity, by alcohol immersion method, were evaluated. Field Emission Scanning electron microscopy (FE-SEM, Zeiss Ultra) microstructural characterization and preliminary Scanning Auger NanoProbe (PHI 710) analyses were conducted to determine the nature of the developed phases and their contribution to the material mechanical strength.

Results and Discussion

Mechanical properties

Tables 1-3 summarize the results for all the tested batches. ALT enhanced the mechanical strength of the material in both the oxidized and reduced state. Pertinent literature reports an average fracture strength between 80 and 130 MPa [20,35] and a Weibull modulus between 5 and 7 [36] for undoped anodes. Most of the values recorded for ALT doped samples fall above these ranges. When compared to the undoped, the oxidized samples showed, for the 5 wt% ALT doped sample, an increase up to 71% of the scaled characteristic strength while for the reduced samples, an increase up to 55% was found for the 10 wt% ALT doped sample.

Table 2.1: Weibull modulus of anode material

	0% ALT	1% ALT	5% ALT	10% ALT
Oxidized (NiO/YSZ)				
m	5.1	3.5	6.9	7.7
90% Confidence Interval	3.8-6.2	2.6-4.3	5.2-8.4	5.8-9.4
Reduced (Ni/YSZ)				
m	7.5	5.6	8.6	10.6
90% Confidence Interval	5.6-9.1	4.2-6.9	6.5-10.5	8.0-12.9

Table 2.2: Mechanical properties of anode material

	0% ALT	1% ALT	5% ALT	10% ALT
Oxidized (NiO/YSZ)				
Average strength σ /MPa	100	136	226	150
$V_{\text{eff}}/\text{mm}^3$	1.8	3.2	1.1	0.9
Scaled Characteristic strength σ_0'/MPa	137	213	234	156
Strength Increase/%	N/A	55	71	14
Reduced (Ni/YSZ)				
Average strength σ /MPa	120	151	164	187
$V_{\text{eff}}/\text{mm}^3$	0.9	1.5	0.7	0.5
Scaled Characteristic strength σ_0'/MPa	120	175	168	186
Strength Increase/%	N/A	46	40	55

Table 2.3: Porosity of anode material

	0% ALT	1% ALT	5% ALT	10% ALT
Oxidized (NiO/YSZ)				
Porosity/%	1.8	1.8	1.9	1.8
Reduced (Ni/YSZ)				
Porosity/%	25.3	23.1	12.5	13.9

Measurement of the fracture strength of bulk ceramic suffers big scatter in the results and must be determined using statistical analyses based on Weibull approach. The

reason for this is that mechanical failure is recognized to be microstructure sensitive, and the weakest spot under stress determines the strength of a brittle material. Figure 1 shows Weibull plots for both the oxidized and reduced sample batches while Table 1 summarizes the Weibull modulus values calculated as the slope of the Weibull plots. The normalized upper and lower bounds on the maximum likelihood estimate of the Weibull modulus (90% confidence interval) has been determined per ASTM C1239 – 13 for batches of 30 samples [37–39]. The Weibull modulus indicates the nature, severity and dispersion of flaws and is used for statistical comparison of the relative quality of two or more test data sets to predict the probability of failure [9,35,40]. A high Weibull modulus is desirable for all materials since it indicates an increased homogeneity in the flaw population and a more predictable failure. On the contrary, a low Weibull modulus is indicative of a large spread within the group and a less predictable failure behavior. Basing on these assumptions, the 10 wt% ALT doped samples seems to offer the best mechanical performance in both the oxidized and reduced stat

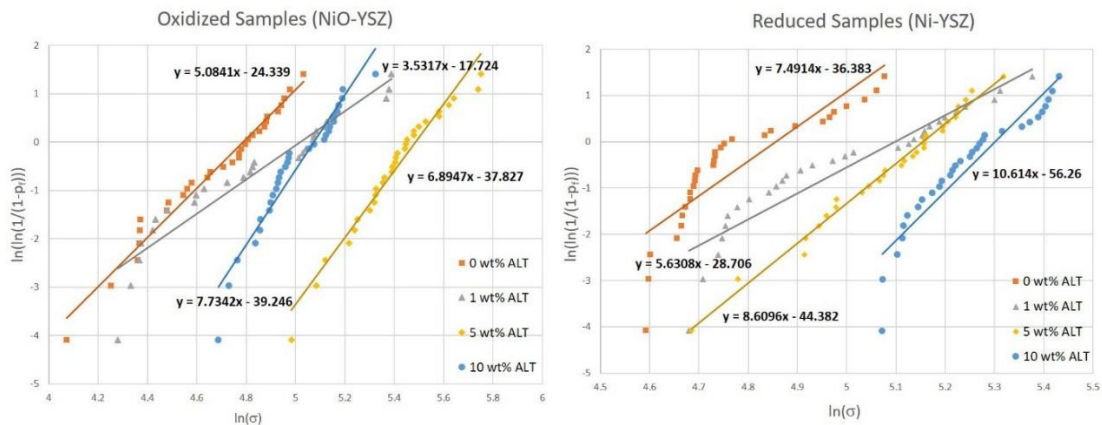


Figure 2.1: Weibull plots of NiO-YSZ (oxidized) and Ni-YSZ (reduced) samples

The Weibull approach considers that the weakest spot under tension determines the strength of the sample. Thus, the measured strength is larger if the tested volume is smaller, giving a wrong impression of a stronger material. Therefore, it is important to account for the effective volume V_{eff} while analyzing the results because the probability to apply stress to a flaw increases if the tested volume under tension is larger [35,41–44]. The effective volume is defined by Equation 1 while Equation 2 defines the scaled characteristic strength [41].

$$V_{eff} = \frac{lwh}{2(m+1)^2} \quad (1)$$

$$\sigma'_0 = \sigma_0 \left(\frac{V_{eff}}{1 \text{ mm}^3} \right)^{\frac{1}{m}} \quad (2)$$

Where l is the distance between support points, w and h are the width the height of the sample, m is the Weibull modulus, and σ_0 is the characteristic strength corresponding to ~63% probability of failure.

Table 2 compares the strength results scaled to the same effective volume of 1 mm^3 . When compared to the undoped, the oxidized samples showed, for the 5 wt% ALT doped sample, an increase up to 71% of the scaled characteristic strength while for the reduced samples, an increase up to 55%. The strength of ceramic is dependent on the porosity distribution within the material [19,20,37,42,43] since the presence of one or more pores in the loaded volume will result is a more fragile material. Table 3 summarizes the porosity values measured for all of the tested batches. For the oxidized samples, despite the fact that changes in the scaled characteristic strength and m were observed, a constant value of the porosity ~1.8% was found. Previous findings [45]

reported that, for samples with a porosity lower than 10%, any discontinuation in the bulk material, as processing induced flaws and/or presence of secondary phases, play a more important role in the failure of the material rather than pores. Variations of size, shape and orientation of these flaws result in a large scatter of the strength data [46]. Due to the nature of the doped material, formation of secondary phases with mechanical properties and composition different from the undoped material and dependent on the ALT amount, is most probably responsible for the increased strength and will be discussed later.

Reduced samples reflect these observations having a porosity between ~12% and 25%, a Weibull modulus between 6 and 11 and a scaled characteristic strength between 120 and 186 MPa. Fan et al. [45] found that ceramic materials with porosity between 10 and 55% resulted in Weibull modulus values in the range between 4 and 11 with a medium to high scatter in the fracture strength regardless of the composition, grain size, testing techniques or surface finish of the specimens. The failure of these kind of materials has been linked to the pore evolution during sintering process. Since the reduction time of the doped samples, when compared to the undoped, was found to be dependent on the amount of ALT; it is thought that, in addition to second phase formation and evolution, the kinetics of the reduction process, where the oxygen release is responsible for the pore formation, plays a fundamental role in defining the ultimate mechanical strength of the material.

Basing on the above discussion there is a clear need to correlate microstructure, Weibull modulus and scaled characteristic strength to define which material is the most reliable in terms of mechanical performance. The highest Weibull modulus was

calculated for 10 wt% ALT doped samples both in the oxidized and reduced states of the material; however, the highest characteristic strength was measured for the 5 wt% ALT doped samples in the oxidized state. Weibull modulus data is limited in the literature and the correlation between the porosity and fracture properties is not clear because of different sensitivity to local features of the crack field geometry [37,47,48].

Figure 1 Weibull plots present a medium to high scatter in the fracture strength data for most of the materials, which will result in the need to include high safety factors in their designs. The 5 wt% ALT doped samples present the lowest strength data scattering both in the oxidized and reduced state suggesting this material as the most reliable one.

The investigation of the reduced materials, showed that a decrease in the porosity corresponds to an increase in the scaled characteristic strength; however, it should be noted that reduction in porosity will reduce the anode catalytic activity. Therefore, investigation of the dependence of fracture stress on other factors, such as pore shape and size is needed and will be of great significance.

Microstructural analyses

Field Emission Scanning Electron Microscopy (FE-SEM) was performed on samples' surface and cross sections. Cross section morphologies confirmed trans-granular fracture for all batches and can be seen in Figures 2 and 3. Figure 4 a-d shows the surface microstructure of the NiO-YSZ samples with 0, 1, 5, and 10 wt% ALT. It can be observed (circled areas of Figure 4b-d) that a secondary phase, here defined as the "rough

phase”, developed proportionally to the doping amount of ALT. A similar microstructure defined as “undulated” was found for TiO_2 doped YSZ material [7].

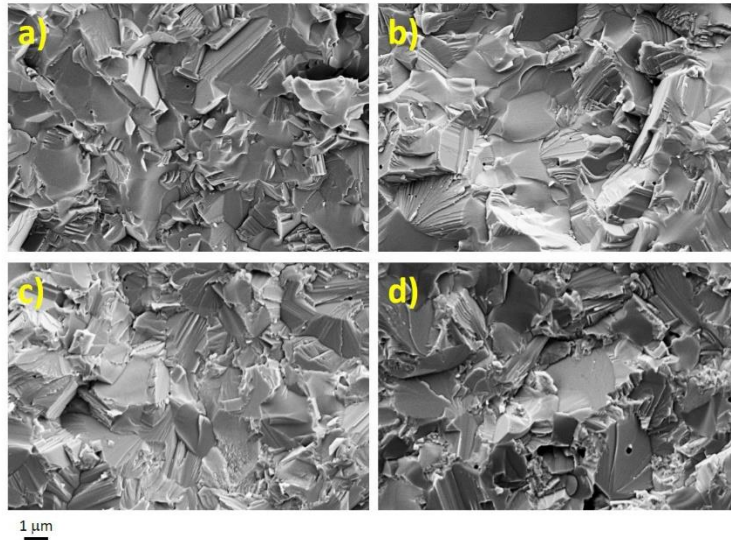


Figure 2.2: FE-SEM cross sectional image of NiO-YSZ + (a) 0 wt%, (b) 1 wt%, (c) 5 wt%, and (d) 10 wt%

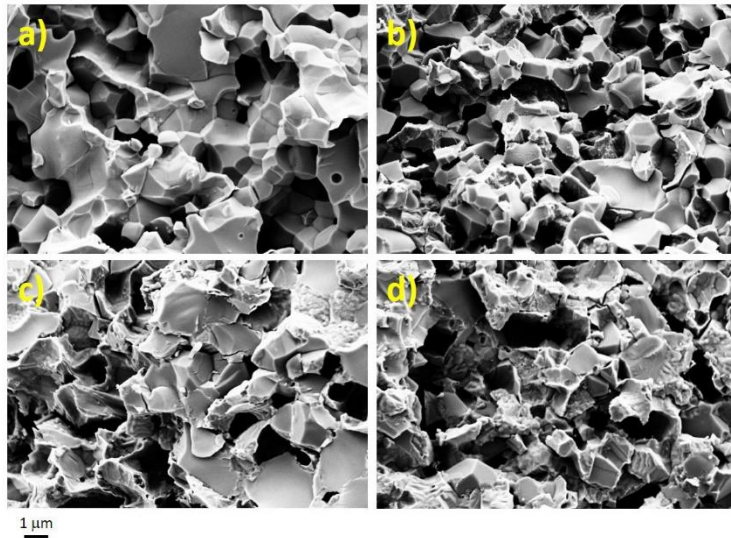


Figure 2.3: FE-SEM cross sectional image of Ni-YSZ + (a) 0 wt%, (b) 1 wt%, (c) 5 wt%, and (d) 10 wt% ALT

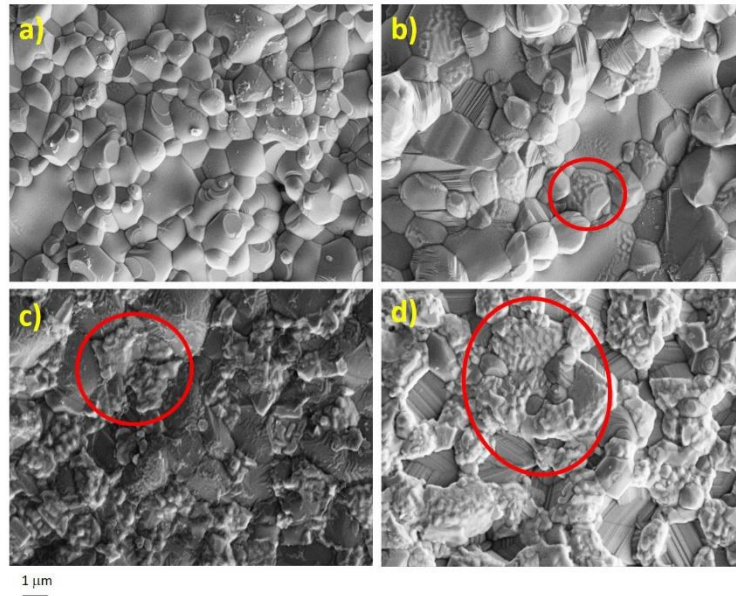


Figure 2.4: FE-SEM surface image of NiO-YSZ + (a) 0 wt%, (b) 1 wt%, (c) 5 wt%, and (d) 10 wt% ALT

Figure 5 a-d shows the surface microstructure of the Ni-YSZ samples with 0, 1, 5, and 10 wt% ALT. The presence of the “rough phase” is confirmed however, a new phase starts to develop as small particles (circled in Figure 5c) in the 5 wt% ALT doped sample and its amount is increased (circled in Figure 5d) in the 10 wt% doped ALT sample. To relate the comparison of the new phases with the increased mechanical strength, preliminary Scanning Auger Nanoprobe analyses were performed on samples’ surface. Figure 6 shows the Auger map collected on the same area with two different element overlays for a Ni-YSZ + 10 wt% ALT sample. Figure 6b shows that the nickel particles, about 1 μm in size (blue areas), are decorated with a layered structure specifically, an immediately adjacent titanium based layer followed by an aluminum based layer; also, the small particle phase is revealed to be nickel clustered on an aluminum substrate. The

“rough phase” is indicated to be titanium preferentially distributed within the zirconium which is found to fill the area between the nickel particles (Figure 6c).

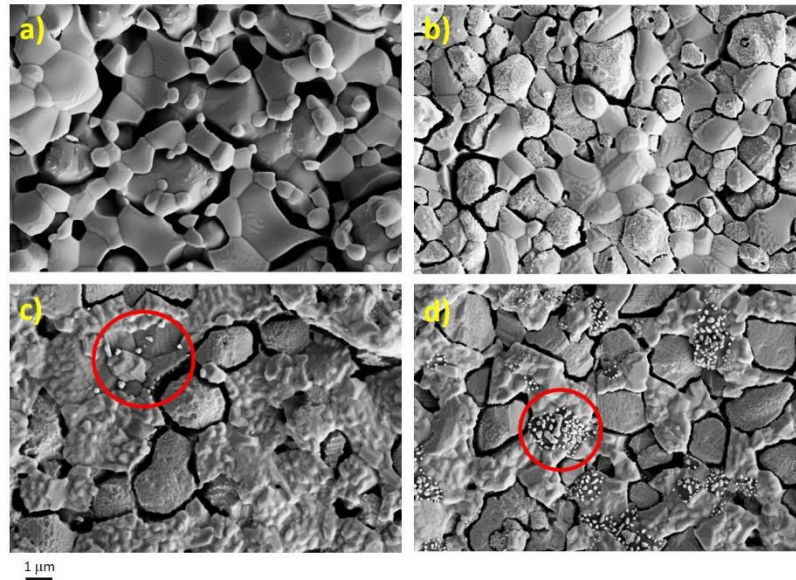


Figure 2.5: FE-SEM surface image of Ni-YSZ + (a) 0 wt%, (b) 1 wt%, (c) 5 wt%, and (d) 10 wt% ALT

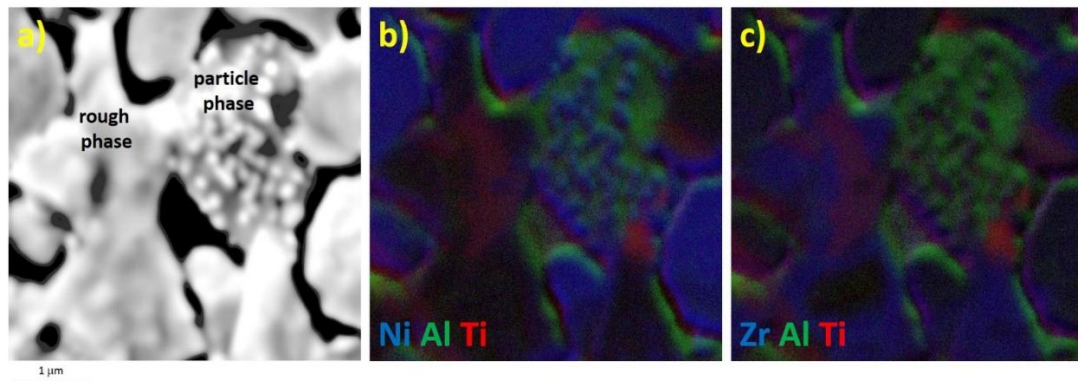


Figure 2.6: Auger elemental map of Ni-YSZ + 10 wt% ALT sample surface: (a) details of mapped areas, (b) Nickel-Blue, Titanium-Red, Aluminum-Green, and (c) Zirconium-Blue, Titanium-Red, Aluminum-Green

In the presented manufacturing conditions, ALT spontaneously decomposes to Al_2O_3 and TiO_2 [31,34,49–51]. Part of the Al_2O_3 initially reacts with NiO to form

NiAl_2O_4 [6,33,34,43,52] proportionally to the amount of Al_2O_3 made available through ALT doping. For the oxidized samples, an enhancement of the scaled characteristic strength was observed for all of the ALT doping amounts. NiAl_2O_4 is expected to have a positive impact on the material strength due to its higher stiffness than YSZ [43,53]. Previous research showed that the threshold amount of Al_2O_3 doping to enhance the flexural strength was 3 wt% [6] which corresponds to ~6 wt% ALT doping. This well relates to the difference in the calculated scaled characteristic strength where the highest and lowest values were found for the 5 wt% (~2.5 wt% Al_2O_3) and the 10 wt% (~5 wt% Al_2O_3), which are respectively below and above the defined threshold. In the oxidized state, the anode material is a composite where NiO, YSZ, Al_2O_3 , and NiAl_2O_4 have different thermal expansion coefficients; which, at a microstructural scale, will cause internal residual stresses contributing to a decrease in strength of the support [43,53].

TiO_2 is thought to react with YSZ enhancing its sintering characteristics [7,33,34] and leading to the formation of a solid YSZ framework [7] here defined as the “rough phase”, which enlarges proportionally to the amount of ALT. Tetragonal domains in the cubic phase were found for TiO_2 doping [7,34,54] and have been confirmed for ALT doping [34]. In addition to second phase formation, the enhanced mechanical strength, could also be related to the volume change resulting from a tetragonal to monoclinic stress-induced phase transformation [7] caused by the discussed thermal expansion mismatch. Further research is needed to quantify residual stresses and clarify the relationship between second phase development and YSZ phase transformation.

Figures 4 and 5 show almost no morphological difference in the Ti-YSZ framework (rough phase) before and after reduction; thus, it is thought that it persists without modification. The differences observed in the scaled characteristic strength are; therefore, to be correlated with the reduction of NiO and NiAl₂O₄. The reduction of NiO to Ni is expected to increase the mechanical strength because of added ductility into the ceramic system. Despite Ni formation, the scaled characteristic strength for undoped reduced samples, when compared to the corresponding oxidized ones, is decreased due to quick reduction time (~3 hours) and associated porosity development (Table 3).

Previous research has shown that NiAl₂O₄ at 800°C in reducing atmosphere has very low reaction kinetics and cannot be reduced during short times (less than 10 hours) [43]. In the 1 wt% ALT doped samples, the scaled characteristic strength is increased when compared to the undoped samples due to NiAl₂O₄ forming and persisting upon reduction (~5 hours); however, this value is lower than that calculated for the oxidized sample due to high porosity. The formation of NiAl₂O₄ depletes the system of available NiO for reduction resulting in a lower porosity when compared to the undoped samples. Under long term exposure, NiAl₂O₄ could progressively be reduced into Ni and Al₂O₃ at 800°C [43]. The decrease in porosity from 23.1% (1 wt% ALT) to 12.5% suggests that for the 5 wt% ALT doped samples, the amount of NiAl₂O₄ is largely increased. The reduction process of the 5 wt% ALT doped samples required ~12 hours which could allow for initial reduction of NiAl₂O₄. Figure 5 supports this, showing that small particles are developing on the sample surface and are believed to be Ni nanoparticles [6,43,55]. Despite the decreased porosity, the scaled characteristic strength is found to be lower than

for the 1 wt% ALT doped samples; this can be explained by the fact that the reduction of NiAl_2O_4 is accompanied by a theoretical volume shrinkage of ~18% that can generate residual stresses detrimental to the system [56].

The reduction for the 10 wt% ALT doped samples was achieved after ~40 hours. This drastic increase in the reaction time is to be correlated with the partial reduction of NiAl_2O_4 . Figure 5d shows a substantial increase in the small particle phase and Figure 6 confirms the presence of Ni nanoparticles within an Al_2O_3 matrix. The Al_2O_3 layer observed in Figure 6b-c around the nickel particles is also probably generated during this process. The nature of the Ti layer immediately adjacent to the nickel particles is yet to be identified. The slight increase in porosity is related to the increased oxygen release while the highest scaled characteristic strength is due to the increase in nickel acting either as crack deflector or stopping the crack propagation due to its ductility [43,55–57]. Experimental measurements showed that the volume decrease during the reduction of NiAl_2O_4 is between 3 and 9% instead of the theoretical 18% indicating that the system, if given enough time, finds a mechanism to avoid generating large volume changes and relaxes the stresses associated with the reduction reaction [56]. This phenomenon can be explained with the interface between the Ni particles and Al_2O_3 , withstanding large stresses from a large coefficient of thermal expansion mismatch, while the interface between the unreduced NiAl_2O_4 and the two-phase mixture of Ni and Al_2O_3 withstanding large volume changes [55].

Despite this work demonstrating the enhanced mechanical strength and reliability of ALT doped materials, the authors understand that further research is needed for the

optimization of the system in fuel cell operative conditions including the evaluation of electrochemical properties and redox cycling.

Conclusions

This study has demonstrated that ALT doping can enhance the mechanical properties of Ni-YSZ systems. Despite the uncertainty of the Weibull modulus falling within the range of those for the other compositions, the Weibull plots showed that the 5 wt% ALT doped samples present the lowest strength data scattering both in the oxidized and reduced state suggesting this material as the most reliable one. The enhanced scaled characteristic strength resulting from ALT addition has been related to the development of secondary phases: Al_2O_3 reacts with NiO to form NiAl_2O_4 while TiO_2 preferentially reacts with YSZ to form a solid YSZ framework defined as the “rough phase”, which enlarges proportionally to the amount of ALT and persists upon reduction. The mechanical behavior of the reduced samples has been related to the presence of NiAl_2O_4 and its partial reduction leading to the formation of Ni nanoparticles within an Al_2O_3 matrix. This work has highlighted the need for further investigation of relationship between mechanical properties and microstructural factors, such as pore shape and size as well as on the quantification of residual stresses and clarification of their effect on second phase development and transformations. Despite this work demonstrating the enhanced mechanical strength and reliability of ALT doped materials, the authors understand that, for the materials to be optimized, more testing in fuel cell operative conditions, including the evaluation of electrochemical properties and redox cycling, is needed.

Acknowledgements

This work was supported by the DOE under award no. DEFE0026192. FE-SEM and Scanning Auger Nanoprobe data were collected at the MSU Image and Chemical Analysis Laboratory.

References

- [1] F. Zhao, A. V. Virkar, *J. Power Sources* **2005**, 141, 79.
- [2] A.C. Müller, D. Herbstritt, E. Ivers-Tiffée, *Solid State Ionics* **2002**, 152–153, 537.
- [3] Z.R. Wang, J.Q. Qian, S.R. Wang, J.D. Cao, T.L. Wen, *Solid State Ionics* **2008**, 179, 1593.
- [4] T. Setoguchi, K. Okamoto, K. Eguchi, H. Arai, *J. Electrochem. Soc.* **1992**, 139, 2875.
- [5] M. Kleitz, F. Petitbon, *Solid State Ionics* **1996**, 92, 65.
- [6] C.R. He, W.G. Wang, *Fuel Cells* **2009**, 9, 630.
- [7] M. Mori, Y. Hiei, H. Itoh, G.A. Tompsett, N.M. Sammes, *Solid State Ionics* **2003**, 160, 1.
- [8] T. Dey, D. Singdeo, M. Bose, R.N. Basu, P.C. Ghosh, *J. Power Sources* **2013**, 233, 290.
- [9] T. Dey, A. Dey, P.C. Ghosh, M. Bose, A.K. Mukhopadhyay, R.N. Basu, *Mater. Des.* **2014**, 53, 182.
- [10] M. Pihlatie, A. Kaiser, M. Mogensen, *J. Eur. Ceram. Soc.* **2009**, 29, 1657.
- [11] N. Mahato, A. Banerjee, A. Gupta, S. Omar, K. Balani, *Prog. Mater. Sci.* **2015**, 72, 141.
- [12] J. Wei, G. Pećanac, J. Malzbender, *Ceram. Int.* **2014**, 40, 15371.
- [13] G. Pećanac, S. Baumann, J. Malzbender, *J. Memb. Sci.* **2011**, 385–386, 263.
- [14] G. Pećanac, L. Kiesel, R. Kriegel, J. Malzbender, *Ceram. Int.* **2014**, 40, 1843.
- [15] A. Atkinson, A. Selçuk, *Solid State Ionics* **2000**, 134, 59.
- [16] M. Lipińska-Chwałek, L. Kiesel, J. Malzbender, *J. Eur. Ceram. Soc.* **2014**, 34, 2519.
- [17] B.X. Huang, V. Vasechko, Q.L. Ma, J. Malzbender, *J. Power Sources* **2012**, 206, 204.
- [18] S. Giraud, J. Canel, *J. Eur. Ceram. Soc.* **2008**, 28, 77.
- [19] M. Radovic, E. Lara-curzio, *J. Am. Ceram. Soc.* **2004**, 87, 2242.
- [20] M. Radovic, E. Lara-Curzio, *Acta Mater.* **2004**, 52, 5747.
- [21] Y. Ye, J. Li, H. Zhou, J. Chen, *Ceram. Int.* **2008**, 34, 1797.
- [22] R. Kubrin, G. Blugan, J. Kuebler, *J. Eur. Ceram. Soc.* **2017**, 37, 1651.

- [23] S. Tekeli, *Mater. Des.* **2006**, 27, 230.
- [24] J.S. Lee, K.H. Choi, B.K. Ryu, B.C. Shin, I.S. Kim, *Ceram. Int.* **2004**, 39, 807.
- [25] H. Xu, H. Yan, Z. Chen, *Mater. Sci. Eng. A* **2007**, 447, 222.
- [26] N. Matsui, D. Kagaku, *J. Electrochem. Soc. Japan* **1990**, 58, 716.
- [27] S.S. Lion, W.L. Worrell, *Appl. Phys. A Solids Surfaces* **1989**, 49, 25.
- [28] Y.I. Kiyoshi Kobayashi, Yukiharu Kai, Shu Yamaguchi, Norihiko Fukatsu, Tsuyoshi Kawashima, K. Kobayashi, Y. Kai, S. Yamaguchi, N. Fukatsu, T. Kawashima, Y. Iguchi, *Solid State Ionics* **1997**, 93, 193.
- [29] K. Kobayashi, K. Kato, T. Kawashima, S. Yamaguchi, Y. Iguchi, *J. Ceram. Soc. Japan* **1998**, 106, 1073.
- [30] K. Swider, W. Worrell, *J. Electrochem. Soc.* **1996**, 143, 3706.
- [31] M. Nagano, S. Nagashima, H. Maeda, A. Kato, *Ceram. Int.* **1999**, 25, 681.
- [32] S.W. Sofie, D.R. Taylor, *Adv. Solid Oxide Fuel Cells III* **2008**, 215.
- [33] C.H. Law, S.W. Sofie, *J. Electrochem. Soc.* **2011**, 158, B1137.
- [34] D.R. Driscoll, M.D. McIntyre, M.M. Welander, S.W. Sofie, R.A. Walker, *Appl. Catal. A Gen.* **2016**, 527, 36.
- [35] A. Nakajo, J. Kuebler, A. Faes, U.F. Vogt, H.J. Schindler, L.K. Chiang, S. Modena, J. Van Herle, T. Hocker, *Ceram. Int.* **2012**, 38, 3907.
- [36] J. Laurencin, G. Delette, F. Lefebvre-Joud, M. Dupeux, *J. Eur. Ceram. Soc.* **2008**, 28, 1857.
- [37] Z. Cui, Y. Huang, H. Liu, *J. Mech. Behav. Biomed. Mater.* **2017**, 71, 10.
- [38] D. Wu, Y. Li, J. Zhang, L. Chang, D. Wu, Z. Fang, Y. Shi, *Chem. Eng. Sci.* **2001**, 56, 7035.
- [39] A. Khalili, K. Kromp, *J. Mater. Sci.* **1991**, 26, 6741.
- [40] H. Peterlik, *J. Fo Ceram. Soc. Japan* **2001**, 109, 121.
- [41] H. Fischer, W. Rentzsch, R. Marx, *Eng. Fract. Mech.* **2002**, 69, 781.
- [42] H.L. Frandsen, T. Ramos, A. Faes, M. Pihlatie, K. Brodersen, *J. Eur. Ceram. Soc.* **2012**, 32, 1041.
- [43] B. Charlas, D.W. Ni, H.L. Frandsen, K. Brodersen, M. Chen, *Fuel Cells* **2017**, 17, 132.
- [44] F. Baratta, W. Matthews, *U.S. Army Mater. Technol. Lab.* **1987**, 16.
- [45] X. Fan, E.D. Case, F. Ren, Y. Shu, M.J. Baumann, *J. Mech. Behav. Biomed.*

Mater. **2012**, 8, 21.

- [46] D.F. Wu, J.C. Zhou, Y.D. Li, *Chem. Eng. Res. Des.* **2006**, 84(A12), 1152.
- [47] A. Caiulo, M. Kachanov, *Int. J. Fract.* **2010**, 164, 155.
- [48] G. Bruno, M. Kachanov, *J. Am. Ceram. Soc.* **2016**, 99, 3829.
- [49] I.M. Low, D. Lawrence, R.I. Smith, *J. Am. Ceram. Soc.* **2005**, 88, 2957.
- [50] G. Tilloca, *J. Mater. Sci.* **1991**, 26, 2809.
- [51] B. Freudenberg, A. Mocellin, *J. Am. Ceram. Soc.* **1987**, 70, 33.
- [52] J. Zygmuntowicz, P. Wiecinska, A. Miazga, K. Konopka, *J. Therm. Anal. Calorim.* **2016**, 125, 1079.
- [53] D.-W. Ni, B. Charlas, K. Kwok, T.T. Molla, P.V. Hendriksen, H.L. Frandsen, *J. Power Sources* **2016**, 311, 1.
- [54] L.S.M. Traqueia, T. Pagnier, F.M.B. Marques, *J. Eur. Ceram. Soc.* **1997**, 17, 1019.
- [55] E. Üstündağ, R. Subramanian, R. Dieckmann, S.L. Sass, *Acta Mater.* **1995**, 43, 383.
- [56] E. Üstündağ, Z. Zhang, M.L. Stocker, P. Rangaswamy, M.A.M. Bourke, J.A. Roberts, S. Subramanian, K.E. Sickafus, S.L. Sass, *Mater. Sci. Eng. A* **1997**, 238, 50.
- [57] M. Lieberthal, W.D. Kaplan, *Mater. Sci. Eng. A* **2001**, 302, 83.

CHAPTER THREE

INVESTIGATION OF THE KINETICS OF THE SOLID-STATE REDUCTION
PROCESS OF UNDOPED AND ALUMINUM TITANATE (Al_2TIO_5) DOPED NIO-
YSZ ANODES FOR SOLID OXIDE FUEL CELLS

Contribution of Authors and Co-Authors

Author: Madisen McCleary

Contributions: Prepared and tested samples, compiled and analyzed numerical data, generated figures/tables and wrote manuscript.

Co-author: Roberta Amendola

Contributions: Provided insight on experimental design and implementation. Aided in manuscript editing and preparation.

Manuscript Information Page

Madisen McCleary, Roberta Amendola

Status of Manuscript:

- Prepared for submission to a peer-reviewed journal
- Officially submitted to a peer-review journal
- Accepted by a peer-reviewed journal
- Published in a peer-reviewed journal

Published by Ceramics International (DOI: 10.1016/j.ceramint.2018.05.218). Accepted with no revisions required.

INVESTIGATION OF THE KINETICS OF THE SOLID-STATE REDUCTION
PROCESS OF UNDOPED AND ALUMINUM TITANATE (Al_2TiO_5) DOPED NIO-
YSZ ANODES FOR SOLID OXIDE FUEL CELLS

Madisen McCleary^a, Roberta Amendola^{a*}

^aMontana State University, Mechanical Engineering, 220 Roberts Hall, Bozeman, MT
59717, United States

*Corresponding author: roberta.amendola@montana.edu, 1 (406) 994-6963

Keywords: Kinetics, E. Fuel cells, D. Al_2TiO_5 , B. Electron microscopy

Abstract

Undoped and 1-10 wt.% aluminum titanate, Al_2TiO_5 , (ALT) doped nickel oxide/yttria-stabilized zirconia (NiO/YSZ) anode materials were kinetically evaluated during isothermal (800°C) H_2 reduction (5% H_2 -95% N_2 and pure H_2 gas). It was found that the two parameter Avrami-Erofe'ev model (AEn) was the most successful in representing reduction kinetics. The reduction mechanisms have been identified as the formation and growth of nuclei and is maintained after aluminum titanate, Al_2TiO_5 , (ALT) doping and when the H_2 concentration in the gas flow is increased. ALT doped samples result in the formation of NiAl_2O_4 ; which, when present in sufficient amounts, slowly reduces causing a shift of the model from the experimental data. This phenomenon has been correlated, through microstructural evaluation, to the formation of Ni nanoparticles. In all investigated cases, the reduction kinetics of the system was accelerated when the H_2 concentration was increased from 5% to 100%.

Introduction

Solid oxide fuel cells (SOFCs) are electrochemical devices that convert chemical energy of gaseous fuels into electrical power. SOFCs have high efficiency, low emissions and are fuel flexible [1-6]. Current research efforts in the area of materials development for SOFCs are focused on decreasing the operating temperature from 1000°C (high temperature SOFCs) to 600–800°C (intermediate temperature SOFCs) to reduce material costs and improve the performance stability. In SOFCs, the anode is the electrode for the electrochemical oxidation of fuels such as hydrogen and natural gas. To minimize the polarization losses of the H₂ oxidation reaction, anode materials should possess high electronic conductivity, sufficient electrocatalytic activity, chemical stability and thermal compatibility with other cell components along with having sufficient porosity for efficient gas transportation [1,2]. Recently, there has been growing interest in anode supported SOFCs because of the better performance at lower temperatures due to decreased ohmic loss achieved through improved interface contact [3–9].

Today, nickel oxide (NiO) and yttria-stabilized zirconia (Y₂O₃ doped ZrO₂, YSZ) powders are still the most common precursors for the manufacturing of SOFCs anodes [3–11]. When the SOFC starts operation, the NiO is reduced to Ni metal at the operating temperature. The reduction process, along with the subsequent Ni behavior in hydrogen, are of vital importance in SOFCs since they determine the structure and performance of the electronic conductor.

The reduction of NiO particles in H₂ begins with an induction period during which nucleation of metallic clusters takes place. Clusters then grow into crystallites at an

approximately linear rate [12,13]. The volume decrease associated with a change from NiO to Ni induces an increase in anode porosity [14]. The reduction then continues at the interface between NiO and the previously reduced porous Ni. At temperatures over 600°C, sintering of the porous Ni takes place [15–17]. The anode material after reduction is a cermet that consists of three percolating interconnected phases: YSZ that constitutes the stable ceramic backbone, metallic Ni that enables the electrical, catalytic and electrochemical properties, and porosity that ensures gas communication [11,17–20]. The electrochemical activity of the cermet for H₂ oxidation depends strongly on the triple phase boundary (TPB) areas where fuel gas, Ni and YSZ phases meet [21,22]. Despite the excellent electrocatalytic properties, the Ni/YSZ cermet suffers degradation due to Ni coarsening related to the high SOFCs operating temperatures. This phenomenon compromises the cermet's continuous electronic pathways because of the decrease in the TPB area and, in turn, becomes detrimental to the SOFC longevity and performance [23–27].

Previous research [25,28–32] has observed that the addition of aluminum titanate, Al₂TiO₅ (ALT), to the Ni/YSZ system stabilizes SOFC performance in terms of slow degradation rates, high power output and improved mechanical strength. Characterization of this system has provided insight into the formation of secondary phases, namely ZrTiO₄, Zr₅Ti₇O₂₄ and NiAl₂O₄, which are proposed to contribute to improved catalyst thermal resilience, mechanical strength as well as processing conditions. At 800 °C in reducing atmosphere, the Zr/Ti phases remain unaltered [25,30,32]. NiAl₂O₄ has instead

very low reaction kinetics and, after at least 10 hours, is progressively reduced to nanosized Ni particles and Al_2O_3 [32,33].

Understanding of the intrinsic kinetics of NiO reduction is crucial for designing efficient SOFC anode materials. Hydrogen reduction of NiO is a complex process, which includes a variety of topological and morphological factors; although a breadth of literature [10,34–41] exists on the topic, the microstructural evolution and its relation to the kinetic models is not well understood. Moreover, most of the published kinetics is limited to the investigation of NiO. This study aims to relate kinetic models with the development of secondary phases observed in ALT doped NiO systems. The suitability of Avrami, geometrical contraction and diffusion-controlled models is investigated and supported by complementary microstructural analyses.

Methods

Experimental

Nickel oxide (NiO) powder (4 μm , Alfa Aesar) and 8 mol.% yttrium stabilized zirconium (8YSZ), powder (300 nm, Tosoh) and aluminum titanate (ALT) powder (25 nm, Sigma Aldrich) were used for sample manufacturing. Powders, in the ratio of 34 wt.% YSZ, 66 wt.% NiO and 0, 1, 5, 10 wt.% ALT, were mechanically mixed for 24 hours with binder (5 wt.% polyethylene glycol, Alfa Aesar) and deionized water and subsequently placed in a freeze drier under a vacuum for at least 48 hours to allow sublimation of the water. Rectangular 25 x 5 x 2 mm samples were manufactured pressing 1.5 grams of powder in a uniaxial hydraulic press under a force of 22 kN for 1 minute. Thermolysis of pressed samples was performed for 2 h in ambient air heating at 2

$^{\circ}\text{C min}^{-1}$ up to 450°C in a box furnace (Thermolyne, 1300). Sintering was conducted with a heating/cooling rate of $5^{\circ}\text{C min}^{-1}$ up to $1,400^{\circ}\text{C}$ and a dwell time of 5 hours (Zircar, Hot Spot 110).

In the presented manufacturing conditions, ALT spontaneously decomposes to Al_2O_3 and TiO_2 [30]. The Al_2O_3 initially reacts with NiO to form NiAl_2O_4 [25,30,33,42] as follows:



Basing on reaction 1, the system is depleted of an amount of NiO proportional to the Al_2O_3 introduced with ALT doping. The amount of NiO available for reduction has therefore been evaluated accounting for NiAl_2O_4 formation.

Reduction was performed in a tube furnace (Thermo Scientific, Lindberg Blue M) for a time sufficient to convert 97 wt.% of NiO into metallic Ni. For this process, the Ni:O ratio was considered to be 1:1. Separate sets of experiments were conducted at 800°C , using 5% H_2 -95% N_2 gas and pure hydrogen for preliminary evaluation of the hydrogen concentration effect. The percentage reduction was evaluated with a Radwag XA 82/220.R2 microscale.

Field emission scanning electron microscopy (FE-SEM, Zeiss Ultra) microstructural characterization was conducted to determine the nature of the developed phases and their contribution to the materials' reduction kinetics.

Kinetic models

NiO reduction is a solid-state reaction which may be represented by different models governed by specific kinetic mechanisms including:

- Reaction-order models (F), assuming a homogeneous reaction process;
- Geometrical contraction models (R), based on a shrinking core model with phase-boundary reaction control of different geometries;
- Diffusion-limited models (D), where the reaction rate is controlled by the transport of reactants and products to and from the active interface;
- Avrami-Erofe'ev nucleation models (AE), involving the formation and growth of nuclei, where the reaction occurs.

The models' description and nomenclature is the same used by Zhou et al. [43] and is maintained here for consistency with available literature. For preliminary model selection, the Hancock-Sharp method [44] was used to evaluate the Avrami-Erofe'ev exponent [45–47] “n”.

The Hancock and Sharp method is based on the Avrami-Erofe'ev nucleation model [45] expressed by Equations 2 and 3:

$$y = 1 - \exp(-kt^n) \quad (2)$$

$$y = \frac{W_{ox} - W_t}{W_{ox} - W_{red}} \quad (3)$$

Where “y” is the NiO fraction transformed in Ni, W_{ox} is the initial weight of the sample, W_{red} is the theoretical fully reduced weight, W_t is the sample weight at a specific time,

“k” is the temperature dependent constant, “t” is time, and “n” is the Avrami-Erofe’ev exponent. Determination of the constants is based on Equation 4 straight-line model:

$$\ln(-\ln(1-y)) = n * \ln(t) + \ln(k) \quad (4)$$

$\ln(-\ln(1-y))$ is then plotted versus $\ln(t)$. The Avrami-Erofe’ev exponent “n” is the slope of the line and $\ln(k)$ is the x-intercept. Calculated values were then matched with available literature [43] to discriminate between the models and identify the reaction mechanisms. The suitability of the identified models was verified by the fitting of the experimental data on a y (fraction reduced) vs t (time) plot.

Results and discussion

Figure 1 shows the Hancock-Sharp plots used to evaluate the Avrami-Erofe’ev exponent “n” presented in Table 1. Data points were collected during the reduction (at least 97% of the initial NiO amount) of undoped and 1-10 wt% ALT doped NiO/YSZ anode material, when 5% H₂-95% N₂ gas (a) and pure hydrogen (b) were used.

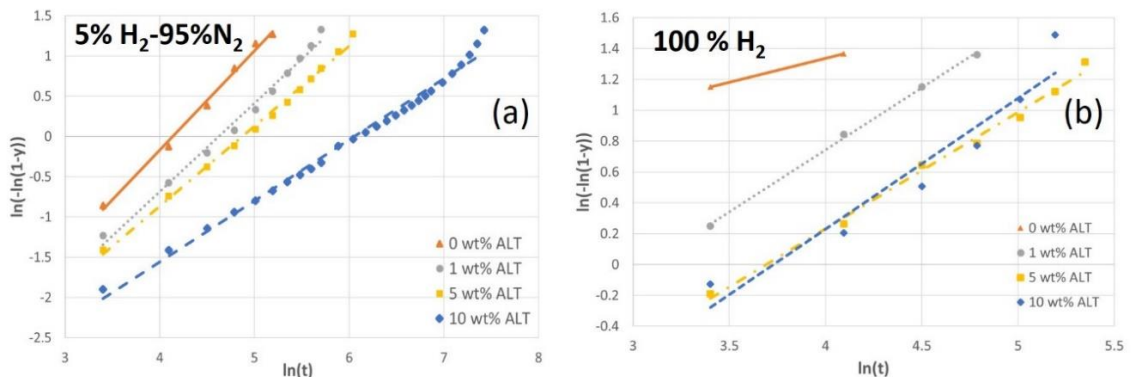


Figure 3.1: Plot of the Hancock and Sharp method for the reduction of undoped and 1-10 wt.% ALT doped NiO-YSZ at 800°C by 5% H₂-95% N₂ gas (a) and pure hydrogen (b)

Table 1 summarizes the calculated Avrami-Erofe'ev exponent “n”, the closest literature matches “n_l” [43] and the identified kinetic model.

Table 3.1: NiO reduction kinetic model selection based on the Hancock-Sharp method

5% H ₂ -95% N ₂			
% wt. ALT	n	n _l	Model
0	1.2348	1.24	R1
1	1.003	1	AE1
5	0.9969	1	AE1
10	0.7592	0.7	F3
100 % H ₂			
% wt. ALT	n	n _l	Model
0	0.3099	N/A	N/A
1	0.8032	0.83	F2
5	0.7442	0.7	F3
10	0.8487	0.83	F2

Table 2 reports the identified reduction mechanism and the corresponding model integral expression [43].

Table 3.2: NiO reduction kinetic model description and corresponding integral expressions

Abbreviation	Kinetic model	Integral expression
R1	Zero-order (Polany-Winger equation) Phase-boundary controlled reaction	x
AE1	First-order Avrami-Erofe'ev (n=1) formation and growth of nuclei	-ln(1-x)
F2	Second order homogeneous reaction process	1/(1-x)- 1
F3	Third order homogeneous reaction process	(1/2)[(1-x) ⁻² - 1]

Figures 2 and 3 show the comparison of the predicted models (solid lines) with experimental data points on a y vs t plot, for the reduction of undoped and 1-10 wt% ALT doped NiO/YSZ anode material when 5% H₂-95% N₂ gas (Figure 2) and pure hydrogen (Figure 3) are used. It becomes apparent that, except for 5 wt% ALT doped

NiO/YSZ, the models identified using the Hancock-Sharp method, do not fit the experimental data and therefore do not accurately describe the reduction kinetic mechanism.

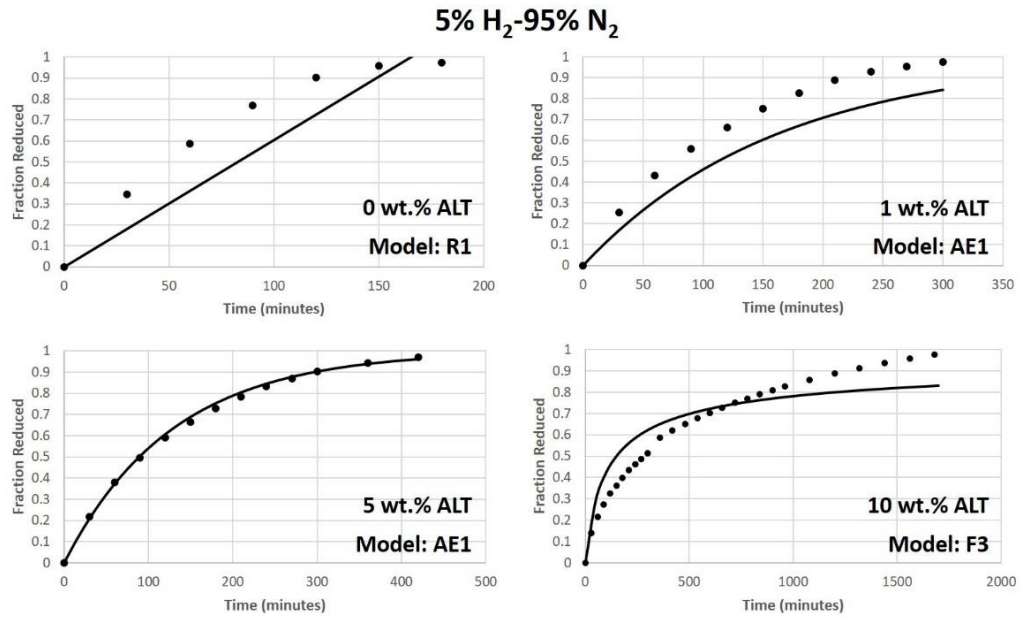


Figure 3.2: Comparison between the experimental data points and models (solid lines) predicted for the reduction of undoped and 1-10 wt% ALT doped NiO-YSZ at 800°C, by 5% H₂-95% N₂ gas

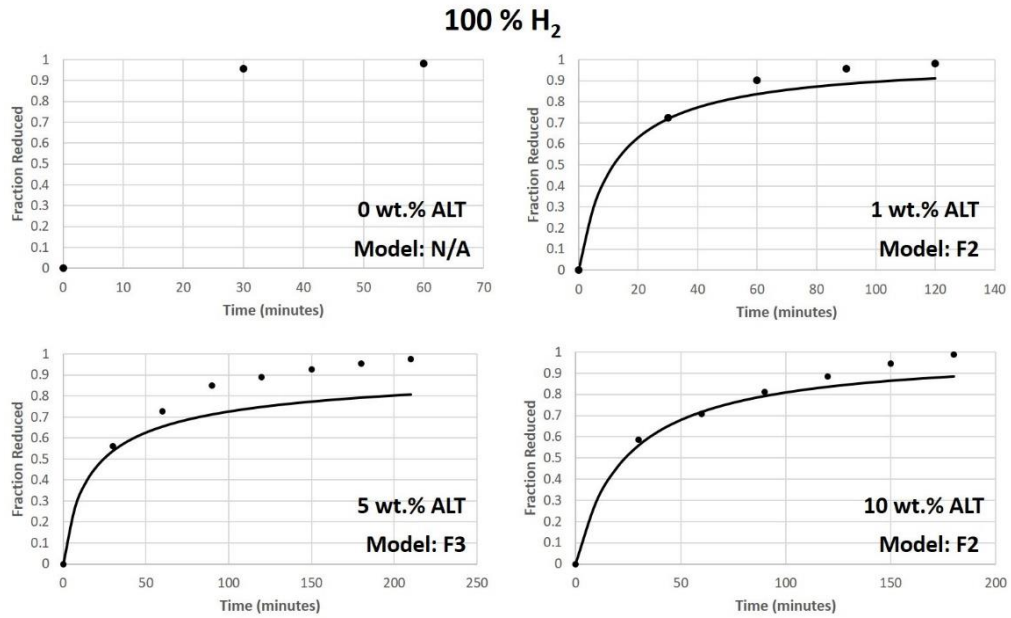


Figure 3.3: Comparison between the experimental data points and models (solid lines) predicted for the reduction of undoped and 1-10 wt.% ALT doped NiO-YSZ at 800°C, by pure hydrogen

In the presented experimental conditions, all the calculated “n” are close to 1. The only exception is for the undoped NiO reduced in pure hydrogen which results in the lowest value (0.3099) and is missing a matching “n_i”. The Hancock-Sharp method was found to be ineffective when the linear plots have similar slopes [43], particularly, for “n” values ~1 because of the theoretical suitability of R, F and AE models as demonstrated in the presented case.

The Avrami-Erofe’ev model (AE) was found to be the most successful in representing reduction kinetics of NiO [37–39,48–54], with the two parameters Avrami-Erofe’ev model AEn, better matching the experimental data [38,39,43,49,54]. The integral expression of the AEn model is $(-\ln(1-x))^{1/n}$ where “n” is the Avrami-Erofe’ev exponent.

Figure 4 shows the y vs t plot comparing the experimental data (markers) with the AEn model (solid lines) for the reduction of undoped and 1-10 wt% ALT doped NiO/YSZ anode material, by 5% H₂-95% N₂ gas (a) and pure hydrogen (b).

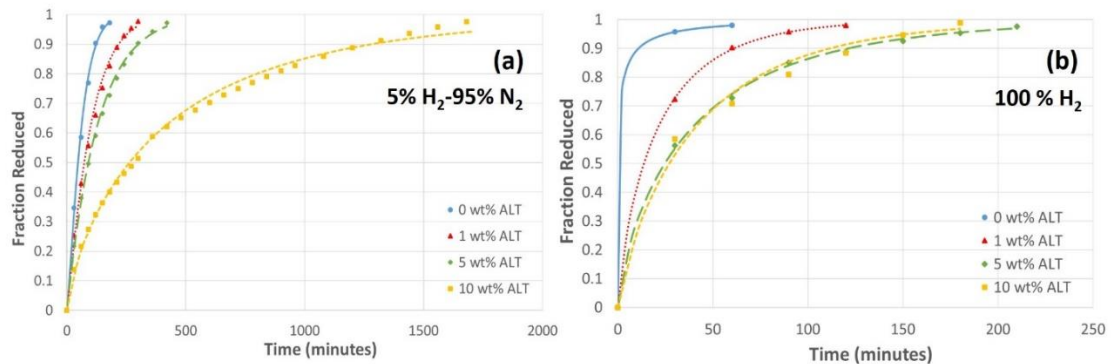


Figure 3.4: Comparison between the experimental data (markers) and AEn models (solid lines) for the reduction of undoped and 1-10 wt.% ALT doped NiO-YSZ at 800°C, by 5% H₂-95% N₂ gas (a) and pure hydrogen (b)

The AEn model is successful in representing reduction kinetics of undoped and 1-10 wt% ALT doped NiO-YSZ at 800°C, by 5% H₂-95% N₂ gas (Figure 4a) and pure hydrogen (Figure 4b). The NiO reduction kinetics mechanism is therefore identified as formation and growth of nuclei and is maintained after ALT doping and when the hydrogen concentration in the gas flow is increased from 5% to 100%.

To further validate the accuracy of the Avrami-Erofe'ev model, AEn, when compared to the models predicted with the Hancock-Sharp method, the residual sum of squares (RSS) has been evaluated. A better fit of the data will be demonstrated by lower RSS values. When the Avrami-Erofe'ev model was used for the reduction of NiAl₂O₄ containing materials at 800 °C, RSS values were found to be in the range 2×10^{-3} - 6×10^{-5} ,

with variability related to manufacturing conditions and reducing gas composition [43].

The calculated RSS values for all of the models, are summarized in Table 3.

Table 3.3: Comparison between the residual sum of squares (RSS) of models predicted with the Hancock-Sharp method and the Avrami-Erofe'ev model for fitting experimental data for the reduction of undoped and 1–10 wt% ALT doped NiO-YSZ at 800 °C, by 5% H₂-95% N₂ gas

5% H ₂ -95% N ₂			
% wt. ALT	Hancock-Sharp Method Predicted Model	RSS Predicted Model	RSS Avrami-Erofe'ev (AEn) Model
0	R1	0.1754	0.0016
1	AE1	0.1926	0.0017
5	AE1	0.0026	0.0043
10	F3	0.2402	0.0081
100% H ₂			
% wt. ALT	Hancock-Sharp Method Predicted Model	RSS Predicted Model	RSS Avrami-Erofe'ev (AEn) Model
0	N/A	N/A	5.322E-10
1	F2	0.0147	5.176E-05
5	F3	0.1220	0.0006
10	F3	0.1862	0.0075

The smaller RSS values calculated for the AEn model, when compared to the predicted ones, confirm the accuracy and suitability of this model. In addition, calculated values are consistent with pertinent literature [44]. The higher RSS values recorded for both gas compositions, when ALT doping is ≥ 5 wt%, well agree with the shift of the AEn model curves from the experimental data observed in Figure 4 a and b. The TiO₂ introduced in the NiO/YSZ system through ALT doping, preferentially reacts with YSZ to form a solid framework which persists upon reduction [32]; as a consequence, it is not considered to have an effect on the reduction kinetics. Hence, the model shift is to be related to the amount of NiAl₂O₄ forming in the system, proportional to ALT doping, and is discussed later.

Table 4 summarizes the Avrami-Erofe'ev exponent “n” and the times required to convert at least 97 wt% of NiO into metallic Ni, in the undoped and 1-10 wt% ALT doped NiO-YSZ system, at 800°C when 5% H₂-95% N₂ gas and pure hydrogen are used.

Table 3.4: Avrami-Erofe'ev exponent “n” and times needed to convert 97 wt% of NiO into metallic Ni, in the undoped and 1–10 wt% ALT doped NiO-YSZ system, at 800 °C when 5% H₂-95% N₂ gas and pure hydrogen are used

5% H ₂ -95% N ₂		
% wt. ALT	n	Reduction Time (min)
0	1.2348	180
1	1.003	300
5	0.9969	420
10	0.7592	1680
100% H ₂		
% wt. ALT	n	Reduction Time (min)
0	0.3099	60
1	0.8032	120
5	0.7442	210
10	0.8487	180

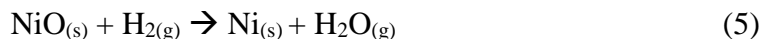
The Avrami-Erofe'ev exponent “n” reflects the crystallite size which is related to the nucleation process active surface, and thus influences the overall reaction rate [43]. For isothermal conditions, $n = 1.5$ represents the nuclei growth of small crystallites, while $n \leq 1$ stands for nuclei growth in considerably larger crystallites [43,55,56]. Basing on these statements, it can be inferred that, when the value of “n” decreases, the crystallite size increases, as well as the active surface for Ni nucleation process, resulting in faster kinetics (shorter reaction time).

For both hydrogen concentrations, the time required for the reduction process varied, in most cases, proportionally to the doping amount of ALT. The only exception is for 100% H₂ where the reduction time of the 5 wt% ALT doped samples is longer than the 10 wt% ALT doped samples. Table 4 shows that, when the ALT doping amount is

increased, opposite trends in the “n” values can be identified and are to be related to the hydrogen concentrations used for the reduction process. Basing on the “n” vs. crystallites size assumption discussed above, when 5% H₂-95% N₂ gas is used, the decreasing “n” values should correspond to a faster reduction process due to the formation of larger crystallites; instead the reduction process is slowed (longer times). On the other hand, when 100% H₂ is used, the longer reduction times observed well agree with the increasing “n” values related to the formation of smaller crystallites. The anomaly of the 10 wt% ALT doped sample will be discussed later.

It becomes apparent that “n” is system dependent because of the difficulty to separate the parameters that could simultaneously influence the reduction process, such as local composition, porosity and pathways for gas transport therefore, no absolute comparison can be performed.

The reduction of NiO with H₂ occurs without any intermediate phase and is described by reaction 5:



A correlation was observed between the concentration of vacancies in the NiO lattice and the reduction rate. Hydrogen molecules predominantly dissociate on Ni atoms that are surrounded by oxygen vacancies [34,36,39–41]. The presence of oxygen vacancies increases the adsorption energy of H₂ lowering the energy barrier associated with the rupture of the H-H bond [39,40]. At the same time, adsorbed hydrogen can induce the migration of oxygen vacancies from the bulk to the surface of the oxide [40].

The reduced Ni then acts as a catalyst for dissociative H₂ adsorption accelerating the NiO reduction near a Ni surface [34,36]. It has been reported that the NiO reduction rate scales with the H₂ concentration [40,57]. This well agrees with Table 4 where the reduction times for undoped and ALT doped materials, are decreased when 5% H₂-95% N₂ gas and pure hydrogen are respectively used.

When Al₂O₃ is introduced in the NiO/YSZ system through ALT doping, a proportional amount of NiAl₂O₄ is formed (reaction 1); therefore, the reduction time should be shorter because of the decreased NiO content instead, the opposite trend is observed with the reduction times increasing proportionally to ALT doping. NiAl₂O₄ at 800°C has very low reaction kinetics; the reduction process starts after ~10 hours of exposure to reducing atmosphere [33] and is completed after ~600 hours [58]. The time needed for the reduction of NiAl₂O₄ decreases when the H₂ concentration in the gas flow is increased [59]. Figure 4 a-b shows that the curves related to ALT doping, are characterized by a first period where the reduction rate is fast followed by a stage of lower reactivity. The first period is attributed to the reduction of free NiO; as this process is completed, the reduction of NiAl₂O₄ begins following a slower pattern [32,37,59,60]. A shift of the model from the experimental data can be observed in Figure 4a after ~ 600 minutes (10 hours) which corresponds to the onset of NiAl₂O₄ reduction. Figure 4b confirms that the reduction kinetics of the system are accelerated when the H₂ concentration is increased. Formal fitting of the kinetic data, however, is not sufficient to characterize the reaction mechanism due to the complex nature of the process.

Field Emission Scanning Electron Microscopy (FE-SEM) was conducted to understand the correlations between the reaction kinetics and microstructural development. Figures 5 a-d and 6 a-d, show the surface microstructure of the NiO-YSZ samples with 0, 1, 5, and 10 wt% ALT doping when 5% H₂-95% N₂ gas and pure hydrogen are used respectively. The microstructural features have been previously identified by the authors as the “rough phase” (square areas) and the “small particle phase” (circular areas) corresponding respectively to a Ti-YSZ framework and Ni nanoparticles resulting from the reduction of NiAl₂O₄ [32]. When 5% H₂-95% N₂ is used, Ni nanoparticles only appear for the 10 wt. % ALT doped sample (Figure 5d). This confirms that, when enough time (1680 minutes corresponding to 28 hours) is given to the system, the onset of the NiAl₂O₄ reduction is reached. When pure hydrogen is used, Ni nanoparticles appear for 5 and 10 wt.% ALT doped samples (Figure 6 c and d) showing that when the H₂ concentration in the gas flow is increased, the NiAl₂O₄ reduction process is more efficient. The formation of NiAl₂O₄, proportional to the ALT doping amount, depletes the system of available NiO for reduction resulting in a lower porosity when compared to the undoped samples. The observed increased reduction times are to be related to the fact that, water produced by the NiO reduction is retained and affects the reaction rate negatively by poisoning of the active sites for H₂ adsorption [34,57].

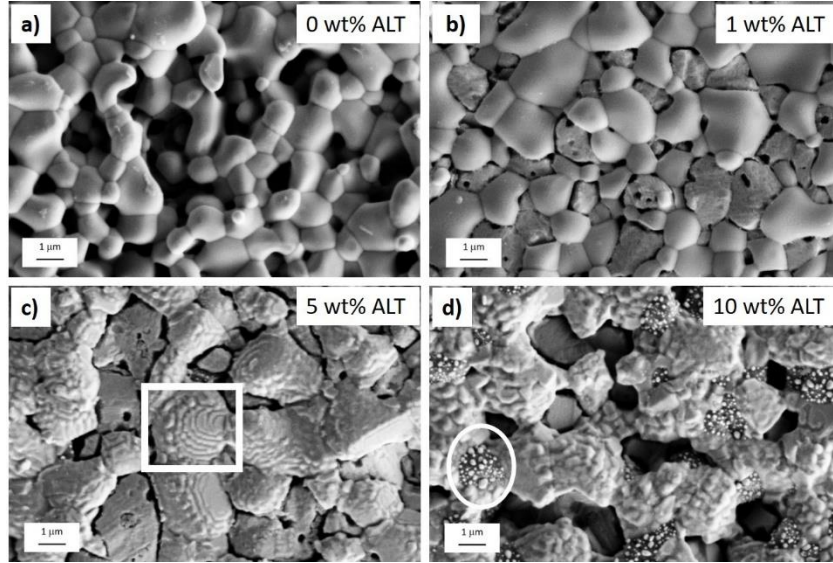


Figure 3.5: FE-SEM surface image of NiO-YSZ + (a) 0 wt%, (b) 1 wt%, (c) 5 wt%, and (d) 10 wt% ALT reduced by 5% H₂-95% N₂ gas

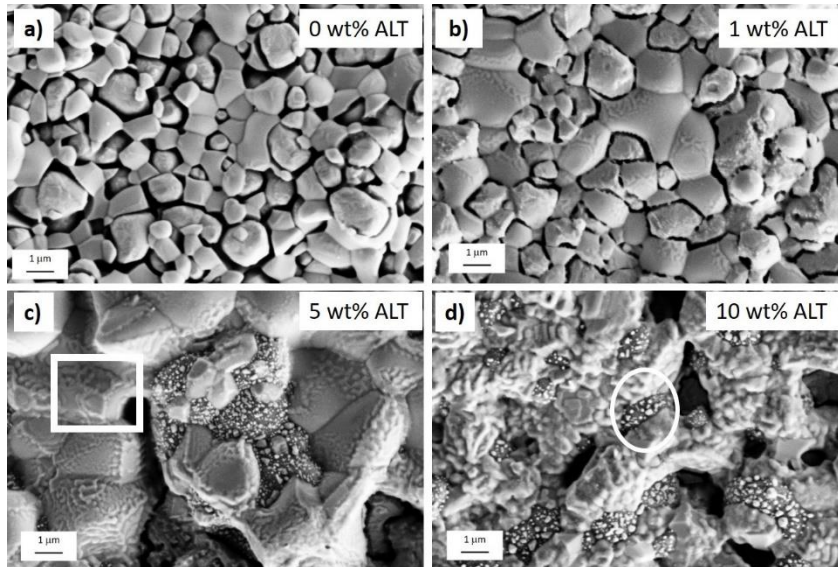


Figure 3.6: FE-SEM surface image of NiO-YSZ + (a) 0 wt%, (b) 1 wt%, (c) 5 wt%, and (d) 10 wt% ALT reduced by 100% H₂ gas

It has been reported [58,61,62] that, when NiAl₂O₄ is reduced at temperatures ~ 800°C, the reduction products include metastable phases that evolve prior to the formation of the equilibrium Al₂O₃ matrix. NiAl₂O₄ can transform from a normal spinel,

(Ni²⁺)[Al₂³⁺]O₄, to an inverse spinel (Al)[NiAl]O₄, with a small energy change [63–65]. In this process, the larger Ni²⁺ ions which occupy the tetrahedral sites in normal spinel, move to the octahedral sites in inverse spinel, while half of the smaller Al³⁺ ions move in the opposite direction. The tetrahedral sites are reported to be more difficult to reduce than the octahedral ones [66,67]. The 10 wt% ALT doped samples, are characterized by the largest amount of NiAl₂O₄. This research has demonstrated that, when pure hydrogen is used, the reduction kinetics are more efficient. Since the unreduced spinel becomes more inverse during reduction [61], it is expected that a larger amount of Ni²⁺ will have moved to the octahedral sites resulting in a system more prone to be reduced. This well agrees with the shorter reduction time recorded for the 10 wt% ALT doped sample when compared to the 5 wt% ALT doped sample.

Examination of microstructure with respect to the reduction kinetics has proven the relationship between Ni nanoparticles development and hydrogen concentration. It has been demonstrated that the Avrami-Erofe'ev exponent “n” is system dependent because of the difficulty to separate the parameters that could simultaneously influence the reduction process, such as local composition, porosity and pathways for gas transport. Despite this work identifying the reduction kinetics mechanism for undoped and ALT doped Ni/YSZ systems, the authors understand that the previously mentioned parameters will vary depending on the manufacturing process. Further research is therefore needed to assess how initial powder size, sintering and porosity development will affect the reduction kinetics.

Conclusions

Undoped and 1-10 wt% doped NiO/YSZ anode materials were kinetically evaluated during H₂ reduction at 800 °C. This investigation revealed that the two parameter Avrami-Erofe'ev model, with “n” ranging from 0.74 to 1.23, was the most successful in representing reduction kinetics. The reduction mechanisms have been identified as formation and growth of nuclei and is maintained after ALT doping and when the H₂ concentration in the gas flow is increased from 5% to 100%. It was shown that “n” is system dependent because of the difficulty to separate the parameters that could simultaneously influence the reduction process, such as local composition, porosity and pathways for gas transport. When Al₂O₃ is introduced into the NiO/YSZ system through ALT doping, a proportional amount of NiAl₂O₄ is formed; as a consequence, the curves related to ALT doping are characterized by a stage of lower reactivity where the reduction of NiAl₂O₄ follows a slower pattern. A shift of the model from the experimental data is observed and corresponds to the onset of NiAl₂O₄ reduction. For all the tested samples, the reduction kinetics of the system are accelerated when the H₂ concentration is increased. The microstructural FE-SEM analyses corroborate the findings showing the formation of Ni nanoparticles from NiAl₂O₄ reduction proportional to the H₂ concentration.

Acknowledgements

This work was supported by the Department of Energy (DOE) [award no. DE-FE0031125]. FE-SEM data was collected at the Montana State University Image and Chemical Analysis Laboratory.

References

- [1] N.Q. Minh, Ceramic Fuel Cells, *J. Am. Ceram. Soc.* 76 (1993) 563–588. doi:10.1111/j.1151-2916.1993.tb03645.x.
- [2] S.P. Jiang, S.H. Chan, A review of anode materials development in solid oxide fuel cells, *J. Mater. Sci.* 39 (2004) 4405–4439.
- [3] F. Zhao, A. V. Virkar, Dependence of polarization in anode-supported solid oxide fuel cells on various cell parameters, *J. Power Sources.* 141 (2005) 79–95. doi:10.1016/j.jpowsour.2004.08.057.
- [4] A.C. Müller, D. Herbstritt, E. Ivers-Tiffée, Development of a multilayer anode for solid oxide fuel cells, *Solid State Ionics.* 152–153 (2002) 537–542. doi:10.1016/S0167-2738(02)00357-0.
- [5] Z.R. Wang, J.Q. Qian, S.R. Wang, J.D. Cao, T.L. Wen, Improvement of anode-supported solid oxide fuel cells, *Solid State Ionics.* 179 (2008) 1593–1596. doi:10.1016/j.ssi.2008.03.022.
- [6] T. Setoguchi, K. Okamoto, K. Eguchi, H. Arai, Effects of anode material and fuel on anodic reaction of solid oxide fuel cells, *J. Electrochem. Soc.* 139 (1992) 2875–2880. doi:10.1149/1.2068998.
- [7] M. Kleitz, F. Petitbon, Optimized SOFC electrode microstructure, *Solid State Ionics.* 92 (1996) 65–74. doi:10.1016/S0167-2738(96)00464-X.
- [8] C.R. He, W.G. Wang, Alumina Doped Ni/YSZ Anode Materials for Solid Oxide Fuel Cells, *Fuel Cells.* 9 (2009) 630–635. doi:10.1002/fuce.200800152.
- [9] M. Mori, Y. Hiei, H. Itoh, G.A. Tompsett, N.M. Sammes, Evaluation of Ni and Ti-doped Y₂O₃ stabilized ZrO₂ cermet as an anode in high-temperature solid oxide fuel cells, *Solid State Ionics.* 160 (2003) 1–14. doi:10.1016/S0167-2738(03)00144-9.
- [10] M.S. Khan, S.B. Lee, R.H. Song, J.W. Lee, T.H. Lim, S.J. Park, Fundamental mechanisms involved in the degradation of nickel-yttria stabilized zirconia (Ni-YSZ) anode during solid oxide fuel cells operation: A review, *Ceram. Int.* 42 (2015) 35–48. doi:10.1016/j.ceramint.2015.09.006.
- [11] W.Z. Zhu, S.C. Deevi, A review on the status of anode materials for solid oxide fuel cells, *Mater. Sci. Eng. A.* 362 (2003) 228–239. doi:10.1016/S0921-5093(03)00620-8.
- [12] D. Sarantaridis, A. Atkinson, Redox cycling of Ni-based solid oxide fuel cell anodes: A review, *Fuel Cells.* 7 (2007) 246–258. doi:10.1002/fuce.200600028.
- [13] M. Ettler, H. Timmermann, J. Malzbender, A. Weber, N.H. Menzler, Durability of Ni anodes during reoxidation cycles, *J. Power Sources.* 195 (2010) 5452–5467.

- [14] M. Radovic, E. Lara-Curzio, Mechanical properties of tape cast nickel-based anode materials for solid oxide fuel cells before and after reduction in hydrogen, *Acta Mater.* 52 (2004) 5747–5756. doi:10.1016/j.actamat.2004.08.023.
- [15] J.T. Richardson, R. Scates, M. V. Twigg, X-ray diffraction study of nickel oxide reduction by hydrogen, *Appl. Catal. A Gen.* 246 (2003) 137–150. doi:10.1016/S0926-860X(02)00669-5.
- [16] T.A. Utigard, M. Wu, G. Plascencia, T. Marin, Reduction kinetics of Goro nickel oxide using hydrogen, *Chem. Eng. Sci.* 60 (2005) 2061–2062. doi:10.1016/j.ces.2004.11.024.
- [17] M.H. Pihlatie, H.L. Frandsen, A. Kaiser, M. Mogensen, Continuum mechanics simulations of NiO/Ni–YSZ composites during reduction and re-oxidation, *J. Power Sources.* 195 (2010) 2677–2690. doi:10.1016/j.jpowsour.2009.11.079.
- [18] N.M. Tikekar, T.J. Armstrong, A. V. Virkar, Reduction and Reoxidation Kinetics of Nickel-Based SOFC Anodes, *J. Electrochem. Soc.* 153 (2006) A654. doi:10.1149/1.2167949.
- [19] N.M. Tikekar, T.J. Armstrong, A. V. Virkar, Reduction and re-oxidation kinetics of nickel-based solid oxide fuel cell anodes, in: S.C. Singhal, M. Dokiya (Eds.), *Electrochem. Soc. Proc.*, 2003: pp. 670–679.
- [20] A. Hagen, H.F. Poulsen, T. Klemensø, R. V. Martins, V. Honkimäki, T. Buslaps, R. Feidenshans'l, A Depth-Resolved In-Situ Study of the Reduction and Oxidation of Ni-Based Anodes in Solid Oxide Fuel Cells, *Fuel Cells.* 6 (2006) 361–366. doi:10.1002/fuce.200600004.
- [21] J. Mizusaki, H. Tagawa, T. Saito, T. Yamamura, K. Kamitani, K. Hirano, S. Ehara, T. Takagi, T. Hikita, M. Ippommatsu, Kinetic studies of the reaction at the nickel pattern electrode on YSZ in H₂-H₂O atmospheres, *Solid State Ionics.* 70–71 (1994) 52–58. doi:10.1016/0167-2738(94)90286-0.
- [22] A. Bieberle, L.J. Gauckler, Reaction Mechanism of Ni Pattern Anodes for Solid Oxide Fuel Cells, *Solid State Ionics.* 135 (2000) 337.
- [23] A.N. Busawon, D. Sarantaridis, A. Atkinson, Ni infiltration as a possible solution to the redox problem of SOFC anodes, *Electrochem. Solid-State Lett.* 11 (2008) B186–B189. doi:10.1149/1.2959078.
- [24] D. Simwonis, F. Tietz, D. Stover, Nickel coarsening in annealed Ni / 8YSZ anode substrates for solid oxide fuel cells, *Solid State Ionics.* 132 (2000) 241–251. doi:10.1016/S0167-2738(00)00650-0.
- [25] C.H. Law, S.W. Sofie, Anchoring of Infiltrated Nickel Electro-Catalyst by Addition of Aluminum Titanate, *J. Electrochem. Soc.* 158 (2011) B1137–B1141. doi:10.1149/1.3610226.
- [26] J.L. Young, V. Vedahara, S. Kung, S. Xia, V.I. Birss, Understanding Nickel

- Oxidation and Reduciton Processes in SOFC Systems, ECS Trans. 7 (2007) 1511–1519.
- [27] A.J. Weisentein, N. Childs, R. Amendola, D. Driscoll, S.W. Sofie, P. Gannon, R. Smith, Processing and characterization of $\text{Sr}_{2-x}\text{VMoO}_{6-\delta}$ double perovskites, *Mater. Chem. Phys.* 139 (2013) 706–718. doi:10.1016/j.matchemphys.2013.02.021.
- [28] D. Driscoll, C. Hunt, J. Muretta, S.W. Sofie, Thermally Stabilized Nickel Electro-Catalyst Introduced by Infiltration for High Temperature Electrochemical Energy Conversion, ECS Trans. 53 (2013) 63–72. doi:10.1149/05309.0063ecst.
- [29] S.W. Sofie, D.R. Taylor, Controlled Thermal Expansion Anode Compositions with Improved Strength for Use in Anode Supported SOFCs, *Adv. Solid Oxide Fuel Cells III.* (2008) 215–223.
- [30] D.R. Driscoll, M.D. McIntyre, M.M. Welander, S.W. Sofie, R.A. Walker, Enhancement of high temperature metallic catalysts: Aluminum titanate in the nickel-zirconia system, *Appl. Catal. A Gen.* 527 (2016) 36–44. doi:10.1016/j.apcata.2016.08.020.
- [31] D.R. Driscoll, B.W. Tokmakian, N.P. Johnson, C.D. Hunt, S.W. Sofie, Catalyst enhancing aluminum titanate for increasing strength of nickel-zirconia cermets, *Mater. Lett.* 209 (2017) 307–310. doi:10.1016/j.matlet.2017.08.035.
- [32] M. McCleary, R. Amendola, Effect of Aluminum Titanate (Al_2TiO_5) Doping on the Mechanical Performance of Solid Oxide Fuel Cell Ni-YSZ Anode, *Fuel Cells.* (2017) 862–868. doi:10.1002/fuce.201700073.
- [33] B. Charlas, D.W. Ni, H.L. Frandsen, K. Brodersen, M. Chen, Mechanical Properties of Supports and Half-Cells for Solid Oxide Electrolysis Influenced by Alumina-Zirconia Composites, *Fuel Cells.* 17 (2017) 132–143. doi:10.1002/fuce.201600036.
- [34] S.B. Simonsen, K. Agersted, K.V. Hansen, T. Jacobsen, J.B. Wagner, T.W. Hansen, L.T. Kuhn, Environmental TEM study of the dynamic nanoscaled morphology of NiO/YSZ during reduction, *Appl. Catal. A Gen.* 489 (2015) 147–154. doi:10.1016/j.apcata.2014.10.045.
- [35] A. Morrissey, J.R. O'Brien, I.E. Reimanis, Microstructure evolution during internal reduction of polycrystalline nickel-doped yttria-stabilized zirconia, *Acta Mater.* 105 (2016) 84–93. doi:10.1016/j.actamat.2015.12.005.
- [36] D. Fouquet, A.C. Müller, a. Weber, E. Ivers-Tiffée, Kinetics of oxidation and reduction of Ni/YSZ cermets, *Ionics (Kiel).* 9 (2003) 103–108. doi:10.1007/BF02376545.
- [37] D. Ipsakis, E. Heracleous, L. Silvester, D.B. Bukur, A.A. Lemonidou, Reduction

- and oxidation kinetic modeling of NiO-based oxygen transfer materials, *Chem. Eng. J.* 308 (2017) 840–852. doi:10.1016/j.cej.2016.09.114.
- [38] B. Janković, Isothermal reduction kinetics of nickel oxide using hydrogen: Conventional and Weibull kinetic analysis, *J. Phys. Chem. Solids.* 68 (2007) 2233–2246. doi:10.1016/j.jpcs.2007.06.014.
- [39] K. V. Manukyan, A.G. Avetisyan, C.E. Shuck, H.A. Chatilyan, S. Rouvimov, S.L. Kharatyan, A.S. Mukasyan, Nickel Oxide Reduction by Hydrogen: Kinetics and Structural Transformations, *J. Phys. Chem. C.* 119 (2015) 16131–16138. doi:10.1021/acs.jpcc.5b04313.
- [40] J.A. Rodriguez, J.C. Hanson, A.I. Frenkel, J.Y. Kim, M. Pérez, Experimental and theoretical studies on the reaction of H₂ with NiO: Role of O vacancies and mechanism for oxide reduction, *J. Am. Chem. Soc.* 124 (2002) 346–354. doi:10.1021/ja0121080.
- [41] R.P. Furstenau, G. McDougall, M.A. Langell, Initial Stages of Hydrogen Reduction of NiO (100), *Surf. Sci.* 150 (1985) 55–79.
- [42] J. Zygmontowicz, P. Wieceńska, A. Miazga, K. Konopka, Characterization of composites containing NiAl₂O₄ spinel phase from Al₂O₃/NiO and Al₂O₃/Ni systems, *J. Therm. Anal. Calorim.* 125 (2016) 1079–1086. doi:10.1007/s10973-016-5357-2.
- [43] Z. Zhou, L. Han, G.M. Bollas, Kinetics of NiO reduction by H₂ and Ni oxidation at conditions relevant to chemical-looping combustion and reforming, *Int. J. Hydrogen Energy.* 39 (2014) 8535–8556. doi:10.1016/j.ijhydene.2014.03.161.
- [44] P. Hancock, J.H. Sharp, Method of Comparing Solid-State Kinetic Data and Its Application to the Decomposition of Kaolinite, Brucite, and BaCO₃, *J. Am. Ceram. Soc.* 55 (1972) 74–77. doi:10.1111/j.1151-2916.1972.tb11213.x.
- [45] M. Avrami, Kinetics of Phase Change. I General Theory, *J. Chem. Phys.* 7 (1939) 1103–1112. doi:10.1063/1.1750380.
- [46] M. Avrami, Kinetics of Phase Change . II Transformation Time Relations for Random Distribution of Nuclei Kinetics of Phase Change . II Transformation-Time Relations for Random Distribution of Nuclei *, *J. Chem. Phys.* 8 (1940) 212. doi:10.1063/1.1750631.
- [47] M. Avrami, Granulation, Phase Change, and Microstructure Kinetics of Phase Change. III, *J. Chem. Phys.* 9 (1941) 177–184. doi:10.1063/1.1750872.
- [48] Q. Jeangros, T.W. Hansen, J.B. Wagner, C.D. Damsgaard, R.E. Dunin-Borkowski, C. Hébert, J. Van Herle, A. Hessler-Wyser, Reduction of nickel oxide particles by hydrogen studied in an environmental TEM, *J. Mater. Sci.* 48 (2013) 2893–2907. doi:10.1007/s10853-012-7001-2.
- [49] M.M. Hossain, M.R. Quddus, H.I. de Lasa, Reduction Kinetics of La Modified

- NiO/La- γ -Al₂O₃ Oxygen Carrier for Chemical-Looping Combustion, *Ind. Eng. Chem. Res.* 49 (2010) 11009–11017. doi:10.1021/ie100424w.
- [50] M.M. Hossain, D. Lopez, J. Herrera, H.I. de Lasa, Nickel on lanthanum-modified γ -Al₂O₃ oxygen carrier for CLC: Reactivity and stability, *Catal. Today*. 143 (2009) 179–186. doi:10.1016/j.cattod.2008.09.006.
- [51] M.M. Hossain, H.I. de Lasa, Chemical-looping combustion (CLC) for inherent CO₂ separations-a review, *Chem. Eng. Sci.* 63 (2008) 4433–4451. doi:10.1016/j.ces.2008.05.028.
- [52] K.E. Sedor, M.M. Hossain, H.I. de Lasa, Reactivity and stability of Ni/Al₂O₃ oxygen carrier for chemical-looping combustion (CLC), *Chem. Eng. Sci.* 63 (2008) 2994–3007. doi:10.1016/j.ces.2008.02.021.
- [53] S.R. Son, S.D. Kim, Chemical-Looping Combustion with NiO and Fe₂O₃ in a Thermobalance and Circulating Fluidized Bed Reactor with Double Loops, *Ind. Eng. Chem. Res.* 45 (2006) 2689–2696. doi:10.1021/ie050919x.
- [54] L. Han, Z. Zhou, G.M. Bollas, Heterogeneous modeling of chemical-looping combustion. Part 2: Particle model, *Chem. Eng. Sci.* 113 (2014) 116–128. doi:10.1016/j.ces.2014.03.030.
- [55] J. Málek, The applicability of Johnson-Mehl-Avrami model in the thermal analysis of the crystallization kinetics of glasses, *Thermochim. Acta.* 267 (1995) 61–73. doi:10.1016/0040-6031(95)02466-2.
- [56] Z.. Yan, S.. He, J.. Li, Y.. Zhou, On the crystallization kinetics of Zr₆₀Al₁₅Ni₂₅ amorphous alloy, *J. Alloys Compd.* 368 (2004) 175–179. doi:10.1016/j.jallcom.2003.08.074.
- [57] T. Hidayat, M.A. Rhamdhani, E. Jak, P.C. Hayes, The kinetics of reduction of dense synthetic nickel oxide in H₂-N₂ and H₂-H₂O atmospheres, *Metall. Mater. Trans. B Process Metall. Mater. Process. Sci.* 40 (2009) 1–16. doi:10.1007/s11663-008-9212-0.
- [58] H. Orui, R. Chiba, K. Nozawa, H. Arai, R. Kanno, High-temperature stability of alumina containing nickel–zirconia cermets for solid oxide fuel cell anodes, *J. Power Sources.* 238 (2013) 74–80. doi:10.1016/j.jpowsour.2013.03.056.
- [59] C. Dueso, M. Ortiz, A. Abad, F. García-Labiano, L.F. De Diego, P. Gayán, J. Adánez, Reduction and oxidation kinetics of nickel-based oxygen-carriers for chemical-looping combustion and chemical-looping reforming, *Chem. Eng. J.* 188 (2012) 142–154. doi:10.1016/j.cej.2012.01.124.
- [60] C. Dueso, A. Abad, F. García-Labiano, L.F. de Diego, P. Gayán, J. Adánez, A. Lyngfelt, Reactivity of a NiO/Al₂O₃ oxygen carrier prepared by impregnation for chemical-looping combustion, *Fuel.* 89 (2010) 3399–3409. doi:10.1016/j.fuel.2010.03.043.

- [61] E. Ustundag, B. Clausen, M.A.M. Bourke, Neutron diffraction study of the reduction of NiAl_2O_4 , *Appl. Phys. Lett.* 76 (2000) 694–696. doi:10.1063/1.125864.
- [62] H. Messaoudi, S. Thomas, A. Djaidja, S. Slyemi, R. Chebout, S. Barama, A. Barama, F. Benaliouche, Hydrogen production over partial oxidation of methane using Ni Mg Al spinel catalysts: A kinetic approach, *Comptes Rendus Chim.* 20 (2017) 738–746. doi:10.1016/j.crci.2017.02.002.
- [63] E. Üstündag, Z. Zhang, M.L. Stocker, P. Rangaswamy, M.A.M. Bourke, J.A. Roberts, S. Subramanian, K.E. Sickafus, S.L. Sass, Influence of residual stresses on the evolution of microstructure during the partial reduction of NiAl_2O_4 , *Mater. Sci. Eng. A.* 238 (1997) 50–65.
- [64] E. Üstündag, R. Subramanian, R. Dieckmann, S.L. Sass, In-situ formation of metal-ceramic microstructures in the Ni-Al-O system by partial reduction reactions, *Acta Mater.* 43 (1995) 383–389. doi:http://dx.doi.org/10.1016/0167-2738(94)00148-L.
- [65] K. Mocala, A. Navrotsky, Structural and Thermodynamic Variation in Nickel Aluminate Spinel, *J. Am. Ceram. Soc.* 72 (1989) 826–832. doi:10.1111/j.1151-2916.1989.tb06225.x.
- [66] M. Wu, D.M. Hercules, Studies of supported nickel catalysts by x-ray photoelectron and ion scattering spectroscopies, *J. Phys. Chem.* 83 (1979) 2003–2008. doi:10.1021/j100478a015.
- [67] A. Cimino, M. Lo Jacono, M. Schiavello, Effect of zinc, gallium, and germanium ions on the structural and magnetic properties of nickel ions supported on alumina, *J. Phys. Chem.* 79 (1975) 243–249. doi:10.1021/j100570a010.

CHAPTER FOUR

ANALYSIS OF THE MECHANICAL STRENGTH AND FAILURE MODE OF
UNDOPED AND ALUMINUM TITANATE (Al_2TIO_5 , ALT) DOPED NI-YSZ SOLID
OXIDE FUEL CELL ANODES UNDER UNIAXIAL AND BIAXIAL STRENGTH
TESTING CONDITIONS

Contribution of Authors and Co-Authors

Author: Madisen McCleary

Contributions: Prepared and tested samples, compiled and analyzed numerical data, generated figures/tables and wrote manuscript.

Co-author: Roberta Amendola

Contributions: Provided insight on experimental design and implementation. Aided in manuscript editing and preparation.

Co-author: Stephen Walsh

Contributions: Provided advanced statistical analyses. Aided in manuscript editing and preparation.

Co-author: Benjamin McHugh

Contributions: Aided in sample preparation and testing along with numerical data analyses.

Manuscript Information Page

Madisen McCleary, Roberta Amendola, Stephen Walsh, Benjamin McHugh
Status of Manuscript:

- Prepared for submission to a peer-reviewed journal
- Officially submitted to a peer-review journal
- Accepted by a peer-reviewed journal
- Published in a peer-reviewed journal

Submitted to Materialia

ANALYSIS OF THE MECHANICAL STRENGTH AND FAILURE MODE OF
UNDOPED AND ALUMINUM TITANATE (Al_2TIO_5 , ALT) DOPED NI-YSZ SOLID
OXIDE FUEL CELL ANODES UNDER UNIAXIAL AND BIAXIAL STRENGTH
TESTING CONDITIONS

Madisen McCleary^a, Roberta Amendola^{a*}, Stephen Walsh^b, Benjamin McHugh^a

^aMechanical & Industrial Engineering Department, Montana State University, 220
Roberts Hall, Bozeman, MT 59717

^bDepartment of Mathematical Sciences, Montana State University, 2-214 Wilson Hall,
Bozeman, MT 59717*corresponding author: Roberta.amendola@montana.edu, 406-994-
6296

Keywords: Ceramic, Mechanical Properties, Fracture Mechanisms, SOFC, Scanning
Electron Microscopy

Abstract

Solid Oxide Fuel Cell (SOFC) anodes were fabricated with NiO-YSZ and 0-10 wt% ALT doping. Samples were manufactured using a tape casting procedure to a thickness of approximately 500 μm . A remarkable enhancement of the mechanical strength, up to 166%, was found when compared to the un-doped samples. The development of secondary phases was observed proportional to the doping amount of aluminum titanate. Mechanical properties evaluation was conducted using uniaxial and biaxial strength testing. Weibull statistics was used for mechanical properties analysis and an advanced statistical analysis was employed to identify the existence of multiple

flaw populations. Fractography was performed on selected samples to elucidate the fracture mechanisms. Biaxial testing was characterized by high mechanical strength with lower Weibull moduli; whereas, uniaxial testing showed lower mechanical strength and higher Weibull moduli. It was found that undoped, 5% and 10% ALT doped samples exhibit a fracture mechanism that is dependent on one flaw population namely porosity and mechanical strength of secondary phases, respectively. Undoped samples were characterized by intergranular fracture while transgranular fracture was found for the 5% and 10% ALT doped samples. For 1% ALT doped samples both flaw populations were identified. Analyses of the fracture surfaces revealed the simultaneous presence of intergranular and transgranular features. It is proposed that secondary phases, developed by ALT doping, increase the mechanical strength of the material shifting the fracture mechanism from intergranular to transgranular.

Introduction

A solid oxide fuel cell (SOFC) is an energy conversion device which electrochemically oxidizes a fuel to produce electrical power and heat. SOFCs are a promising renewable energy system; therefore, over the past several decades, research efforts have focused on improving their performance and longevity. A single SOFC unit, comprised of anode, electrolyte and cathode contacting layers, does not produce enough power to be considered for any application. To overcome this issue, units are stacked in electrical series where contact between cells is achieved through high clamping pressures e.g., 65–70 kPa [1,2]. Recently, there has been growing interest in anode supported SOFCs because of the improved single cell performance [3–9]. In these systems, the

anode layer is the thickest and provides the mechanical strength of the stack. Ni–YSZ composites are widely used as anode material but, in contrast to the vast amount of data available on their electrochemical properties, little data on the mechanical performance exists.

Previous research has shown that the formation of secondary phases, due to doping of the ceramic anode material during the manufacturing process, has resulted in improved mechanical strength [8–16] without compromising the electrochemical performance; however, novel compositions require further reliability investigation because of the inherently brittle nature of the ceramic material.

The mechanical performance of ceramics depends on random microstructural flaw distribution; specifically, the weakest spot under stress determines the material strength [17]. Uniaxial flexural tests, such as three- or four-point bending, have long been used to determine ceramic material strength. During these testing, a rectangular sample is submitted to uniaxial load. The maximum stress goes from tensile to compressive through the sample thickness and is experienced at the surface. This measurement technique; however, may only provide a partial characterization of the material load bearing capacity due to the sample's geometry that introduces low curvature radius defects (sample edges) acting like stress concentrators [18]. Also, advanced engineering ceramic components fail often due to multiaxial stress conditions. For these reasons, several multiaxial strength tests have been developed. Biaxial flexural tests on disc-shaped specimens like ring-on-ring or ball-on-ring are particularly favored

because the maximum tensile stress occurs at the center of the surface opposite to load application; consequently, edge flaws do not influence the results [19–26].

While the fuel cell is operational, the anode is exposed to thermo-mechanical stresses that may result in premature catastrophic failure. It is thus essential to develop reliable failure criteria to predict the service performance of these materials. If the mechanical strength must be characterized, not every test method is suitable and when different testing methodologies are selected, direct correlation of the results cannot be performed because of the influence of geometrical and microstructural variables; however, performing different tests may offer a more comprehensive view of the material behavior.

The inherently brittle nature of the anode causes big scatter in fracture strength measurement. Large batches of material must be tested and Weibull statistical analyzes must be used basing on the assumption that the weakest spot under tension determines the strength of the sample. The “size effect” relative to tensile strength is quite prominent in ceramics. As the size of a test specimen is increased, then, on average, the tensile strength of the component decreases giving the wrong impression of a weaker material. The reason is that as the sample volume is increased, the likelihood of encountering a critical flaw with deleterious orientations to the load applied increases [27–31].

Correlation of results obtained by different testing methodologies is possible when the same volume of material under tension is considered. This variable is known as the “effective volume” [32]. The effective volume is a function of the sample geometry and corresponds to the size of a hypothetical tension test specimen that, when stressed to

the same level as the sample in question, has the same probability of failure. It is implied that the same type of volume distributed flaws control strength in each geometry.

Through effective volume, Weibull parameters and measured characteristic strength, the strength values obtained with different testing methodologies and sample geometries can be scaled and properly compared.

This study aims to evaluate the mechanical strength of undoped and aluminum titanate (Al_2TiO_5 , ALT) doped Ni-YSZ SOFC anodes under uniaxial and biaxial strength testing conditions. The validity of both testing methods is discussed based on the experimental evidence. Advanced statistical analyses and fractography are then used to elucidate the material failure mechanism.

Experimental

Powders of nickel oxide (NiO) (4 μm , Alfa Aesar), 8 mol% yttria-stabilized zirconia (YSZ) (300 nm, Tosoh) and aluminum titanate (ALT) (25 nm, Sigma Aldrich) were used for manufacturing of the anode material. Powders, in the ratio of 34 wt.% YSZ, 66 wt.% NiO and 0–10 wt.% ALT, were mechanically mixed for 24 h with binder and deionized water. Tape casting was used for sample manufacturing. The slurry was taped with a doctor blade gap of 2 mm and dried in ambient conditions. Subsequently, 6 x 40 mm rectangular samples for uniaxial strength testing (three-point bending, 3PB) were cut with a rotary blade and 32 mm circular samples were punched out for biaxial strength testing (ring on ring, ROR).

Binder thermolysis was performed in a Thermolyne 1300 furnace as follows: 1) heating to 150°C at 2 °C/min, 2) 2 hours dwell, 3) heating to 450°C at 0.5 °C/min, 4)

heating to 1,100°C at 5 °C/min 5) 2 hours dwell for partial sintering, and 6) cooling to room temperature at 10 °C/min Partial sintering was performed to allow for safe sample handling while transferring to the Zircar, Hot Spot 110 for subsequent sintering.

Sintering was conducted with a heating/cooling rate of 5 °C/min up to 1,500 °C and a 2 hours dwell time. Final sintered size for the rectangular samples was 5 x 0.5 x 25 mm and ϕ 25 x 0.5 mm for the circular ones.

Reduction was performed in a Thermo Scientific, Lindberg Blue M tube furnace flowing 5% H₂ - 95% N₂ gas, at 800 °C for a time sufficient time to convert 97 wt% of NiO into metallic nickel. The percentage reduction was evaluated with a Radwag XA 82/220.R2 microscale. Time required for the reduction process varied proportionally to the doping amount of ALT. In the presented manufacturing conditions, ALT spontaneously decomposes to Al₂O₃ and TiO₂ [33]. The Al₂O₃ initially reacts with NiO to form NiAl₂O₄ [30,33–36] as follows:



Basing on reaction (1), the system is depleted of an amount of NiO proportional to the Al₂O₃ introduced with ALT doping. The amount of NiO available for reduction has therefore been evaluated accounting for NiAl₂O₄ formation.

Un-doped and 1, 5 and 10 wt% ALT doped batches of 30 reduced samples were loaded at a rate of 0.2 mm/min in a TPB apparatus (Pasco Scientific 8236) and in a ROR apparatus (Instron 5543) as per ASTM C1161-13 and ASTM C1499 – 15 standards, respectively [21,37]. For both testing methods, recorded strength corresponded to the maximum values obtained under monotonic application of the load which refers to a test

conducted at the selected constant rate in a continuous fashion, with no reversals from test initiation to final fracture. Fracture strength, effective volume (V_{eff}), scaled characteristic strength (σ_0'), Weibull modulus (m) with normalized upper and lower bounds, and porosity, by alcohol immersion method, were evaluated for both of the testing conditions. Field emission scanning electron microscopy (FE-SEM, Zeiss Ultra) was conducted to determine the nature of the developed phases and their contribution to the mechanical strength and to elucidate the material failure mechanism.

Results and Discussion

Mechanical Properties

The maximum likelihood Weibull approach which considers that the weakest flaw under tension determines the strength of the material has been used. Weibull plots are created by formulating the two-parameter Weibull equation (Equation 2) into a straight line form (Equation 3) where the slope is the Weibull modulus [38].

$$p_s = \exp\left(-\frac{\sigma}{\sigma_0}\right)^m \quad (2)$$

$$\ln(\ln(1/p_s)) = m \ln(\sigma/\sigma_0) \quad (3)$$

Where p_s is the probability of survival for each sample, m is the Weibull modulus, σ is the flexural strength (MPa) of each sample, and σ_0 is the characteristic strength (MPa) calculated at a probability of failure of $1/e$. Figure 1 shows the Weibull plots, along with the corresponding Weibull moduli.

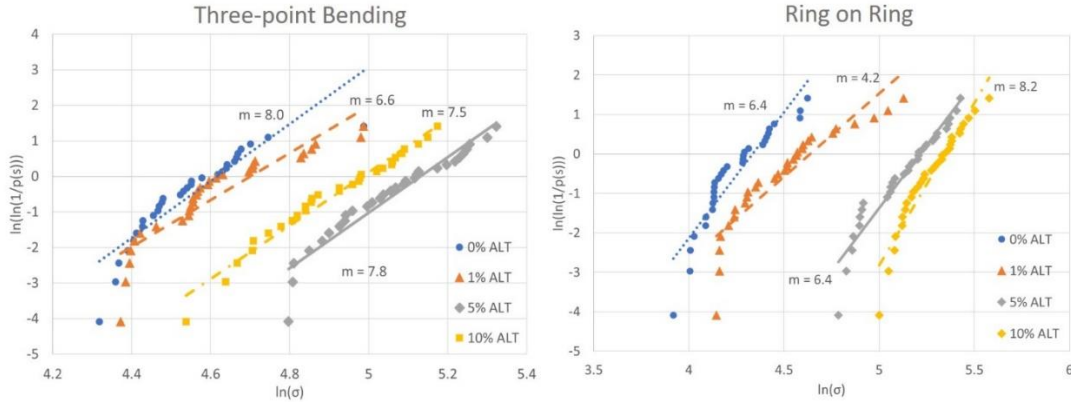


Figure 4.1: Weibull plots of uniaxial (TPB) and biaxial (ROR) strength testing

Since the probability to encounter a flaw depends on the tested volume, the effective volume (V_{eff}) was calculated and averaged for each batch of 30 samples. As the TPB and ROR samples have different geometries, two different equations (Equations 4 and 5) were used for the calculation as follows [32]:

$$V_{\text{eff}3PB} = \frac{lwh}{2(m+1)^2} \quad (4)$$

$$V_{\text{eff}ROR} = \left\{ \frac{\pi}{2} D_L^2 \right\} \left\{ 1 + \left[\frac{44(1+\nu)}{3(1+m)} \right] \left[\frac{5+m}{2+m} \right] \left(\frac{D_S - D_L}{D_S D} \right)^2 \left[\frac{2D^2(1+\nu) + (D_S - D_L)^2(1-\nu)}{(3+\nu)(1+3\nu)} \right] \right\} \left\{ \frac{h}{2(m+1)} \right\} \quad (5)$$

Where l is the span between bottom support points in mm, w is the width of the sample in mm, h is the height of the sample in mm, m is the Weibull modulus, D_L is the diameter of the loading ring in mm, D_S is the diameter of the support ring in mm, D is the diameter of the sample in mm, ν is the Poisson's ratio (assumed to be 0.3) [27].

Considering the effective volume, the characteristic strength for each batch can be scaled for comparison. Equation 6 has been used to calculate the scaled characteristic strength [30].

$$\sigma_0' = \sigma_0 \left(\frac{V_{eff}}{1 \text{ mm}^3} \right)^{\frac{1}{m}} \quad (6)$$

Where σ_0' is the scaled characteristic strength in MPa, σ_0 is the characteristic strength in MPa, V_{eff} is the effective volume in mm³, and m is the Weibull modulus.

The 90% confidence interval of the Weibull modulus was determined per ASTM C1239-13 for each batch of 30 samples [39–41]. Table 1 summarizes the mechanical properties and the porosity of undoped and ALT doped anode material tested in the TPB and the ROR fixtures.

Table 4.1: Mechanical properties and porosity of uniaxial (TPB) and biaxial (ROR) strength testing samples

	0 wt% ALT	1 wt% ALT	5 wt% ALT	10 wt% ALT
TPB				
Porosity (%)	45.5	42.5	29.7	23.0
Weibull Modulus	8.0	6.6	7.8	7.5
90% Confidence Interval	6.0 - 9.8	4.9 - 8.0	5.8 - 9.5	5.6 - 9.1
Average Strength (MPa)	95	102	159	137
V_{eff} (mm ³)	0.28	0.32	0.27	0.35
Scaled Characteristic Strength (MPa)	82	87	142	127
Strength Increase (%)	N/A	6	73	54
ROR				
Porosity (%)	45.9	42.0	29.1	23.1
Weibull Modulus	6.4	4.2	6.4	8.2
90% Confidence Interval	4.8 - 7.8	3.2 - 5.1	4.8 - 7.8	6.2 - 10.0
Average Strength (MPa)	71	93	171	197
V_{eff} (mm ³)	2.23	3.75	2.43	1.67
Scaled Characteristic Strength (MPa)	82	128	212	220
Strength Increase (%)	N/A	55	157	166

An increased characteristic strength for ALT doped samples, when compared to the undoped ones, is found for both testing methodologies. This confirms the benefit of ALT doping that was previously observed for bulk material (2 mm thick) of the same composition [12]; showing that, such benefit, transfers to a smaller thickness (500 μm) which is more appropriate to be considered for an anode supported fuel cell architecture. Secondary phase formation related to this phenomenon will be discussed later.

The same manufacturing process was used for all the tested batches and well relates to the consistency of the porosity values. During the sintering process, the decomposition of ALT leads to the formation of NiAl_2O_4 proportional to the ALT doping amount. This reaction depletes the system of NiO available for reduction resulting in a lower porosity when compared to the undoped samples [36]. The strength of ceramics is dependent on the porosity distribution within the material [29,30,42–44] since the presence of one or more pores in the loaded volume will result in a more fragile material.

It was previously found [45] that ceramics with porosity between 10 and 55%, which well represents the materials of this study, resulted in Weibull modulus values in the range between 4 and 11 with a medium to high scatter in the fracture strength regardless of the composition, grain size, testing techniques or surface finish of the specimens. The failure of these kind of materials has been linked to the pore evolution during the sintering process. A few anomalies, however, point out the fact that porosity may not be the only mechanism responsible for the failure of the material and needs further investigation.

Studies comparing uniaxial and biaxial strength testing in ceramics [18,46–48], show higher strength values for biaxial than uniaxial testing, in accordance with this study. Processing flaws, which mostly concentrate upon the surface of specimens, facilitate crack initiation and fracture. Comparing with TPB specimens, ROR specimens were not influenced by the presence of edge flaws; therefore, ROR testing recorded higher characteristic strength values when compared to TPB and may better represent the material intrinsic behavior.

The effect of the V_{eff} is another factor that should be considered in the material evaluation because the probability to apply stress to a flaw increases if the tested volume under tension is larger. Thus, the measured strength is larger if the tested volume is smaller, giving a wrong impression of a stronger material.

For the TBP samples, the undoped and 5% ALT doped material show very similar Weibull moduli and V_{eff} ; specifically, 8 and 0.28 mm^3 for the undoped versus 7.8 and 0.27 mm^3 for the 5% ALT doped samples. The recorded scaled characteristic strength values are 82 and 142 MPa, respectively. Basing on the very similar V_{eff} , the 73% strength increase may be related to the decrease in porosity from 45.5% to 29.7% and seems to support what was stated earlier. For the 10% ALT doped samples, the Weibull modulus and effective volume are 7.5 and 0.35 mm^3 , porosity decreases to 23% while the scaled characteristic strength decreases to 127 MPa. When considering the 10% ALT doped samples, it is expected that the ~7% additional decrease in porosity from the 5% ALT doped value, would nullify the effect of the 0.8 mm^3 increase in the V_{eff} ; instead, a 19% decrease of the scaled characteristic strength is observed when compared to the 5%

ALT doped samples. This shows that porosity is not the only variable responsible for the failure of the material. This comparison shows that the Weibull modulus is not enough to provide information on the material reliability since values were all very close but other variables must be accounted for. It is hypothesized that a concurrent mechanism contributing to the material failure is related to the mechanical strength of secondary phases developed with the doping process and will be discussed later.

For the ROR samples, a proportionality between ALT doping amount and characteristic strength is observed. The 1% ALT doped samples show that indeed, a decrease in porosity prevails over an increased V_{eff} resulting in higher characteristic strength when compared to the undoped samples.

For both TPB and ROR testing, the lowest Weibull modulus was calculated for the 1% ALT doped samples. When compared to the undoped material, the decreased porosity (from ~45% to ~42%), should result in lower data scattering which should be reflected in an increased Weibull modulus. Instead the opposite behavior is observed while an increased scaled characteristic strength is recorded. The lower Weibull modulus confirms the possibility of a porosity concurrent failure mechanism that relates to the change in the material microstructure due to the dopant effect. To support this hypothesis is the fact that the undoped material resulted in the same scaled characteristic strength value not depending on the testing methodology as per reference [45].

Advanced statistical analyses along with fractography of select samples will be discussed in the next sections to further elucidate the material failure mechanisms.

Advanced Statistical Analysis to Identify Presences of Multiple Fractographic Populations

ASTM C1239-13 provides detailed methodology for characterizing data when multiple flaw populations are present, often expressed as a non-linear pattern in the Weibull-linear plot. When multiple flaw populations are evident the standard approaches to parameter estimation (e.g. Weibull modulus and characteristic strength) are not applicable [49] because multiple flaw distributions may not be well-characterized by a single set of Weibull parameters, and if so a more detailed analysis is required.

Two different flaw populations are suspected for the material in this study: a first one related to porosity and a second one related to the mechanical strength of secondary phases developed during the doping process. An advanced statistical modeling technique, finite mixture distribution modeling, was implemented as follows to measure the strength of evidence provided by each specimen data set in support of multiple populations:

1. **Identify presence of multiple populations:** Assess each batch of strength data for evidence of multiple fractographic populations via finite mixture modeling. If the data provides evidence for more than one population, each individual specimen will then be classified into a sub-population distribution.
2. **For each identified population:** Select representative samples across the strength distribution for fractographic analysis to characterize the fracture mechanism. To accurately represent the entire strength distribution, samples were selected based on the 5-number summary of the strength distribution: minimum, 25%tile, median, 75%tile, maximum.

Finite Mixture Modeling and Assessing Evidence for Multiple Strength Distributions

A sample batch containing a single strength distribution may be characterized by a single Weibull distribution via estimating the parameters of the following probability density function (Equation 7):

$$f(x; \boldsymbol{\theta} = (m, \beta)) = \left(\frac{m}{\beta}\right) \left(\frac{x}{\beta}\right)^{m-1} \exp\left[-\left(\frac{x}{\beta}\right)^m\right] \quad (7)$$

where x represents the strength measurement of a single specimen, m is the Weibull modulus and β is the characteristic strength.

If the strengths are generated by $K < \infty$ distinct flaw distributions (fractographic populations), then the probability density function for this situation (Equation 8) may be written as:

$$g(x; \boldsymbol{\theta}_1, \dots, \boldsymbol{\theta}_K) = \sum_{i=1}^K \pi_i * f(x; \boldsymbol{\theta}_i) \quad (8)$$

where $\boldsymbol{\theta}_i$ is a distinct set of Weibull parameters for the i th component of the mixture distribution and π_i represents the probability weighting of each mixture component where $\sum_{i=1}^K \pi_i = 1$. The model has several unknown parameters for a given data set: K (number of distributions in the mixture), each set of Weibull parameters $\boldsymbol{\theta}_i$, and the mixture probabilities π_i . Advanced statistical methods, specifically the Expectation-Maximization algorithm, were developed to determine the best parameters for a specific set of data [50]. The ‘mixR’ package from the R statistical programming language, which has validated applications of these algorithms [51,52], was used. The procedure was implemented as follows:

1. **Assess the best number of mixture components K for a specific specimen set:**

Up to $K = 3$ distributions were searched in each strength data set. Evidence for

the best number of mixture components is provided by the *Bayesian Information Criteria (BIC)* [50,52]. The model with the smallest BIC is selected as best representation of the data.

2. **Classify:** Based on the selected model, each specimen is classified into a specific distribution via estimation of *responsibilities* [53]. Responsibilities are estimates of posterior probabilities *for each specimen* that communicate how likely the specimen is to belong to a specific component of the mixture.

As a first assessment, distribution summaries are presented in graphical form in Figure 2. The plots show the probability density of the strength data for each specimen with an overlying curve estimating its distribution. Multiple modes in the density curve present some evidence for existence of multiple distributions. If 2 populations are identified as proposed in section 3.1, the expected pattern is bi-modal (presenting two peaks). As this assessment is only qualitative, further tools must be implemented to confirm the presence of multiple populations in the data.

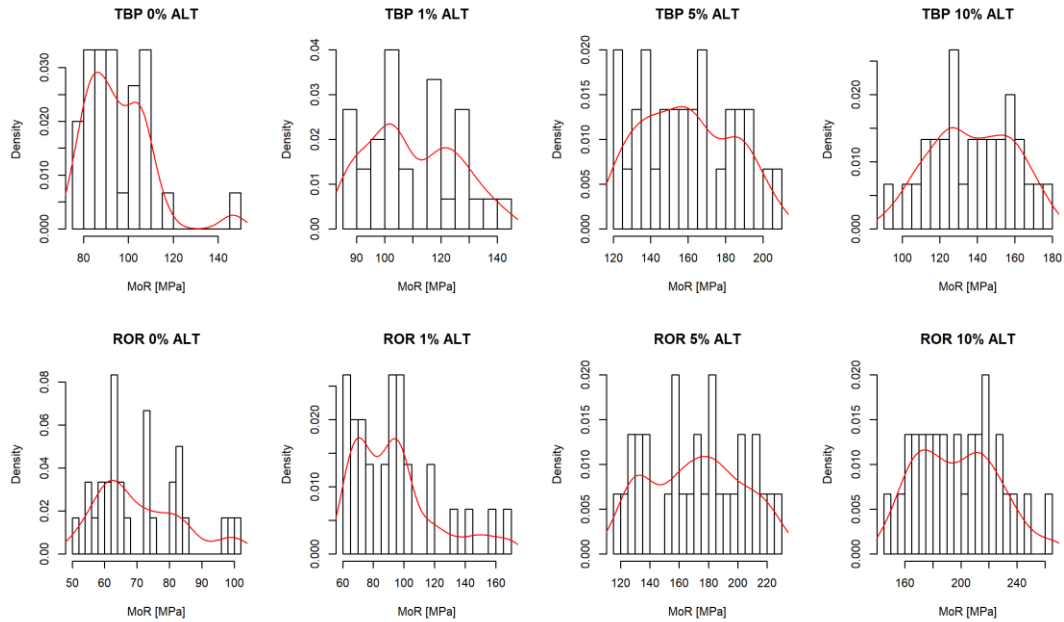


Figure 4.2: Histograms and Probability Density Estimates for the TPB and ROR sample data, 0-10% ALT

To quantify the evidence for multiple populations mixture distributions are fit with $K = 1, 2, 3$ components. BIC is used to select the best model. Table 2 summarizes the data which are minimum BIC subtracted with $\Delta BIC_K = BIC_K - \min(BIC)$. Therefore, the best model corresponds to a $\Delta BIC = 0$. It is common to use $\Delta BIC_K < 2$ as a measure of equal evidence in support of competing models while $2 < \Delta BIC_K < 6$ as positive but not conclusive evidence in support of a model.

Table 4.2: BIC values for model selection

	Number of Populations			Minimum ΔBIC
	1	2	3	
	Model BIC			
TPB				
0 wt% ALT	0.0000	N/A	N/A	N/A
1 wt% ALT	0.0000	2.9327	10.9575	2.9327
5 wt% ALT	0.0000	6.1595	13.4104	6.1595
10 wt% ALT	0.0000	7.2083	16.0234	7.2083
ROR				
0 wt% ALT	1.7373	0.0000	1.7282	1.7282
1 wt% ALT	0.0773	0.0000	9.1568	0.0773
5 wt% ALT	0.0000	7.6213	6.8657	6.8657
10 wt% ALT	0.0000	5.9976	13.9862	5.9976

For both TPB and ROR 5% and 10% ALT doped sample batches, 1 population was confirmed. $K = 1$ mixture components presented the strongest evidence with $\Delta BIC_K = 0$ and the next largest $\Delta BIC_K > 6$. For the TPB 0% sample batch, only the $K = 1$ model can be applied.

For the ROR test, the $K = 2$ mixture component model was strongly supported for 0% and 1% ALT doped batches. For the TPB test, the 1% ALT doped batch, the $K = 2$ model is positively but not conclusively supported ($\Delta BIC_2 = 2.9327$). For these batches, the $K = 2$ mixture component model was applied, then model responsibilities were estimated. Model responsibilities are defined as the probability that each individual specimen belongs to each distribution. The result of this analysis is shown in Figure 3. The left panel shows the full probability density and each fitted mixture density on the histogram. The right panel shows, for each specimen, the responsibility. Data have been classified into distribution 1 or 2 by selecting a threshold of 0.5.

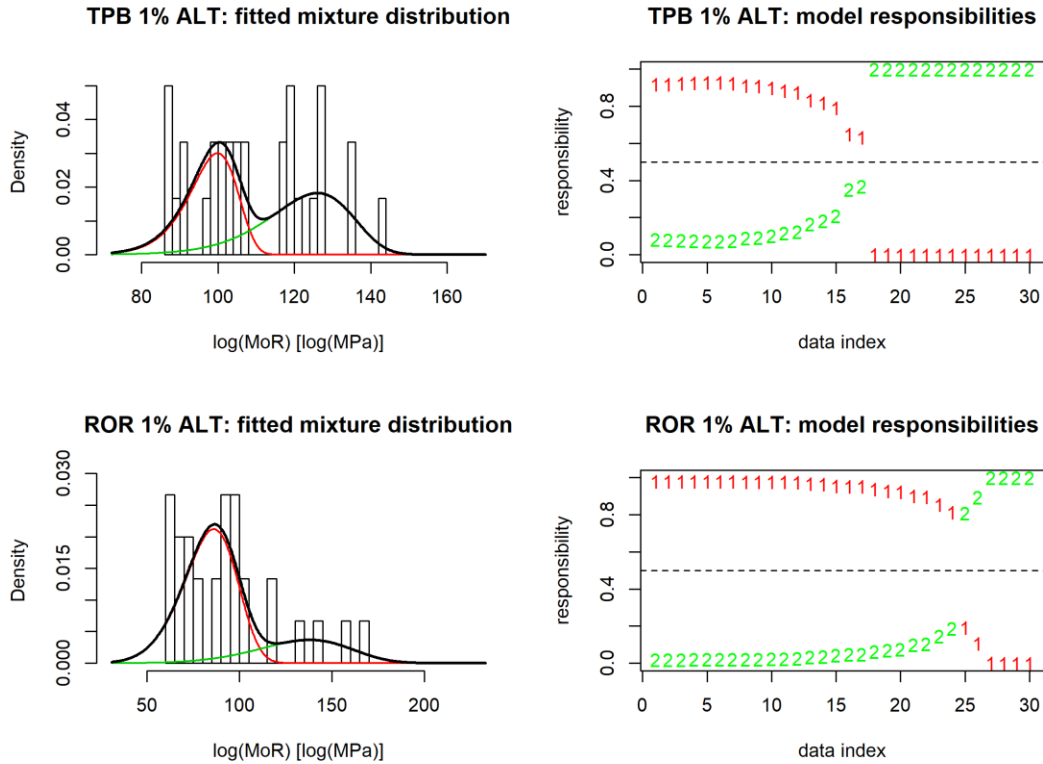


Figure 4.3: Probability Density with Fitted Weibull Mixture Distribution (left) and Model Responsibilities for Each Specimen (right)

With each data characterized to distribution 1 or 2, fractographic characterization by FE-SEM was performed on selected representatives from each strength distribution (minimum, 25%tile, median, 75%tile, maximum) to elucidate the failure mechanism.

Microstructural Analyses

Investigation of samples' surfaces by FE-SEM was performed to assess secondary phases development. Since the same manufacturing process was used for all batches, the same morphology was found on both TPB and ROR samples and is presented in Figure 4. The developed phases are consistent with previous author's findings [12]. The "rough phase" (circled in Figure 4c), forms during the sintering process, persists unaltered after reduction and it enlarges proportionally to the ALT doping amount. TiO₂ from ALT

decomposition, preferentially reacts with YSZ enhancing its sintering characteristics [9,33,34] and leading to the formation of a solid YSZ framework. The contribution to the enhanced doped material mechanical strength is to be related to the volume change resulting from a tetragonal to monoclinic stress induced phase transformation caused by the thermal expansion mismatch with the other material components while in the oxidized state namely NiO, YSZ, Al₂O₃, and NiAl₂O₄ [9,12]. The “small particle phase” (boxed in Figure 4d) is due to the partial reduction of NiAl₂O₄ leading to the formation of Ni nanoparticles within an Al₂O₃ matrix [12,36,54]. The contribution to the enhanced doped material strength is due to the nickel acting either as crack deflector or stopping the crack propagation due to its ductility [12,30,54–56].

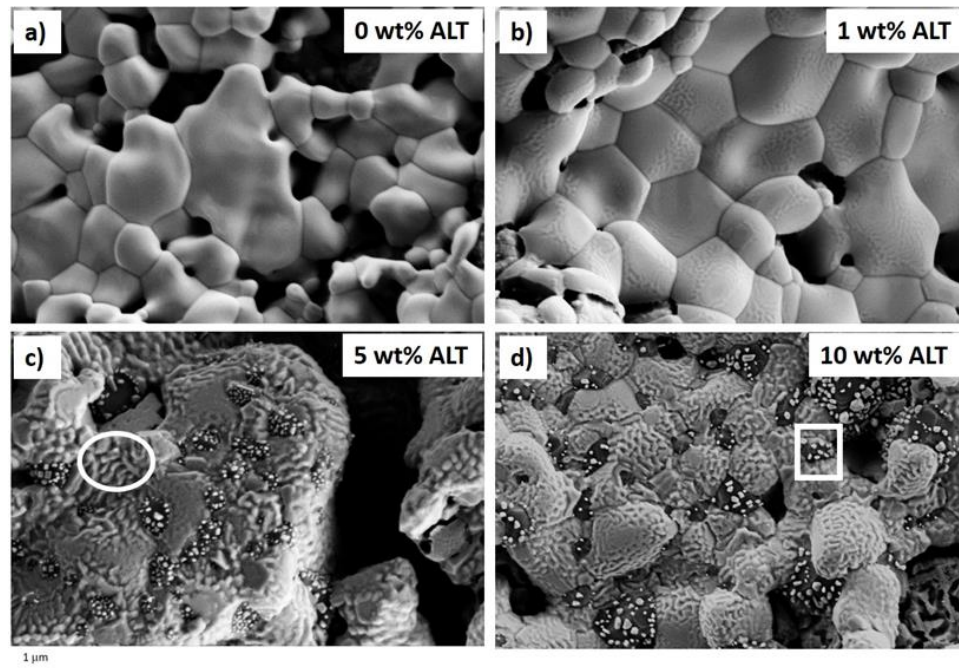


Figure 4.4: FE-SEM surface morphology of uniaxial (TPB) and biaxial (ROR) strength testing samples with a) 0 wt% ALT, b) 1 wt% ALT, c) 5 wt% ALT and d) 10 wt% ALT

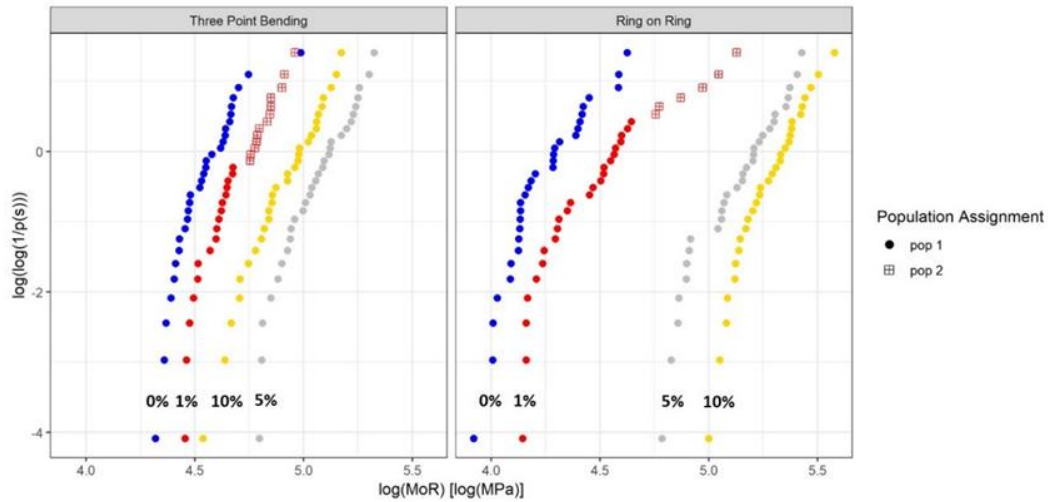


Figure 4.5: Weibull plots with populations denoted for uniaxial (TPB) and biaxial (ROR) strength testing

Despite the non-linear pattern in the Weibull plot of the undoped samples, evidence showed that there is only one flaw population to be considered. The same “cluttered” pattern, with several data points lying on the same line, was found for both testing methodologies. It is thought that porosity is the volume flaw responsible for the material failure not depending on the testing method [45]. Figure 6 is representative of the fracture surface of the undoped sample batches. Selected samples, as described earlier, were analyzed and the fracture surface morphology was found to be similar for all of them showing a clear intergranular (along the grain) fracture pattern. The data points “cluttering” phenomenon is hypothesized to be related to flaws generating cracks that require a similar amount of energy to propagate.

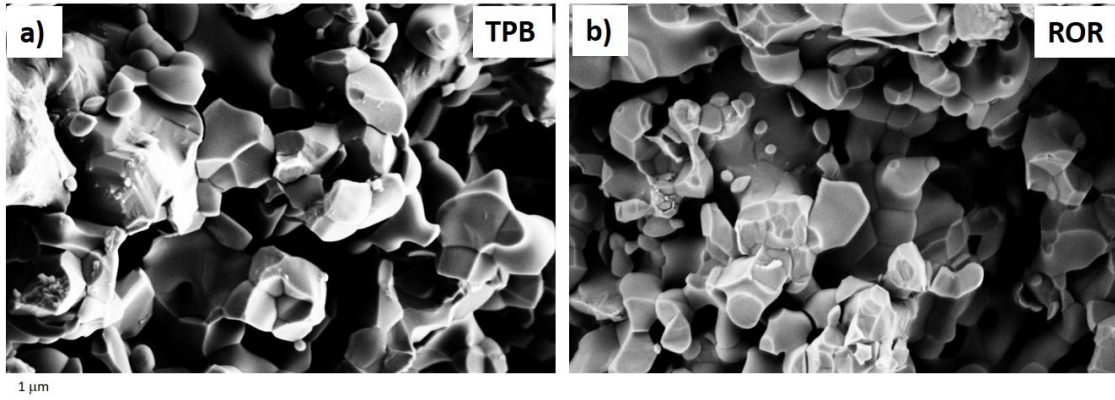


Figure 4.6: Fracture surface of undoped sample batches with a) TPB and b) ROR testing methods

The 5% and 10% ALT doped batches also showed evidence of single flaw population. Very similar fracture surface morphologies were found for the representative samples and are shown in Figure 7.

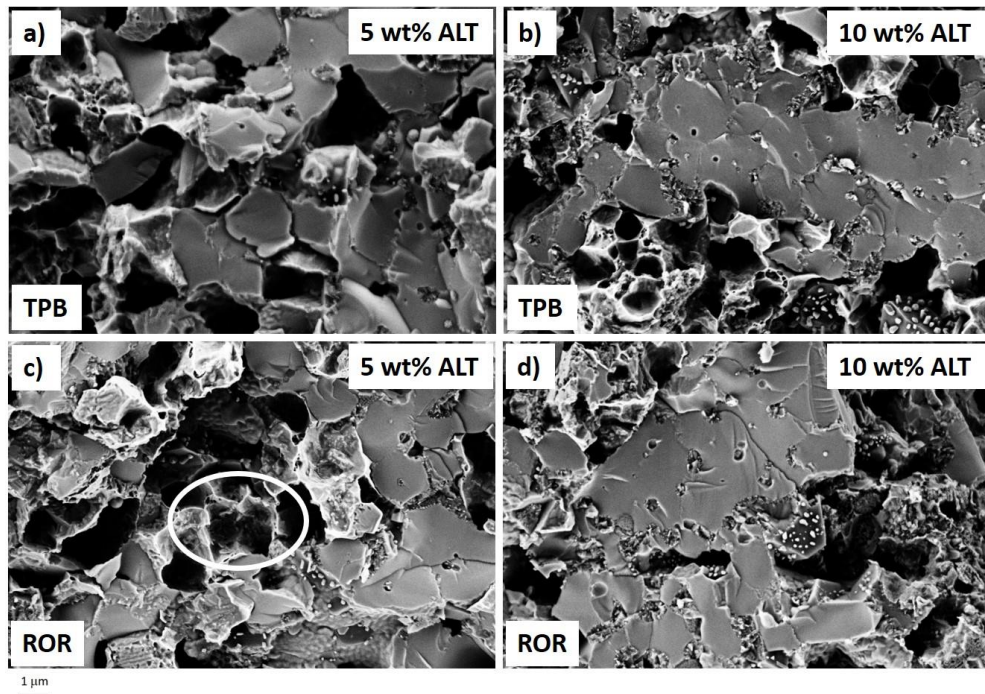


Figure 4.7: Fracture surfaces of a,c) 5% and b,d) 10% ALT doped sample batches fractured with a,b) TPB and c,d) ROR testing methods

For all samples, a clean and flat surface corresponding to transgranular (through the grain) failure can be observed. The lower values of the scaled characteristic strength recorded for the TPB when compared to the ROR are related to the “edge effect” but the mechanisms responsible for the failure of the material is proposed to be the same. In the “small particle” phase, tensile stresses are generated within the Ni particles due to the coefficient of thermal expansion mismatch experienced during the sintering and reduction processes [12,54]. This places the surrounding Al_2O_3 phase in a state of compressive stress increasing its strength. It is hypothesized that the interface between the nickel particles and Al_2O_3 is the volume flaw responsible for the material failure. The mechanical strength of such interface varies within the material depending on the aforementioned stress distribution.

Figure 4 shows how, within the material, regions of the “small particle” phase are distributed within region of the “rough phase” (YSZ framework). It is hypothesized that, in the “small particle” phase, a crack grows under an increasing applied load until it reaches a critical size where the remaining uncracked section of the material (YSZ framework) can no longer support the applied stress at which point complete fracture occurs. Figure 7 supports this hypothesis showing that a small amount of plastic deformation (circled ductile lips in Figure 7c) occurred before fracture. It is believed that this is due to the nickel adding ductility to the system. During crack propagation, stresses will be transferred from the Al_2O_3 substrate to the metallic phase which will yield, deform and then ultimately fail allowing for the crack to reach the undamaged material.

The 1% ALT doped samples showed evidence of the two identified flaw populations. Fractographic analyses confirmed the presence of both intergranular and transgranular features, circled and boxed in Figure 8, respectively. When compared to the undoped samples, the strength increase recorded with TPB and ROR testing are 6% and 55% (Table 1). It must be noted that, the scaled characteristic strength increases due to the formation of NiAl_2O_4 and the Ti-YSZ framework [12]. The onset of the NiAl_2O_4 reduction process requires ~ 10 hours [36]. The 97% reduction at this doping amount, is reached after ~ 4 hours; therefore, the small particle phase does not form. Population 2 (mechanical strength of secondary phases) is defined as the one including data points falling in the upper tail of the strength distribution (Figure 5). For TPB testing, thirteen data points out of the thirty belong to population 2, while for biaxial strength testing it is six. This research has highlighted that ROR strength testing better depicts the overall material mechanical performance. The low ALT doping amount (1%) results in a smaller volume covered by the secondary phases; therefore, the overall beneficial effect is expected to be limited. This well agrees with a smaller number of data points belonging to population 2.

In these cases, where one population distribution occurs in a small number of test specimens, it is not necessary to re-estimate Weibull parameters. Estimates of the Weibull parameters for this flaw distribution would be potentially biased with wide confidence bounds [49].

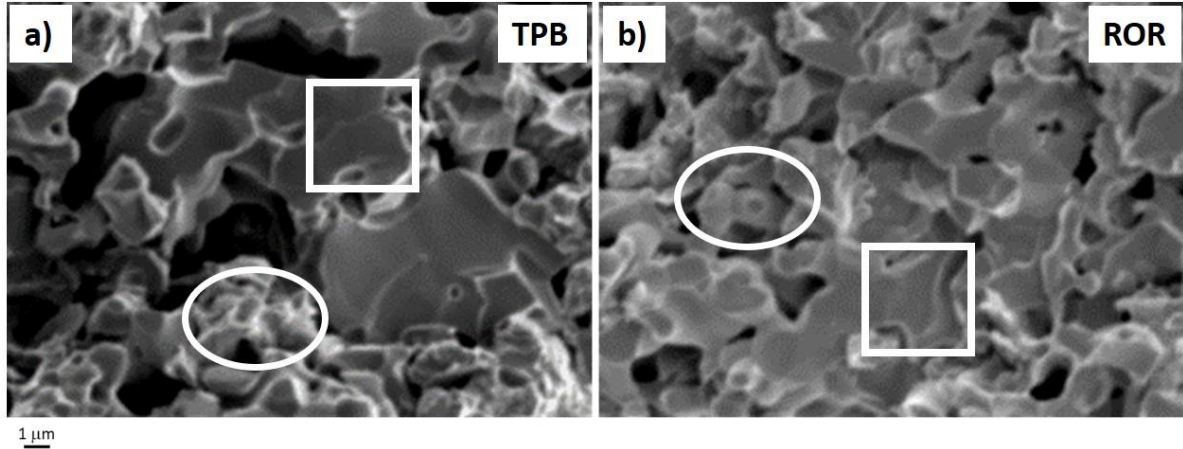


Figure 4.8: Fracture Surface Morphology of 1% ALT doped Ni-YSZ after a) TPB and b) ROR testing

Conclusions

This study has demonstrated that ALT doping can enhance the mechanical properties of Ni-YSZ systems through secondary phases development. Uniaxial and biaxial strength testing have been used to evaluate mechanical properties. An enhancement of the characteristic strength up to 166% has been observed for 10% ALT doping with biaxial strength testing. It has been found that biaxial strength testing better depicts the overall material mechanical performance. The use of different testing methodologies along with advanced statistical analyses has allowed for the identification of two flaw populations that are responsible for the material failure namely, porosity and mechanical strength of secondary phases. Fractography performed on selected samples has allowed for elucidation of the failure mechanism. A single flaw population has been identified for undoped samples. Intergranular fracture has been observed and the failure has been linked to porosity. Samples with ALT doping $\geq 5\%$ are also characterized by a single flaw population. Transgranular fracture has been observed and the failure has been

linked to the mechanical strength of the secondary phases; specifically, the strength of the interface between nickel nanoparticles and their alumina substrate. The presence of both flaw populations was found for the low ALT doping level (1%). Fracture surfaces have been characterized by the presence of both intergranular and transgranular features. It has been proposed that secondary phases, developed by ALT doping, increase the mechanical strength of the material shifting the fracture mechanism from intergranular to transgranular.

Acknowledgements

This work was supported by the DOE under award number DE-FE0031125. FE-SEM analyses were conducted at the Montana State University Image and Chemical Analysis Laboratory.

References

- [1] T. Dey, D. Singdeo, M. Bose, R.N. Basu, P.C. Ghosh, Study of contact resistance at the electrode-interconnect interfaces in planar type Solid Oxide Fuel Cells, *J. Power Sources*. 233 (2013) 290–298. doi:10.1016/j.jpowsour.2013.01.111.
- [2] T. Dey, A. Dey, P.C. Ghosh, M. Bose, A.K. Mukhopadhyay, R.N. Basu, Influence of microstructure on nano-mechanical properties of single planar solid oxide fuel cell in pre- and post-reduced conditions, *Mater. Des.* (2014). doi:10.1016/j.matdes.2013.06.052.
- [3] F. Zhao, A. V. Virkar, Dependence of polarization in anode-supported solid oxide fuel cells on various cell parameters, *J. Power Sources*. 141 (2005) 79–95. doi:10.1016/j.jpowsour.2004.08.057.
- [4] A.C. Müller, D. Herbstritt, E. Ivers-Tiffée, Development of a multilayer anode for solid oxide fuel cells, *Solid State Ionics*. 152–153 (2002) 537–542. doi:10.1016/S0167-2738(02)00357-0.
- [5] Z.R. Wang, J.Q. Qian, S.R. Wang, J.D. Cao, T.L. Wen, Improvement of anode-supported solid oxide fuel cells, *Solid State Ionics*. 179 (2008) 1593–1596. doi:10.1016/j.ssi.2008.03.022.
- [6] T. Setoguchi, K. Okamoto, K. Eguchi, H. Arai, Effects of anode material and fuel on anodic reaction of solid oxide fuel cells, *J. Electrochem. Soc.* 139 (1992) 2875–2880. doi:10.1149/1.2068998.
- [7] M. Kleitz, F. Petitbon, Optimized SOFC electrode microstructure, *Solid State Ionics*. 92 (1996) 65–74. doi:10.1016/S0167-2738(96)00464-X.
- [8] C.R. He, W.G. Wang, Alumina Doped Ni/YSZ Anode Materials for Solid Oxide Fuel Cells, *Fuel Cells*. 9 (2009) 630–635. doi:10.1002/fuce.200800152.
- [9] M. Mori, Y. Hiei, H. Itoh, G.A. Tompsett, N.M. Sammes, Evaluation of Ni and Ti-doped Y₂O₃ stabilized ZrO₂ cermet as an anode in high-temperature solid oxide fuel cells, *Solid State Ionics*. 160 (2003) 1–14. doi:10.1016/S0167-2738(03)00144-9.
- [10] Y. Ye, J. Li, H. Zhou, J. Chen, Microstructure and mechanical properties of yttria-stabilized ZrO₂/Al₂O₃ nanocomposite ceramics, *Ceram. Int.* 34 (2008) 1797–1803. doi:10.1016/j.ceramint.2007.06.005.
- [11] R. Kubrin, G. Blugan, J. Kuebler, Influence of cerium doping on mechanical properties of tetragonal scandium-stabilized zirconia, *J. Eur. Ceram. Soc.* 37 (2017) 1651–1656. doi:10.1016/j.jeurceramsoc.2016.11.038.

- [12] M. McCleary, R. Amendola, Effect of Aluminum Titanate (Al_2TiO_5) Doping on the Mechanical Performance of Solid Oxide Fuel Cell Ni-YSZ Anode, *Fuel Cells*. (2017) 862–868. doi:10.1002/fuce.201700073.
- [13] S. Tekeli, The flexural strength, fracture toughness, hardness and densification behaviour of various amount of Al_2O_3 -doped 8YSCZ/ Al_2O_3 composites used as an electrolyte for solid oxide fuel cell, *Mater. Des.* 27 (2006) 230–235. doi:10.1016/j.matdes.2004.10.011.
- [14] H. Xu, H. Yan, Z. Chen, The flexural strength and densification behavior of Al_2O_3 -doped $\text{Ce}_{0.8}\text{Y}_{0.2}\text{O}_{1.9}$ electrolyte composites, *Mater. Sci. Eng. A.* 447 (2007) 222–226. doi:10.1016/j.msea.2006.10.027.
- [15] D.R. Driscoll, B.W. Tokmakian, N.P. Johnson, C.D. Hunt, S.W. Sofie, Catalyst enhancing aluminum titanate for increasing strength of nickel-zirconia cermets, *Mater. Lett.* 209 (2017) 307–310. doi:10.1016/j.matlet.2017.08.035.
- [16] S.W. Sofie, D.R. Taylor, Controlled Thermal Expansion Anode Compositions with Improved Strength for Use in Anode Supported SOFCs, *Adv. Solid Oxide Fuel Cells III*. (2008) 215–223.
- [17] J.R. Lund, J.P. Byrne, Leonardo Da Vinci's tensile strength tests: Implications for the discovery of engineering mechanics, *Civ. Eng. Environ. Syst.* 18 (2001) 243–250. doi:10.1080/02630250108970302.
- [18] Y. Xu, J. Han, H. Lin, L. An, Comparative study of flexural strength test methods on CAD/CAM Y-TZP dental ceramics, *Regen. Biomater.* 2 (2015) 239–244. doi:10.1093/rb/rbv020.
- [19] D. Munz, T. Fett, *Ceramics: Mechanical Properties, Failure Behaviour, Materials Selection*, 2001. doi:10.1070/sm1981v038n03abeh001340.
- [20] R. Morrell, N.J. McCormick, J. Bevan, M. Lodeiro, J. Margetson, Biaxial disc flexure – modulus and strength testing, *Br. Ceram. Trans.* 98 (1999) 234–240. doi:10.1179/096797899680507.
- [21] ASTM C1499-15, Standard Test Method for Monotonic Equibiaxial Flexural Strength of Advanced Ceramics at Ambient Temperature, *ASTM Int.* (2015) 1–19. doi:10.1017/CBO9781107415324.004.
- [22] D.K. Shetty, A.R. Rosenfield, P. McGuire, G.K. Bansal, W.H. Duckworth, Biaxial flexure tests for ceramics, *Am. Ceram. Soc.* 12 (1980) 1193–1197.

- [23] M.N. GIOVAN, G. SINES, Biaxial and Uniaxial Data for Statistical Comparisons of a Ceramic's Strength, *J. Am. Ceram. Soc.* 62 (1979) 510–515. doi:10.1111/j.1151-2916.1979.tb19117.x.
- [24] B.J. Hulm, J.D. Parker, W.J. Evans, Biaxial strength of advanced materials, *J. Mater. Sci.* 33 (1998) 3255–3266. doi:10.1023/A:1013216825960.
- [25] M.I. Abu-Hassan, O.A. Abu-Hammad, A. Harrison, Strains and tensile stress distribution in loaded disc-shaped ceramic specimens. An FEA study, *J. Oral Rehabil.* 25 (1998) 490–495. doi:10.1046/j.1365-2842.1998.00267.x.
- [26] G.A. Thompson, Determining the slow crack growth parameter and weibull two-parameter estimates of bilaminate disks by constant displacement-rate flexural testing, *Dent. Mater.* 20 (2004) 51–62. doi:10.1016/S0109-5641(03)00068-X.
- [27] A. Nakajo, J. Kuebler, A. Faes, U.F. Vogt, H.J. Schindler, L.K. Chiang, S. Modena, J. Van Herle, T. Hocker, Compilation of mechanical properties for the structural analysis of solid oxide fuel cell stacks. Constitutive materials of anode-supported cells, *Ceram. Int.* 38 (2012) 3907–3927. doi:10.1016/j.ceramint.2012.01.043.
- [28] H. Fischer, W. Rentzsch, R. Marx, A modified size effect model for brittle nonmetallic materials, *Eng. Fract. Mech.* 69 (2002) 781–791. doi:10.1016/S0013-7944(01)00126-6.
- [29] H.L. Frandsen, T. Ramos, A. Faes, M. Pihlatie, K. Brodersen, Optimization of the strength of SOFC anode supports, *J. Eur. Ceram. Soc.* (2012). doi:10.1016/j.jeurceramsoc.2011.11.015.
- [30] B. Charlas, D.W. Ni, H.L. Frandsen, K. Brodersen, M. Chen, Mechanical Properties of Supports and Half-Cells for Solid Oxide Electrolysis Influenced by Alumina-Zirconia Composites, *Fuel Cells.* 17 (2017) 132–143. doi:10.1002/fuce.201600036.
- [31] F. Baratta, W. Matthews, Errors Associated with Flexure Testing of Brittle Materials, *U.S. Army Mater. Technol. Lab.* (1987) 16, 41–42.
- [32] ASTM C1683-10, Standard Practice for Size Scaling of Tensile Strengths Using Weibull Statistics for Advanced Ceramics, *ASTM Int.* (2015) 1–18. doi:10.1520/C1683.
- [33] D.R. Driscoll, M.D. McIntyre, M.M. Welander, S.W. Sofie, R.A. Walker, Enhancement of high temperature metallic catalysts: Aluminum titanate in the nickel-zirconia system, *Appl. Catal. A Gen.* 527 (2016) 36–44. doi:10.1016/j.apcata.2016.08.020.

- [34] C.H. Law, S.W. Sofie, Anchoring of Infiltrated Nickel Electro-Catalyst by Addition of Aluminum Titanate, *J. Electrochem. Soc.* 158 (2011) B1137–B1141. doi:10.1149/1.3610226.
- [35] J. Zyguntowicz, P. Wicinska, A. Miazga, K. Konopka, Characterization of composites containing NiAl₂O₄ spinel phase from Al₂O₃/NiO and Al₂O₃/Ni systems, *J. Therm. Anal. Calorim.* 125 (2016) 1079–1086. doi:10.1007/s10973-016-5357-2.
- [36] M. McCleary, R. Amendola, Reduction kinetics of undoped and aluminum titanate (Al₂TiO₅) doped NiO-YSZ solid oxide fuel cell anodes, *Ceram. Int.* 44 (2018) 15557–15564. doi:10.1016/j.ceramint.2018.05.218.
- [37] ASTM C1161-13, Standard Test Method for Flexural Strength of Advanced Ceramics at Ambient Temperature, *ASTM Int.* (2013) 1–19. doi:10.1520/C1161-13.2.
- [38] J.B. Quinn, G.D. Quinn, A practical and systematic review of Weibull statistics for reporting strengths of dental materials, *Dent. Mater.* 26 (2010) 135–147. doi:10.1016/j.dental.2009.09.006.
- [39] Z. Cui, Y. Huang, H. Liu, Predicting the mechanical properties of brittle porous materials with various porosity and pore sizes, *J. Mech. Behav. Biomed. Mater.* 71 (2017) 10–22. doi:10.1016/j.jmbbm.2017.02.014.
- [40] D. Wu, Y. Li, J. Zhang, L. Chang, D. Wu, Z. Fang, Y. Shi, Effects of the number of testing specimens and the estimation methods on the Weibull parameters of solid catalysts, *Chem. Eng. Sci.* 56 (2001) 7035–7044. doi:10.1016/S0009-2509(01)00340-2.
- [41] A. Khalili, K. Kromp, Statistical properties of Weibull estimators, *J. Mater. Sci.* 26 (1991) 6741–6752.
- [42] M. Radovic, E. Lara-curzio, Elastic Properties of Nickel-Based Anodes for Solid Oxide Fuel Cells as a Function of the Fraction of Reduced NiO, *J. Am. Ceram. Soc.* 87 (2004) 2242–2247. doi:10.1111/j.1151-2916.2004.tb07499.x.
- [43] M. Radovic, E. Lara-Curzio, Mechanical properties of tape cast nickel-based anode materials for solid oxide fuel cells before and after reduction in hydrogen, *Acta Mater.* 52 (2004) 5747–5756. doi:10.1016/j.actamat.2004.08.023.
- [44] Z. Cui, Y. Huang, H. Liu, Predicting the mechanical properties of brittle porous materials with various porosity and pore sizes, *J. Mech. Behav. Biomed. Mater.* 71 (2017) 10–22. doi:10.1016/j.jmbbm.2017.02.014.
- [45] X. Fan, E.D. Case, F. Ren, Y. Shu, M.J. Baumann, Part I: Porosity dependence of the Weibull modulus for hydroxyapatite and other brittle materials, *J. Mech. Behav. Biomed. Mater.* 8 (2012) 21–36. doi:10.1016/j.jmbbm.2011.12.010.

- [46] J. Jin, H. Takahashi, N. Iwasaki, Effect of test method on flexural strength of recent dental ceramics, *Dent. Mater. J.* 23 (2004) 490–496. doi:10.4012/dmj.23.490.
- [47] G.K.R. Pereira, M. Amaral, R. Simoneti, G.C. Rocha, P.F. Cesar, L.F. Valandro, Effect of grinding with diamond-disc and -bur on the mechanical behavior of a Y-TZP ceramic, *J. Mech. Behav. Biomed. Mater.* 37 (2014) 133–140. doi:10.1016/j.jmbbm.2014.05.010.
- [48] K. Zeng, A. Odén, D. Rowcliffe, Flexure tests on dental ceramics., *Int. J. Prosthodont.* 9 (1996) 434–9. <http://www.ncbi.nlm.nih.gov/pubmed/9108743>.
- [49] ASTM C1239-13, Standard Practice for Reporting Uniaxial Strength Data and Estimating Weibull Distribution Parameters for Advanced Ceramics, *ASTM Int.* (2013) 1–9. doi:10.1520/C1239-13.Scope.
- [50] D.D. Boos, L.A. Stefanski, *Essential Statistical Inference: Theory and Methods*, New York, 2013. doi:10.1016/j.peva.2007.06.006.
- [51] R. Gentleman, R. Ihaka, *R Computer Program*, (2019). <https://www.r-project.org/>.
- [52] Y. Youjiao, *mixR: Finite Mixture Modeling for Raw and Binned Data*, (2018). <https://cran.r-project.org/package=mixR>.
- [53] C. Bishop, *Pattern Recognition and Machine Learning*, New York, 2006. doi:10.1021/jo01026a014.
- [54] E. Üstündağ, R. Subramanian, R. Dieckmann, S.L. Sass, In-situ formation of metal-ceramic microstructures in the Ni-Al-O system by partial reduction reactions, *Acta Mater.* 43 (1995) 383–389. doi:[http://dx.doi.org/10.1016/0167-2738\(94\)00148-L](http://dx.doi.org/10.1016/0167-2738(94)00148-L).
- [55] E. Üstündağ, Z. Zhang, M.L. Stocker, P. Rangaswamy, M.A.M. Bourke, J.A. Roberts, S. Subramanian, K.E. Sickafus, S.L. Sass, Influence of residual stresses on the evolution of microstructure during the partial reduction of NiAl₂O₄, *Mater. Sci. Eng. A.* 238 (1997) 50–65.
- [56] M. Lieberthal, W.D. Kaplan, Processing and properties of Al₂O₃ nanocomposites reinforced with sub-micron Ni and NiAl₂O₄, *Mater. Sci. Eng. A.* 302 (2001) 83–91. doi:10.1016/S0921-5093(00)01358-7.

CHAPTER FIVE

EFFECT OF REDOX CYCLING ON THE MECHANICAL PERFORMANCE OF
UNDOPED AND ALUMINUM TITANATE (Al_2TIO_5 , ALT) DOPED NIO-YSZ
SOLID OXIDE FUEL CELL ANODES

Contribution of Authors and Co-Authors

Author: Madisen McCleary

Contributions: Prepared and tested samples, compiled and analyzed numerical data, generated figures/tables and wrote manuscript.

Co-author: Roberta Amendola

Contributions: Provided insight on experimental design and implementation. Aided in manuscript editing and preparation.

Co-author: Benjamin McHugh

Contributions: Aided in preparation and testing of samples. Aided in data analyses.

Manuscript Information Page

Madisen McCleary, Roberta Amendola, Benjamin McHugh
Status of Manuscript:

- Prepared for submission to a peer-reviewed journal
- Officially submitted to a peer-review journal
- Accepted by a peer-reviewed journal
- Published in a peer-reviewed journal

EFFECT OF REDOX CYCLING ON THE MECHANICAL PERFORMANCE OF
UNDOPED AND ALUMINUM TITANATE DOPED NiO-YSZ SOLID OXIDE FUEL
CELL ANODES

Madisen McCleary, Roberta Amendola*, Benjamin McHugh

Montana State University, Mechanical and Industrial Engineering, 220 Roberts Hall,
Bozeman, MT 59717, United States

[*] Corresponding author, Roberta.amendola@montana.edu

The following work is in progress to be submitted for publication.

Abstract

The mechanical properties of aluminum titanate (ALT) doped NiO-YSZ anodes were evaluated after undergoing full redox cycles. ALT was added from 0 -10 wt% to undoped anodes (NiO-YSZ) by mechanical mixing and subsequent tape casting. Reduction was performed at 800°C and oxidation at 675°C. Samples were mechanically tested after undergoing 1, 2 or 5 redox cycles. Mechanical testing was conducted using a three-point bending apparatus and Weibull statistics were employed to evaluate mechanical strength. Increased amounts of ALT decreased the strength of the material and surface cracking is visible for 5 and 10 wt% ALT doping. This is thought to be due to decreased porosity leading to the inability to dissipate stresses involved in redox cycling. 5 redox cycled samples showed increased mechanical strength. This is thought to be due to an increased nickel network after redox cycling that increases strength due to added ductility.

Introduction

A solid oxide fuel cell (SOFC) is a renewable energy device that produces power through electrochemical oxidation of a fuel. For commercial viability of SOFCs, materials selection for the components is crucial. Researchers are investigating the use of anode supported SOFCs that may allow for lower temperature operation with similar efficiencies. NiO-YSZ composite anodes are the most heavily researched due to their high power to cost ratio [1,2]. Anode research has recently been focused on cells with excellent single cell performance [3–9] but until further research has been conducted, to produce sufficient power many single SOFCs must be stacked in electrical series. To ensure excellent contact between adjacent cells, the SOFC stack must be clamped with pressures between 65-70 kPa [10,11].

For an anode-supported cell, the anode provides the mechanical strength for the stack assembly, but little fundamental data exists on the mechanical properties of anode materials. Due to the brittle nature of the ceramic components, the strength and reliability of the SOFC depends on the thermo-mechanical properties such as the coefficient of thermal expansion, elastic behavior and fracture mechanics. Therefore, it is crucial to study the mechanical behavior of SOFC anode materials before using it in a stack. There has been much research into new anodes materials, but further investigation is needed before implementation into the SOFC stack [12–20]. The mechanical properties of ceramics are sensitive to changes in material chemistry and manufacturing process but it has been shown that the introduction of secondary phases, that do not compromise the

electrochemical performance of the cell, can also improve mechanical performance [8,9,21,22].

Previous research has shown benefits to the mechanical performance of Al_2O_3 and TiO_2 doping of YSZ electrolytes [8,9,21,23–30]. Researchers have also found that doping Ni/YSZ based anode material with aluminum titanate, Al_2TiO_5 , (ALT) increases the mechanical performance along with stabilization of the SOFC in terms of slow degradation rates and high power output due to the formation of two secondary phases during sintering and subsequent reduction [31–35]. These two phase allow for stress distribution and compensation increasing the mechanical strength [35].

SOFCs' lifetimes are proposed to be on the order of more than 40,000 hours [36]. During operation, fuel is supplied to the anode reducing the NiO to Ni metal. This process is necessary for power production of the SOFC by creating a Ni network for electron transport. As long as fuel (namely H_2) is continuously supplied to the anode, it will stay in a reduced state (Ni-YSZ) and continue to produce power. However, if the supply of fuel is interrupted then, at the operating temperatures of SOFCs (800°C), Ni will oxidize to NiO. This is either due to intentional or unintentional loss of fuel to the anode during its long operation lifetime.

Once the fuel is restored, the NiO will re-reduce but the structure has been permanently compromised [37–43]. The reduction and re-oxidation of NiO causes volume changes within the material generating stresses that damage the microstructure of the anode [38,40,41,44–46]. The molar volume of NiO is approximately 1.66 times larger than Ni [43,47–49]. This increase in volume during re-oxidation causes mechanical stress

within the anode that results in cracking and/or failure of the SOFC. The redox stability of Ni-YSZ anode materials has been receiving increased attention due to the possibility for use of these systems for residential and industrial power generation and auxiliary power units where they will be powered on and off more frequently. NiO/YSZ anode materials under redox cycles have been heavily researched [41,43,50–52] but little data exists on the effects of secondary phases on the redox stability of NiO/YSZ anodes.

Previous research into the effects of ALT doping on NiO-YSZ anodes after redox cycling has been studied in terms of electrochemical performance [47,53]. It was found that in comparison with undoped anodes, ALT doping showed less degradation after each redox cycle [53]. It is believed that the lower degradation of the ALT doped cell is due to the formation of secondary phases [53]. To complement the electrochemical studies on this material, for this study, anode material (NiO-YSZ) doped with ALT was mechanically tested to investigate the role of secondary phase formations on the stability of the anode and its ability to compensate for stress generated by redox cycling. In this study, anodes doped with ALT (0-10 wt%) were subjected to full redox cycling where the samples were reduced or oxidized to over 90% for each cycle. Mechanical testing was then performed after 1, 2 or 5 redox cycles.

Methods

Nickel Oxide (NiO) powder (4 μm , Alfa Aesar), 8 mol% Ytria Stabilized Zirconia (8YSZ) powder (300 nm, Tosoh) and Aluminum Titanate (ALT) powder (25 nm, Sigma Aldrich) were used for sample manufacturing. Powders, in the ratio of 34 wt% YSZ, 66 wt% NiO and 0-10 wt% ALT, were mechanically mixed for 24 hours with

binder and deionized water and subsequently tape cast with a doctor blade thickness of 2 mm.

Rectangular 40 x 6 mm samples were cut from the tape cast using a rotary cutter. Thermolysis of green tape cast samples was performed in ambient air with the following procedure: 1) 2°C/min up to 150°C, 2) dwell for 2 hours, 3) 0.5 °C/min up to 450°C, 4) 5 °C/min up to 1100°C, 5) dwell for 2 hours, 6) 10 °C/min to room temperature. Thermolysis and partial sintering was performed in a box furnace (Thermolyne, 1300). Sintering was conducted with a heating/cooling rate of 5°C/min up to 1500°C and a dwell time of 2 hours (Zircar, Hot Spot 110).

Full redox cycling was performed in a tube furnace (Thermo Scientific, Lindberg Blue M) flowing 5% H₂ and 95% N₂ gas, at 800°C for reduction. For oxidation, the samples were placed in a tube furnace at 675°C. Oxidation was performed at this temperature to lower the re-oxidation rate allowing for lower curvature of the samples to allow for accurate mechanical testing. For all redox cycles, the samples reached at least 90% reduction/oxidation before the subsequent reduction/oxidation. The samples were reduced to 97% for final reduction before fracture. Starting from the oxidized state after sintering, the samples were exposed as follows for one redox cycle: 1) reduction to at least 90%, 2) oxidation to at least 90%, and 3) final reduction to at least 97%.

The percentage reduction/oxidation was calculated using the initial and final weight of each sample. In these manufacturing conditions, ALT is known to spontaneously decompose during sintering to Al₂O₃ and TiO₂. Al₂O₃ reacts with NiO to form NiAl₂O₄ (Equation 1).



NiAl₂O₄ has slow reaction kinetics and does not begin to reduce until over 10 hours at 800°C and does not fully reduce until over ~600 hours [54–56]. It is assumed that under these reducing conditions NiAl₂O₄ does not reduce and for calculations all available Al₂O₃ reacts to form the maximum amount of NiAl₂O₄. This weight is then removed from the available NiO for reduction. The percentage reduction/oxidation was evaluated with a Radwag XA 82/220.R2 microscale. Time required for the reduction/oxidation process varied proportionally to the doping amount of ALT. Sample batches were redox cycled 1, 2 or 5 times before fracture.

After the selected number of redox cycles (1, 2 and 5 cycles), un-doped and 1, 5 and 10 wt% ALT doped batches of 30 samples were loaded at a rate of 0.2 mm/min in a three-point bending apparatus (Pasco Scientific 8236) as per ASTM C1161-13 standard. Fracture strength, effective volume V_{eff} , scaled characteristic strength σ_0' , Weibull modulus (m) with normalized upper and lower bounds, and open porosity, by alcohol immersion method, were evaluated. Weibull statistics were performed under the guidance of ASTM C1239-13 [57]. Field Emission Scanning electron microscopy (FE-SEM, Zeiss Ultra) microstructural characterization and fractography was conducted to determine the nature of the developed phases and their contribution to the material mechanical strength.

Results and Discussion

Mechanical Properties

Table 1 shows the mechanical properties data for the ALT doped Ni-YSZ sample batches after undergoing 1, 2 or 5 redox cycles. The characteristic strength, based off Weibull statistics, is calculated at a probability of failure of 63.2% according to ASTM C1239-13 [57]. Discussion of the effective volume, V_{eff} , and the scaled characteristic strength can be found below. It can be observed that ALT doping increases the characteristic strength for most doping levels when compared to the undoped samples. Literature reports values for undoped NiO-YSZ anodes at between 80 and 130 MPa [19,58] for the characteristic strength without undergoing redox cycling. It can be observed that the undoped samples' characteristic strength values fall within this range. ALT doping increases the characteristic strength to the top of the cited range. Further discussion in relation to the mechanical properties can be found below.

Table 5.1: Mechanical properties of ALT doped Ni-YSZ anodes after undergoing 1, 2 or 5 redox cycles

	0 wt% ALT	1 wt% ALT	5 wt% ALT	10 wt% ALT
1 Redox Cycle				
Average Strength (MPa)	110	135	121	94
V_{eff} (mm ³)	0.17	0.34	0.70	0.86
Scaled Characteristic Strength (MPa)	93	115	124	97
Strength Increase (%)	N/A	24	34	4
2 Redox Cycles				
Average Strength (MPa)	94	133	120	106
V_{eff} (mm ³)	0.30	0.27	0.58	0.37
Scaled Characteristic Strength (MPa)	85	112	115	85
Strength Increase (%)	N/A	32	35	0
5 Redox Cycles				
Average Strength (MPa)	114	170	83	105
V_{eff} (mm ³)	0.19	0.16	0.70	0.69
Scaled Characteristic Strength (MPa)	97	142	72	101
Strength Increase (%)	N/A	47	-25	4

Ceramic fracture suffers from large scatter in the data due to the nature of brittle fracture. Ceramic materials undergo little to no strain before fracture; so, the weakest spot under tension determines the strength of the material. These weak spots are usually flaws within the material such as manufacturing defects or pores. Due to the variability in flaw distribution, mechanical strength values between individual samples vary significantly; therefore, statistical analyses are necessary for accurate mechanical properties analyses. Weibull statistical methods are commonly used by researchers for the calculation of the mechanical strength of advanced ceramics [59–62]. Using this method, the Weibull distribution equation has two parameters that are calculated that relate to the mechanical

strength of the material, the characteristic strength and the Weibull modulus [57]. The Weibull distribution can be found in Equation 2:

$$p_s = \exp\left(-\frac{\sigma}{\sigma_0}\right)^m \quad (2)$$

Where p_s is the probability of survival for each sample, σ is the flexural strength of each sample (MPa), σ_0 is the characteristic strength (MPa), and m is the Weibull modulus.

The characteristic strength as discussed earlier is used to determine the overall flexural strength of the material for the batch tested. The Weibull modulus indicates the nature, severity and dispersion of flaws and is used for statistical comparison of two or more test data sets to predict the probability of failure [10,58,63]. A high Weibull modulus is desirable for all materials since it indicates an increased homogeneity in the flaw population and a more predictable failure. On the contrary, a low Weibull modulus is indicative of a large spread of flexural strength data within the group and a less predictable failure behavior. Table 2 shows the Weibull modulus data along with the normalized upper and lower bounds on the maximum likelihood estimate of the Weibull modulus (90% confidence interval). These values were calculated according to ASTM standard C1239-13 [57]. It can be observed in Table 2 that ALT doping decreases the Weibull modulus value indicating a less homogeneous flaw population within the sample batch. This finding seems contradictory as previous research into ALT doped anode materials has found an increase in the Weibull modulus with ALT doping for anode materials that have not undergone redox cycling [64]. Further discussion of the decrease in Weibull modulus can be found below.

Table 5.2: Weibull modulus and 90% confidence interval for ALT doped NiO-YSZ anodes after undergoing 1, 2 or 5 redox cycles

	0 wt% ALT	1 wt% ALT	5 wt% ALT	10 wt% ALT
1 Redox Cycle				
Weibull Modulus	9.7	6.2	4.2	3.4
90% Confidence Interval	7.3 - 11.8	4.7 - 7.6	3.2 - 5.2	2.5 - 4.1
2 Redox Cycles				
Weibull Modulus	7.2	7.2	4.4	5.4
90% Confidence Interval	5.4 - 8.8	5.4 - 8.8	3.3 - 5.4	4.1 - 6.6
5 Redox Cycles				
Weibull Modulus	8.9	9.0	3.8	4.0
90% Confidence Interval	6.7 - 10.9	6.7 - 10.9	2.9 - 4.7	3.0 - 4.9

Due to the nature of Weibull calculations, the Weibull modulus and characteristic strength do not fully characterize the mechanical properties. Figure 1 below shows the Weibull plots for the anode sample batches after undergoing 1, 2 or 5 redox cycles. The Weibull plots are created by manipulation of the Weibull distribution equation (Equation 2) into straight line form (Equation 3).

$$\ln(\ln(1/p_s)) = m \ln(\sigma/\sigma_0) \quad (3)$$

Where p_s is the probability of survival for each sample, σ is the flexural strength of each sample (MPa), σ_0 is the characteristic strength (MPa), and m is the Weibull modulus.

These plots are used to determine the reliability of the batch data in correlation with the Weibull modulus. If the strength data calculated for each sample well aligns with the Weibull modulus linear trendline then it can be said that the batch data well agrees with the Weibull statistics and has a more reliable and predictable failure. Usually, the batch

with the highest Weibull modulus will also correspond with the data points more closely fitting the linear trendline but is not always the case; therefore, the Weibull plots must be analyzed to determine if the strength data trends agree with the Weibull modulus calculated.

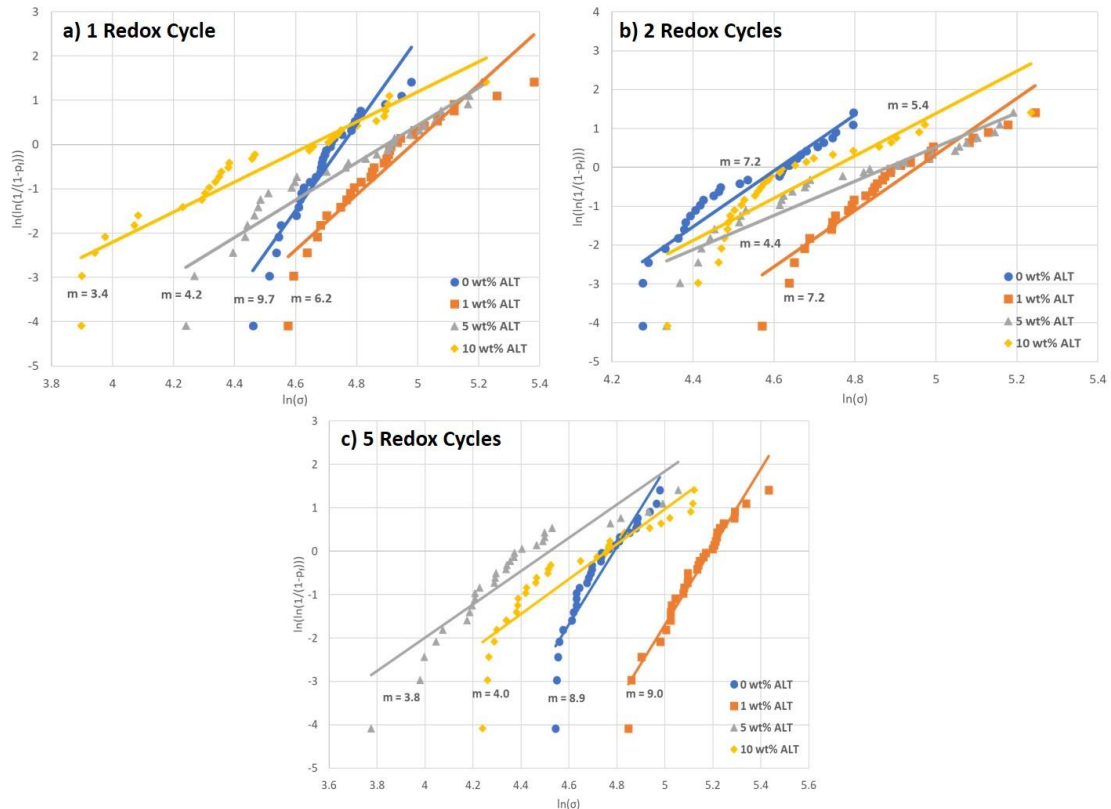


Figure 5.1: Weibull plots of ALT doped NiO-YSZ anodes after undergoing a) 1, b) 2 or c) 5 redox cycles

It can be observed in Figure 1 that for the sample batches after undergoing 1 redox cycle (Figure 1a), the data points lie closest to the linear trendline for the undoped samples which corresponds to the highest Weibull modulus at 9.7; therefore, it can be concluded that the undoped sample batch after one redox cycle likely had the most

reliable fracture characteristics. For the sample batches after undergoing 2 redox cycles, the data lies closest to the linear trendline for the 1 wt% ALT sample batch and this corresponds to the highest Weibull modulus and characteristic strength; therefore, 1 wt% ALT doping seems to have the highest strength and reliability for 2 redox cycles. For the 5 redox cycled sample batches, the 1 wt% ALT sample batches' data lie closest to the linear trendline and corresponds to the highest Weibull modulus and highest mechanical strength. This again confirms the highest strength and reliability for the 1 wt% ALT doped samples. Observing the Weibull data and plots, it seems that the 1 wt% ALT sample batches resulted in the highest strength and reliability for the anode material after redox cycling.

According to Weibull statistical methods, fracture occurs in brittle ceramic materials when the weakest spot under tension fails. If the volume over which tension is applied is larger then there is a higher likelihood of stressing a flaw, causing an apparently lower strength for that sample. Conversely, if the tested volume is smaller, then the likelihood of stressing a flaw is lower and the apparent strength will be higher. Therefore, it is important to account for the volume under tension or the effective volume, V_{eff} , to make accurate comparisons between sample batches [55,58,65–67]. The effective volume for samples fractured in three-point bending can be found in Equation 1 and the scaled characteristic strength is defined in Equation 2.

$$V_{eff} = \frac{lwh}{2(m+1)^2} \quad (1)$$

$$\sigma'_0 = \sigma_0 \left(\frac{V_{eff}}{1 \text{ mm}^3} \right)^{\frac{1}{m}} \quad (2)$$

Where l is the length between support points (mm), w is the width of the sample (mm), h is the height of the sample (mm), m is the Weibull modulus, V_{eff} is the effective volume (mm^3), σ_0 is the characteristic strength (MPa) and σ_0' is the scaled characteristic strength (MPa). The scaled characteristic strength converts the characteristic strength of each batch to the same effective volume for more accurate comparison between the batches.

When observing the scaled characteristic strength values (Table 1), the strength of the samples after 2 redox cycles is the lowest and 5 redox cycles is highest on average. For the undoped, 1 and 10 wt% ALT samples, the highest strength is observed for the 5 redox cycled sample batch. For the 5 wt% ALT doped samples, the 1 redox cycle sample batch has the highest strength. The lowest strength for the undoped, 1 and 10 wt% ALT sample batches was calculated for 2 redox cycles. The lowest strength for the 5 wt% ALT sample batches was observed for 5 redox cycles. When observing the effects of ALT doping on mechanical strength it can be observed that the highest strength was found for the 1 wt% ALT sample batch for all redox cycles. 5 wt% ALT doping does show increased strength when compared to undoped anodes but not as high as 1 wt% ALT doping; whereas, 10 wt% ALT doping shows strength values close to undoped anodes. Previous research has observed increases in strength up to 10 wt% ALT doping for anodes that have not undergone redox cycling [35]. The apparent contradiction in ALT doping effects will be further discussed below.

Porosity of ceramic materials greatly influences the mechanical strength. Pores act as stress concentrators within the material and the severity is determined by the size, shape and distribution of these pores. It is well known that an increase in porosity usually

results in lower mechanical strength due to an increase in pores (flaws) under tension.

Due to the dependence of mechanical strength on porosity, the open porosity of selected samples from each batch was measured according to Archimedes' method.

Table 3 shows the porosity measurements for each of the sample batches tested. It can be observed that the porosity values decrease with increasing amount of ALT. This has been previously observed as the result of the formation of secondary phases during sintering and subsequent reduction [64]. Comparing the different amounts of redox cycles, it can be observed that the porosity only slightly changes during redox cycling. Previous research has seen a more drastic decline in the porosity with ALT doping before redox cycling [64]. A decrease of ~50% in porosity has been measured in previous work in contrast to the ~30% decrease for these samples [35]. The less drastic decrease in porosity at higher amounts of ALT could be due to an increase in pore channels. Due to the method used for measurement of the porosity, only pores that are connected and open to the environment will be measured; whereas, pores that are completely enclosed will not be measured. Redox cycling could through microcracking, increase the open channels for porosity measurement. Also, cracks developed within the bulk of the material will be treated as porosity using the alcohol immersion method not allowing for distinguishing between pores and cracks. Further work is needed to determine the porosity distribution within redox cycled materials including pore shape, size and distribution. Porosity will be further discussed below in regard to microstructural analyses.

Table 5.3: Porosity measurements for ALT doped NiO-YSZ anodes after undergoing 1, 2 or 5 redox cycles

	0 wt% ALT	1 wt% ALT	5 wt% ALT	10 wt% ALT
1 Redox Cycle				
Porosity (%)	48	41	37	33
2 Redox Cycles				
Porosity (%)	49	40	37	34
5 Redox Cycles				
Porosity (%)	48	40	38	36

Microstructural Analyses

To further investigate the effects of ALT doping on mechanical strength, fractography and surface analyses were performed using FE-SEM. Figure 2 shows the surface morphology of the ALT doped NiO-YSZ anode material after 1 redox cycle. It can be observed that there is the presence of two secondary phases after 5 wt% ALT doping. The rough phase (circled in Figure 2c) has been previously determined to be the Ti/YSZ framework [9,64]. The small particle phase (circled in Figure 2d) has been identified as the partial reduction of NiAl_2O_4 to Ni nanoparticles atop an Al_2O_3 matrix [64,68–70]. Large surface cracks are visible in the 5 and 10 wt% ALT doped samples. It appears that the cracks are propagating through the rough phase and around the small particle phase. Further discussion of the presence of the cracking can be found below. Figures 3 and 4 show the surface morphology of the ALT doped Ni-YSZ sample batches after undergoing 2 and 5 redox cycles, respectively. It can be observed that the surface morphologies of these samples are similar to the 1 redox cycled sample batch (Figure 2). The surface cracks for these sample batches also appear to be traveling through the rough phase and around the small particle phase. This is due to the nature of the phase

developed within the microstructure. The rough phase has high stiffness while the small particle phase has added ductility. Due to the high stiffness of the rough phase when compared to the small particle phase, it is more likely that this phase will crack before the small particle phase. Further discussion of the influence of the secondary phases can be found below.

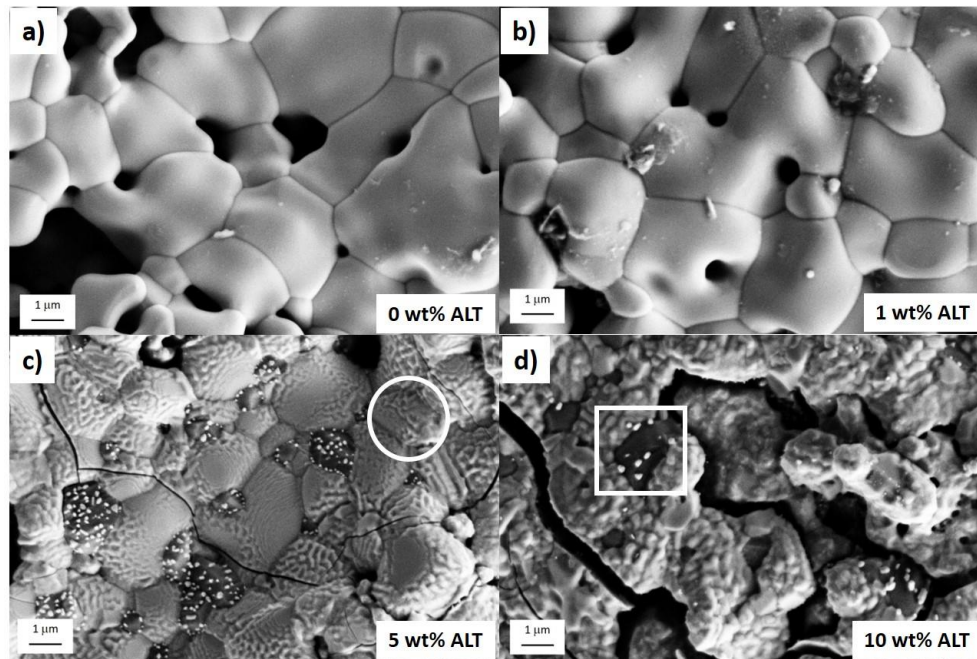


Figure 5.2: FE-SEM surface morphology of a) 0 wt% ALT, b) 1 wt% ALT, c) 5 wt% ALT and d) 10 wt% ALT doped NiO-YSZ anode material after undergoing 1 redox cycle

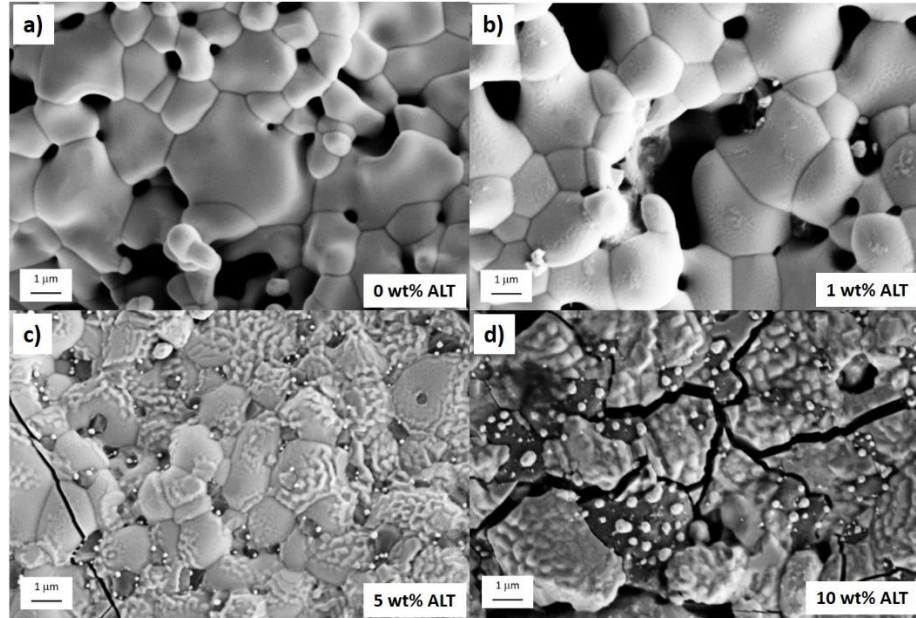


Figure 5.3: FE-SEM surface morphology of a) 0 wt% ALT, b) 1 wt% ALT, c) 5 wt% ALT and d) 10 wt% ALT doped NiO-YSZ anode material after undergoing 2 redox cycles

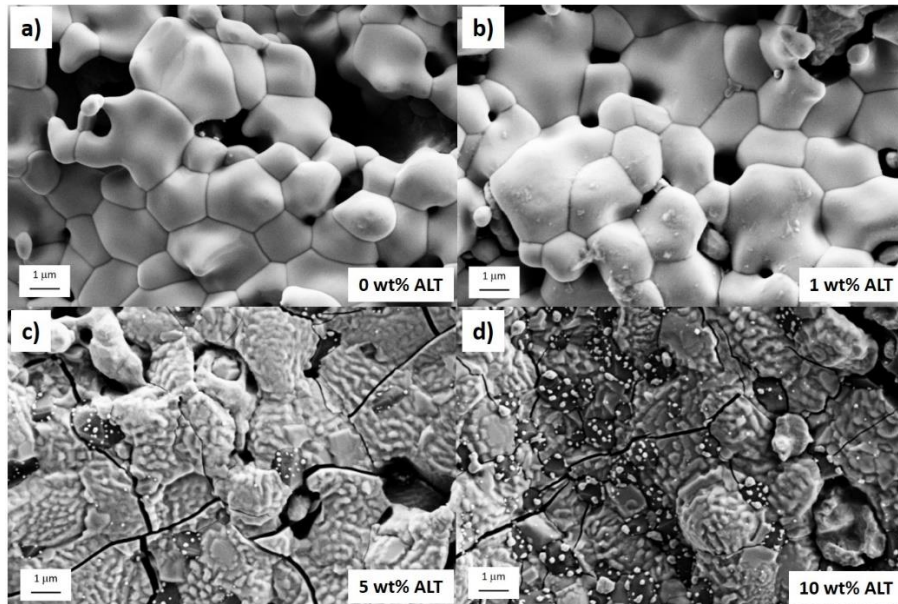


Figure 5.4: FE-SEM surface morphology of a) 0 wt% ALT, b) 1 wt% ALT, c) 5 wt% ALT and d) 10 wt% ALT doped NiO-YSZ anode material after undergoing 5 redox cycles

Previous researchers have investigated the effect of the microstructure on the redox behavior of NiO-YSZ anode materials. One major factor in redox stability was the initial porosity in the bulk [41,52]. During reduction, the conversion of NiO to Ni does not cause large volume change within the anode material due to the YSZ framework adding rigidity that allows for shrinkage of the NiO to Ni without loss of integrity [50]. During re-oxidation, the volume expansion of Ni to NiO is greater than the previous oxidized state due to the microstructural difference in NiO grains after re-oxidation. The volume expansion from Ni to NiO is approximately 40% [48]. It has been observed that the morphology of the NiO particles after re-oxidation has a “sponge” like characteristic due to the necessity for gas transport during re-oxidation [41]. These NiO particles are not visible in these surface images as the samples were fractured in the reduced state. Further research could investigate the phase formations after re-oxidation to investigate surface morphology with ALT doping. The large increase in volume from re-oxidation adds residual compressive stress to the NiO while putting the YSZ framework into tension [51,71,72]. Due to the large volume change needed for re-oxidation, it was suggested that a higher amount of porosity allowed the material to compensate for the stress of volume changes due to the re-oxidation by addition space (pores) for volume expansion.

Taking this into account, during reduction of ALT doped samples, the Ti/YSZ framework will allow for low volume change with little disruption to the overall mechanical integrity of the anode material. Given that NiAl_2O_4 needs sufficient time for the onset of reduction to the small particle phase (~10 hours at 800°C), it can be assumed

that only a small amount will reduce during the initial reduction depending on the doping amount of ALT [54]. The residual NiAl_2O_4 that has not been reduced can act as additional framework due to its high stiffness [55,73]. After initial reduction, the material will have added porosity from NiO to Ni phase change with a small amount of reduced NiAl_2O_4 while the framework of Ti/YSZ and NiAl_2O_4 support the volume change. As not all the NiAl_2O_4 has reduced, the amount of porosity that could be available to the system will be less than undoped anodes.

Between the undoped and 1 wt% ALT doped anode materials there is a strength increase while also a decrease in porosity. Given the previous discussion, a decrease in porosity should result in a decrease in strength due to the need for volume expansion during re-oxidation from Ni to NiO . Instead, the opposite is found for the 1 wt% ALT doped samples. During re-oxidation of the ALT doped samples, the Ti/YSZ framework is thought to be able to undergo an increased amount of tensile stress due to the destabilization of the YSZ crystal structure [35,74]. This increase in strength of the YSZ allows for more stress before failure; therefore, the increased stress from volume expansion can be compensated by the strength of the rough phase. For the 1 wt% ALT doped samples, the partial reduction of NiAl_2O_4 is unlikely due to the high amount of thermal energy needed for reduction. Previous research has shown that the reduction of NiAl_2O_4 does not begin until after ~10 hours at 800°C . The 1 wt% ALT doped samples only require about ~5 hours in the furnace for full reduction making the reduction of NiAl_2O_4 improbable. It is assumed for the 1 wt% ALT doped samples that NiAl_2O_4 remains unchanged during reduction and re-oxidation. The NiAl_2O_4 during re-oxidation

will be in tension from the volume expansion of Ni to NiO. Due to the higher stiffness of NiAl₂O₄, similarly to the Ti/YSZ framework, the stresses from the volume expansion will not be able to overcome the tensile strength of the phase causing failure. The increased stiffness of the Ti/YSZ framework and NiAl₂O₄ allow for higher stresses from volume expansion and explains the increased strength with lower porosity for the 1 wt% ALT doped samples.

For the samples with higher doping amounts of ALT (5 and 10 wt%), during reduction there will be a small amount of NiAl₂O₄ reduction due to the increased reduction time. The reduction time for 5 and 10 wt% ALT doped samples is over 10 hours with the 10 wt% ALT samples taking longer to reduce [54]. The increase in reduction time will allow for a small amount of partial reduction of NiAl₂O₄ for the 5 wt% ALT doped sample with an increased amount for the 10 wt% ALT doped sample. During re-oxidation, the partial reduction of NiAl₂O₄ to form the small particle phase is thought to remain unchanged as there is insufficient thermal energy for reformation of NiAl₂O₄. Further investigation into the phases present after re-oxidation will need to be conducted to determine the validity of this theory. During the reduction of NiAl₂O₄, there is an associated theoretical volume decrease of ~18% [70]. This will add residual stresses during the reduction process which should be controlled by the Ti/YSZ framework similarly to the reduction of NiO to Ni. The small particle phase adds ductility to the system in the reduced state which should allow for the increased stress of volume change from Ni to NiO without damage to the microstructure. Due to the large cracks observed for the 5 wt% ALT doped sample batches, it would appear that the strength should be

decreased significantly when compared to the 1 wt% ALT doped samples. On the contrary, for the 1 and 2 redox cycled samples, the strength is comparable to the 1 wt% ALT doped sample batches. This maintenance in strength for the 5 wt% ALT doped sample batches could be due to the increased ductility from the reduction of NiAl_2O_4 without compromising the integrity of the framework.

It can be observed that the amount of the small particle phase for the 10 wt% ALT doped samples increases with increasing cycle number. The small particle phase should add ductility to the system by the formation of nickel nanoparticles atop the alumina matrix. It can be observed though that the strength decreases substantially for the 10 wt% ALT doped sample batches. Given the increase in the small particle phase, the stress of re-oxidation should be compensated for by added ductility. The large cracks observed in the surface are more substantial than for the 5 wt% ALT doped samples. This could indicate that the system could not compensate for the stress of re-oxidation. This could be due to the lack of porosity for volume expansion and the residual stress from the formation and subsequent reduction of NiAl_2O_4 . Due to the volume decrease when the small particle phase is formed it would be logical to assume that this added volume would allow for the NiO volume change. In fact, the opposite is true. This could be due to the residual stresses involved after the formation of the small particle phase. These added stresses could cause premature failure of the sample, decreasing the strength. Further investigation would need to be performed to determine the root cause of the cracking and methods for increasing strength.

Figures 5, 6 and 7 show the fracture surface morphology for the ALT doped NiO-YSZ anodes with 1, 2 or 5 redox cycles, respectively. It can be observed that many of the fracture surfaces show indications of mixed modes of failure (intergranular and transgranular fracture). Transgranular fracture is characterized by smooth fracture planes due to the crack propagation through the grains. This crack path requires high energy and usually indicates a stronger material. In contrast, intergranular fracture propagates around the grain boundaries giving the fracture surface a rough texture. This fracture path requires lower energy and is usually indicative of a weaker material. It can be observed in Figure 6c, that there is indication of plastic deformation within the microstructure by the presence of ductile lips. The presence of ductility was discussed earlier and should increase strength of the material and allow for stress compensation by the formation of the small particle phase. This plasticity has been observed by other researchers [75,76] and will be discussed further below.

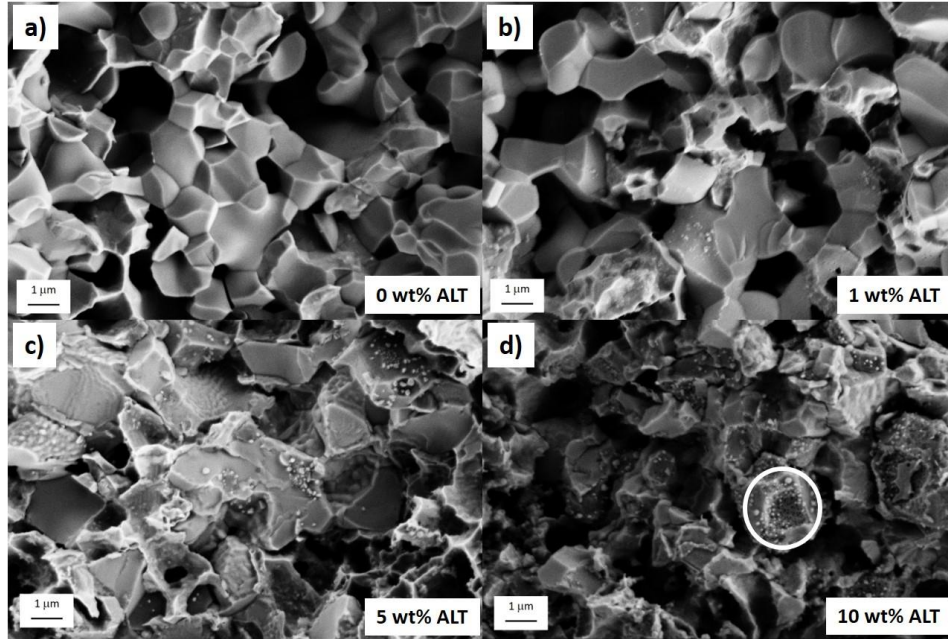


Figure 5.5: FE-SEM fracture surface morphology of a) 0 wt% ALT, b) 1 wt% ALT, c) 5 wt% ALT and d) 10 wt% ALT doped NiO-YSZ anode material after undergoing 1 redox cycle

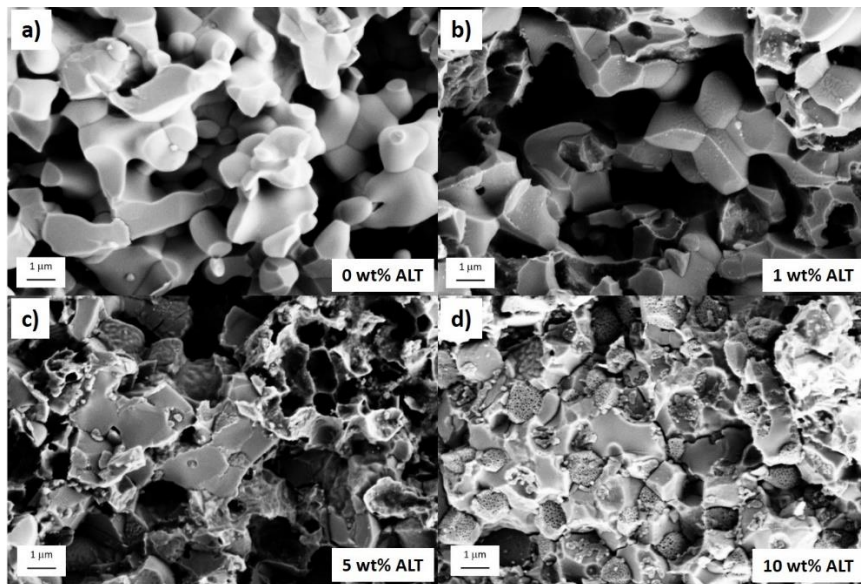


Figure 5.6: FE-SEM fracture surface morphology of a) 0 wt% ALT, b) 1 wt% ALT, c) 5 wt% ALT and d) 10 wt% ALT doped NiO-YSZ anode material after undergoing 2 redox cycles

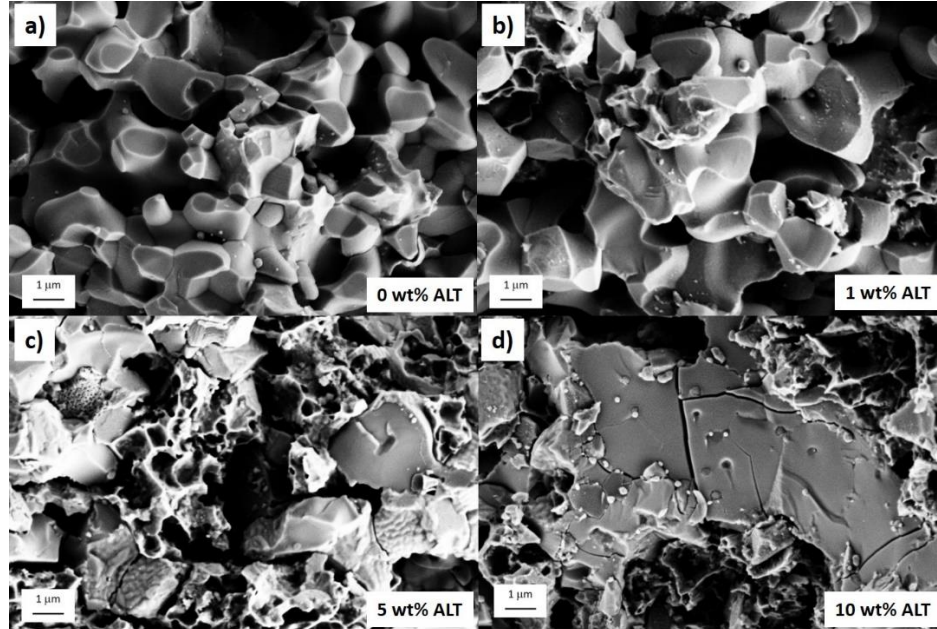


Figure 5.7: FE-SEM fracture surface morphology of a) 0 wt% ALT, b) 1 wt% ALT, c) 5 wt% ALT and d) 10 wt% ALT doped NiO-YSZ anode material after undergoing 5 redox cycles

Further examination of the fracture surfaces for the 5 wt% ALT sample batches (Figure 5c, 6c, and 7c) shows a decrease in the amount of transgranular fracture regions for the samples after 1 redox cycle. A higher amount of transgranular fracture indicates a stronger sample which confirms mechanical strength data where, for 5 wt% ALT doping, mechanical strength was highest after 1 redox cycle. Ductile lips can be observed in the fracture surfaces but as previously discussed the added ductility from the reduction of the small particle phase is thought to not be enough to compensate for the stress of volume change for re-oxidation. It can be observed in Figure 7c, that there are cracks present within the bulk of the material (crack circled). The presence of cracks within the bulk cannot be seen for the 1 and 2 redox cycled samples indicating an increase in the stress with increased redox cycles causing cracking within the bulk. This cracking in the bulk

well relates to the lower strength observed for the 5 wt% ALT samples after undergoing 5 redox cycles.

When examining the fracture surfaces for the 10 wt% ALT sample batches (Figure 5d, 6d and 7d) it can be observed that a higher amount of transgranular fracture is visible for the sample batch after undergoing 5 redox cycles. This increase in transgranular fracture well aligns with the increase in mechanical strength calculated for the sample batches. As previously discussed, the mechanical strength of the 10 wt% ALT sample bathes is much lower than the other ALT doped sample batches. This decrease in strength is evident in the fracture surface where cracks are present in the bulk of the material indicating a weaker material due to the presence of preexisting cracks.

It has been previously discussed that mechanical strength is highest for the 5 redox cycled sample batches and lowest for the 2 redox cycled batches. As previously discussed, during reduction there is little volume change whereas during re-oxidation there is an overall volume increase. This cannot be recovered and results in strain after the redox cycle [77]. This increase in strain after 2 redox cycles could have detrimental effects on the microstructure resulting in decreased strength. It would be probable that this same reasoning would cause the 5 redox cycled samples to have the lowest strength whereas the opposite is true and will be further discussed.

Researchers have found increased mechanical strength for undoped anode materials after multiple redox cycles, similar to what has been found in this study [75,76]. During high temperature reduction, the nickel particles will sinter with their neighbors increasing the surface area of the nickel primary crystal; therefore, the increase in

strength is due to the formation of this ductile nickel network. During subsequent re-oxidation, several small NiO crystals are formed at high temperatures [75]. The formation of smaller NiO crystals lessens the stress on the surrounding YSZ resulting in increased mechanical strength. Each subsequent redox cycle increases the nickel network by further sintering during reduction. The increase in the network of ductile nickel in the reduced samples increases the mechanical strength of the anode material. The added ductility allows for larger stresses within the material before failure increasing the overall strength. This increase in ductility explains the increased strength after 5 redox cycles for the undoped, 1 and 10 wt% ALT doped anodes. For the 5 and 10 wt% ALT doped samples, the interaction of the previously formed small particle phase and Ni during subsequent reductions could influence the mechanical strength. Depending on the distribution of the nickel network within rough phase, the interaction of the small particle phase and the nickel network could have detrimental effects similar to the decrease in strength observed for the 10 wt% ALT doped samples. As discussed previously, further research into residual stresses formed during reduction and re-oxidation must be investigated to determine the various causes for strength decrease.

Conclusion

Aluminum titanate (ALT) doped NiO-YSZ anodes were tested after full redox cycling up to 5 cycles. It was found that mechanical strength is increased for 1 and 5 wt% ALT doping when compared to undoped anodes. It is thought that this is due to secondary phase formations that can compensate for the stresses of volume change during re-oxidation from Ni to NiO. Surface cracking is visible for 5 and 10 wt% ALT doping

for all redox cycles. Cracking is thought to be due to stress buildup in the material during redox cycling due to lack of stress compensation for volume expansion upon re-oxidation. Even with surface cracking, the strength of the 5 wt% ALT doped anode is maintained due to the secondary phases compensating for increased stress of volume changes and added ductility. Future work includes residual stress analyses after re-oxidation to determine stress in individual phases.

Acknowledgements

This work was supported by the DOE under award no. DE-FE0031125. FE-SEM image data were collected at the Montana State University Image and Chemical Analysis Laboratory.

References

- [1] M. Pihlatie, A. Kaiser, M. Mogensen, Mechanical properties of NiO/Ni–YSZ composites depending on temperature, porosity and redox cycling, *J. Eur. Ceram. Soc.* 29 (2009) 1657–1664. doi:10.1016/j.jeurceramsoc.2008.10.017.
- [2] N. Mahato, A. Banerjee, A. Gupta, S. Omar, K. Balani, Progress in material selection for solid oxide fuel cell technology: A review, *Prog. Mater. Sci.* 72 (2015) 141–337. doi:10.1016/j.pmatsci.2015.01.001.
- [3] F. Zhao, A. V. Virkar, Dependence of polarization in anode-supported solid oxide fuel cells on various cell parameters, *J. Power Sources.* 141 (2005) 79–95. doi:10.1016/j.jpowsour.2004.08.057.
- [4] A.C. Müller, D. Herbstritt, E. Ivers-Tiffée, Development of a multilayer anode for solid oxide fuel cells, *Solid State Ionics.* 152–153 (2002) 537–542. doi:10.1016/S0167-2738(02)00357-0.
- [5] Z.R. Wang, J.Q. Qian, S.R. Wang, J.D. Cao, T.L. Wen, Improvement of anode-supported solid oxide fuel cells, *Solid State Ionics.* 179 (2008) 1593–1596. doi:10.1016/j.ssi.2008.03.022.
- [6] T. Setoguchi, K. Okamoto, K. Eguchi, H. Arai, Effects of anode material and fuel on anodic reaction of solid oxide fuel cells, *J. Electrochem. Soc.* 139 (1992) 2875–2880. doi:10.1149/1.2068998.
- [7] M. Kleitz, F. Petitbon, Optimized SOFC electrode microstructure, *Solid State Ionics.* 92 (1996) 65–74. doi:10.1016/S0167-2738(96)00464-X.
- [8] C.R. He, W.G. Wang, Alumina Doped Ni/YSZ Anode Materials for Solid Oxide Fuel Cells, *Fuel Cells.* 9 (2009) 630–635. doi:10.1002/fuce.200800152.
- [9] M. Mori, Y. Hiei, H. Itoh, G.A. Tompsett, N.M. Sammes, Evaluation of Ni and Ti-doped Y₂O₃ stabilized ZrO₂ cermet as an anode in high-temperature solid oxide fuel cells, *Solid State Ionics.* 160 (2003) 1–14. doi:10.1016/S0167-2738(03)00144-9.
- [10] T. Dey, A. Dey, P.C. Ghosh, M. Bose, A.K. Mukhopadhyay, R.N. Basu, Influence of microstructure on nano-mechanical properties of single planar solid oxide fuel cell in pre- and post-reduced conditions, *Mater. Des.* (2014). doi:10.1016/j.matdes.2013.06.052.
- [11] T. Dey, D. Singdeo, M. Bose, R.N. Basu, P.C. Ghosh, Study of contact resistance at the electrode-interconnect interfaces in planar type Solid Oxide Fuel Cells, *J. Power Sources.* 233 (2013) 290–298. doi:10.1016/j.jpowsour.2013.01.111.
- [12] J. Wei, G. Pećanac, J. Malzbender, Review of mechanical characterization methods for ceramics used in energy technologies, *Ceram. Int.* 40 (2014) 15371–15380. doi:10.1016/j.ceramint.2014.07.089.

- [13] G. Pećanac, S. Baumann, J. Malzbender, Mechanical properties and lifetime predictions for Ba_{0.5}Sr_{0.5}Co_{0.8}Fe_{0.2}O_{3-δ} membrane material, *J. Memb. Sci.* 385–386 (2011) 263–268. doi:10.1016/j.memsci.2011.10.005.
- [14] G. Pećanac, L. Kiesel, R. Kriegel, J. Malzbender, Comparison of thermo-mechanical characteristics of non-doped and 3 mol% B-site Zr-doped Ba_{0.5}Sr_{0.5}Co_{0.8}Fe_{0.2}O_{3-??}, *Ceram. Int.* 40 (2014) 1843–1850. doi:10.1016/j.ceramint.2013.07.086.
- [15] A. Atkinson, A. Selçuk, Mechanical behaviour of ceramic oxygen ion-conducting membranes, *Solid State Ionics.* 134 (2000) 59–66. doi:10.1016/S0167-2738(00)00714-1.
- [16] M. Lipińska-Chwałek, L. Kiesel, J. Malzbender, Mechanical properties of porous MgO substrates for membrane applications, *J. Eur. Ceram. Soc.* 34 (2014) 2519–2524. doi:10.1016/j.jeurceramsoc.2014.03.009.
- [17] B.X. Huang, V. Vasechko, Q.L. Ma, J. Malzbender, Thermo-mechanical properties of (Sr,Y)TiO₃ as anode material for solid oxide fuel cells, *J. Power Sources.* 206 (2012) 204–209. doi:10.1016/j.jpowsour.2012.01.137.
- [18] S. Giraud, J. Canel, Young's modulus of some SOFCs materials as a function of temperature, *J. Eur. Ceram. Soc.* 28 (2008) 77–83. doi:10.1016/j.jeurceramsoc.2007.05.009.
- [19] M. Radovic, E. Lara-curzio, Elastic Properties of Nickel-Based Anodes for Solid Oxide Fuel Cells as a Function of the Fraction of Reduced NiO, *J. Am. Ceram. Soc.* 87 (2004) 2242–2247. doi:10.1111/j.1151-2916.2004.tb07499.x.
- [20] M. Radovic, E. Lara-Curzio, Mechanical properties of tape cast nickel-based anode materials for solid oxide fuel cells before and after reduction in hydrogen, *Acta Mater.* 52 (2004) 5747–5756. doi:10.1016/j.actamat.2004.08.023.
- [21] Y. Ye, J. Li, H. Zhou, J. Chen, Microstructure and mechanical properties of yttria-stabilized ZrO₂/Al₂O₃ nanocomposite ceramics, *Ceram. Int.* 34 (2008) 1797–1803. doi:10.1016/j.ceramint.2007.06.005.
- [22] R. Kubrin, G. Blugan, J. Kuebler, Influence of cerium doping on mechanical properties of tetragonal scandium-stabilized zirconia, *J. Eur. Ceram. Soc.* 37 (2017) 1651–1656. doi:10.1016/j.jeurceramsoc.2016.11.038.
- [23] K. Swider, W. Worrell, Electronic Conduction Mechanism in Yttria- Stabilized Zirconia-Titania under Reducing Atmospheres, *J. Electrochem. Soc.* 143 (1996) 3706–3711. <http://jes.ecsdl.org/content/143/11/3706.short>.
- [24] S. Tekeli, The flexural strength, fracture toughness, hardness and densification behaviour of various amount of Al₂O₃-doped 8YSCZ/Al₂O₃ composites used as an electrolyte for solid oxide fuel cell, *Mater. Des.* 27 (2006) 230–235. doi:10.1016/j.matdes.2004.10.011.

- [25] J.S. Lee, K.H. Choi, B.K. Ryu, B.C. Shin, I.S. Kim, Effects of gallia additions on sintering behavior of gadolinia-doped ceria, *Ceram. Int.* 39 (2004) 807–812. doi:10.1016/j.materresbull.2004.07.022.
- [26] H. Xu, H. Yan, Z. Chen, The flexural strength and densification behavior of Al₂O₃-doped Ce_{0.8}Y_{0.2}O_{1.9} electrolyte composites, *Mater. Sci. Eng. A.* 447 (2007) 222–226. doi:10.1016/j.msea.2006.10.027.
- [27] N. Matsui, D. Kagaku, No Title, *J. Electrochem. Soc. Japan.* 58 (1990) 716.
- [28] S.S. Lion, W.L. Worrell, Electrical properties of novel mixed-conducting oxides, *Appl. Phys. A Solids Surfaces.* 49 (1989) 25–31. doi:10.1007/BF00615461.
- [29] Y.I. Kiyoshi Kobayashi, Yukiharu Kai, Shu Yamaguchi, Norihiko Fukatsu, Tsuyoshi Kawashima, K. Kobayashi, Y. Kai, S. Yamaguchi, N. Fukatsu, T. Kawashima, Y. Iguchi, Electronic conductivity measurements of 5 mol% TiO₂-doped YSZ by a d.c.-polarization technique, *Solid State Ionics.* 93 (1997) 193–199. doi:10.1016/S0167-2738(96)00534-6.
- [30] K. Kobayashi, K. Kato, T. Kawashima, S. Yamaguchi, Y. Iguchi, Total Electrical Conductivity Measurements of TiO₂ Doped YSZ Ceramics, *J. Ceram. Soc. Japan.* 106 (1998) 1073.
- [31] M. Nagano, S. Nagashima, H. Maeda, A. Kato, Sintering behavior of Al₂TiO₅ base ceramics and their thermal properties, *Ceram. Int.* 25 (1999) 681–687. doi:10.1016/S0272-8842(98)00083-2.
- [32] S.W. Sofie, D.R. Taylor, Controlled Thermal Expansion Anode Compositions with Improved Strength for Use in Anode Supported SOFCs, *Adv. Solid Oxide Fuel Cells III.* (2008) 215–223.
- [33] C.H. Law, S.W. Sofie, Anchoring of Infiltrated Nickel Electro-Catalyst by Addition of Aluminum Titanate, *J. Electrochem. Soc.* 158 (2011) B1137–B1141. doi:10.1149/1.3610226.
- [34] D.R. Driscoll, M.D. McIntyre, M.M. Welander, S.W. Sofie, R.A. Walker, Enhancement of high temperature metallic catalysts: Aluminum titanate in the nickel-zirconia system, *Appl. Catal. A Gen.* 527 (2016) 36–44. doi:10.1016/j.apcata.2016.08.020.
- [35] M. Mcleary, R. Amendola, Effect of Aluminum Titanate (Al₂TiO₅) Doping on the Mechanical Performance of Solid Oxide Fuel Cell Ni-YSZ Anode, *Fuel Cells.* (2017) 862–868. doi:10.1002/fuce.201700073.
- [36] H.U. Anderson, F. Tietz, *High-temperature Solid Oxide Fuel Cells: Fundamentals, Design and Applications*, Elsevier Science, 2003.
- [37] T. Klemens, C.C. Appel, M. Mogensen, In Situ Observations of Microstructural Changes in SOFC Anodes during Redox Cycling, *Electrochem. Solid-State Lett.* 9

- (2006) A403. doi:10.1149/1.2214303.
- [38] T. Klemensø, C. Chung, P.H. Larsen, M. Mogensen, The Mechanism Behind Redox Instability of Anodes in High-Temperature SOFCs, *J. Electrochem. Soc.* 152 (2005) A2186. doi:10.1149/1.2048228.
- [39] D. Waldbillig, A. Wood, D.G. Ivey, Thermal analysis of the cyclic reduction and oxidation behaviour of SOFC anodes, *Solid State Ionics*. 176 (2005) 847–859. doi:10.1016/j.ssi.2004.12.002.
- [40] D. Waldbillig, A. Wood, D.G. Ivey, Electrochemical and microstructural characterization of the redox tolerance of solid oxide fuel cell anodes, *J. Power Sources*. 145 (2005) 206–215. doi:10.1016/j.jpowsour.2004.12.071.
- [41] J. Malzbender, E. Wessel, R.W. Steinbrech, Reduction and re-oxidation of anodes for solid oxide fuel cells, *Solid State Ionics*. 176 (2005) 2201–2203. doi:10.1016/j.ssi.2005.06.014.
- [42] Y. Zhang, B. Liu, B. Tu, Y. Dong, M. Cheng, Redox cycling of Ni-YSZ anode investigated by TPR technique, *Solid State Ionics*. 176 (2005) 2193–2199. doi:10.1016/j.ssi.2005.06.016.
- [43] D. Fouquet, A.C. Müller, a. Weber, E. Ivers-Tiffée, Kinetics of oxidation and reduction of Ni/YSZ cermets, *Ionics (Kiel)*. 9 (2003) 103–108. doi:10.1007/BF02376545.
- [44] D. Sarantaridis, A. Atkinson, Redox cycling of Ni-based solid oxide fuel cell anodes: A review, *Fuel Cells*. 7 (2007) 246–258. doi:10.1002/fuce.200600028.
- [45] A. Wood, M. Pastula, D. Waldbillig, D.G. Ivey, Initial Testing of Solutions to Redox Problems with Anode-Supported SOFC, *J. Electrochem. Soc.* 153 (2006) A1929. doi:10.1149/1.2240085.
- [46] M. Pihlatie, A. Kaiser, P.H. Larsen, M. Mogensen, Dimensional Behavior of Ni-YSZ Composites during Redox Cycling, *J. Electrochem. Soc.* 156 (2009) B322. doi:10.1149/1.3046121.
- [47] M.M. Welander, M.S. Zachariasen, S.W. Sofie, R.A. Walker, Enhancing Ni-YSZ Anode Resilience to Environmental Redox Stress with Aluminum Titanate Secondary Phases, *ACS Appl. Energy Mater.* 1 (2018) 6295–6302. doi:10.1021/acsaem.8b01288.
- [48] A. Faes, A. Hessler-Wyser, A. Zryd, J. Van Herle, A review of RedOx cycling of solid oxide fuel cells anode, *Membranes (Basel)*. 2 (2012) 585–664. doi:10.3390/membranes2030585.
- [49] T. Kawada, S. Watanabe, T. Hashida, H. Yugami, J. Mizusaki, S. Sukino, F. Iguchi, K. Sato, Effect of Redox Cycling on Mechanical Properties of Ni-YSZ Cermets for SOFC Anodes, *ECS Trans.* 35 (2011) 1473–1482. doi:10.1149/1.3570133.

- [50] M. Pihlatie, A. Kaiser, M. Mogensen, Redox stability of SOFC: Thermal analysis of Ni-YSZ composites, *Solid State Ionics*. 180 (2009) 1100–1112. doi:10.1016/j.ssi.2009.04.011.
- [51] M. Ettl, H. Timmermann, J. Malzbender, A. Weber, N.H. Menzler, Durability of Ni anodes during reoxidation cycles, *J. Power Sources*. 195 (2010) 5452–5467.
- [52] M. Pihlatie, T. Ramos, A. Kaiser, Testing and improving the redox stability of Ni-based solid oxide fuel cells, *J. Power Sources*. 193 (2009) 322–330. doi:10.1016/j.jpowsour.2008.11.140.
- [53] M.M. Welander, M.S. Zachariasen, C.D. Hunt, S.W. Sofie, R.A. Walker, Operando Studies of Redox Resilience in ALT Enhanced NiO-YSZ SOFC Anodes, *J. Electrochem. Soc.* 165 (2018) F152–F157. doi:10.1149/2.0531803jes.
- [54] M. McCleary, R. Amendola, Reduction kinetics of undoped and aluminum titanate (Al₂TiO₅) doped NiO-YSZ solid oxide fuel cell anodes, *Ceram. Int.* 44 (2018) 15557–15564. doi:10.1016/j.ceramint.2018.05.218.
- [55] B. Charlas, D.W. Ni, H.L. Frandsen, K. Brodersen, M. Chen, Mechanical Properties of Supports and Half-Cells for Solid Oxide Electrolysis Influenced by Alumina-Zirconia Composites, *Fuel Cells*. 17 (2017) 132–143. doi:10.1002/fuce.201600036.
- [56] H. Orui, R. Chiba, K. Nozawa, H. Arai, R. Kanno, High-temperature stability of alumina containing nickel–zirconia cermets for solid oxide fuel cell anodes, *J. Power Sources*. 238 (2013) 74–80. doi:10.1016/j.jpowsour.2013.03.056.
- [57] ASTM C1239-13, Standard Practice for Reporting Uniaxial Strength Data and Estimating Weibull Distribution Parameters for Advanced Ceramics, *ASTM Int.* (2013) 1–9. doi:10.1520/C1239-13.Scope.
- [58] A. Nakajo, J. Kuebler, A. Faes, U.F. Vogt, H.J. Schindler, L.K. Chiang, S. Modena, J. Van Herle, T. Hocker, Compilation of mechanical properties for the structural analysis of solid oxide fuel cell stacks. Constitutive materials of anode-supported cells, *Ceram. Int.* 38 (2012) 3907–3927. doi:10.1016/j.ceramint.2012.01.043.
- [59] H.L. Frandsen, T. Ramos, A. Faes, M. Pihlatie, K. Brodersen, Optimization of the strength of SOFC anode supports, *J. Eur. Ceram. Soc.* 32 (2012) 1041–1052. doi:10.1016/j.jeurceramsoc.2011.11.015.
- [60] T. Dey, A. Dey, P.C. Ghosh, M. Bose, A.K. Mukhopadhyay, R.N. Basu, Influence of microstructure on nano-mechanical properties of single planar solid oxide fuel cell in pre- and post-reduced conditions, *Mater. Des.* 53 (2014) 182–191. doi:10.1016/j.matdes.2013.06.052.
- [61] D.N. Boccaccini, H.L. Frandsen, S. Soprani, M. Cannio, T. Klemensø, V. Gil, P.V. Hendriksen, Influence of porosity on mechanical properties of tetragonal stabilized

- zirconia, *J. Eur. Ceram. Soc.* (2018). doi:10.1016/j.jeurceramsoc.2017.09.029.
- [62] B. Timurkutluk, S. Celik, E. Ucar, Influence of doctor blade gap on the properties of tape cast NiO/YSZ anode supports for solid oxide fuel cells, *Ceram. Int.* (2018). doi:10.1016/j.ceramint.2018.10.221.
- [63] H. Peterlik, Relationship of Strength and Defects of Ceramic Materials and Their Treatment by Weibull Theory, *J. Fo Ceram. Soc. Japan.* 109 (2001) 121–126. doi:10.1007/s13398-014-0173-7.2.
- [64] M. McCleary, R. Amendola, Effect of Aluminum Titanate (Al_2TiO_5) Doping on the Mechanical Performance of Solid Oxide Fuel Cell Ni-YSZ Anode, *Fuel Cells.* 17 (2017). doi:10.1002/fuce.201700073.
- [65] H. Fischer, W. Rentzsch, R. Marx, A modified size effect model for brittle nonmetallic materials, *Eng. Fract. Mech.* 69 (2002) 781–791. doi:10.1016/S0013-7944(01)00126-6.
- [66] H.L. Frandsen, T. Ramos, A. Faes, M. Pihlatie, K. Brodersen, Optimization of the strength of SOFC anode supports, *J. Eur. Ceram. Soc.* (2012). doi:10.1016/j.jeurceramsoc.2011.11.015.
- [67] F. Baratta, W. Matthews, Errors Associated with Flexure Testing of Brittle Materials, *U.S. Army Mater. Technol. Lab.* (1987) 16, 41–42.
- [68] R. Subramanian, E. Üstündağ, S.L. Sass, R. Dieckmann, In-situ formation of metal-ceramic microstructures by partial reduction reactions, *Solid State Ionics.* 75 (1995) 241–255. doi:10.1016/0167-2738(94)00148-L.
- [69] E. Üstündağ, R. Subramanian, R. Dieckmann, S.L. Sass, In-situ formation of metal-ceramic microstructures in the Ni-Al-O system by partial reduction reactions, *Acta Mater.* 43 (1995) 383–389. doi:http://dx.doi.org/10.1016/0167-2738(94)00148-L.
- [70] E. Üstündağ, Z. Zhang, M.L. Stocker, P. Rangaswamy, M.A.M. Bourke, J.A. Roberts, S. Subramanian, K.E. Sickafus, S.L. Sass, Influence of residual stresses on the evolution of microstructure during the partial reduction of NiAl_2O_4 , *Mater. Sci. Eng. A.* 238 (1997) 50–65.
- [71] D. Sarantaridis, R.A. Rudkin, A. Atkinson, Oxidation failure modes of anode-supported solid oxide fuel cells, *J. Power Sources.* 180 (2008) 704–710. doi:10.1016/j.jpowsour.2008.03.011.
- [72] I. Küppenbender, M. Schütze, The deformation behavior of NiO scales on Ni in argon and air at temperatures from 20 to 800°C with respect to the relief of growth stresses, *Oxid. Met.* 42 (1994) 109–144. doi:10.1007/BF01061927.
- [73] D.W. Ni, B. Charlas, K. Kwok, T.T. Molla, P.V. Hendriksen, H.L. Frandsen, Influence of temperature and atmosphere on the strength and elastic modulus of

solid oxide fuel cell anode supports, *J. Power Sources*. 311 (2016) 1–12.
doi:10.1016/j.jpowsour.2016.02.027.

- [74] D.R. Driscoll, B.W. Tokmakian, N.P. Johnson, C.D. Hunt, S.W. Sofie, Catalyst enhancing aluminum titanate for increasing strength of nickel-zirconia cermets, *Mater. Lett.* 209 (2017) 307–310. doi:10.1016/j.matlet.2017.08.035.
- [75] Y. Zhang, B. Liu, B. Tu, Y. Dong, M. Cheng, Understanding of redox behavior of Ni-YSZ cermets, *Solid State Ionics*. 180 (2009) 1580–1586.
doi:10.1016/j.ssi.2009.10.011.
- [76] B.D. Vasylyv, V.Y. Podhurs'ka, O.P. Ostash, O.D. Vasyl'ev, E.M. Brodnikovs'kyi, Influence of reducing and oxidizing media on the physicochemical properties of ScCeSZ-NiO and YSZ-NiO ceramics, *Mater. Sci.* 49 (2013) 135–144.
doi:10.1007/s11003-013-9593-3.
- [77] L. Kang, Strain Accumulation Study of Ni-based Anode-Supported Solid Oxide Fuel Cells under Partial-Redox Cycling Conditions, *Int. J. Electrochem. Sci.* 11 (2016) 5596–5606. doi:10.20964/2016.07.28.

CHAPTER SIX

MECHANICAL PERFORMANCE OF ALUMINUM TITANATE (Al_2TiO_5 , ALT)

DOPED NIO-YSZ SOFC HALF CELLS

Contribution of Authors and Co-Authors

Author: Madisen McCleary

Contributions: Prepared and tested samples, compiled and analyzed numerical data, generated figures/tables and wrote manuscript.

Co-author: Roberta Amendola

Contributions: Provided insight on experimental design and implementation. Aided in manuscript editing and preparation.

Manuscript Information Page

Madisen McCleary, Roberta Amendola

Status of Manuscript:

- Prepared for submission to a peer-reviewed journal
- Officially submitted to a peer-review journal
- Accepted by a peer-reviewed journal
- Published in a peer-reviewed journal

MECHANICAL PERFORMANCE OF ALUMINUM TITANATE (Al_2TiO_5 , ALT)

DOPED NiO-YSZ SOFC HALF CELLS

Madisen McCleary, Roberta Amendola*

Montana State University, Mechanical Engineering, 220 Roberts Hall, Bozeman, MT

59717, United States

[*] Corresponding author, Roberta.amendola@montana.edu

The following work is in progress to be submitted for publication.

Abstract

The mechanical properties of aluminum titanate (Al_2TiO_5 , ALT) doped NiO-YSZ anode SOFC half cells were evaluated with equibiaxial (ring on ring) testing. Half cells were assembled with a NiO-YSZ anode layer that was doped with 5 wt% ALT. A YSZ electrolyte was spin coated onto green substrates then co-sintered. Mechanical testing showed increased mechanical strength for the ALT doped half cells over undoped half cells of similar composition. FE-SEM surface morphology showed the formation of two secondary phases on the anode that aid in material strengthening. Fractography showed that anode fracture mechanisms could possibly transfer to the electrolyte.

Introduction

There is a growing need in society for sustainable and reliable renewable energy systems. Solid oxide fuel cells (SOFCs) are one such system that produce power by the electrochemical oxidation of a fuel. SOFCs are heavily researched as they are fuel

flexible (hydrogen or hydrocarbons as fuel) and they only produce water, heat and electricity [1–3]. For SOFCs to be marketable, the cost for each unit must be as inexpensive as possible and has led to strategic materials choices. NiO-YSZ anode supported SOFCs have been heavily researched as they have the ability to operate at lower temperatures [4]. Researchers are currently focused on increasing single cell performance from anode supported SOFCs [5–10] but NiO-YSZ based anodes are still the most common due to their high power output to cost ratio [11,12]. New anode materials are under investigation but much research is still needed before they can be used in SOFC stacks [13–21]. A single SOFC cannot produce enough power currently for everyday operation; so, single cells are stacked and electrically connected to produce sufficient power. To increase the electrical connection between single cells, the stack is clamped with high pressures on the order of 65-70 kPa [22,23].

For anode supported SOFCs, the anode provides the mechanical strength for the stack assembly. Little fundamental data exists for the mechanical properties of SOFC materials while there continues to be an abundance of research regarding the electrochemical performance [24–26]. Due to the brittle nature of the ceramic materials that compose the SOFC, the strength and reliability of the cell depends on the thermo-mechanical properties of the materials. This includes the fracture strength along with the coefficient of thermal expansion, young's modulus, etc. Fracture of brittle ceramics is unpredictable and catastrophic; therefore, it is crucial to study the mechanical behavior of the material before implementation into the SOFC stack. Ceramic materials are sensitive to changes in material composition and manufacturing process, but research has shown

that the addition of secondary phases that do not compromise the electrochemical performance have the possibility of also improving mechanical behavior [10,27–29].

Previous research has shown that the addition of Al_2O_3 and TiO_2 to undoped NiO-YSZ anodes and YSZ electrolytes can increase mechanical performance [10,27,28,30–37]. Researchers have also found that the addition of aluminum titanate (Al_2TiO_5 , ALT) increases mechanical performance while slowing degradation rates and increasing electrochemical efficiencies [38–42]. Previous research has shown that 5 wt% ALT doping of NiO-YSZ anodes has benefits of increased mechanical strength and electrochemical properties [43,44]. At this doping level, it has been shown that electrochemical properties are heightened along with increase mechanical strength. Above this doping level, electrochemical efficiencies are decreased.

For implementation of this ALT doped anode into the SOFC stack, mechanical testing must be conducted on the material when in contact with the electrolyte. The mechanical reliability of the SOFC stack depends heavily on the coefficient of thermal expansion for each component. Large differences in thermal expansion can cause cracking and delamination in and between the components at operating temperatures, decreasing power output or causing complete failure of the cell. As ALT addition decreases the coefficient of thermal expansion of the anode material [39], the mismatch between the YSZ electrolyte and the NiO-YSZ anode material should be lessened. A closer match in thermal expansion coefficients should allow for increased mechanical strength in and between the anode and electrolyte. To test the mechanical compatibility of the doped anode material and the YSZ electrolyte, mechanical testing was conducted on

co-sintered half-cell assemblies with 5 wt% ALT doping of the anode material (NiO-YSZ) and a YSZ electrolyte. Using this initial testing as a baseline, further research will be conducted on different mechanical testing methods and various half-cell assemblies.

Methods

Nickel Oxide (NiO) powder (4 μm , Alfa Aesar), 8 mol% Ytria Stabilized Zirconia (8YSZ) powder (300 nm, Tosoh) and Aluminum Titanate (ALT) powder (25 nm, Sigma Aldrich) were used for sample manufacturing. Powders, in the ratio of 34 wt% YSZ, 66 wt% NiO and 5 wt% ALT, were mechanically mixed for 24 hours with binder and deionized water and subsequently tape cast with a doctor blade thickness of 2 mm. It has previously been determined that 5 wt% ALT doping increases mechanical strength while maintaining electrochemical properties as discussed previously [43,44].

Circular samples with a diameter of 32 mm were cut from the tape cast using a circular punch. Thermolysis of green tape cast samples was performed in ambient air with the following procedure: 1) 2°C/min up to 150°C, 2) dwell for 2 hours, 3) 0.5 °C/min up to 450°C, 4) 5 °C/min up to 1100°C, 5) dwell for 2 hours, 6) 10 °C/min to room temperature. Thermolysis and partial sintering was performed in a box furnace (Thermolyne, 1300). Prior to sintering, samples were coated with a YSZ electrolyte. Coating slurry was 1:10 mol% of 8YSZ to Alpha Terpineol. Samples were coated using a spin coater to create a uniform thickness electrolyte layer (~10 μm after sintering). After coating, co-sintering was conducted with a heating/cooling rate of 5°C/min up to 1500°C and a dwell time of 2 hours (Zircar, Hot Spot 110). Reduction was performed in a tube

furnace (Thermo Scientific, Lindberg Blue M) flowing 5% H₂ and 95% N₂ gas, at 800°C for 10 hours for all samples.

After reduction the half-cell assembly batch of 30 samples was loaded at a rate of 0.2 mm/min in a ring on ring testing apparatus (Instron 5543) as per ASTM C1499-15 standard [45]. Samples were loaded with anode support in tension (anode on bottom ring). In this configuration, the electrolyte is under compression. As the electrolyte is stiffer than the anode, this setup ensures fracture of the anode before the electrolyte [46,47]. Further studies will need to be conducted on the fracture characteristics of this material when the electrolyte is under tension along with studies of pure YSZ to fully characterize the fracture mechanisms. Fracture strength, effective volume V_{eff} , scaled characteristic strength σ_0' , Weibull modulus (m) with normalized upper and lower bounds, and porosity, by alcohol immersion method, were evaluated. Weibull statistics were conducted under the guidance of ASTM 1239-13 [48]. Field Emission Scanning electron microscopy (FE-SEM, Zeiss Ultra) microstructural characterization was conducted to determine the nature of fracture, influence of secondary phase formations and the interface of the anode and electrolyte.

Results and Discussion

Mechanical Properties

Table 1 shows the mechanical properties results for the half cell assembly. Previous research into undoped NiO-YSZ half cells with YSZ electrolyte have found characteristic strengths between 60 and 160 MPa [49,50]. When compared to previous research with ALT doped material, the strength of the 5 wt% ALT doped anode material

is stronger with the added electrolyte [43]. This is most likely due to the YSZ electrolyte which is stiffer than the NiO-YSZ anode [50]. It can be observed that the scaled characteristic strength of the 5 wt% ALT doped anode with electrolyte is significantly higher than undoped materials [49,50]. For this study, the Weibull modulus calculated was 4.3 which is lower than typical anodes that are in the range of 5 to 7 [51].

Table 6.1: Mechanical properties of anode/electrolyte assembly

Weibull modulus	4.3
90% Confidence Interval	3.2 - 5.3
Average Strength (MPa)	184
V_{eff} (mm ³)	4.2
Scaled Characteristic Strength (MPa)	272

Due to the brittle nature of ceramics fracture, mechanical strength is varied and leads to the necessity for a statistical approach. Flaws within the material are responsible for failure when the weakest one under tension fails. These flaws can be either manufacturing defects or microstructural features such as porosity. Brittle materials also fail with little to no strain leading to unpredictable failure; therefore, Weibull statistics were employed to more accurately characterize the strength of the material. Weibull distributions assume the weakest link theory where the weakest flaw under tension will cause fracture of the material. The Weibull distribution (Equation 1) has two parameters that must be solved for to characterize the strength of the material, the characteristic strength and the Weibull modulus [48].

$$p_s = \exp\left(-\frac{\sigma}{\sigma_0}\right)^m \quad (1)$$

Where p_s is the probability of survival for each sample, σ is the flexural strength of each sample (MPa), σ_0 is the characteristic strength (MPa), and m is the Weibull modulus. The characteristic strength corresponds to the flexural strength at a probability of failure of 63.2%.

The Weibull modulus indicates the nature, severity and dispersion of flaws within a sample batch. A high Weibull modulus is indicative of a homogeneous flaw distribution and strength data is consistent with low variability. A high Weibull modulus is preferable as it indicates a more reliable fracture strength which is crucial when characterizing the mechanical properties as unpredictable failure could lead to unexpected failures of the material. A low Weibull modulus has a less homogenous flaw distribution which leads to more unpredictable failure. The Weibull modulus for this material is low when compared to similar materials. Due to the coefficient of thermal expansion mismatch between the anode support and electrolyte, it is probable that residual stress is present in the material after co-sintering at high temperatures [52]. The larger coefficient of thermal expansion for the anode material will cause compressive stress on the anode while putting the electrolyte into tension. Researchers have found that these residual stresses make the material more fragile and could lower their Weibull modulus [52]. The residual stresses could cause stress on preexisting defects that causes premature failure and lowers the Weibull modulus.

Due to the nature of Weibull statistics, characterization of the material cannot be fully explored through just the two parameters for the batch. Figure 1 shows the Weibull plot for the half cell assembly batch. The Weibull plot is created by the reorganization of

the Weibull distribution equation into straight line form where the Weibull modulus is the slope of the line. The straight-line form of the Weibull distribution can be found in Equation 2.

$$\ln(\ln(1/p_s)) = m \ln(\sigma/\sigma_0) \quad (3)$$

Where p_s is the probability of survival for each sample, σ is the flexural strength of each sample (MPa), σ_0 is the characteristic strength (MPa), and m is the Weibull modulus. The Weibull plot is used for determining how well the strength data aligns with the Weibull distribution. For this analysis, a more reliable material will have data points that lie along the linear trendline with little deviation. It can be seen in the Weibull plot that the data points do not lie close to the linear trendline showing a less reliable material. This behavior is indicative of the possibility of multiple modes of fracture. This analysis requires further statistical calculations that were not conducted in the present study. Future work will require these analyses.

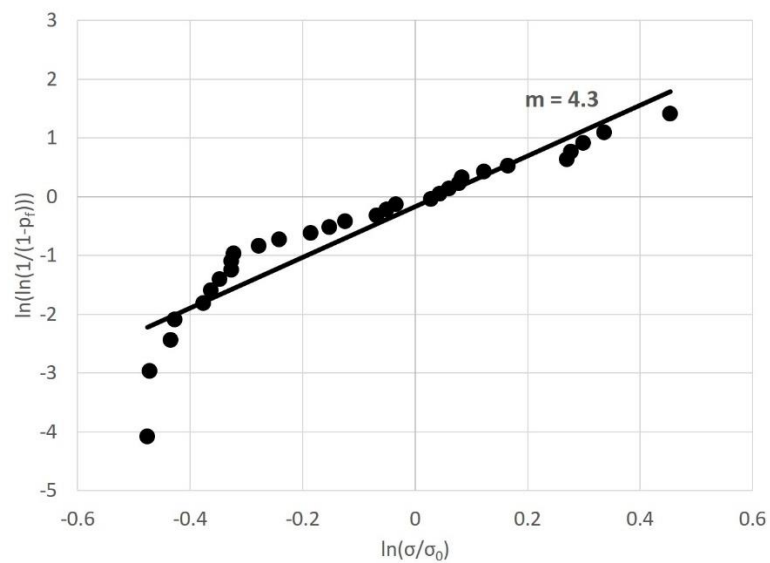


Figure 6.1: Weibull plot of anode/electrolyte assembly

Microstructural Analysis

Fractography was conducted on the samples that withstood the highest, lowest and median load from the batch. Figures 2 and 3 show the surface morphology of the anode and electrolyte sides, respectively, for the three samples characterized. It can be observed that there is the formation of two secondary phases in Figure 2 for the ALT doped NiO-YSZ anode. During sintering, ALT decomposes to its constituents of Al_2O_3 and TiO_2 . The TiO_2 reacts with YSZ to form the rough phase (circled in Figure 2a) which has been previously identified as the Ti/YSZ framework [43]. Al_2O_3 reacts with NiO to form NiAl_2O_4 . The small particle phase (boxed in Figure 2a) is the partial reduction of NiAl_2O_4 to Ni nanoparticles atop an alumina matrix [43]. These phases are more prevalent for the sample with the highest strength. This could be due to the sintering of the samples that did not allow for large formations of the secondary phases. Previous research has found the benefit of these phases for material strengthening; therefore, further research of these samples must be conducted to determine cause of this surface morphology. In Figure 3, the grains of YSZ are large in comparison to the anode material. There does not appear to be any defects, imperfections, cracks or secondary phases in the electrolyte layer. The presence of no cracks or defects in the electrolyte indicates that the coefficient of thermal expansion mismatch did not cause cracking of the thin electrolyte.

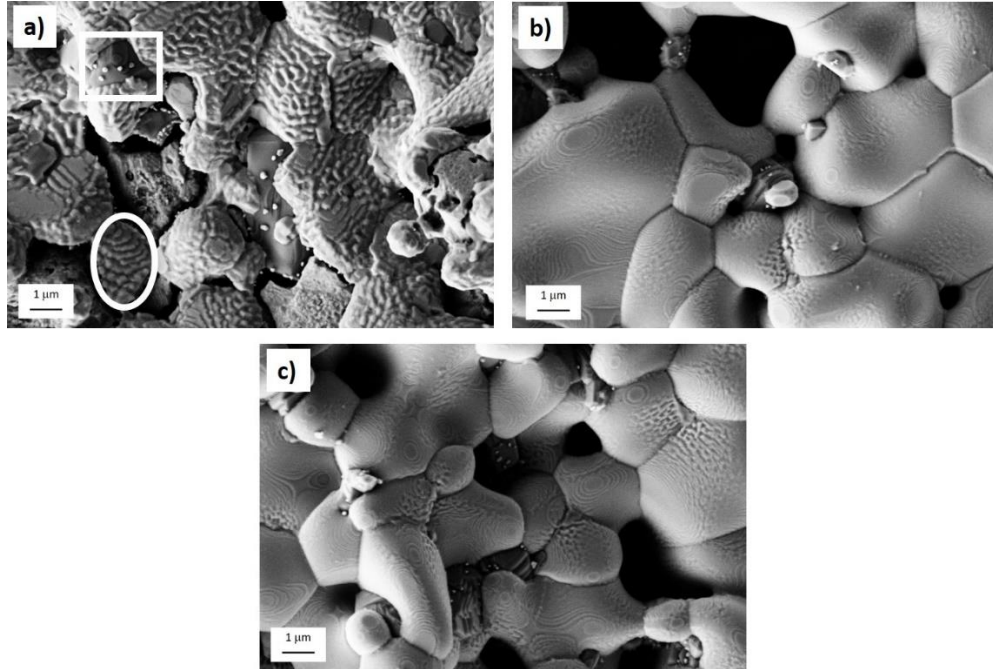


Figure 6.2: FE-SEM surface morphology of anode side of 5 wt% ALT doped sample with a) max strength, b) median strength and c) minimum strength

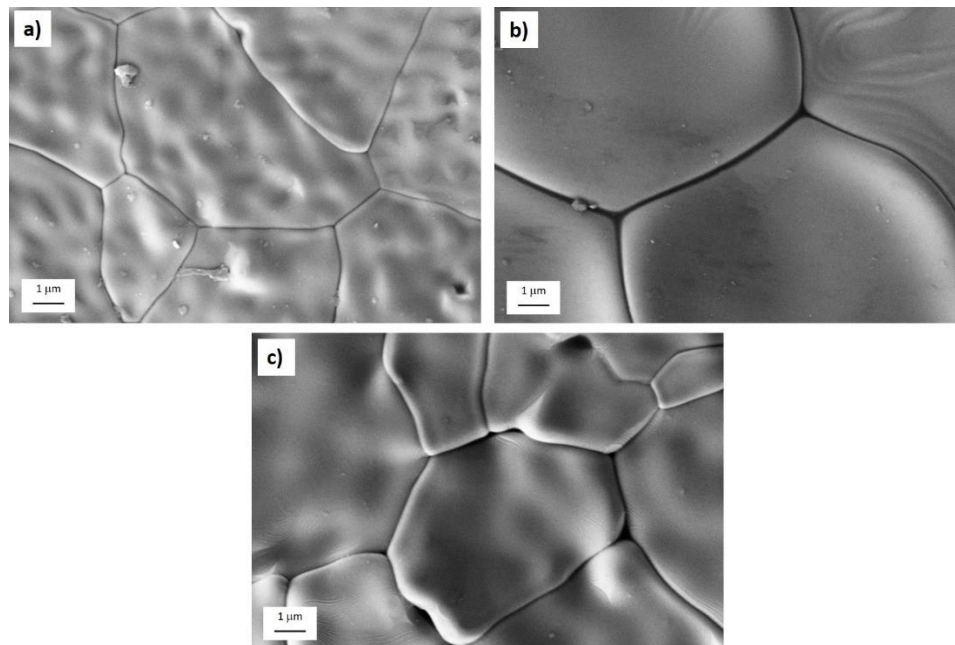


Figure 6.3: FE-SEM surface morphology of electrolyte side of sample with a) max strength, b) median strength and c) minimum strength

Figure 4 shows the fracture surface for the anode portion of the samples. It can be observed that transgranular fracture is most likely the mechanism for failure in the highest strength sample. Transgranular fracture is indicated by smooth fracture surface as the crack propagated through the grains. Transgranular fracture is indicative of a higher energy fracture path and usually corresponds to a higher strength material. A decrease in strength sees a shift from transgranular fracture to intergranular fracture which is consistent when compared to the mechanical strength. Intergranular fracture is characterized by failure at the grain boundaries and corresponds to a lower strength material. Due to the loading configuration, the fracture will most likely originate in the anode [50,52].

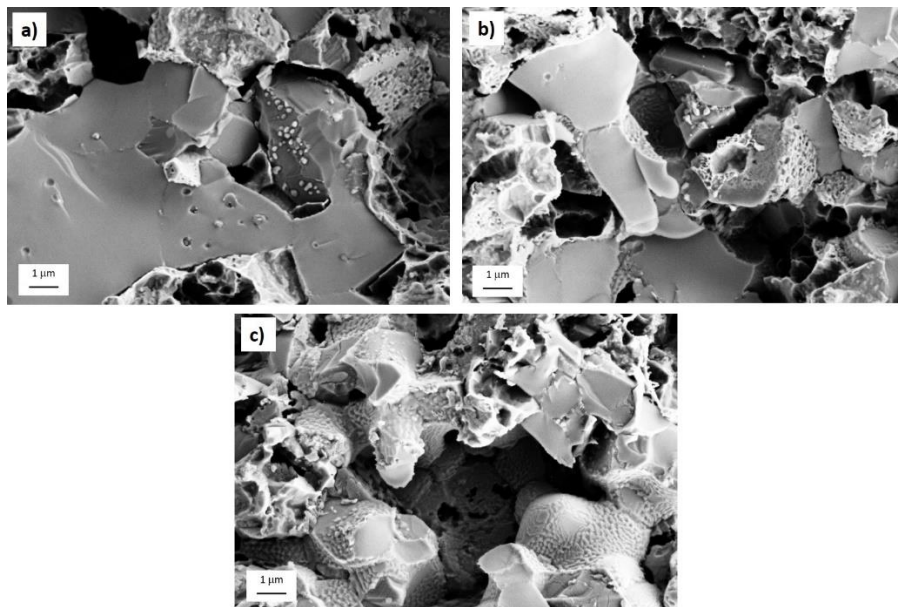


Figure 6.4: FE-SEM fracture surface morphology of anode side of 5 wt% ALT doped sample with a) max strength, b) median strength and c) minimum strength

Fractography of the samples confirms that the transgranular fracture observed corresponds to the high strength fracture of the sample. With a low Weibull modulus calculated for this sample batch and the Weibull plot data, it is probable that there are two modes of fracture within the batch. Given that the lowest strength sample shows evidence of intergranular fracture in comparison with transgranular fracture for the highest strength sample, the batch could have two sub populations for each fracture mechanism. More in-depth analyses need to be performed to validate this theory and will be the topic of future research.

Figures 5 and 6 show the fracture surface for the interface between the electrolyte and anode at low and high magnification, respectively. In Figure 5, it can be observed that the electrolyte fracture is visibly different between the various strength samples. When comparing the highest strength sample (Figure 5a) to the median strength sample (Figure 5b), it can be seen that the electrolyte fracture is smoother. The lowest strength sample (Figure 5c) shows inconsistency in the electrolyte thickness and could be part of the reason for poor mechanical strength. Given these different fracture surface morphologies, it could be that the fracture mechanisms between the anode and the electrolyte are linked. Further studies must be conducted on the half-cell assembly where the electrolyte is in tension and for pure YSZ materials. Once the fracture mechanisms have been identified then holistic analyses of the half-cell assembly fracture mechanics can be made.

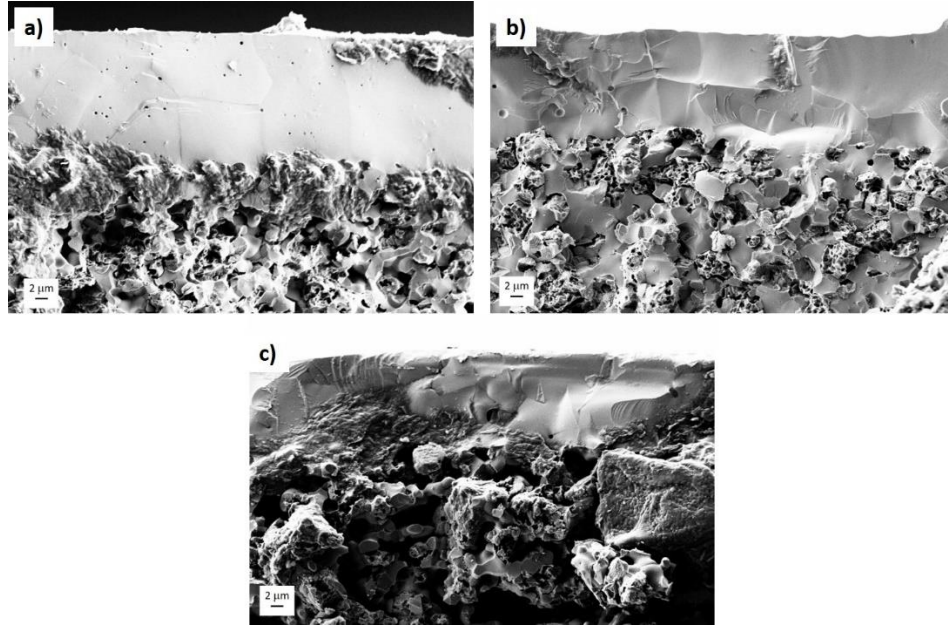


Figure 6.5: FE-SEM fracture surface morphology of anode-electrolyte interface of sample with a) max strength, b) median strength and c) minimum strength

In Figure 6, the same trends occur where the highest strength sample has a smooth fracture surface when compared to the lower strength samples. The loading configuration should instigate failure in the anode due to it being loaded in tension and the electrolyte in compression. Observing the fractography, it can be seen that the fracture of the electrolyte appears to correspond with the fracture patterns in the anode. As discussed previously, this will need to be confirmed with further analyses.

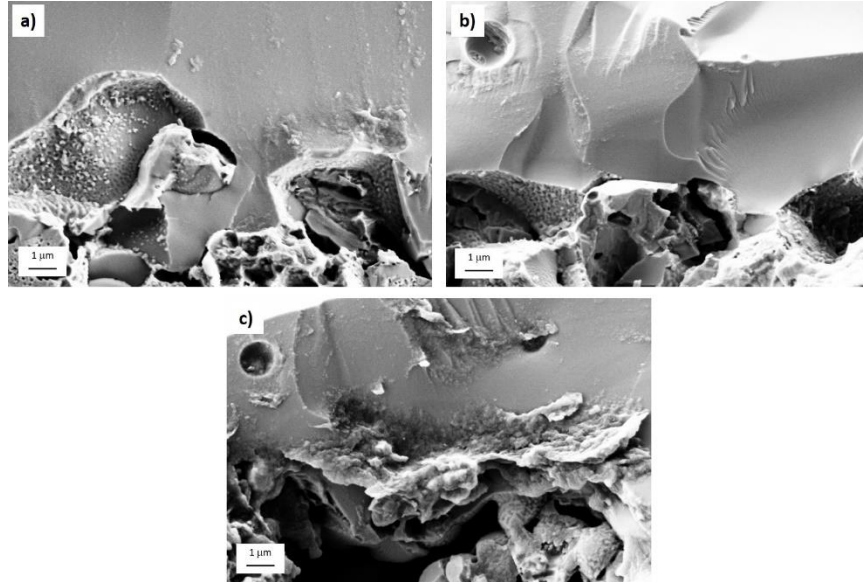


Figure 6.6: FE-SEM fracture surface morphology of anode-electrolyte interface of sample with a) max strength, b) median strength and c) minimum strength

Observing the fractography holistically, it can be seen that the mechanisms for fracture could correspond between the anode and electrolyte. Further investigation is needed to fully characterize the ALT doped anode material with electrolyte layer. Further studies will be conducted on the role of loading direction (electrolyte in tension) and anode supports with a functional and support layers. Even with further analyses needed, this study has confirmed that ALT doping increases the strength of the half-cell assembly over undoped NiO-YSZ half cells.

Conclusions

Co-sintered half-cell assemblies of 5 wt% ALT doped NiO-YSZ anodes and YSZ electrolytes were tested by equibiaxial (ring on ring) mechanical testing. It was found that the scaled characteristic strength of the half cells was higher than undoped half cells

tested in a similar manner. FE-SEM surface morphology showed the formation of two secondary phases in the ALT doped anode. Fractography showed increased amounts of transgranular fracture for the anode portion of the sample which held the highest load; conversely, the sample which held the lowest load was dominated by intergranular fracture. Fracture in the electrolyte was similar in nature to the fracture characteristics found in the anode which could be related to the anode fracture energy. Further investigation of ALT doped half cells will be conducted to determine the fracture mechanisms of this assembly.

Acknowledgements

This work was supported by the Department of Energy (DOE) (Award no. DE-FE0031125). FE-SEM data was collected at the Montana State University Image and Chemical Analysis Laboratory.

References

- [1] Y. Shiratori, T. Oshima, K. Sasaki, Feasibility of direct-biogas SOFC, *Int. J. Hydrogen Energy*. 33 (2008) 6316–6321. doi:10.1016/j.ijhydene.2008.07.101.
- [2] Y. Shiratori, T. Ijichi, T. Oshima, K. Sasaki, Internal reforming SOFC running on biogas, *Int. J. Hydrogen Energy*. 35 (2010) 7905–7912. doi:10.1016/j.ijhydene.2010.05.064.
- [3] C.J. Laycock, J.Z. Staniforth, R.M. Ormerod, Biogas as a fuel for solid oxide fuel cells and synthesis gas production: effects of ceria-doping and hydrogen sulfide on the performance of nickel-based anode materials., *Dalton Trans.* 40 (2011) 5494–5504. doi:10.1039/c0dt01373k.
- [4] K.H. Ng, H.A. Rahman, M.R. Somalu, Review: Enhancement of composite anode materials for low-temperature solid oxide fuels, *Int. J. Hydrogen Energy*. (2018). doi:10.1016/j.ijhydene.2018.01.073.
- [5] F. Zhao, A. V. Virkar, Dependence of polarization in anode-supported solid oxide fuel cells on various cell parameters, *J. Power Sources*. 141 (2005) 79–95. doi:10.1016/j.jpowsour.2004.08.057.
- [6] A.C. Müller, D. Herbstritt, E. Ivers-Tiffée, Development of a multilayer anode for solid oxide fuel cells, *Solid State Ionics*. 152–153 (2002) 537–542. doi:10.1016/S0167-2738(02)00357-0.
- [7] Z.R. Wang, J.Q. Qian, S.R. Wang, J.D. Cao, T.L. Wen, Improvement of anode-supported solid oxide fuel cells, *Solid State Ionics*. 179 (2008) 1593–1596. doi:10.1016/j.ssi.2008.03.022.
- [8] T. Setoguchi, K. Okamoto, K. Eguchi, H. Arai, Effects of anode material and fuel on anodic reaction of solid oxide fuel cells, *J. Electrochem. Soc.* 139 (1992) 2875–2880. doi:10.1149/1.2068998.
- [9] M. Kleitz, Optimized SOFC electrode microstructure, *Solid State Ionics*. 92 (1996) 65–74. doi:10.1016/S0167-2738(96)00464-X.
- [10] M. Mori, Y. Hiei, H. Itoh, G.A. Tompsett, N.M. Sammes, Evaluation of Ni and Ti-doped Y₂O₃ stabilized ZrO₂ cermet as an anode in high-temperature solid oxide fuel cells, *Solid State Ionics*. 160 (2003) 1–14. doi:10.1016/S0167-2738(03)00144-9.
- [11] M. Pihlatie, A. Kaiser, M. Mogensen, Mechanical properties of NiO/Ni–YSZ composites depending on temperature, porosity and redox cycling, *J. Eur. Ceram. Soc.* 29 (2009) 1657–1664. doi:10.1016/j.jeurceramsoc.2008.10.017.
- [12] N. Mahato, A. Banerjee, A. Gupta, S. Omar, K. Balani, Progress in material selection for solid oxide fuel cell technology: A review, *Prog. Mater. Sci.* 72 (2015) 141–337. doi:10.1016/j.pmatsci.2015.01.001.

- [13] J. Wei, G. Pećanac, J. Malzbender, Review of mechanical characterization methods for ceramics used in energy technologies, *Ceram. Int.* 40 (2014) 15371–15380. doi:10.1016/j.ceramint.2014.07.089.
- [14] G. Pećanac, S. Baumann, J. Malzbender, Mechanical properties and lifetime predictions for Ba_{0.5}Sr_{0.5}Co_{0.8}Fe_{0.2}O_{3-δ} membrane material, *J. Memb. Sci.* 385–386 (2011) 263–268. doi:10.1016/j.memsci.2011.10.005.
- [15] G. Pećanac, L. Kiesel, R. Kriegel, J. Malzbender, Comparison of thermo-mechanical characteristics of non-doped and 3 mol% B-site Zr-doped Ba_{0.5}Sr_{0.5}Co_{0.8}Fe_{0.2}O_{3-??}, *Ceram. Int.* 40 (2014) 1843–1850. doi:10.1016/j.ceramint.2013.07.086.
- [16] A. Atkinson, A. Selçuk, Mechanical behaviour of ceramic oxygen ion-conducting membranes, *Solid State Ionics.* 134 (2000) 59–66. doi:10.1016/S0167-2738(00)00714-1.
- [17] M. Lipińska-Chwałek, L. Kiesel, J. Malzbender, Mechanical properties of porous MgO substrates for membrane applications, *J. Eur. Ceram. Soc.* 34 (2014) 2519–2524. doi:10.1016/j.jeurceramsoc.2014.03.009.
- [18] B.X. Huang, V. Vasechko, Q.L. Ma, J. Malzbender, Thermo-mechanical properties of (Sr,Y)TiO₃ as anode material for solid oxide fuel cells, *J. Power Sources.* 206 (2012) 204–209. doi:10.1016/j.jpowsour.2012.01.137.
- [19] S. Giraud, J. Canel, Young's modulus of some SOFCs materials as a function of temperature, *J. Eur. Ceram. Soc.* 28 (2008) 77–83. doi:10.1016/j.jeurceramsoc.2007.05.009.
- [20] M. Radovic, E. Lara-curzio, Elastic Properties of Nickel-Based Anodes for Solid Oxide Fuel Cells as a Function of the Fraction of Reduced NiO, *J. Am. Ceram. Soc.* 87 (2004) 2242–2247. doi:10.1111/j.1151-2916.2004.tb07499.x.
- [21] M. Radovic, E. Lara-Curzio, Mechanical properties of tape cast nickel-based anode materials for solid oxide fuel cells before and after reduction in hydrogen, *Acta Mater.* 52 (2004) 5747–5756. doi:10.1016/j.actamat.2004.08.023.
- [22] T. Dey, D. Singdeo, M. Bose, R.N. Basu, P.C. Ghosh, Study of contact resistance at the electrode-interconnect interfaces in planar type Solid Oxide Fuel Cells, *J. Power Sources.* 233 (2013) 290–298. doi:10.1016/j.jpowsour.2013.01.111.
- [23] T. Dey, A. Dey, P.C. Ghosh, M. Bose, A.K. Mukhopadhyay, R.N. Basu, Influence of microstructure on nano-mechanical properties of single planar solid oxide fuel cell in pre- and post-reduced conditions, *Mater. Des.* (2014). doi:10.1016/j.matdes.2013.06.052.
- [24] D. Klotz, A. Leonide, A. Weber, E. Ivers-Tiffée, Electrochemical model for SOFC and SOEC mode predicting performance and efficiency, *Int. J. Hydrogen Energy.* 39 (2014) 20844–20849. doi:10.1016/j.ijhydene.2014.08.139.

- [25] Y. Ding, Y. Li, G. Liu, K. Yu, Y. Luo, H. Liu, W. Sun, G. Chen, S. Geng, Electrochemical performance of a new structured low temperature SOFC with BZY electrolyte, *Int. J. Hydrogen Energy*. 43 (2018) 12765–12772. doi:10.1016/j.ijhydene.2018.04.006.
- [26] J. Moreno-Blanco, F. Elizalde-Blancas, J.M. Riesco-Avila, J.M. Belman-Flores, A. Gallegos-Muñoz, On the effect of gas channels-electrode interface area on SOFCs performance, *Int. J. Hydrogen Energy*. 4 (2019) 446–456. doi:10.1016/j.ijhydene.2018.02.108.
- [27] C.R. He, W.G. Wang, Alumina Doped Ni/YSZ Anode Materials for Solid Oxide Fuel Cells, *Fuel Cells*. 9 (2009) 630–635. doi:10.1002/face.200800152.
- [28] Y. Ye, J. Li, H. Zhou, J. Chen, Microstructure and mechanical properties of yttria-stabilized ZrO₂/Al₂O₃ nanocomposite ceramics, *Ceram. Int.* 34 (2008) 1797–1803. doi:10.1016/j.ceramint.2007.06.005.
- [29] R. Kubrin, G. Blugan, J. Kuebler, Influence of cerium doping on mechanical properties of tetragonal scandium-stabilized zirconia, *J. Eur. Ceram. Soc.* 37 (2017) 1651–1656. doi:10.1016/j.jeurceramsoc.2016.11.038.
- [30] K. Swider, W. Worrell, Electronic Conduction Mechanism in Yttria-Stabilized Zirconia-Titania under Reducing Atmospheres, *J. Electrochem. Soc.* 143 (1996) 3706–3711. <http://jes.ecsdl.org/content/143/11/3706.short>.
- [31] S. Tekeli, The flexural strength, fracture toughness, hardness and densification behaviour of various amount of Al₂O₃-doped 8YSCZ/Al₂O₃ composites used as an electrolyte for solid oxide fuel cell, *Mater. Des.* 27 (2006) 230–235. doi:10.1016/j.matdes.2004.10.011.
- [32] J.S. Lee, K.H. Choi, B.K. Ryu, B.C. Shin, I.S. Kim, Effects of gallia additions on sintering behavior of gadolinia-doped ceria, *Ceram. Int.* 39 (2004) 807–812. doi:10.1016/j.materresbull.2004.07.022.
- [33] H. Xu, H. Yan, Z. Chen, The flexural strength and densification behavior of Al₂O₃-doped Ce_{0.8}Y_{0.2}O_{1.9} electrolyte composites, *Mater. Sci. Eng. A*. 447 (2007) 222–226. doi:10.1016/j.msea.2006.10.027.
- [34] N. Matsui, D. Kagaku, No Title, *J. Electrochem. Soc. Japan*. 58 (1990) 716.
- [35] S.S. Lion, W.L. Worrell, Electrical properties of novel mixed-conducting oxides, *Appl. Phys. A Solids Surfaces*. 49 (1989) 25–31. doi:10.1007/BF00615461.
- [36] Y.I. Kiyoshi Kobayashi, Yukiharu Kai, Shu Yamaguchi, Norihiko Fukatsu, Tsuyoshi Kawashima, K. Kobayashi, Y. Kai, S. Yamaguchi, N. Fukatsu, T. Kawashima, Y. Iguchi, Electronic conductivity measurements of 5 mol% TiO₂-doped YSZ by a d.c.-polarization technique, *Solid State Ionics*. 93 (1997) 193–199. doi:10.1016/S0167-2738(96)00534-6.
- [37] K. Kobayashi, K. Kato, T. Kawashima, S. Yamaguchi, Y. Iguchi, Total Electrical

- Conductivity Measurements of TiO₂ Doped YSZ Ceramics, *J. Ceram. Soc. Japan*. 106 (1998) 1073.
- [38] M. Nagano, S. Nagashima, H. Maeda, A. Kato, Sintering behavior of Al₂TiO₅ base ceramics and their thermal properties, *Ceram. Int.* 25 (1999) 681–687. doi:10.1016/S0272-8842(98)00083-2.
- [39] S.W. Sofie, D.R. Taylor, Controlled Thermal Expansion Anode Compositions with Improved Strength for Use in Anode Supported SOFCs, *Adv. Solid Oxide Fuel Cells III*. (2008) 215–223.
- [40] C.H. Law, S.W. Sofie, Anchoring of Infiltrated Nickel Electro-Catalyst by Addition of Aluminum Titanate, *J. Electrochem. Soc.* 158 (2011) B1137–B1141. doi:10.1149/1.3610226.
- [41] D.R. Driscoll, M.D. McIntyre, M.M. Welander, S.W. Sofie, R.A. Walker, Enhancement of high temperature metallic catalysts: Aluminum titanate in the nickel-zirconia system, *Appl. Catal. A Gen.* 527 (2016) 36–44. doi:10.1016/j.apcata.2016.08.020.
- [42] D. Driscoll, C. Hunt, J. Muretta, S.W. Sofie, Thermally Stabilized Nickel Electro-Catalyst Introduced by Infiltration for High Temperature Electrochemical Energy Conversion, *ECS Trans.* 53 (2013) 63–72. doi:10.1149/05309.0063ecst.
- [43] M. McCleary, R. Amendola, Effect of Aluminum Titanate (Al₂TiO₅) Doping on the Mechanical Performance of Solid Oxide Fuel Cell Ni-YSZ Anode, *Fuel Cells*. 17 (2017). doi:10.1002/fuce.201700073.
- [44] D.R. Driscoll, B.W. Tokmakian, N.P. Johnson, C.D. Hunt, S.W. Sofie, Catalyst enhancing aluminum titanate for increasing strength of nickel-zirconia cermets, *Mater. Lett.* 209 (2017) 307–310. doi:10.1016/j.matlet.2017.08.035.
- [45] ASTM C1499-15, Standard Test Method for Monotonic Equibiaxial Flexural Strength of Advanced Ceramics at Ambient Temperature, *ASTM Int.* (2015) 1–19. doi:10.1017/CBO9781107415324.004.
- [46] J. Malzbender, R.W. Steinbrech, L. Singheiser, Failure probability of solid oxide fuel cells, *Ceram. Eng. Sci. Proc.* 26 (2005) 293.
- [47] W. Fischer, J. Malzbender, G. Blass, R.W. Steinbrech, Residual stresses in planar solid oxide fuel cells, *J. Power Sources*. 150 (2005) 73–77. doi:10.1016/j.jpowsour.2008.04.035.
- [48] ASTM C1239-13, Standard Practice for Reporting Uniaxial Strength Data and Estimating Weibull Distribution Parameters for Advanced Ceramics, *ASTM Int.* (2013) 1–9. doi:10.1520/C1239-13.Scope.
- [49] J. Wei, T. Osipova, J. Malzbender, M. Krüger, Mechanical characterization of SOFC/SOEC cells, *Ceram. Int.* 44 (2018) 11094–11100.

doi:10.1016/j.ceramint.2018.03.103.

- [50] J. Malzbender, R.W. Steinbrech, Threshold fracture stress of thin ceramic components, *J. Eur. Ceram. Soc.* 28 (2008) 247–252. doi:10.1016/j.jeurceramsoc.2007.05.017.
- [51] J. Laurencin, G. Delette, F. Lefebvre-Joud, M. Dupeux, A numerical tool to estimate SOFC mechanical degradation: Case of the planar cell configuration, *J. Eur. Ceram. Soc.* 28 (2008) 1857–1869. doi:10.1016/j.jeurceramsoc.2007.12.025.
- [52] B. Charlas, H.L. Frandsen, K. Brodersen, P.V. Henriksen, M. Chen, Residual stresses and strength of multilayer tape cast solid oxide fuel and electrolysis half-cells, *J. Power Sources.* 288 (2015) 243–252. doi:10.1016/j.jpowsour.2015.04.105.

CHAPTER SEVEN

CONCLUSIONS

Summary of Work

Initial testing of the ALT doped NiO-YSZ anode material sought to discover if the addition of the ALT dopant increased the mechanical strength over the undoped material. In Chapter 2, testing of the bulk anode material was conducted on isostatic pressed samples with ALT addition up to 10 wt%. For the initial baseline analyses, samples were tested in both the oxidized (NiO-YSZ) and reduced states (Ni-YSZ). Weibull statistical analyses found that the 5 wt% ALT dopant amount was the most reliable material in terms of mechanical performance. The strengthening of the anode material was attributed to the formation of two secondary phases during sintering and subsequent reduction. ALT during sintering will spontaneously decompose to Al_2O_3 and TiO_2 . Al_2O_3 reacts with NiO to form NiAl_2O_4 and TiO_2 reacts with YSZ to form a stiff framework. The amount of the Ti/YSZ phase increases proportionally to the doping amount of ALT and persists after the reduction process and has been termed the “rough phase”. During reduction, NiAl_2O_4 partially reduces to Ni nanoparticles within an Al_2O_3 matrix.

Reduction of the anode material is crucial for SOFC operation; so, increased time could lead to increased operation costs for the SOFC. During initial testing of the

material, it was found that the reduction time for the ALT doped material increased proportional to the doping amount. To determine how ALT affects the reduction kinetics of NiO-YSZ anodes, a study was conducted on ALT doped NiO-YSZ reduced in 5% H₂ – 95% N₂ and 100% H₂ at 800°C. In Chapter 3, it was discussed that the two parameter Avrami-Erofe'ev model had the best fit to the reduction data. The Avrami-Erofe'ev reduction model is based on the formation and growth of nuclei. This model well applies to both H₂ concentrations. It was also found that the “n” parameter for the Avrami-Erofe'ev model is system dependent because of the many factors that influence this value including local composition, porosity, and pathways for gas transport. The amount of ALT added to the NiO-YSZ would form a proportional amount of NiAl₂O₄. NiAl₂O₄ has very low reaction kinetics and would cause deviations of the data from the proposed trendline. A shift of the data can be seen corresponding to the onset of NiAl₂O₄ reduction. For all doping levels, the use of 100% H₂ vastly increased the reduction kinetics of the material and the formation of secondary phases. FE-SEM microstructural characterization was used to confirm the findings.

Chapter 4 discusses the manufacturing and testing of Ni-YSZ doped with an ALT doping level between 0 and 10 wt% samples of produced using a tape casting procedure to commercial anode thickness of ~500 μm. A remarkable enhancement of the mechanical strength, up to 166%, was found when compared to the un-doped samples. The development of secondary phases was observed proportional to the doping amount of aluminum titanate. Mechanical properties evaluation was conducted using uniaxial and biaxial strength testing. Weibull statistics was used for mechanical properties analysis

and an advanced statistical analysis was employed to identify the existence of multiple flaw populations. Fractography was performed on selected samples to elucidate the fracture mechanisms. Biaxial testing was characterized by high mechanical strength with lower Weibull moduli; whereas, uniaxial showed lower mechanical strength and higher Weibull moduli. It was found that undoped, 5% and 10% ALT doped samples exhibit a fracture mechanism that is dependent on one flaw population namely porosity and mechanical strength of secondary phases, respectively. Undoped samples were characterized by intergranular fracture while transgranular fracture was found for the 5% and 10% ALT doped samples. For 1% ALT doped samples both flaw populations were identified. Analyses of the fracture surfaces revealed the simultaneous presence of intergranular and transgranular features. It is proposed that secondary phases, developed by ALT doping, increase the mechanical strength of the material shifting the fracture mechanism from intergranular to transgranular.

After characterizing the material for fracture mechanisms, operational testing must be performed. Chapter 5 discussed testing of the ALT doped NiO-YSZ anodes after redox cycling. This cycling has detrimental effects on NiO-YSZ based anodes due to stress caused by the volume expansion of Ni to NiO during re-oxidation. 0-10 wt% ALT doped NiO-YSZ anodes were full redox cycled 1, 2 or 5 times before fracture. It was found that 1 wt% ALT doping had the highest strength with decreases in strength for 5 and 10 wt% doping. Surface cracking is present for the 5 and 10 wt% ALT doped anode material for all redox cycles. This decrease in strength and surface cracking is thought to be due to residual stresses in the material during redox cycling. Increased mechanical

strength was observed for sample batches after 5 redox cycles. It is thought that this is due to the formation of a nickel metal network that is continually refined after every redox cycle. Further research into residual stresses formed during redox cycling is needed to fully characterize the material behavior during redox cycling.

For future use of the doped anode materials in SOFC stacks, further testing must be conducted on SOFC assemblies. For initial testing of the anode material in a SOFC, Chapter 6 discusses the mechanical testing of 5 wt% ALT doped NiO-YSZ anode materials with a YSZ electrolyte. The doping amount of 5 wt% ALT was chosen due to previous research on both the electrochemical and mechanical properties of ALT doped anodes. At this doping level, electrochemical and mechanical performance are both maximized without compromising the performance of either. Samples were co-sintered and tested using an equibiaxial (ring on ring) strength testing system. It was found that the ALT doped half cells were mechanical stronger when compared to an undoped half-cell. It was also found that the strength of the half-cell was higher when compared to the 5 wt% ALT doped anode. Fractography of the half-cell assembly showed that the fracture mode in the anode seem to correlate with the fracture observed in the electrolyte. Due to the how testing was conducted, fracture started within the anode and propagated through the electrolyte. Future investigation of different testing configurations and assembly structures is needed to fully characterize the material along with pure YSZ fracture mechanisms analyses.

Final Remarks

SOFCs will continue to be on the forefront of research into possible renewable energy systems to replace the use of fossil fuels. NiO-YSZ based anodes are the most common due to their high power to cost ratio. Due to the brittle nature of ceramic materials used for the anode component, there is a necessity to better understand the thermo-mechanical properties. This dissertation studied the influence that ALT addition has on the NiO-YSZ based anode material. The mechanical properties studies outlined in this research can be applied more fundamentally to the tailoring of secondary phase formations to engineer the stress/strain behavior in ceramic materials. Overall, it has been shown in this body of research that the addition of ALT does enhance the mechanical properties of NiO-YSZ based anode materials.

This enhancement stems from the formation of two secondary phases (NiAl_2O_4 and Ti/YSZ) that help to stabilize the microstructure by control of mechanical stresses within the material during sintering, reduction and mechanical testing. Initial research found that the Ti/YSZ phase creates a framework which can withstand high mechanical stresses while the NiAl_2O_4 phase and its partial reduction add ductility to the system. Both Al_2O_3 and TiO_2 are needed for strength enhancement in the material due to their fundamental roles in stress distribution within the material.

This dissertation research has led to multiple avenues for future research. Due to the need for stress dissipation during redox cycling, research could be performed to engineer ALT doped materials to better resist the stresses caused from the volume changes within the NiO-YSZ anode material. Along with this, research could be

conducted into pore morphology and distribution to further increase the mechanical strength. Further research into assembly structures is needed. Testing of the ALT doped anodes with electrolyte and/or cathodes is needed for future marketability. Anode assemblies with a support and functional layer would also lead to improved anode materials with tailored microstructures for further strengthening. In this assembly, the support layer holds the mechanical strength to the SOFC while the functional layer is designed for improved electrochemical performance.

REFERENCES CITED

- [1] A. Lanzini, P. Leone, Experimental investigation of direct internal reforming of biogas in solid oxide fuel cells, *Int. J. Hydrogen Energy*. 35 (2010) 2463–2476. doi:10.1016/j.ijhydene.2009.12.146.
- [2] A. Lanzini, P. Leone, M. Pieroni, M. Santarelli, D. Beretta, S. Ginocchio, Experimental investigations and modeling of direct internal reforming of biogases in tubular solid oxide fuel cells, *Fuel Cells*. 11 (2011) 697–710. doi:10.1002/fuce.201000173.
- [3] C.J. Laycock, J.Z. Staniforth, R.M. Ormerod, Biogas as a fuel for solid oxide fuel cells and synthesis gas production: effects of ceria-doping and hydrogen sulfide on the performance of nickel-based anode materials., *Dalton Trans.* 40 (2011) 5494–5504. doi:10.1039/c0dt01373k.
- [4] P. Piroonlerkgul, S. Assabumrungrat, N. Laosiripojana, A.A. Adesina, Selection of appropriate fuel processor for biogas-fuelled SOFC system, *Chem. Eng. J.* 140 (2008) 341–351. doi:10.1016/j.cej.2007.10.007.
- [5] Y. Shiratori, T. Oshima, K. Sasaki, Feasibility of direct-biogas SOFC, *Int. J. Hydrogen Energy*. 33 (2008) 6316–6321. doi:10.1016/j.ijhydene.2008.07.101.
- [6] Y. Shiratori, T. Ijichi, T. Oshima, K. Sasaki, Internal reforming SOFC running on biogas, *Int. J. Hydrogen Energy*. 35 (2010) 7905–7912. doi:10.1016/j.ijhydene.2010.05.064.
- [7] J. Staniforth, R.M. Ormerod, Implications for using biogas as a fuel source for solid oxide fuel cells: Internal dry reforming in a small tubular solid oxide fuel cell, *Catal. Letters*. 81 (2002) 19–23. doi:10.1023/A:1016000519280.
- [8] I. Wheeldon, C. Caners, K. Karan, B. Peppley, Utilization of Biogas Generated from Ontario Wastewater Treatment Plants in Solid Oxide Fuel Cell Systems: A Process Modeling Study, *Int. J. Green Energy*. 4 (2007) 221–231. doi:10.1080/15435070601015585.
- [9] I. V. Yentekakis, Open- and closed-circuit study of an intermediate temperature SOFC directly fueled with simulated biogas mixtures, *J. Power Sources*. 160 (2006) 422–425. doi:10.1016/j.jpowsour.2005.12.069.
- [10] C.-C. Yu, J.D. Baek, C.-H. Su, L. Fan, J. Wei, Y.-C. Liao, P.-C. Su, Inkjet-printed Porous Silver Thin Film as a Cathode for Low-Temperature Solid Oxide Fuel Cell, *ACS Appl. Mater. Interfaces*. (2016) acsami.6b01943. doi:10.1021/acsami.6b01943.
- [11] A. V. Call, J.G. Railsback, H. Wang, S.A. Barnett, Degradation of nano-scale cathodes: a new paradigm for selecting low-temperature solid oxide cell materials, *Phys. Chem. Chem. Phys.* 18 (2016) 13216–13222. doi:10.1039/C6CP02590K.

- [12] K.C. Neoh, G.D. Han, M. Kim, J.W. Kim, H.J. Choi, S.W. Park, J.H. Shim, Nanoporous silver cathode surface treated by atomic layer deposition of CeO_x for low-temperature solid oxide fuel cells., *Nanotechnology*. 27 (2016) 185403. doi:10.1088/0957-4484/27/18/185403.
- [13] F. Ye, Q. Zhou, K. Xu, Z. Zhang, X. Han, L. Yang, J. Xu, H. Xu, K. Wu, Y. Guan, Phase stability and electrochemical performance of Y_{0.5}Ca_{0.5-x}In_xBaCo_{3.2}Ga_{0.8}O_{7+??} (x = 0 and 0.1) as cathodes for intermediate temperature solid oxide fuel cells, *J. Alloys Compd.* 680 (2016) 163–168. doi:10.1016/j.jallcom.2016.04.028.
- [14] Y. Zhu, W. Zhou, Y. Chen, Z. Shao, An Aurivillius Oxide Based Cathode with Excellent CO₂ Tolerance for Intermediate-Temperature Solid Oxide Fuel Cells, *Angew. Chemie Int. Ed.* 6845 (2016) 8988–8993. doi:10.1002/anie.201604160.
- [15] X. Lv, X. Liu, C. Gu, Y. Weng, Determination of safe operation zone for an intermediate-temperature solid oxide fuel cell and gas turbine hybrid system, *Energy*. 99 (2016) 91–102. doi:10.1016/j.energy.2016.01.047.
- [16] a Atkinson, S. Barnett, R.J. Gorte, J.T.S. Irvine, a J. McEvoy, M. Mogensen, S.C. Singhal, J. Vohs, Advanced anodes for high-temperature fuel cells., *Nat. Mater.* 3 (2004) 17–27. doi:10.1038/nmat1040.
- [17] M. Irshad, K. Siraj, R. Raza, A. Ali, P. Tiwari, B. Zhu, A. Rafique, A. Ali, M. Kaleem Ullah, A. Usman, A Brief Description of High Temperature Solid Oxide Fuel Cell's Operation, *Materials, Design, Fabrication Technologies and Performance, Appl. Sci.* 6 (2016) 75. doi:10.3390/app6030075.
- [18] R. Irankhah, B. Raissi, A. Maghsoudipour, A. Irankhah, S. Ghashghai, NiFe₂O₄ Spinel Protection Coating for High-Temperature Solid Oxide Fuel Cell Interconnect Application, *J. Mater. Eng. Perform.* 25 (2016) 1515–1525. doi:10.1007/s11665-016-1949-z.
- [19] E. De Guire, NexTech's SOFC interconnect coating surpasses one-year mark, (2012). <http://ceramics.org/ceramic-tech-today/nextechs-sofc-interconnect-coating-surpasses-one-year-mark> (accessed August 9, 2016).
- [20] A.N. Busawon, D. Sarantaridis, A. Atkinson, Ni infiltration as a possible solution to the redox problem of SOFC anodes, *Electrochem. Solid-State Lett.* 11 (2008) B186–B189. doi:10.1149/1.2959078.
- [21] G.B. Johnson, P. Hjalmarsson, K. Norrman, U.S. Ozkan, A. Hagen, Biogas Catalytic Reforming Studies on Nickel-Based Solid Oxide Fuel Cell Anodes, *Fuel Cells*. 16 (2016) 219–234. doi:10.1002/fuce.201500179.
- [22] D. Kennouche, Y. -c. K. Chen-Wiegart, J.S. Cronin, J. Wang, S. a. Barnett, Three-Dimensional Microstructural Evolution of Ni- Ytria-Stabilized Zirconia Solid Oxide Fuel Cell Anodes At Elevated Temperatures, *J. Electrochem. Soc.* 160 (2013) F1293–F1304. doi:10.1149/2.084311jes.

- [23] T.P. Holme, C. Lee, F.B. Prinz, Atomic layer deposition of LSM cathodes for solid oxide fuel cells, *Solid State Ionics*. 179 (2008) 1540–1544. doi:10.1016/j.ssi.2007.12.100.
- [24] L. Dos Santos-Gomez, E.R. Losilla, F. Martin, J.R. Ramos-Barrado, D. Marrero-Lopez, Novel microstructural strategies to enhance the electrochemical performance of La_{0.8}Sr_{0.2}MnO_{3-d} cathodes, *ACS Appl. Mater. Interfaces*. 7 (2015) 7197–7205. doi:10.1021/acsami.5b00255.
- [25] X. Fan, C.Y. You, J.L. Zhu, L. Chen, C.R. Xia, Fabrication of LSM-SDC composite cathodes for intermediate-temperature solid oxide fuel cells, *Ionics (Kiel)*. 21 (2015) 2253–2258. doi:10.1007/s11581-015-1396-0.
- [26] T. Park, G.Y. Cho, Y.H. Lee, W.H. Tanveer, W. Yu, Y. Lee, Y. Kim, J. An, S.W. Cha, Effect of anode morphology on the performance of thin film solid oxide fuel cell with PEALD YSZ electrolyte, *Int. J. Hydrogen Energy*. 41 (2016) 2–7. doi:10.1016/j.ijhydene.2016.04.092.
- [27] C.N. Ginestra, R. Sreenivasan, A. Karthikeyan, S. Ramanathan, P.C. McIntyre, Atomic Layer Deposition of Y₂O₃/ZrO₂ Nanolaminates: A Route to Ultrathin Solid-State Electrolyte Membranes, *Electrochem. Solid-State Lett.* 10 (2007) B161. doi:10.1149/1.2759606.
- [28] D.Y. Jang, H.K. Kim, J.W. Kim, K. Bae, M.V.F. Schlupp, S.W. Park, M. Prestat, J.H. Shim, Low-temperature performance of yttria-stabilized zirconia prepared by atomic layer deposition, *J. Power Sources*. 274 (2015) 611–618. doi:10.1016/j.jpowsour.2014.10.022.
- [29] J.H. Shim, S. Kang, S.W. Cha, W. Lee, Y.B. Kim, J.S. Park, T.M. Gur, F.B. Prinz, C.C. Chao, J.W. An, Atomic layer deposition of thin-film ceramic electrolytes for high-performance fuel cells, *J. Mater. Chem. A*. 1 (2013) 12695–12705. doi:10.1039/c3ta11399j.
- [30] F. Zhao, A. V. Virkar, Dependence of polarization in anode-supported solid oxide fuel cells on various cell parameters, *J. Power Sources*. 141 (2005) 79–95. doi:10.1016/j.jpowsour.2004.08.057.
- [31] A.C. Müller, D. Herbstritt, E. Ivers-Tiffée, Development of a multilayer anode for solid oxide fuel cells, *Solid State Ionics*. 152–153 (2002) 537–542. doi:10.1016/S0167-2738(02)00357-0.
- [32] Z.R. Wang, J.Q. Qian, S.R. Wang, J.D. Cao, T.L. Wen, Improvement of anode-supported solid oxide fuel cells, *Solid State Ionics*. 179 (2008) 1593–1596. doi:10.1016/j.ssi.2008.03.022.
- [33] T. Setoguchi, K. Okamoto, K. Eguchi, H. Arai, Effects of anode material and fuel on anodic reaction of solid oxide fuel cells, *J. Electrochem. Soc.* 139 (1992) 2875–2880. doi:10.1149/1.2068998.

- [34] M. Kleitz, F. Petitbon, Optimized SOFC electrode microstructure, *Solid State Ionics*. 92 (1996) 65–74. doi:10.1016/S0167-2738(96)00464-X.
- [35] C.R. He, W.G. Wang, Alumina Doped Ni/YSZ Anode Materials for Solid Oxide Fuel Cells, *Fuel Cells*. 9 (2009) 630–635. doi:10.1002/face.200800152.
- [36] M. Mori, Y. Hiei, H. Itoh, G.A. Tompsett, N.M. Sammes, Evaluation of Ni and Ti-doped Y₂O₃ stabilized ZrO₂ cermet as an anode in high-temperature solid oxide fuel cells, *Solid State Ionics*. 160 (2003) 1–14. doi:10.1016/S0167-2738(03)00144-9.
- [37] J.E. Hammer, S.J. Laney, R.W. Jackson, K. Coyne, F.S. Pettit, G.H. Meier, The oxidation of ferritic stainless steels in simulated solid-oxide fuel-cell atmospheres, *Oxid. Met.* 67 (2007) 1–38. doi:10.1007/s11085-006-9041-y.
- [38] R. Amendola, P. Gannon, B. Ellingwood, K. Hoyt, P. Piccardo, P. Genocchio, Oxidation behavior of coated and preoxidized ferritic steel in single and dual atmosphere exposures at 800°C, *Surf. Coatings Technol.* 206 (2012) 2173–2180. doi:10.1016/j.surfcoat.2011.09.054.
- [39] J. Rufner, P. Gannon, P. White, M. Deibert, S. Teintze, R. Smith, H. Chen, Oxidation behavior of stainless steel 430 and 441 at 800 C in single (air/air) and dual atmosphere (air/hydrogen) exposures, *Int. J. Hydrogen Energy*. 33 (2008) 1392–1398. doi:10.1016/j.ijhydene.2007.12.067.
- [40] T. Dey, D. Singdeo, M. Bose, R.N. Basu, P.C. Ghosh, Study of contact resistance at the electrode-interconnect interfaces in planar type Solid Oxide Fuel Cells, *J. Power Sources*. 233 (2013) 290–298. doi:10.1016/j.jpowsour.2013.01.111.
- [41] T. Dey, A. Dey, P.C. Ghosh, M. Bose, A.K. Mukhopadhyay, R.N. Basu, Influence of microstructure on nano-mechanical properties of single planar solid oxide fuel cell in pre- and post-reduced conditions, *Mater. Des.* (2014). doi:10.1016/j.matdes.2013.06.052.
- [42] D. Klotz, A. Leonide, A. Weber, E. Ivers-Tiffée, Electrochemical model for SOFC and SOEC mode predicting performance and efficiency, *Int. J. Hydrogen Energy*. 39 (2014) 20844–20849. doi:10.1016/j.ijhydene.2014.08.139.
- [43] C. Jiang, J.T.S. Irvine, Catalysis and oxidation of carbon in a hybrid direct carbon fuel cell, *J. Power Sources*. 196 (2011) 7318–7322. doi:10.1016/j.jpowsour.2010.11.066.
- [44] M.R. Somalu, V. Yufit, N.P. Brandon, The effect of solids loading on the screen-printing and properties of nickel/scandia-stabilized-zirconia anodes for solid oxide fuel cells, *Int. J. Hydrogen Energy*. 38 (2013) 9500–9510. doi:10.1016/j.ijhydene.2012.06.061.
- [45] T. Shimura, Z. Jiao, S. Hara, N. Shikazono, Quantitative analysis of solid oxide fuel cell anode microstructure change during redox cycles, *J. Power Sources*. 267

- (2014) 58–68. doi:10.1016/j.jpowsour.2014.04.152.
- [46] A. Bertei, E. Ruiz-Trejo, K. Kareh, V. Yufit, X. Wang, F. Tariq, N.P. Brandon, The fractal nature of the three-phase boundary: A heuristic approach to the degradation of nanostructured solid oxide fuel cell anodes, *Nano Energy*. (2017). doi:10.1016/j.nanoen.2017.06.028.
- [47] J. Kong, K. Sun, D. Zhou, N. Zhang, J. Mu, J. Qiao, Ni-YSZ gradient anodes for anode-supported SOFCs, *J. Power Sources*. 166 (2007) 337–342. doi:10.1016/j.jpowsour.2006.12.042.
- [48] M. Radovic, E. Lara-curzio, Elastic Properties of Nickel-Based Anodes for Solid Oxide Fuel Cells as a Function of the Fraction of Reduced NiO, *J. Am. Ceram. Soc.* 87 (2004) 2242–2247. doi:10.1111/j.1151-2916.2004.tb07499.x.
- [49] M. Radovic, E. Lara-Curzio, Mechanical properties of tape cast nickel-based anode materials for solid oxide fuel cells before and after reduction in hydrogen, *Acta Mater.* 52 (2004) 5747–5756. doi:10.1016/j.actamat.2004.08.023.
- [50] J. Wei, T. Osipova, J. Malzbender, M. Krüger, Mechanical characterization of SOFC/SOEC cells, *Ceram. Int.* 44 (2018) 11094–11100. doi:10.1016/j.ceramint.2018.03.103.
- [51] J.R. Wilson, S. a. Barnett, Solid Oxide Fuel Cell Ni–YSZ Anodes: Effect of Composition on Microstructure and Performance, *Electrochem. Solid-State Lett.* 11 (2008) B181. doi:10.1149/1.2960528.
- [52] W.Z. Zhu, S.C. Deevi, A review on the status of anode materials for solid oxide fuel cells, *Mater. Sci. Eng. A*. 362 (2003) 228–239. doi:10.1016/S0921-5093(03)00620-8.
- [53] M. Pihlatie, A. Kaiser, M. Mogensen, Mechanical properties of NiO/Ni–YSZ composites depending on temperature, porosity and redox cycling, *J. Eur. Ceram. Soc.* 29 (2009) 1657–1664. doi:10.1016/j.jeurceramsoc.2008.10.017.
- [54] N. Mahato, A. Banerjee, A. Gupta, S. Omar, K. Balani, Progress in material selection for solid oxide fuel cell technology: A review, *Prog. Mater. Sci.* 72 (2015) 141–337. doi:10.1016/j.pmatsci.2015.01.001.
- [55] L. Holzer, B. Iwanschitz, T. Hocker, B. M??nch, M. Prestat, D. Wiedenmann, U. Vogt, P. Holtappels, J. Sfeir, A. Mai, T. Graule, Microstructure degradation of cermet anodes for solid oxide fuel cells: Quantification of nickel grain growth in dry and in humid atmospheres, *J. Power Sources*. 196 (2011) 1279–1294. doi:10.1016/j.jpowsour.2010.08.017.
- [56] Z. Jiao, N. Shikazono, N. Kasagi, Quantitative Characterization of SOFC Nickel-YSZ Anode Microstructure Degradation Based on Focused-Ion-Beam 3D-Reconstruction Technique, *J. Electrochem. Soc.* 159 (2012) B285. doi:10.1149/2.045203jes.

- [57] S. Kim, H. Moon, S. Hyun, J. Moon, J. Kim, H. Lee, Performance and durability of Ni-coated YSZ anodes for intermediate temperature solid oxide fuel cells, *Solid State Ionics*. 177 (2006) 931–938. doi:10.1016/j.ssi.2006.02.007.
- [58] G.J. Nelson, K.N. Grew, J.R. Izzo, J.J. Lombardo, W.M. Harris, A. Faes, A. Hessler-Wyser, J. Van Herle, S. Wang, Y.S. Chu, A. V. Virkar, W.K.S. Chiu, Three-dimensional microstructural changes in the Ni-YSZ solid oxide fuel cell anode during operation, *Acta Mater.* 60 (2012) 3491–3500. doi:10.1016/j.actamat.2012.02.041.
- [59] D. Simwonis, F. Tietz, D. Stover, Nickel coarsening in annealed Ni / 8YSZ anode substrates for solid oxide fuel cells, *Solid State Ionics*. 132 (2000) 241–251. doi:10.1016/S0167-2738(00)00650-0.
- [60] J. Wei, G. Pećanac, J. Malzbender, Review of mechanical characterization methods for ceramics used in energy technologies, *Ceram. Int.* 40 (2014) 15371–15380. doi:10.1016/j.ceramint.2014.07.089.
- [61] G. Pećanac, S. Baumann, J. Malzbender, Mechanical properties and lifetime predictions for Ba_{0.5}Sr_{0.5}Co_{0.8}Fe_{0.2}O_{3-δ} membrane material, *J. Memb. Sci.* 385–386 (2011) 263–268. doi:10.1016/j.memsci.2011.10.005.
- [62] G. Pećanac, L. Kiesel, R. Kriegel, J. Malzbender, Comparison of thermo-mechanical characteristics of non-doped and 3 mol% B-site Zr-doped Ba_{0.5}Sr_{0.5}Co_{0.8}Fe_{0.2}O_{3-??}, *Ceram. Int.* 40 (2014) 1843–1850. doi:10.1016/j.ceramint.2013.07.086.
- [63] A. Atkinson, A. Selçuk, Mechanical behaviour of ceramic oxygen ion-conducting membranes, *Solid State Ionics*. 134 (2000) 59–66. doi:10.1016/S0167-2738(00)00714-1.
- [64] M. Lipińska-Chwałek, L. Kiesel, J. Malzbender, Mechanical properties of porous MgO substrates for membrane applications, *J. Eur. Ceram. Soc.* 34 (2014) 2519–2524. doi:10.1016/j.jeurceramsoc.2014.03.009.
- [65] B.X. Huang, V. Vasechko, Q.L. Ma, J. Malzbender, Thermo-mechanical properties of (Sr,Y)TiO₃ as anode material for solid oxide fuel cells, *J. Power Sources*. 206 (2012) 204–209. doi:10.1016/j.jpowsour.2012.01.137.
- [66] S. Giraud, J. Canel, Young's modulus of some SOFCs materials as a function of temperature, *J. Eur. Ceram. Soc.* 28 (2008) 77–83. doi:10.1016/j.jeurceramsoc.2007.05.009.
- [67] Y. Ye, J. Li, H. Zhou, J. Chen, Microstructure and mechanical properties of yttria-stabilized ZrO₂/Al₂O₃ nanocomposite ceramics, *Ceram. Int.* 34 (2008) 1797–1803. doi:10.1016/j.ceramint.2007.06.005.
- [68] R. Kubrin, G. Blugan, J. Kuebler, Influence of cerium doping on mechanical properties of tetragonal scandium-stabilized zirconia, *J. Eur. Ceram. Soc.* 37

- (2017) 1651–1656. doi:10.1016/j.jeurceramsoc.2016.11.038.
- [69] S. Tekeli, The flexural strength, fracture toughness, hardness and densification behaviour of various amount of Al₂O₃-doped 8YSCZ/Al₂O₃ composites used as an electrolyte for solid oxide fuel cell, *Mater. Des.* 27 (2006) 230–235. doi:10.1016/j.matdes.2004.10.011.
- [70] J.S. Lee, K.H. Choi, B.K. Ryu, B.C. Shin, I.S. Kim, Effects of gallia additions on sintering behavior of gadolinia-doped ceria, *Ceram. Int.* 39 (2004) 807–812. doi:10.1016/j.materresbull.2004.07.022.
- [71] H. Xu, H. Yan, Z. Chen, The flexural strength and densification behavior of Al₂O₃-doped Ce_{0.8}Y_{0.2}O_{1.9} electrolyte composites, *Mater. Sci. Eng. A.* 447 (2007) 222–226. doi:10.1016/j.msea.2006.10.027.
- [72] N. Matsui, D. Kagaku, No Title, *J. Electrochem. Soc. Japan.* 58 (1990) 716.
- [73] S.S. Lion, W.L. Worrell, Electrical properties of novel mixed-conducting oxides, *Appl. Phys. A Solids Surfaces.* 49 (1989) 25–31. doi:10.1007/BF00615461.
- [74] Y.I. Kiyoshi Kobayashi, Yukiharu Kai, Shu Yamaguchi, Norihiko Fukatsu, Tsuyoshi Kawashima, K. Kobayashi, Y. Kai, S. Yamaguchi, N. Fukatsu, T. Kawashima, Y. Iguchi, Electronic conductivity measurements of 5 mol% TiO₂-doped YSZ by a d.c.-polarization technique, *Solid State Ionics.* 93 (1997) 193–199. doi:10.1016/S0167-2738(96)00534-6.
- [75] K. Kobayashi, K. Kato, T. Kawashima, S. Yamaguchi, Y. Iguchi, Total Electrical Conductivity Measurements of TiO₂ Doped YSZ Ceramics, *J. Ceram. Soc. Japan.* 106 (1998) 1073.
- [76] K. Swider, W. Worrell, Electronic Conduction Mechanism in Ytria- Stabilized Zirconia-Titania under Reducing Atmospheres, *J. Electrochem. Soc.* 143 (1996) 3706–3711. <http://jes.ecsdl.org/content/143/11/3706.short>.
- [77] M. Nagano, S. Nagashima, H. Maeda, A. Kato, Sintering behavior of Al₂TiO₅ base ceramics and their thermal properties, *Ceram. Int.* 25 (1999) 681–687. doi:10.1016/S0272-8842(98)00083-2.
- [78] S.W. Sofie, D.R. Taylor, Controlled Thermal Expansion Anode Compositions with Improved Strength for Use in Anode Supported SOFCs, *Adv. Solid Oxide Fuel Cells III.* (2008) 215–223.
- [79] C.H. Law, S.W. Sofie, Anchoring of Infiltrated Nickel Electro-Catalyst by Addition of Aluminum Titanate, *J. Electrochem. Soc.* 158 (2011) B1137–B1141. doi:10.1149/1.3610226.
- [80] D.R. Driscoll, M.D. McIntyre, M.M. Welander, S.W. Sofie, R.A. Walker, Enhancement of high temperature metallic catalysts: Aluminum titanate in the nickel-zirconia system, *Appl. Catal. A Gen.* 527 (2016) 36–44. doi:10.1016/j.apcata.2016.08.020.

- [81] D.N. Boccaccini, H.L. Frandsen, S. Soprani, M. Cannio, T. Klemensø, V. Gil, P.V. Hendriksen, Influence of porosity on mechanical properties of tetragonal stabilized zirconia, *J. Eur. Ceram. Soc.* (2018). doi:10.1016/j.jeurceramsoc.2017.09.029.
- [82] Z. Cui, Y. Huang, H. Liu, Predicting the mechanical properties of brittle porous materials with various porosity and pore sizes, *J. Mech. Behav. Biomed. Mater.* 71 (2017) 10–22. doi:10.1016/j.jmbbm.2017.02.014.
- [83] A. Bertei, C. Nicoletta, Percolation theory in SOFC composite electrodes: Effects of porosity and particle size distribution on effective properties, *J. Power Sources.* 196 (2011) 9429–9436. doi:10.1016/j.jpowsour.2011.06.087.
- [84] W.D. Callister, D.G. Rethwisch, *Fundamentals of Materials Science and Engineering: An Integrated Approach*, 5th Editio, Wiley, 2015.
- [85] ASTM C1161-13, Standard Test Method for Flexural Strength of Advanced Ceramics at Ambient Temperature, *ASTM Int.* (2013) 1–19. doi:10.1520/C1161-13.2.
- [86] ASTM C1499-15, Standard Test Method for Monotonic Equibiaxial Flexural Strength of Advanced Ceramics at Ambient Temperature, *ASTM Int.* (2015) 1–19. doi:10.1017/CBO9781107415324.004.
- [87] B. Timurkutluk, M.D. Mat, Effects of anode fabrication parameters on the performance and redox behavior of solid oxide fuel cells, *J. Power Sources.* 258 (2014) 108–116. doi:10.1016/j.jpowsour.2014.02.023.
- [88] H.L. Frandsen, M. Makowska, F. Greco, C. Chatzichristodoulou, D.W. Ni, D.J. Curran, M. Strobl, L.T. Kuhn, P. V. Hendriksen, Accelerated creep in solid oxide fuel cell anode supports during reduction, *J. Power Sources.* 323 (2016) 78–89. doi:10.1016/j.jpowsour.2016.04.097.
- [89] H. Fischer, W. Rentzsch, R. Marx, A modified size effect model for brittle nonmetallic materials, *Eng. Fract. Mech.* 69 (2002) 781–791. doi:10.1016/S0013-7944(01)00126-6.
- [90] B. Charlas, D.W. Ni, H.L. Frandsen, K. Brodersen, M. Chen, Mechanical Properties of Supports and Half-Cells for Solid Oxide Electrolysis Influenced by Alumina-Zirconia Composites, *Fuel Cells.* 17 (2017) 132–143. doi:10.1002/fuce.201600036.
- [91] D.-W. Ni, B. Charlas, K. Kwok, T.T. Molla, P.V. Hendriksen, H.L. Frandsen, Influence of temperature and atmosphere on the strength and elastic modulus of solid oxide fuel cell anode supports, *J. Power Sources.* 311 (2016) 1–12. doi:10.1016/j.jpowsour.2016.02.027.
- [92] B. Charlas, H.L. Frandsen, K. Brodersen, P.V. Henriksen, M. Chen, Residual stresses and strength of multilayer tape cast solid oxide fuel and electrolysis half-cells, *J. Power Sources.* 288 (2015) 243–252. doi:10.1016/j.jpowsour.2015.04.105.

- [93] H.L. Frandsen, T. Ramos, A. Faes, M. Pihlatie, K. Brodersen, Optimization of the strength of SOFC anode supports, *J. Eur. Ceram. Soc.* (2012). doi:10.1016/j.jeurceramsoc.2011.11.015.
- [94] A. Nakajo, J. Kuebler, A. Faes, U.F. Vogt, H.J. Schindler, L.K. Chiang, S. Modena, J. Van Herle, T. Hocker, Compilation of mechanical properties for the structural analysis of solid oxide fuel cell stacks. Constitutive materials of anode-supported cells, *Ceram. Int.* 38 (2012) 3907–3927. doi:10.1016/j.ceramint.2012.01.043.
- [95] M. Radovic, E. Lara-curzio, B. Armstrong, C. Walls, Elastic properties, biaxial strength and fracture toughness of nickel-based anode materials for solid oxide fuel cells, in: *Dev. SOLid Oxide Fuel Cells Lithium Ion Batter.*, 2005: pp. 31–40.
- [96] ASTM C1239-13, Standard Practice for Reporting Uniaxial Strength Data and Estimating Weibull Distribution Parameters for Advanced Ceramics, *ASTM Int.* (2013) 1–9. doi:10.1520/C1239-13.Scope.
- [97] J. Laurencin, G. Delette, F. Lefebvre-Joud, M. Dupeux, A numerical tool to estimate SOFC mechanical degradation: Case of the planar cell configuration, *J. Eur. Ceram. Soc.* 28 (2008) 1857–1869. doi:10.1016/j.jeurceramsoc.2007.12.025.
- [98] A. Nakajo, J. Kuebler, A. Faes, U.F. Vogt, H.J. Schindler, L.K. Chiang, S. Modena, J. Van Herle, T. Hocker, Compilation of mechanical properties for the structural analysis of solid oxide fuel cell stacks. Constitutive materials of anode-supported cells, *Ceram. Int.* 38 (2012) 3907–3927. doi:10.1016/j.ceramint.2012.01.043.
- [99] H.L. Frandsen, T. Ramos, A. Faes, M. Pihlatie, K. Brodersen, Optimization of the strength of SOFC anode supports, *J. Eur. Ceram. Soc.* 32 (2012) 1041–1052. doi:10.1016/j.jeurceramsoc.2011.11.015.
- [100] F. Baratta, W. Matthews, Errors Associated with Flexure Testing of Brittle Materials, *U.S. Army Mater. Technol. Lab.* (1987) 16, 41–42.
- [101] T. Dey, A. Dey, P.C. Ghosh, M. Bose, A.K. Mukhopadhyay, R.N. Basu, Influence of microstructure on nano-mechanical properties of single planar solid oxide fuel cell in pre- and post-reduced conditions, *Mater. Des.* 53 (2014) 182–191. doi:10.1016/j.matdes.2013.06.052.
- [102] Z. Cui, Y. Huang, H. Liu, Predicting the mechanical properties of brittle porous materials with various porosity and pore sizes, *J. Mech. Behav. Biomed. Mater.* 71 (2017) 10–22. doi:10.1016/j.jmbbm.2017.02.014.
- [103] D. Wu, Y. Li, J. Zhang, L. Chang, D. Wu, Z. Fang, Y. Shi, Effects of the number of testing specimens and the estimation methods on the Weibull parameters of solid catalysts, *Chem. Eng. Sci.* 56 (2001) 7035–7044. doi:10.1016/S0009-2509(01)00340-2.

- [104] A. Khalili, K. Kromp, Statistical properties of Weibull estimators, *J. Mater. Sci.* 26 (1991) 6741–6752.
- [105] H. Peterlik, Relationship of Strength and Defects of Ceramic Materials and Their Treatment by Weibull Theory, *J. Fo Ceram. Soc. Japan.* 109 (2001) 121–126. doi:10.1007/s13398-014-0173-7.2.
- [106] H. Fischer, W. Rentzsch, R. Marx, A modified size effect model for brittle nonmetallic materials, *Eng. Fract. Mech.* 69 (2002) 781–791. doi:10.1016/S0013-7944(01)00126-6.
- [107] X. Fan, E.D. Case, F. Ren, Y. Shu, M.J. Baumann, Part I: Porosity dependence of the Weibull modulus for hydroxyapatite and other brittle materials, *J. Mech. Behav. Biomed. Mater.* 8 (2012) 21–36. doi:10.1016/j.jmbbm.2011.12.010.
- [108] D.F. Wu, J.C. Zhou, Y.D. Li, Distribution of the Mechanical Strength of Solid Catalysts, *Chem. Eng. Res. Des.* 84(A12) (2006) 1152–1157. doi:http://dx.doi.org/10.1205/cherd05015.
- [109] A. Caiulo, M. Kachanov, On absence of quantitative correlations between strength and stiffness in microcracking materials, *Int. J. Fract.* 164 (2010) 155–158. doi:10.1007/s10704-010-9486-5.
- [110] G. Bruno, M. Kachanov, Microstructure–Property Connections for Porous Ceramics: The Possibilities Offered by Micromechanics, *J. Am. Ceram. Soc.* 99 (2016) 3829–3852. doi:10.1111/jace.14624.
- [111] I.M. Low, D. Lawrence, R.I. Smith, Factors controlling the thermal stability of aluminum titanate ceramics in vacuum, *J. Am. Ceram. Soc.* 88 (2005) 2957–2961. doi:10.1111/j.1551-2916.2005.00518.x.
- [112] G. Tilloca, Thermal stabilization of aluminium titanate and properties of aluminium titanate solid solutions, *J. Mater. Sci.* 26 (1991) 2809–2814. doi:10.1007/BF00545574.
- [113] B. Freudenberg, A. Mocellin, Aluminum Titanate Formation by Solid-state Reaction of Fine Al₂O₃ and TiO₂ Powders, *J. Am. Ceram. Soc.* 70 (1987) 33–38.
- [114] J. Zygmontowicz, P. Wicinska, A. Miazga, K. Konopka, Characterization of composites containing NiAl₂O₄ spinel phase from Al₂O₃/NiO and Al₂O₃/Ni systems, *J. Therm. Anal. Calorim.* 125 (2016) 1079–1086. doi:10.1007/s10973-016-5357-2.
- [115] L.S.M. Traqueia, T. Pagnier, F.M.B. Marques, Structural and electrical characterization of titania-doped YSZ, *J. Eur. Ceram. Soc.* 17 (1997) 1019–1026. doi:10.1016/S0955-2219(96)00172-0.
- [116] E. Üstündağ, R. Subramanian, R. Dieckmann, S.L. Sass, In-situ formation of metal-ceramic microstructures in the Ni-Al-O system by partial reduction reactions, *Acta Mater.* 43 (1995) 383–389. doi:http://dx.doi.org/10.1016/0167-

2738(94)00148-L.

- [117] E. Üstündag, Z. Zhang, M.L. Stocker, P. Rangaswamy, M.A.M. Bourke, J.A. Roberts, S. Subramanian, K.E. Sickafus, S.L. Sass, Influence of residual stresses on the evolution of microstructure during the partial reduction of NiAl₂O₄, *Mater. Sci. Eng. A.* 238 (1997) 50–65.
- [118] M. Lieberthal, W.D. Kaplan, Processing and properties of Al₂O₃ nanocomposites reinforced with sub-micron Ni and NiAl₂O₄, *Mater. Sci. Eng. A.* 302 (2001) 83–91. doi:10.1016/S0921-5093(00)01358-7.
- [119] N.Q. Minh, Ceramic Fuel Cells, *J. Am. Ceram. Soc.* 76 (1993) 563–588. doi:10.1111/j.1151-2916.1993.tb03645.x.
- [120] S.P. Jiang, S.H. Chan, A review of anode materials development in solid oxide fuel cells, *J. Mater. Sci.* 39 (2004) 4405–4439.
- [121] M.S. Khan, S.B. Lee, R.H. Song, J.W. Lee, T.H. Lim, S.J. Park, Fundamental mechanisms involved in the degradation of nickel-yttria stabilized zirconia (Ni-YSZ) anode during solid oxide fuel cells operation: A review, *Ceram. Int.* 42 (2015) 35–48. doi:10.1016/j.ceramint.2015.09.006.
- [122] D. Sarantaridis, A. Atkinson, Redox cycling of Ni-based solid oxide fuel cell anodes: A review, *Fuel Cells.* 7 (2007) 246–258. doi:10.1002/face.200600028.
- [123] M. Ettler, H. Timmermann, J. Malzbender, A. Weber, N.H. Menzler, Durability of Ni anodes during reoxidation cycles, *J. Power Sources.* 195 (2010) 5452–5467.
- [124] J.T. Richardson, R. Scates, M. V. Twigg, X-ray diffraction study of nickel oxide reduction by hydrogen, *Appl. Catal. A Gen.* 246 (2003) 137–150. doi:10.1016/S0926-860X(02)00669-5.
- [125] T.A. Utigard, M. Wu, G. Plascencia, T. Marin, Reduction kinetics of Goro nickel oxide using hydrogen, *Chem. Eng. Sci.* 60 (2005) 2061–2062. doi:10.1016/j.ces.2004.11.024.
- [126] M.H. Pihlatie, H.L. Frandsen, A. Kaiser, M. Mogensen, Continuum mechanics simulations of NiO/Ni-YSZ composites during reduction and re-oxidation, *J. Power Sources.* 195 (2010) 2677–2690. doi:10.1016/j.jpowsour.2009.11.079.
- [127] N.M. Tikekar, T.J. Armstrong, A. V. Virkar, Reduction and Reoxidation Kinetics of Nickel-Based SOFC Anodes, *J. Electrochem. Soc.* 153 (2006) A654. doi:10.1149/1.2167949.
- [128] N.M. Tikekar, T.J. Armstrong, A. V. Virkar, Reduction and re-oxidation kinetics of nickel-based solid oxide fuel cell anodes, in: S.C. Singhal, M. Dokiya (Eds.), *Electrochem. Soc. Proc.*, 2003: pp. 670–679.
- [129] A. Hagen, H.F. Poulsen, T. Klemensø, R. V. Martins, V. Honkimäki, T. Buslaps, R. Feidenshans'l, A Depth-Resolved In-Situ Study of the Reduction and Oxidation

- of Ni-Based Anodes in Solid Oxide Fuel Cells, *Fuel Cells*. 6 (2006) 361–366. doi:10.1002/fuce.200600004.
- [130] J. Mizusaki, H. Tagawa, T. Saito, T. Yamamura, K. Kamitani, K. Hirano, S. Ehara, T. Takagi, T. Hikita, M. Ippommatsu, Kinetic studies of the reaction at the nickel pattern electrode on YSZ in H₂-H₂O atmospheres, *Solid State Ionics*. 70–71 (1994) 52–58. doi:10.1016/0167-2738(94)90286-0.
- [131] A. Bieberle, L.J. Gauckler, Reaction Mechanism of Ni Pattern Anodes for Solid Oxide Fuel Cells, *Solid State Ionics*. 135 (2000) 337.
- [132] J.L. Young, V. Vedahara, S. Kung, S. Xia, V.I. Birss, Understanding Nickel Oxidation and Reduciton Processes in SOFC Systems, *ECS Trans*. 7 (2007) 1511–1519.
- [133] A.J. Weisentein, N. Childs, R. Amendola, D. Driscoll, S.W. Sofie, P. Gannon, R. Smith, Processing and characterization of Sr_{2-x}VMoO_{6-δ} double perovskites, *Mater. Chem. Phys*. 139 (2013) 706–718. doi:10.1016/j.matchemphys.2013.02.021.
- [134] D. Driscoll, C. Hunt, J. Muretta, S.W. Sofie, Thermally Stabilized Nickel Electro-Catalyst Introduced by Infiltration for High Temperature Electrochemical Energy Conversion, *ECS Trans*. 53 (2013) 63–72. doi:10.1149/05309.0063ecst.
- [135] D.R. Driscoll, B.W. Tokmakian, N.P. Johnson, C.D. Hunt, S.W. Sofie, Catalyst enhancing aluminum titanate for increasing strength of nickel-zirconia cermets, *Mater. Lett*. 209 (2017) 307–310. doi:10.1016/j.matlet.2017.08.035.
- [136] M. Mcclery, R. Amendola, Effect of Aluminum Titanate (Al₂TiO₅) Doping on the Mechanical Performance of Solid Oxide Fuel Cell Ni-YSZ Anode, *Fuel Cells*. (2017) 862–868. doi:10.1002/fuce.201700073.
- [137] S.B. Simonsen, K. Agersted, K.V. Hansen, T. Jacobsen, J.B. Wagner, T.W. Hansen, L.T. Kuhn, Environmental TEM study of the dynamic nanoscaled morphology of NiO/YSZ during reduction, *Appl. Catal. A Gen*. 489 (2015) 147–154. doi:10.1016/j.apcata.2014.10.045.
- [138] A. Morrissey, J.R. O’Brien, I.E. Reimanis, Microstructure evolution during internal reduction of polycrystalline nickel-doped yttria-stabilized zirconia, *Acta Mater*. 105 (2016) 84–93. doi:10.1016/j.actamat.2015.12.005.
- [139] D. Fouquet, A.C. Müller, a. Weber, E. Ivers-Tiffée, Kinetics of oxidation and reduction of Ni/YSZ cermets, *Ionics (Kiel)*. 9 (2003) 103–108. doi:10.1007/BF02376545.
- [140] D. Ipsakis, E. Heracleous, L. Silvester, D.B. Bukur, A.A. Lemonidou, Reduction and oxidation kinetic modeling of NiO-based oxygen transfer materials, *Chem. Eng. J*. 308 (2017) 840–852. doi:10.1016/j.cej.2016.09.114.

- [141] B. Janković, Isothermal reduction kinetics of nickel oxide using hydrogen: Conventional and Weibull kinetic analysis, *J. Phys. Chem. Solids.* 68 (2007) 2233–2246. doi:10.1016/j.jpcs.2007.06.014.
- [142] K. V. Manukyan, A.G. Avetisyan, C.E. Shuck, H.A. Chatilyan, S. Rouvimov, S.L. Kharatyan, A.S. Mukasyan, Nickel Oxide Reduction by Hydrogen: Kinetics and Structural Transformations, *J. Phys. Chem. C.* 119 (2015) 16131–16138. doi:10.1021/acs.jpcc.5b04313.
- [143] J.A. Rodriguez, J.C. Hanson, A.I. Frenkel, J.Y. Kim, M. Pérez, Experimental and theoretical studies on the reaction of H₂ with NiO: Role of O vacancies and mechanism for oxide reduction, *J. Am. Chem. Soc.* 124 (2002) 346–354. doi:10.1021/ja0121080.
- [144] R.P. Furstenau, G. McDougall, M.A. Langell, Initial Stages of Hydrogen Reduction of NiO (100), *Surf. Sci.* 150 (1985) 55–79.
- [145] Z. Zhou, L. Han, G.M. Bollas, Kinetics of NiO reduction by H₂ and Ni oxidation at conditions relevant to chemical-looping combustion and reforming, *Int. J. Hydrogen Energy.* 39 (2014) 8535–8556. doi:10.1016/j.ijhydene.2014.03.161.
- [146] P. Hancock, J.H. Sharp, Method of Comparing Solid-State Kinetic Data and Its Application to the Decomposition of Kaolinite, Brucite, and BaCO₃, *J. Am. Ceram. Soc.* 55 (1972) 74–77. doi:10.1111/j.1151-2916.1972.tb11213.x.
- [147] M. Avrami, Kinetics of Phase Change. I General Theory, *J. Chem. Phys.* 7 (1939) 1103–1112. doi:10.1063/1.1750380.
- [148] M. Avrami, Kinetics of Phase Change . II Transformation Time Relations for Random Distribution of Nuclei Kinetics of Phase Change . II Transformation-Time Relations for Random Distribution of Nuclei *, *J. Chem. Phys.* 8 (1940) 212. doi:10.1063/1.1750631.
- [149] M. Avrami, Granulation, Phase Change, and Microstructure Kinetics of Phase Change. III, *J. Chem. Phys.* 9 (1941) 177–184. doi:10.1063/1.1750872.
- [150] Q. Jeangros, T.W. Hansen, J.B. Wagner, C.D. Damsgaard, R.E. Dunin-Borkowski, C. Hébert, J. Van Herle, A. Hessler-Wyser, Reduction of nickel oxide particles by hydrogen studied in an environmental TEM, *J. Mater. Sci.* 48 (2013) 2893–2907. doi:10.1007/s10853-012-7001-2.
- [151] M.M. Hossain, M.R. Quddus, H.I. de Lasa, Reduction Kinetics of La Modified NiO/La- γ -Al₂O₃ Oxygen Carrier for Chemical-Looping Combustion, *Ind. Eng. Chem. Res.* 49 (2010) 11009–11017. doi:10.1021/ie100424w.
- [152] M.M. Hossain, D. Lopez, J. Herrera, H.I. de Lasa, Nickel on lanthanum-modified γ -Al₂O₃ oxygen carrier for CLC: Reactivity and stability, *Catal. Today.* 143 (2009) 179–186. doi:10.1016/j.cattod.2008.09.006.
- [153] M.M. Hossain, H.I. de Lasa, Chemical-looping combustion (CLC) for inherent

- CO₂ separations-a review, *Chem. Eng. Sci.* 63 (2008) 4433–4451.
doi:10.1016/j.ces.2008.05.028.
- [154] K.E. Sedor, M.M. Hossain, H.I. de Lasa, Reactivity and stability of Ni/Al₂O₃ oxygen carrier for chemical-looping combustion (CLC), *Chem. Eng. Sci.* 63 (2008) 2994–3007. doi:10.1016/j.ces.2008.02.021.
- [155] S.R. Son, S.D. Kim, Chemical-Looping Combustion with NiO and Fe₂O₃ in a Thermobalance and Circulating Fluidized Bed Reactor with Double Loops, *Ind. Eng. Chem. Res.* 45 (2006) 2689–2696. doi:10.1021/ie050919x.
- [156] L. Han, Z. Zhou, G.M. Bollas, Heterogeneous modeling of chemical-looping combustion. Part 2: Particle model, *Chem. Eng. Sci.* 113 (2014) 116–128.
doi:10.1016/j.ces.2014.03.030.
- [157] J. Málek, The applicability of Johnson-Mehl-Avrami model in the thermal analysis of the crystallization kinetics of glasses, *Thermochim. Acta.* 267 (1995) 61–73.
doi:10.1016/0040-6031(95)02466-2.
- [158] Z.. Yan, S.. He, J.. Li, Y.. Zhou, On the crystallization kinetics of Zr₆₀Al₁₅Ni₂₅ amorphous alloy, *J. Alloys Compd.* 368 (2004) 175–179.
doi:10.1016/j.jallcom.2003.08.074.
- [159] T. Hidayat, M.A. Rhamdhani, E. Jak, P.C. Hayes, The kinetics of reduction of dense synthetic nickel oxide in H₂-N₂ and H₂-H₂O atmospheres, *Metall. Mater. Trans. B Process Metall. Mater. Process. Sci.* 40 (2009) 1–16. doi:10.1007/s11663-008-9212-0.
- [160] H. Orui, R. Chiba, K. Nozawa, H. Arai, R. Kanno, High-temperature stability of alumina containing nickel–zirconia cermets for solid oxide fuel cell anodes, *J. Power Sources.* 238 (2013) 74–80. doi:10.1016/j.jpowsour.2013.03.056.
- [161] C. Dueso, M. Ortiz, A. Abad, F. García-Labiano, L.F. De Diego, P. Gayán, J. Adánez, Reduction and oxidation kinetics of nickel-based oxygen-carriers for chemical-looping combustion and chemical-looping reforming, *Chem. Eng. J.* 188 (2012) 142–154. doi:10.1016/j.cej.2012.01.124.
- [162] C. Dueso, A. Abad, F. García-Labiano, L.F. de Diego, P. Gayán, J. Adánez, A. Lyngfelt, Reactivity of a NiO/Al₂O₃ oxygen carrier prepared by impregnation for chemical-looping combustion, *Fuel.* 89 (2010) 3399–3409.
doi:10.1016/j.fuel.2010.03.043.
- [163] E. Ustundag, B. Clausen, M.A.M. Bourke, Neutron diffraction study of the reduction of NiAl₂O₄, *Appl. Phys. Lett.* 76 (2000) 694–696.
doi:10.1063/1.125864.
- [164] H. Messaoudi, S. Thomas, A. Djaidja, S. Slyemi, R. Chebout, S. Barama, A. Barama, F. Benaliouche, Hydrogen production over partial oxidation of methane using Ni Mg Al spinel catalysts: A kinetic approach, *Comptes Rendus Chim.* 20

- (2017) 738–746. doi:10.1016/j.crci.2017.02.002.
- [165] K. Mocala, A. Navrotsky, Structural and Thermodynamic Variation in Nickel Aluminate Spinel, *J. Am. Ceram. Soc.* 72 (1989) 826–832. doi:10.1111/j.1151-2916.1989.tb06225.x.
- [166] M. Wu, D.M. Hercules, Studies of supported nickel catalysts by x-ray photoelectron and ion scattering spectroscopies, *J. Phys. Chem.* 83 (1979) 2003–2008. doi:10.1021/j100478a015.
- [167] A. Cimino, M. Lo Jacono, M. Schiavello, Effect of zinc, gallium, and germanium ions on the structural and magnetic properties of nickel ions supported on alumina, *J. Phys. Chem.* 79 (1975) 243–249. doi:10.1021/j100570a010.
- [168] M. McCleary, R. Amendola, Reduction kinetics of undoped and aluminum titanate (Al₂TiO₅) doped NiO-YSZ solid oxide fuel cell anodes, *Ceram. Int.* 44 (2018) 15557–15564. doi:10.1016/j.ceramint.2018.05.218.
- [169] J.B. Quinn, G.D. Quinn, A practical and systematic review of Weibull statistics for reporting strengths of dental materials, *Dent. Mater.* 26 (2010) 135–147. doi:10.1016/j.dental.2009.09.006.
- [170] ASTM C1683-10, Standard Practice for Size Scaling of Tensile Strengths Using Weibull Statistics for Advanced Ceramics, *ASTM Int.* (2015) 1–18. doi:10.1520/C1683.
- [171] D. Wu, Y. Li, J. Zhang, L. Chang, D. Wu, Z. Fang, Y. Shi, Effects of the number of testing specimens and the estimation methods on the Weibull parameters of solid catalysts, *Chem. Eng. Sci.* 56 (2001) 7035–7044. doi:10.1016/S0009-2509(01)00340-2.
- [172] J. Jin, H. Takahashi, N. Iwasaki, Effect of test method on flexural strength of recent dental ceramics, *Dent. Mater. J.* 23 (2004) 490–496. doi:10.4012/dmj.23.490.
- [173] G.K.R. Pereira, M. Amaral, R. Simoneti, G.C. Rocha, P.F. Cesar, L.F. Valandro, Effect of grinding with diamond-disc and -bur on the mechanical behavior of a Y-TZP ceramic, *J. Mech. Behav. Biomed. Mater.* 37 (2014) 133–140. doi:10.1016/j.jmbbm.2014.05.010.
- [174] Y. Xu, J. Han, H. Lin, L. An, Comparative study of flexural strength test methods on CAD/CAM Y-TZP dental ceramics, *Regen. Biomater.* 2 (2015) 239–244. doi:10.1093/rb/rbv020.
- [175] K. Zeng, A. Odén, D. Rowcliffe, Flexure tests on dental ceramics., *Int. J. Prosthodont.* 9 (1996) 434–9. <http://www.ncbi.nlm.nih.gov/pubmed/9108743>.
- [176] D.D. Boos, L.A. Stefanski, *Essential Statistical Inference: Theory and Methods*, New York, 2013. doi:10.1016/j.peva.2007.06.006.

- [177] R. Gentleman, R. Ihaka, R Computer Program, (2019). <https://www.r-project.org/>.
- [178] Y. Youjiao, mixR: Finite Mixture Modeling for Raw and Binned Data, (2018). <https://cran.r-project.org/package=mixR>.
- [179] C. Bishop, Pattern Recognition and Machine Learning, New York, 2006. doi:10.1021/jo01026a014.
- [180] H. Xu, H. Yan, Z. Chen, The flexural strength and densification behavior of Al₂O₃-doped Ce_{0.8}Y_{0.2}O_{1.9} electrolyte composites, Mater. Sci. Eng. A. 447 (2007) 222–226. doi:10.1016/j.msea.2006.10.027.
- [181] H.U. Anderson, F. Tietz, High-temperature Solid Oxide Fuel Cells: Fundamentals, Design and Applications, Elsevier Science, 2003.
- [182] T. Klemensø, C.C. Appel, M. Mogensen, In Situ Observations of Microstructural Changes in SOFC Anodes during Redox Cycling, Electrochem. Solid-State Lett. 9 (2006) A403. doi:10.1149/1.2214303.
- [183] T. Klemensø, C. Chung, P.H. Larsen, M. Mogensen, The Mechanism Behind Redox Instability of Anodes in High-Temperature SOFCs, J. Electrochem. Soc. 152 (2005) A2186. doi:10.1149/1.2048228.
- [184] D. Waldbillig, A. Wood, D.G. Ivey, Thermal analysis of the cyclic reduction and oxidation behaviour of SOFC anodes, Solid State Ionics. 176 (2005) 847–859. doi:10.1016/j.ssi.2004.12.002.
- [185] D. Waldbillig, A. Wood, D.G. Ivey, Electrochemical and microstructural characterization of the redox tolerance of solid oxide fuel cell anodes, J. Power Sources. 145 (2005) 206–215. doi:10.1016/j.jpowsour.2004.12.071.
- [186] J. Malzbender, E. Wessel, R.W. Steinbrech, Reduction and re-oxidation of anodes for solid oxide fuel cells, Solid State Ionics. 176 (2005) 2201–2203. doi:10.1016/j.ssi.2005.06.014.
- [187] Y. Zhang, B. Liu, B. Tu, Y. Dong, M. Cheng, Redox cycling of Ni-YSZ anode investigated by TPR technique, Solid State Ionics. 176 (2005) 2193–2199. doi:10.1016/j.ssi.2005.06.016.
- [188] A. Wood, M. Pastula, D. Waldbillig, D.G. Ivey, Initial Testing of Solutions to Redox Problems with Anode-Supported SOFC, J. Electrochem. Soc. 153 (2006) A1929. doi:10.1149/1.2240085.
- [189] M. Pihlatie, A. Kaiser, P.H. Larsen, M. Mogensen, Dimensional Behavior of Ni-YSZ Composites during Redox Cycling, J. Electrochem. Soc. 156 (2009) B322. doi:10.1149/1.3046121.
- [190] M.M. Welander, M.S. Zachariasen, S.W. Sofie, R.A. Walker, Enhancing Ni-YSZ Anode Resilience to Environmental Redox Stress with Aluminum Titanate Secondary Phases, ACS Appl. Energy Mater. 1 (2018) 6295–6302.

doi:10.1021/acsaem.8b01288.

- [191] A. Faes, A. Hessler-Wyser, A. Zryd, J. Van Herle, A review of RedOx cycling of solid oxide fuel cells anode, *Membranes (Basel)*. 2 (2012) 585–664. doi:10.3390/membranes2030585.
- [192] T. Kawada, S. Watanabe, T. Hashida, H. Yugami, J. Mizusaki, S. Sukino, F. Iguchi, K. Sato, Effect of Redox Cycling on Mechanical Properties of Ni-YSZ Cermets for SOFC Anodes, *ECS Trans.* 35 (2011) 1473–1482. doi:10.1149/1.3570133.
- [193] M. Pihlatie, T. Ramos, A. Kaiser, Testing and improving the redox stability of Ni-based solid oxide fuel cells, *J. Power Sources*. 193 (2009) 322–330. doi:10.1016/j.jpowsour.2008.11.140.
- [194] M. Pihlatie, A. Kaiser, M. Mogensen, Redox stability of SOFC: Thermal analysis of Ni-YSZ composites, *Solid State Ionics*. 180 (2009) 1100–1112. doi:10.1016/j.ssi.2009.04.011.
- [195] M.M. Welander, M.S. Zachariassen, C.D. Hunt, S.W. Sofie, R.A. Walker, Operando Studies of Redox Resilience in ALT Enhanced NiO-YSZ SOFC Anodes, *J. Electrochem. Soc.* 165 (2018) F152–F157. doi:10.1149/2.0531803jes.
- [196] B. Timurkutluk, S. Celik, E. Ucar, Influence of doctor blade gap on the properties of tape cast NiO/YSZ anode supports for solid oxide fuel cells, *Ceram. Int.* (2018). doi:10.1016/j.ceramint.2018.10.221.
- [197] M. McCleary, R. Amendola, Effect of Aluminum Titanate (Al_2TiO_5) Doping on the Mechanical Performance of Solid Oxide Fuel Cell Ni-YSZ Anode, *Fuel Cells*. 17 (2017). doi:10.1002/fuce.201700073.
- [198] R. Subramanian, E. Üstündağ, S.L. Sass, R. Dieckmann, In-situ formation of metal-ceramic microstructures by partial reduction reactions, *Solid State Ionics*. 75 (1995) 241–255. doi:10.1016/0167-2738(94)00148-L.
- [199] D. Sarantaridis, R.A. Rudkin, A. Atkinson, Oxidation failure modes of anode-supported solid oxide fuel cells, *J. Power Sources*. 180 (2008) 704–710. doi:10.1016/j.jpowsour.2008.03.011.
- [200] I. Küppenbender, M. Schütze, The deformation behavior of NiO scales on Ni in argon and air at temperatures from 20 to 800°C with respect to the relief of growth stresses, *Oxid. Met.* 42 (1994) 109–144. doi:10.1007/BF01061927.
- [201] D.W. Ni, B. Charlas, K. Kwok, T.T. Molla, P.V. Hendriksen, H.L. Frandsen, Influence of temperature and atmosphere on the strength and elastic modulus of solid oxide fuel cell anode supports, *J. Power Sources*. 311 (2016) 1–12. doi:10.1016/j.jpowsour.2016.02.027.
- [202] Y. Zhang, B. Liu, B. Tu, Y. Dong, M. Cheng, Understanding of redox behavior of

- Ni-YSZ cermets, *Solid State Ionics*. 180 (2009) 1580–1586.
doi:10.1016/j.ssi.2009.10.011.
- [203] B.D. Vasylyv, V.Y. Podhurs'ka, O.P. Ostash, O.D. Vasyly'ev, E.M. Brodnikovs'kyi, Influence of reducing and oxidizing media on the physicochemical properties of ScCeSZ-NiO and YSZ-NiO ceramics, *Mater. Sci.* 49 (2013) 135–144.
doi:10.1007/s11003-013-9593-3.
- [204] L. Kang, Strain Accumulation Study of Ni-based Anode-Supported Solid Oxide Fuel Cells under Partial-Redox Cycling Conditions, *Int. J. Electrochem. Sci.* 11 (2016) 5596–5606. doi:10.20964/2016.07.28.
- [205] K.H. Ng, H.A. Rahman, M.R. Somalu, Review: Enhancement of composite anode materials for low-temperature solid oxide fuels, *Int. J. Hydrogen Energy*. (2018).
doi:10.1016/j.ijhydene.2018.01.073.
- [206] M. Kleitz, Optimized SOFC electrode microstructure, *Solid State Ionics*. 92 (1996) 65–74. doi:10.1016/S0167-2738(96)00464-X.
- [207] Y. Ding, Y. Li, G. Liu, K. Yu, Y. Luo, H. Liu, W. Sun, G. Chen, S. Geng, Electrochemical performance of a new structured low temperature SOFC with BZY electrolyte, *Int. J. Hydrogen Energy*. 43 (2018) 12765–12772.
doi:10.1016/j.ijhydene.2018.04.006.
- [208] J. Moreno-Blanco, F. Elizalde-Blancas, J.M. Riesco-Avila, J.M. Belman-Flores, A. Gallegos-Muñoz, On the effect of gas channels-electrode interface area on SOFCs performance, *Int. J. Hydrogen Energy*. 4 (2019) 446–456.
doi:10.1016/j.ijhydene.2018.02.108.
- [209] J. Malzbender, R.W. Steinbrech, L. Singheiser, Failure probability of solid oxide fuel cells, *Ceram. Eng. Sci. Proc.* 26 (2005) 293.
- [210] W. Fischer, J. Malzbender, G. Blass, R.W. Steinbrech, Residual stresses in planar solid oxide fuel cells, *J. Power Sources*. 150 (2005) 73–77.
doi:10.1016/j.jpowsour.2008.04.035.
- [211] J. Malzbender, R.W. Steinbrech, Threshold fracture stress of thin ceramic components, *J. Eur. Ceram. Soc.* 28 (2008) 247–252.
doi:10.1016/j.jeurceramsoc.2007.05.017.

APPENDICES

APPENDIX A: Effect of Particle Size on the Mechanical Performance of Undoped and Aluminum Titanate (Al_2TiO_5) Doped Ni-YSZ Solid Oxide Fuel Cell Anodes

What follows is a draft of a manuscript for publication. Please note that changes will be made before publication.

Effect of Particle Size on the Mechanical Performance of Undoped and Aluminum Titanate (Al_2TiO_5) Doped NiO-YSZ Solid Oxide Fuel Cell Anodes

Madisen McCleary, Roberta Amendola*, Clay Hunt

Montana State University, Mechanical Engineering, 220 Roberts Hall, Bozeman, MT
59717, United States

[*] Corresponding author, Roberta.amendola@montana.edu

Abstract

The mechanical properties of aluminum titanate (Al_2TiO_5 , ALT) doped NiO-YSZ anode materials were mechanically tested using three-point bending. Two different NiO powder sizes were used: micro ($\sim 4 \mu\text{m}$) and nano (350 nm) to study the effect of particle size on the mechanical properties of the ALT doped anode. Anodes were doped with ALT up to 10 wt% to study material strengthening. The mechanical strength of the sample batches with nano NiO powder was, on average, higher than the micro NiO powder sample batches. This is thought to be due to sintering characteristics of nano NiO powder resulting in a denser and less porous material. Grain size of nano NiO samples

was larger than corresponding micro NiO sample batches. This is thought to increase strength by the formation of larger, more robust grains of secondary phases. Weibull statistics and fractography were used to verify mechanical strengthening.

Introduction

As society faces a global energy crisis, the need for a reliable renewable energy source has been the focus of much research in the past several decades. Solid oxide fuel cells (SOFCs) have been heavily researched because they electrochemically produce power using hydrogen gas and air with by-products of only water and heat. Recent work has focused on improving the performance and durability of low-cost materials for potential marketability of SOFCs. Anode supported cells have been investigated because of their advantages for lower temperature operation and high-power output [1–7]. At this time, a single SOFC cannot produce enough power for commercial use; therefore, single cells are stacked in electrical series and clamped to increase contact between the cells. These clamping pressures are high, between 65-70 kPa [8,9], and can cause failure of the brittle ceramic components of the cell.

When considering the brittle nature of ceramics, the strength and durability of the material is of utmost importance for long-term operation of the cells. Moreover, little fundamental data is known about the mechanical performance of SOFC materials including their thermo-mechanical properties such as fracture strength, fracture characteristics, coefficient of thermal expansion, and elastic behavior. At this time, nickel oxide (NiO) and yttria-stabilized zirconia (YSZ) are the most commonly used anode materials because of their low cost to power ratio [10,11]. Researchers have been actively

searching for new anode materials [12–20], but much study needs to be conducted before implementation as ceramics are sensitive to changes in materials chemistry and processing.

Research has shown that the addition of a second phase can increase mechanical performance without compromising the electrochemical properties of the material [6,7,21,22]. Previous research has shown that the addition of aluminum titanate (Al_2TiO_5 , ALT) can increase the mechanical performance by the formation of toughening phases during sintering and subsequent reduction of the anode material [23]. It has also been shown that ALT doping stabilizes the Ni-YSZ anode in terms of slow degradation rates and high power output [24–27].

As stated previously, ceramic materials are sensitive to changes in their material chemistry and manufacturing process. To test the sensitivity of the ALT doped NiO-YSZ anode material, samples were manufactured with two different powder particle sizes for NiO. Research was conducted for micro sized NiO powder ($\sim 4 \mu\text{m}$) along with nano sized NiO powder ($\sim 350 \text{ nm}$) to investigate how particle size of the NiO can affect the mechanical performance in ALT doped anode material. This large difference in powder size could lead to different microstructural features affecting mechanical properties. This study could help to elucidate how particle size could affect the mechanisms for mechanical strengthening.

Experimental

Nickel Oxide (NiO) powder (350 nm, Sigma Aldrich and $4 \mu\text{m}$, Alfa Aesar), 8 mol% Yttria Stabilized Zirconia (8YSZ) powder (300 nm, Tosoh) and Aluminum

Titanate (ALT) powder (25 nm, Sigma Aldrich) were used for sample manufacturing. Powders, in the ratio of 34 wt% YSZ, 66 wt% NiO and 0-10 wt% ALT, were ball milled for 24 hours with binder. After milling, the ceramic slurry was tape cast in ambient conditions with a doctor blade thickness of 2 mm. Rectangular 40 x 6 mm samples were cut from the dried green tape cast with a rotary blade. Thermolysis of tape cast samples was performed in ambient air using a box furnace (Thermolyne, 1300) with the following procedure: 1) heating at 2°C/min up to 150°C, 2) dwell for 2 hours, 3) heating to 450°C at 0.5 °C/min, 4) heating to 1100°C at 5 °C/min, 5) dwell for 2 hours, 6) cooling to room temperature at 10 °C/min. Sintering was conducted with a heating/cooling rate of 5°C/min up to 1500°C and a dwell time of 2 hours (Zircar, Hot Spot 110). Reduction was performed in a tube furnace (Thermo Scientific, Lindberg Blue M) flowing 5% H₂-95% N₂ gas, at 800°C for a time sufficient to convert 97 wt% of NiO into metallic nickel [23,28].

Un-doped and 1, 5 and 10 wt% ALT doped batches of 30 oxidized and reduced samples were manufactured for testing. The same sample batches were made for both the micro and nano NiO powder which totals to 16 overall batches (8 oxidized and 8 reduced). Samples were loaded at a rate of 0.2 mm/min in a three-point bending apparatus (Pasco Scientific 8236) as per ASTM C1161-13 standard [29]. Fracture strength, effective volume V_{eff} , scaled characteristic strength σ_0' , Weibull modulus (m) [30] with normalized upper and lower bounds, and porosity, by alcohol immersion method, were evaluated. Field Emission Scanning electron microscopy (FE-SEM, Zeiss

Ultra) microstructural characterization was conducted to determine the nature of the developed phases and their contribution to the material mechanical strength.

Results and Discussion

Mechanical properties

Table 1 shows the mechanical properties results for the micro and nano NiO-YSZ anodes in an oxidized state. It can be observed that the characteristic strength increased with the addition of ALT. The characteristic strength is calculated using Weibull statistics following ASTM standard C1239-13 [30]. The characteristic strength is calculated at a probability of failure of 63.2%. For undoped Ni-YSZ anode material, literature reports values of strength between 80 and 130 MPa [19,31]. For the undoped samples, it can be observed that the characteristic strength falls above this range for the nano NiO and at the bottom of the range for the micro NiO. With the addition of ALT, the characteristic strength is well above the cited range showing a strength increase with doping. The highest characteristic strength for the micro NiO-YSZ oxidized samples is 235 MPa for 10 wt% ALT doping. For the nano NiO-YSZ oxidized samples, the highest strength is also observed with 10 wt% ALT doping with a strength of 252 MPa. There is a decrease in strength observed between 1 and 5 wt% ALT doping for the nano NiO powder batches and will be further discussed below. Along with this, the characteristic strength for the micro NiO powder batches has a significant change between 1 and 5 wt% ALT doping and will be further discussed.

Table 1: Mechanical properties data for undoped and ALT doped NiO-YSZ anode material

	0 wt% ALT	1 wt% ALT	5 wt% ALT	10 wt% ALT
Micro NiO-YSZ				
Characteristic Strength (MPa)	82	88	220	235
V_{eff} (mm ³)	0.31	0.50	0.19	0.10
Scaled Characteristic Strength (MPa)	71	78	182	197
Strength Increase (%)	N/A	9	155	177
Nano NiO-YSZ				
Characteristic Strength (MPa)	185	229	218	252
V_{eff} (mm ³)	0.46	0.14	0.09	0.19
Scaled Characteristic Strength (MPa)	157	184	176	203
Strength Increase (%)	N/A	17	12	29

Table 2 shows the mechanical properties data for the micro and nano NiO-YSZ samples after undergoing reduction. It can be observed that ALT doping increases the mechanical strength for both the micro and nano Ni-YSZ anodes. Due to the introduction of porosity, the strength on average is lower when compared to the oxidized samples. For the micro Ni-YSZ, the highest strength is observed for the 5 wt% ALT doping with a strength of 168 MPa. It is well known that in these manufacturing conditions, Al₂O₃ will react with NiO to form NiAl₂O₄ [23,27,28,32]. It has been previously observed that depending on manufacturing and reduction conditions, the material may not be able to compensate for the stress of formation and reduction of NiAl₂O₄ [23,28]. This could explain the decrease in strength at 10 wt% ALT doping for the micro Ni-YSZ batch. It

can be observed that the strength for the undoped and 1 wt% ALT doped micro Ni-YSZ batches is higher than the similar oxidized samples. This will be further discussed below. For the nano Ni-YSZ, the highest strength was also observed for the 5 wt% ALT samples with a strength of 156 MPa. The strength trend for the nano Ni-YSZ sample batches is similar to the micro Ni-YSZ batches.

Table 2: Mechanical properties data for undoped and ALT doped Ni-YSZ anode material

	0 wt% ALT	1 wt% ALT	5 wt% ALT	10 wt% ALT
Micro Ni-YSZ (Reduced 5%H₂-95%N₂)				
Characteristic Strength (MPa)	96	115	168	146
V _{eff} (mm ³)	0.28	0.23	0.27	0.35
Scaled Characteristic Strength (MPa)	82	96	142	127
Strength Increase (%)	N/A	17	73	54
Nano Ni-YSZ (Reduced 5%H₂-95%N₂)				
Characteristic Strength (MPa)	139	143	156	153
V _{eff} (mm ³)	0.52	0.25	0.24	0.55
Scaled Characteristic Strength (MPa)	120	114	127	134
Strength Increase (%)	N/A	-5	6	12

Brittle materials fail with little to no strain and have unpredictable and catastrophic failures. The brittle nature of ceramic materials leads to high scatter in the strength data; therefore, Weibull statistics must be used to analyze mechanical strength. Literature values of Weibull moduli (m) for undoped anode materials falls between 5 and 7 [33]. These are low Weibull modulus values because of the nature of crack propagation through the brittle ceramic. Cracks are initiated at the weakest spot under stress and fracture occurs with no yielding. The Weibull modulus (m) is related to the distribution of flaws within the samples. Higher Weibull moduli are indicative of a homogeneous

flaw population that manifests in low scatter in the fracture data; therefore, a more reliable strength for the material. Low Weibull moduli are characteristic of a non-homogeneous flaw population leading to high scatter in the fracture data and a less reliable material.

Tables 3 and 4 below show the Weibull modulus values calculated for the micro and nano NiO-YSZ in an oxidized (Table 3) and reduced (Table 4) state with the 90% confidence interval calculated according to ASTM C1239-13 [30]. It can be observed that a consistent trend does not exist for the Weibull modulus values. Further explanation for the cause of this will be discussed. Purely from the Weibull modulus, the 10 wt% ALT batch for the micro NiO-YSZ and the 5 wt% ALT batch for the nano NiO-YSZ should be the most reliable because they have the highest Weibull modulus (Table 3). In Table 4, it can be observed that the highest Weibull modulus was calculated for the 1 wt% ALT doping amount for the micro Ni-YSZ and 5 wt% ALT for the nano Ni-YSZ.

Table 3: Weibull modulus and 90% confidence interval for micro and nano NiO-YSZ

	0 wt% ALT	1 wt% ALT	5 wt% ALT	10 wt% ALT
Micro NiO-YSZ				
Weibull Modulus	7.9	5.7	8.8	12.8
90% Confidence Interval	5.9 - 9.6	4.3 - 7.0	6.6 - 10.7	9.6 - 15.6
Nano NiO-YSZ				
Weibull Modulus	4.8	8.8	11.2	7.5
90% Confidence Interval	3.6 - 5.8	6.6 - 10.7	8.4 - 13.6	5.6 - 9.1

Table 4: Weibull modulus and 90% confidence interval for micro and nano Ni-YSZ

	0 wt% ALT	1 wt% ALT	5 wt% ALT	10 wt% ALT
Micro Ni-YSZ (Reduced 5%H₂-95%N₂)				
Weibull Modulus	8.0	8.2	7.8	7.5
90% Confidence Interval	6.0 - 9.8	6.1 - 10.0	5.8 - 9.5	5.6 - 9.1
Nano Ni-YSZ (Reduced 5%H₂-95%N₂)				
Weibull Modulus	4.4	5.7	6.7	4.5
90% Confidence Interval	3.3 - 5.4	4.3 - 7.0	5.0 - 8.2	3.4 - 5.5

Due to the nature of ceramic fracture, the Weibull modulus value does not give the full picture of fracture data. Figure 1 shows the Weibull plots for the micro and nano NiO-YSZ samples. This graph is created by manipulating the Weibull equation (Equation 1) into straight-line form (Equation 2) to determine the Weibull modulus (m) according to ASTM C1239-13 [30]. Figure 1 shows all the data points and corresponding trendlines for each of the batches tested for the oxidized samples. Figure 2 shows the data for the micro and nano Ni-YSZ sample batches after undergoing reduction. Using the Weibull plots, the strength data for each sample can be compared to the Weibull modulus linear trendline. From comparison of the data to the trendline, it can be determined how consistent the strength data is to the Weibull distribution. Data points that line close to the linear trend show a more consistent fracture pattern in accordance to the Weibull distribution.

$$p(s) = e^{-\left(\frac{\sigma}{\sigma_0}\right)^m} \quad (1)$$

$$\ln \left(\ln \left(\frac{1}{p(s)} \right) \right) = m * \ln \left(\frac{\sigma}{\sigma_0} \right) \quad (2)$$

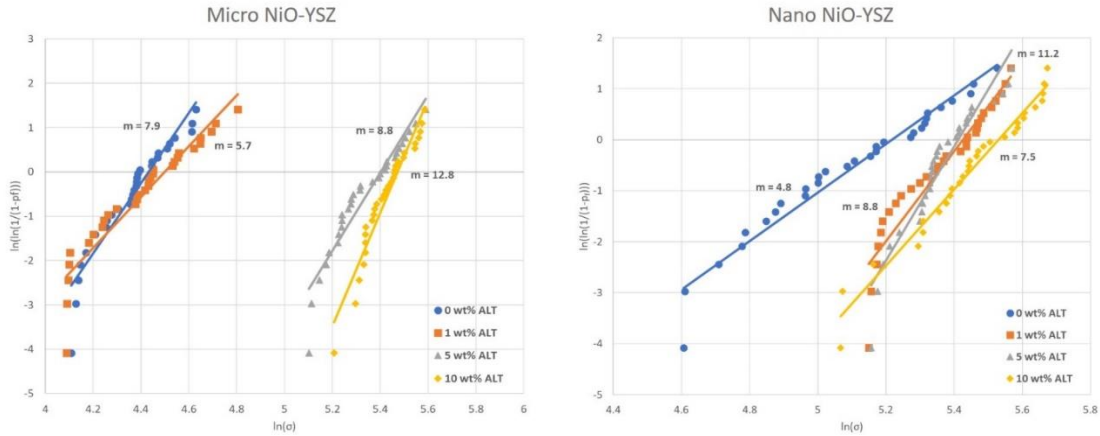


Figure 1: Weibull plots of undoped and ALT doped micro (left) and nano (right) NiO-YSZ samples

For the oxidized samples, the 10 wt% ALT data points for the micro NiO-YSZ samples more closely lie on the corresponding trendline and this is the data set with the highest Weibull modulus. It can be observed that, the data points for the undoped and 1 wt% ALT doped are significantly lower than the 5 and 10 wt% ALT sample batches. This is due to the drastic change in characteristic strength between 1 and 5 wt% ALT doping. For the nano NiO-YSZ samples, the 10 wt% ALT samples tend to more closely fit the trendline, but this data set does not have the highest Weibull modulus. As the 10 wt% ALT sample batch has the highest characteristic strength, the findings from the Weibull plots seem to well align with strength values calculated. It can be observed that the data points for the 1 and 5 wt% ALT doping stray from the linear trendline significantly. This is indicative of multiple fracture populations within the data set. Further investigation is needed to confirm the presence of this. For this study, only one fracture mechanism for each batch is assumed. For both the nano and micro NiO-YSZ sample batches, the

Weibull plots align with the highest characteristic strength at 10 wt% ALT doping. In the oxidized state, 10 wt% ALT doping should allow for the highest reliability for both NiO powder sizes.

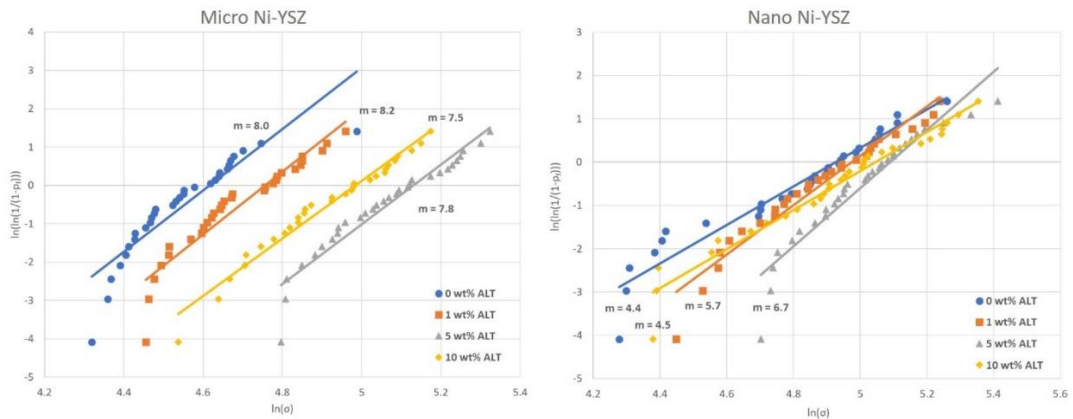


Figure 2: Weibull plots of undoped and ALT doped micro and nano Ni-YSZ samples

Figure 2 shows the Weibull plots for the micro and nano Ni-YSZ sample batches. It can be observed that the data points for the 5 wt% ALT sample batch lie most closely to the trendline for the micro Ni-YSZ batches corresponding to the highest strength sample batch. 5 wt% ALT doping does not correspond with the highest Weibull modulus for the micro Ni-YSZ. This could be due to the deviations of the sample strength data from the linear trendline. As previously discussed, there appears to be evidence for multiple populations within the batches which could give a less accurate measure for the Weibull modulus. Considering the Weibull plots and characteristic strength values, the 5 wt% ALT doping amount for micro Ni-YSZ has the highest reliability. For the nano Ni-YSZ, the 5 wt% ALT sample batch lies most closely to the trendline and corresponds to the highest Weibull modulus and the highest characteristic strength. In the reduced state,

5 wt% ALT doping seems to correspond to the highest reliability for both NiO powder sizes.

As previously discussed, ceramic materials are sensitive to flaws within the material that are created during the manufacturing process. As the strength of a brittle ceramic depends on the weakest flaw in the material under stress, a smaller volume under tension would lead to a higher possibility of meeting a flaw; therefore, a lower strength will be recorded for that sample. Conversely, a larger volume under tension would have a lower likelihood of encountering a flaw leading to a higher recorded strength. To more accurately compare different samples and batches, the data were adjusted taking into account the effective volume (V_{eff}) for each sample (Equation 3). After calculation of the effective volume, the characteristic strength (σ_0) can be scaled to the same volume (Equation 4).

$$V_{eff} = \frac{lwh}{2(m+1)^2} \quad (3)$$

$$\sigma'_0 = \sigma_0 \left(\frac{V_{eff}}{1 \text{ mm}^3} \right)^{\frac{1}{m}} \quad (4)$$

Where l is the distance between support points (m), w and h are the width and height of the sample (m) respectively, m is the Weibull modulus, V_{eff} is the effective volume (mm^3), σ_0 is the characteristic strength (MPa), and σ'_0 is the scaled characteristic strength (MPa).

The scaled characteristic strength for each batch is recorded in Table 1 and 2. It can be observed that the trend of increased strength with ALT addition still holds true. It

can also be observed that the strength for the reduced samples is lower than in the oxidized state on average. For the undoped and 1 wt% ALT doped samples for the micro NiO powder the strength for the oxidized samples is lower than the reduced batches. This decrease in strength could be due to the lower Weibull modulus calculated for these two batches when compared to the 5 and 10 wt% ALT doped samples. A low Weibull modulus is usually indicative of a lower strength sample batch. This could explain the decrease in strength observed for the undoped and 1 wt% ALT doped sample batches.

It is well known that increased porosity in ceramic samples decreases overall strength [19,20,34–36]. During the reduction process, the reaction of NiO with H₂ creates Ni metal and water vapor leaving large pores. This addition of new pores creates more stress concentration sites for crack propagation. Observing the strength values for the nano NiO-YSZ sample batches after reduction, the strength trend for the characteristic strength does not correspond to the same trend for the scaled characteristic strength. The effective volumes calculated for the 1 and 5 wt% ALT doped sample batches are significantly lower than those for the undoped and 10 wt% ALT doped. This could explain why the trend does not hold true when comparing the two. Considering the trend observed for the characteristic strength values, it can be theorized that given similar effective volumes, the scaled characteristic strength would follow the same trend.

Tables 5 and 6 show the porosity measured for each of the batches. It can be observed that for all batches tested, the porosity decreases with increasing amount of ALT. The porosity is high for the undoped samples due to the tape casting manufacturing process. The decreasing trend in porosity from the addition of ALT is consistent with

previous findings where increased ALT leads to the formation of NiAl_2O_4 which has a volume expansion during formation [23]. For the nano NiO-YSZ sample batches, the porosity is much lower with the highest porosity of 16% for the undoped samples. It is thought that this reduced amount of porosity is due to the sintering characteristics of the nano NiO powder and will be further discussed below.

Table 5: Porosity measured for the micro and nano NiO-YSZ sample batches

	0 wt% ALT	1 wt% ALT	5 wt% ALT	10 wt% ALT
Micro NiO-YSZ				
Porosity (%)	34	26	8	6
Nano NiO-YSZ				
Porosity (%)	16	8	6	6

Table 6: Porosity measured for the micro and nano Ni-YSZ sample batches

	0 wt% ALT	1 wt% ALT	5 wt% ALT	10 wt% ALT
Micro Ni-YSZ (Reduced 5%H_2-95%N_2)				
Porosity (%)	45	42	31	23
Nano Ni-YSZ (Reduced 5%H_2-95%N_2)				
Porosity (%)	40	32	30	26

In contrast, for the reduced samples, the porosity is larger when compared to the oxidized samples due to the reduction process. Similar to the oxidized samples, the porosity for the nano NiO sample batches is lower than the corresponding micro NiO powder batches. The higher amount of porosity seen for the reduced samples well aligns with the lower strength observed.

Previous research has found a strength increase with addition of ALT due to the formation of secondary phases that aid in material strengthening [23]. Due to the formation of these phases, the characteristic strength increased when compared to the undoped material. For the nano NiO-YSZ sample batches, the strength of the 5 wt% ALT sample batch is lower than the 1 wt% ALT batch. This could be due to stress distribution within the material due to phase formations during sintering which would result in lower characteristic strength. Along with this, the low effective volume and the high Weibull modulus value will affect the scaled characteristic strength value. These values could explain the lower strength calculated for the 5 wt% ALT doped sample batch.

During sintering, ALT will spontaneously decompose to Al_2O_3 and TiO_2 [23,27,28,32]. Alumina is thought to bond with the nickel (or nickel oxide) to form nickel aluminate (NiAl_2O_4). TiO_2 is thought to go into 8YSZ as a solid solution. If this is true, TiO_2 could cause the stabilization of the tetragonal phase of 8YSZ. The oxidation states and corresponding ionic radii of titanium are $2+$ and $1.00 \cdot \text{\AA}$, $3+$ and $0.81 \cdot \text{\AA}$, and $4+$ and $0.745 \cdot \text{\AA}$. The radius of the zirconium ion in the fluorite structure is $0.86 \cdot \text{\AA}$. [37]. The similarity in the ionic radii suggest that TiO_2 ions could occupy the zirconia crystal structure.

The work of Driscoll et al. suggests that the addition of ALT to 8YSZ destabilizes the cubic phase of 8YSZ [27]. This transition from cubic to tetragonal YSZ would result in greater mechanical strength through stress-transformation toughening [38]. Stress-transformation toughening refers to the stress-induced tetragonal to monoclinic phase

change that tetragonal YSZ exhibits. The associated volume expansion of the crystal structure of this phase change is thought to suppress crack growth, giving tetragonal YSZ its superior mechanical properties when compared to cubic zirconia. This reasoning explains the increased mechanical strength observed with ALT doped NiO-YSZ anodes.

Previous research has also shown a decrease in the reduction kinetics with the addition of ALT due to the formation of NiAl_2O_4 during sintering [28]. The difference in reduction kinetics could lead to changes in the pores that are forming during reduction; therefore, altering the mechanical properties of the material. ALT acts as a sintering aid for 8YSZ [39]. The particle size of the ALT powder added was 25 nm and the YSZ powder was 300 nm. The particle size of the micro and nano NiO powders was about 4 μm and 350 nm, respectively. Mixing particles of different sizes does not always result in the random distribution of those particles. Results concerned with the mixing of different-sized particles indicate size-induced segregation of particles is a common result [40]. ALT in these studies was probably segregated by the mixing process. This segregation probably resulted in regions of higher ALT concentration than other regions. Regions of high ALT concentration would have sintered differently than regions of lower ALT concentration. This difference in sintering could result in the observed decrease in sample uniformity, and therefore, a decreased Weibull modulus as observed for the nano NiO powders in the reduced state.

Maximum packing efficiency of spheres of similar size is about 74%. Random packing of spheres is about 64% efficient. Random packing with spheres that are different in size can lead to greater packing efficiencies because the smaller particles can

tend to fill the large voids created with the packing of the large spheres. This increased initial density can lead to greater sintered density as well as decreased sintered porosity as observed with the nano NiO powders. This is observed with the higher strength calculated for the nano NiO sample batches and the lower porosity observed with the use of nano NiO powder.

Stress moves through material in a gradual way. For both the micro and nano NiO precursor powder, the nickel metal makes up 50% of the material by volume. The mechanical strength of the Ni-YSZ cermet depends on the strength of the nickel. As this material is composed of NiO, YSZ and ALT, stress distributes through this composite material, the YSZ pulls on the nickel metal until either the bond between the nickel and the YSZ fails or the YSZ breaks. Due to the high ductility of metallic nickel, the nickel will tend to deform before fracture. In contrast, the YSZ will fracture at about 0.1% strain with no plastic deformation. It is reasonable to conclude that in a Ni-YSZ cermet made with large NiO precursor powder, more metal is interfacing with metal, and that in a Ni-YSZ cermet made with small NiO precursor powder, there are more Ni-YSZ interfaces. The increase in strength observed for the nano NiO powder could be due to a more homogeneous dispersion of phases within the material. This dispersed network could allow for further strengthening by the stress compensation. Decreased porosity could also result in increased strength consistent to the data found in this study.

Microstructural analyses

Along with Weibull statistical analyses, FE-SEM was conducted on selected samples from each of the 16 batches. Figure 3 shows the surface morphology of the micro and nano NiO-YSZ samples, respectively. It can be observed in Figure 3 that a new phase (circled in Figure 3c) is clearly visible after 5 wt% ALT doping. This secondary phase has been previously described as the “rough phase” [23]. During sintering, it is well known that ALT decomposes into its constituent components of Al_2O_3 and TiO_2 [26,27]. Previous work with Auger analyses found this phase to be a Ti/YSZ rich phase and was previously discussed in regards to mechanical properties [23]. When comparing the surface morphology of the samples manufactured with micro and nano NiO powder it can be observed that the particle size is much larger for the nano NiO samples. This could be due to the sintering characteristics of the small initial particle size making the sintered density higher. This confirms the low porosity measurements for the nano NiO powder batches as discussed earlier.

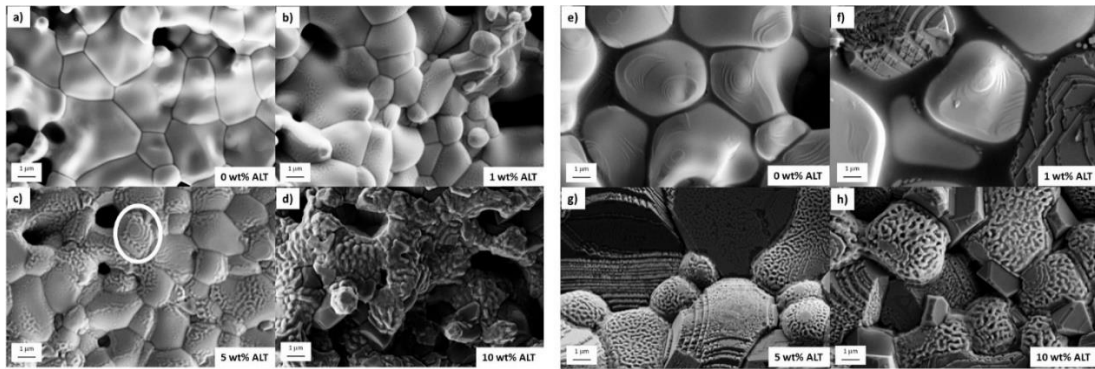


Figure 3: FE-SEM surface morphology of micro (left) and nano (right) NiO-YSZ samples with a,e) 0 wt% ALT, b,f) 1 wt% ALT, c,g) 5 wt% ALT and d,h) 10 wt% ALT

Figure 4 shows the surface morphology of the micro and nano NiO-YSZ sample batches after undergoing reduction. It can be observed in Figure 4 that there is the presence of the rough phase (circled in Figure 4c) but also the addition of what has been termed the “small particle phase” (boxed in Figure 4d) [23]. As with the rough phase, this formation has been characterized with Auger analyses to be consisting of Ni-rich particles atop an Al-rich matrix. This formation occurs upon reduction because it is believed to be formed by the partial reduction of NiAl_2O_4 . It is well known that NiO and Al_2O_3 will react to form NiAl_2O_4 at the sintering temperatures used in this study [26,27,36,41–43]. It is also known that the NiAl_2O_4 is stable and will not begin to reduce until after 10+ hours of reduction in H_2 at 800°C [36,44]. As has been seen in previous work, it is possible that for the 5 wt% ALT sample, there was sufficient thermal energy to begin reduction of the NiAl_2O_4 . There is a larger amount seen for the 10 wt% ALT sample because of the increased reduction time leading to increased thermal energy. When comparing the micro and nano NiO powder batches, it can be observed that, similarly to the oxidize samples, the particle sizes of the undoped and 1 wt% ALT doped samples are much larger for the nano NiO powder than for the micro NiO powder. The pores visible in the images are similar confirming the similarity in porosity measurements for these samples.

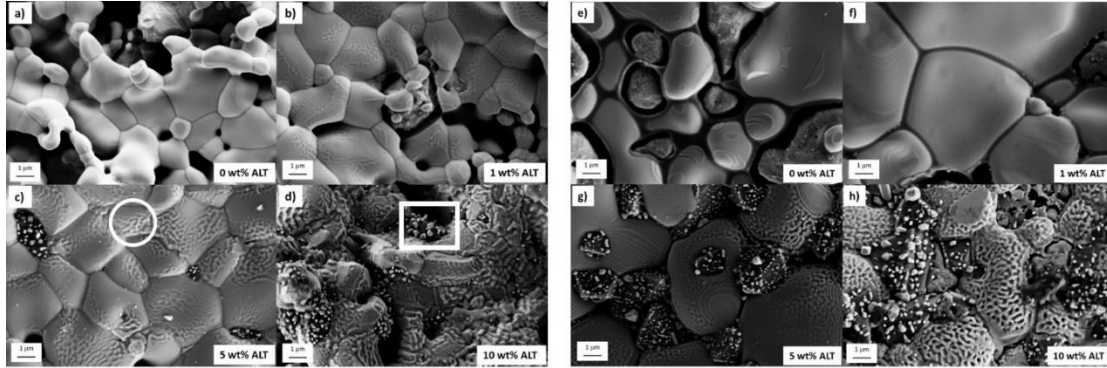


Figure 4: FE-SEM surface morphology of micro (left) and nano (right) Ni-YSZ samples with a,e) 0 wt% ALT, b,f) 1 wt% ALT, c,g) 5 wt% ALT and d,h) 10 wt% ALT

Figure 5 shows the fracture surfaces of the micro and nano NiO-YSZ sample batches. It can be observed that transgranular fracture is the predominant mode of fracture due to the sharp planes visible in the cross section. Transgranular fracture is indicative of a high energy fracture path confirming the high strength values observed and discussed earlier. The micro NiO sample batches with 0 and 1 wt% ALT (Figure 5a and b) show a slightly mixed mode of fracture with indications of intergranular fracture. Evidence of intergranular fracture confirms the lower mechanical strength values observed.

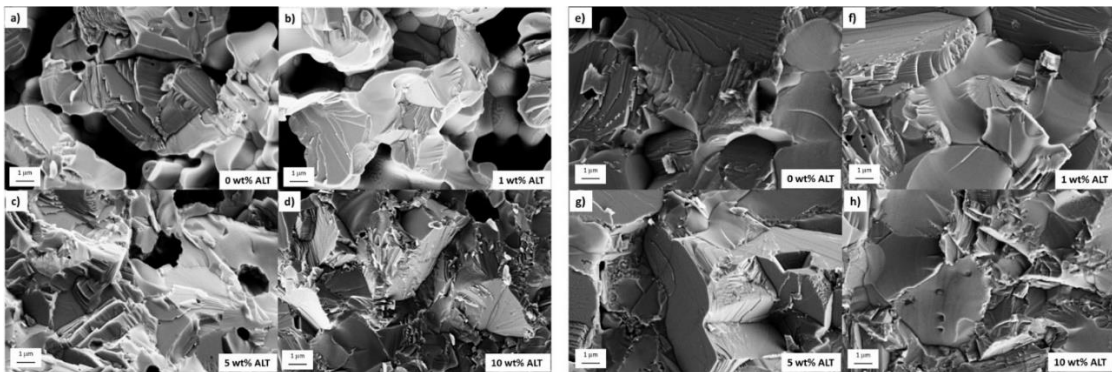


Figure 5: FE-SEM fracture surface morphology of micro (left) and nano (right) NiO-YSZ samples with a,e) 0 wt% ALT, b,f) 1 wt% ALT, c,g) 5 wt% ALT and d,h) 10 wt% ALT

Figure 6 shows the fracture surface morphology of the micro and nano NiO-YSZ sample batches after undergoing reduction. Porosity is evident in the cross sections due to the reduction process. It can be observed that, similarly to the oxidized samples, the fracture surface is mostly transgranular in nature. For the undoped and 1 wt% ALT doped samples for the micro NiO powder (Figure 6a and b), it can be observed that there is little evidence of transgranular fracture but predominantly intergranular fracture. This is consistent with previously found results and is confirmed by the low strength values calculated for these sample batches. When compared to the same doping levels for the nano NiO powder (Figure 6e and f), it is visible that the fracture mode was transgranular in nature indicating a stronger material.

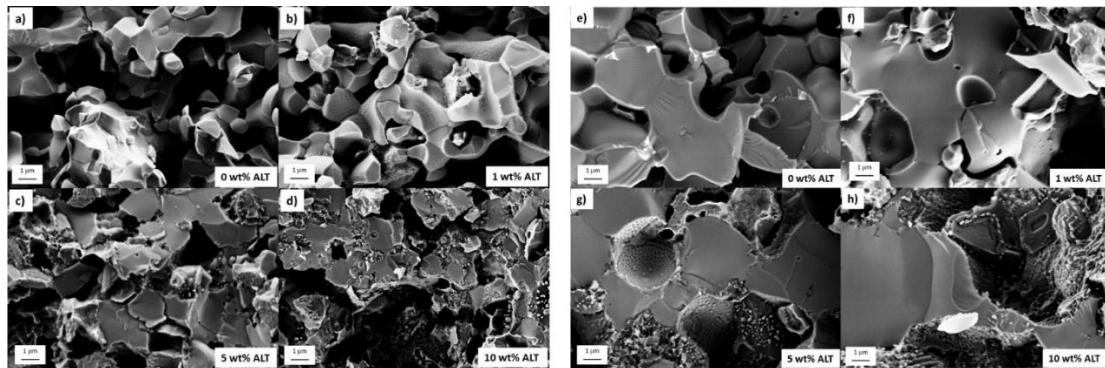


Figure 6: FE-SEM fracture surface morphology of micro (left) and nano (right) Ni-YSZ samples with a,e) 0 wt% ALT, b,f) 1 wt% ALT, c,g) 5 wt% ALT and d,h) 10 wt% ALT

It can be observed in Figure 6c, d, g and h that the transgranular fracture planes appear to be through the rough phase. Auger results suggest greater concentrations of Ti on the rough phase [23]. If these surfaces are transgranular surfaces, and if those surfaces are rich in Ti, then these results suggest segregation of Ti to the grain boundaries, that fracture of NiO-YSZ and Ni-YSZ occurs through these grains, and that the addition of

ALT to NiO-YSZ creates a grain-boundary with a higher concentration of the tetragonal phase of YSZ than the grain interior. Due to the high stiffness of YSZ and low strain before fracture, it is probable that the Ti/YSZ phase holds the strength of the material.

Comparing the fracture surfaces for the micro and nano Ni-YSZ sample batches (Figure 6), it can be observed that the transgranular fracture planes for the nano Ni-YSZ batches are larger when compared to the micro Ni-YSZ batches. This increase in transgranular planes corresponds with increase in mechanical strength observed for the nano Ni-YSZ sample batches.

Conclusions

Results suggest ALT addition to NiO-YSZ anodes increases the mechanical strength of the material for both the micro and nano NiO powder sizes. Strength of the nano NiO powder was found to be on average higher than the micro NiO powder. This increase in strength could be due to higher density and decreased porosity formed during sintering and subsequent reduction. Along with this, the grains formed in the nano NiO powder are much larger when compared to the micro NiO powder. This could lead to increases in the size of the secondary phases forming leading to higher strength. In this work, it is suggested that this strength increase is due to the formation of NiAl_2O_4 in the nickel metal and that the fracture that occurs in Ni-YSZ anodes occurs through the Ti/YSZ phase. TiO_2 enriches the grain boundaries of the YSZ in the Ni-YSZ, stabilizing the tetragonal phase in the region of the structure where fracture is most likely to occur. Overall, the use of nano NiO powder could increase mechanical strength of the anode material with ALT addition.

Acknowledgements

This work was supported by the DOE under award no. DEFE0026192. FE-SEM data were collected at the MSU Image and Chemical Analysis Laboratory.

References

- [1] F. Zhao, A. V. Virkar, Dependence of polarization in anode-supported solid oxide fuel cells on various cell parameters, *J. Power Sources*. 141 (2005) 79–95. doi:10.1016/j.jpowsour.2004.08.057.
- [2] A.C. Müller, D. Herbstritt, E. Ivers-Tiffée, Development of a multilayer anode for solid oxide fuel cells, *Solid State Ionics*. 152–153 (2002) 537–542. doi:10.1016/S0167-2738(02)00357-0.
- [3] Z.R. Wang, J.Q. Qian, S.R. Wang, J.D. Cao, T.L. Wen, Improvement of anode-supported solid oxide fuel cells, *Solid State Ionics*. 179 (2008) 1593–1596. doi:10.1016/j.ssi.2008.03.022.
- [4] T. Setoguchi, K. Okamoto, K. Eguchi, H. Arai, Effects of anode material and fuel on anodic reaction of solid oxide fuel cells, *J. Electrochem. Soc.* 139 (1992) 2875–2880. doi:10.1149/1.2068998.
- [5] M. Kleitz, F. Petitbon, Optimized SOFC electrode microstructure, *Solid State Ionics*. 92 (1996) 65–74. doi:10.1016/S0167-2738(96)00464-X.
- [6] C.R. He, W.G. Wang, Alumina Doped Ni/YSZ Anode Materials for Solid Oxide Fuel Cells, *Fuel Cells*. 9 (2009) 630–635. doi:10.1002/fuce.200800152.
- [7] M. Mori, Y. Hiei, H. Itoh, G.A. Tompsett, N.M. Sammes, Evaluation of Ni and Ti-doped Y₂O₃ stabilized ZrO₂ cermet as an anode in high-temperature solid oxide fuel cells, *Solid State Ionics*. 160 (2003) 1–14. doi:10.1016/S0167-2738(03)00144-9.
- [8] T. Dey, D. Singdeo, M. Bose, R.N. Basu, P.C. Ghosh, Study of contact resistance at the electrode-interconnect interfaces in planar type Solid Oxide Fuel Cells, *J. Power Sources*. 233 (2013) 290–298. doi:10.1016/j.jpowsour.2013.01.111.
- [9] T. Dey, A. Dey, P.C. Ghosh, M. Bose, A.K. Mukhopadhyay, R.N. Basu, Influence of microstructure on nano-mechanical properties of single planar solid oxide fuel cell in pre- and post-reduced conditions, *Mater. Des.* 53 (2014) 182–191. doi:10.1016/j.matdes.2013.06.052.
- [10] M. Pihlatie, A. Kaiser, M. Mogensen, Mechanical properties of NiO/Ni–YSZ composites depending on temperature, porosity and redox cycling, *J. Eur. Ceram. Soc.* 29 (2009) 1657–1664. doi:10.1016/j.jeurceramsoc.2008.10.017.
- [11] N. Mahato, A. Banerjee, A. Gupta, S. Omar, K. Balani, Progress in material selection for solid oxide fuel cell technology: A review, *Prog. Mater. Sci.* 72 (2015) 141–337. doi:10.1016/j.pmatsci.2015.01.001.
- [12] J. Wei, G. Pećanac, J. Malzbender, Review of mechanical characterization methods for ceramics used in energy technologies, *Ceram. Int.* 40 (2014) 15371–15380. doi:10.1016/j.ceramint.2014.07.089.

- [13] G. Pećanac, S. Baumann, J. Malzbender, Mechanical properties and lifetime predictions for Ba_{0.5}Sr_{0.5}Co_{0.8}Fe_{0.2}O_{3-δ} membrane material, *J. Memb. Sci.* 385–386 (2011) 263–268. doi:10.1016/j.memsci.2011.10.005.
- [14] G. Pećanac, L. Kiesel, R. Kriegel, J. Malzbender, Comparison of thermo-mechanical characteristics of non-doped and 3 mol% B-site Zr-doped Ba_{0.5}Sr_{0.5}Co_{0.8}Fe_{0.2}O_{3-??}, *Ceram. Int.* 40 (2014) 1843–1850. doi:10.1016/j.ceramint.2013.07.086.
- [15] A. Atkinson, A. Selçuk, Mechanical behaviour of ceramic oxygen ion-conducting membranes, *Solid State Ionics.* 134 (2000) 59–66. doi:10.1016/S0167-2738(00)00714-1.
- [16] M. Lipińska-Chwałek, L. Kiesel, J. Malzbender, Mechanical properties of porous MgO substrates for membrane applications, *J. Eur. Ceram. Soc.* 34 (2014) 2519–2524. doi:10.1016/j.jeurceramsoc.2014.03.009.
- [17] B.X. Huang, V. Vasechko, Q.L. Ma, J. Malzbender, Thermo-mechanical properties of (Sr,Y)TiO₃ as anode material for solid oxide fuel cells, *J. Power Sources.* 206 (2012) 204–209. doi:10.1016/j.jpowsour.2012.01.137.
- [18] S. Giraud, J. Canel, Young's modulus of some SOFCs materials as a function of temperature, *J. Eur. Ceram. Soc.* 28 (2008) 77–83. doi:10.1016/j.jeurceramsoc.2007.05.009.
- [19] M. Radovic, E. Lara-curzio, Elastic Properties of Nickel-Based Anodes for Solid Oxide Fuel Cells as a Function of the Fraction of Reduced NiO, *J. Am. Ceram. Soc.* 87 (2004) 2242–2247. doi:10.1111/j.1151-2916.2004.tb07499.x.
- [20] M. Radovic, E. Lara-Curzio, Mechanical properties of tape cast nickel-based anode materials for solid oxide fuel cells before and after reduction in hydrogen, *Acta Mater.* 52 (2004) 5747–5756. doi:10.1016/j.actamat.2004.08.023.
- [21] Y. Ye, J. Li, H. Zhou, J. Chen, Microstructure and mechanical properties of yttria-stabilized ZrO₂/Al₂O₃ nanocomposite ceramics, *Ceram. Int.* 34 (2008) 1797–1803. doi:10.1016/j.ceramint.2007.06.005.
- [22] R. Kubrin, G. Blugan, J. Kuebler, Influence of cerium doping on mechanical properties of tetragonal scandium-stabilized zirconia, *J. Eur. Ceram. Soc.* 37 (2017) 1651–1656. doi:10.1016/j.jeurceramsoc.2016.11.038.
- [23] M. McCleary, R. Amendola, Effect of Aluminum Titanate (Al₂TiO₅) Doping on the Mechanical Performance of Solid Oxide Fuel Cell Ni-YSZ Anode, *Fuel Cells.* (2017) 862–868. doi:10.1002/face.201700073.
- [24] M. Nagano, S. Nagashima, H. Maeda, A. Kato, Sintering behavior of Al₂TiO₅ base ceramics and their thermal properties, *Ceram. Int.* 25 (1999) 681–687. doi:10.1016/S0272-8842(98)00083-2.

- [25] S.W. Sofie, D.R. Taylor, Controlled Thermal Expansion Anode Compositions with Improved Strength for Use in Anode Supported SOFCs, *Adv. Solid Oxide Fuel Cells III*. (2008) 215–223.
- [26] C.H. Law, S.W. Sofie, Anchoring of Infiltrated Nickel Electro-Catalyst by Addition of Aluminum Titanate, *J. Electrochem. Soc.* 158 (2011) B1137–B1141. doi:10.1149/1.3610226.
- [27] D.R. Driscoll, M.D. McIntyre, M.M. Welander, S.W. Sofie, R.A. Walker, Enhancement of high temperature metallic catalysts: Aluminum titanate in the nickel-zirconia system, *Appl. Catal. A Gen.* 527 (2016) 36–44. doi:10.1016/j.apcata.2016.08.020.
- [28] M. McCleary, R. Amendola, Reduction kinetics of undoped and aluminum titanate (Al₂TiO₅) doped NiO-YSZ solid oxide fuel cell anodes, *Ceram. Int.* 44 (2018) 15557–15564. doi:10.1016/j.ceramint.2018.05.218.
- [29] ASTM C1161-18, Standard Test Method for Flexural Strength of Advanced Ceramics at Ambient Temperature, *ASTM Int.* (2018) 1–19. doi:10.1017/CBO9781107415324.004.
- [30] ASTM C1239-13, Standard Practice for Reporting Uniaxial Strength Data and Estimating Weibull Distribution Parameters for Advanced Ceramics, *ASTM Int.* (2013) 1–9. doi:10.1520/C1239-13.Scope.
- [31] A. Nakajo, J. Kuebler, A. Faes, U.F. Vogt, H.J. Schindler, L.K. Chiang, S. Modena, J. Van Herle, T. Hocker, Compilation of mechanical properties for the structural analysis of solid oxide fuel cell stacks. Constitutive materials of anode-supported cells, *Ceram. Int.* 38 (2012) 3907–3927. doi:10.1016/j.ceramint.2012.01.043.
- [32] D. Driscoll, C. Hunt, J. Muretta, S.W. Sofie, Thermally Stabilized Nickel Electro-Catalyst Introduced by Infiltration for High Temperature Electrochemical Energy Conversion, *ECS Trans.* 53 (2013) 63–72. doi:10.1149/05309.0063ecst.
- [33] J. Laurencin, G. Delette, F. Lefebvre-Joud, M. Dupeux, A numerical tool to estimate SOFC mechanical degradation: Case of the planar cell configuration, *J. Eur. Ceram. Soc.* 28 (2008) 1857–1869. doi:10.1016/j.jeurceramsoc.2007.12.025.
- [34] Z. Cui, Y. Huang, H. Liu, Predicting the mechanical properties of brittle porous materials with various porosity and pore sizes, *J. Mech. Behav. Biomed. Mater.* 71 (2017) 10–22. doi:10.1016/j.jmbbm.2017.02.014.
- [35] H.L. Frandsen, T. Ramos, A. Faes, M. Pihlatie, K. Brodersen, Optimization of the strength of SOFC anode supports, *J. Eur. Ceram. Soc.* (2012). doi:10.1016/j.jeurceramsoc.2011.11.015.
- [36] B. Charlas, D.W. Ni, H.L. Frandsen, K. Brodersen, M. Chen, Mechanical Properties of Supports and Half-Cells for Solid Oxide Electrolysis Influenced by

- Alumina-Zirconia Composites, *Fuel Cells*. 17 (2017) 132–143. doi:10.1002/fuce.201600036.
- [37] R.. Shannon, C.. Prewitt, Effective Ionic Radii in Oxides and Fluorides, *Acta Cryst.* (1969) 925. doi:10.1016/0022-1902(70)80629-7.
- [38] R.H.J. Hannink, P.M. Kelly, B.C. Muddle, Transformation Toughening in Zirconia-Containing Ceramics, *J. Am. Ceram. Soc.* 83 (2000) 461–487. doi:10.1111/j.1151-2916.2000.tb01221.x.
- [39] D.R. Driscoll, B.W. Tokmakian, N.P. Johnson, C.D. Hunt, S.W. Sofie, Catalyst enhancing aluminum titanate for increasing strength of nickel-zirconia cermets, *Mater. Lett.* 209 (2017) 307–310. doi:10.1016/j.matlet.2017.08.035.
- [40] J.M. Ottino, D. V Khakhar, Mixing and Segregation of Granular Materials, *Annu. Mech.* 32 (2000) 55–91.
- [41] J.E. Readman, A. Olafsen, J.B. Smith, R. Blom, Chemical Looping Combustion Using NiO/NiAl₂O₄: Mechanisms and Kinetics of Reduction–Oxidation (Red-Ox) Reactions from In Situ Powder X-ray Diffraction and Thermogravimetry Experiments, *Energy & Fuels*. 20 (2006) 1382–1387. doi:10.1021/ef0504319.
- [42] M. Sokić, Ž. Kamberović, V. Nikolić, B. Marković, M. Korać, Z. Anić, M. Gavrilovski, Kinetics of NiO and NiCl₂ hydrogen reduction as precursors and properties of produced Ni/Al₂O₃ and Ni-Pd/Al₂O₃ catalysts, *Sci. World J.* 2015 (2015). doi:10.1155/2015/601970.
- [43] J. Zygmuntowicz, P. Wieceńska, A. Miazga, K. Konopka, Characterization of composites containing NiAl₂O₄ spinel phase from Al₂O₃/NiO and Al₂O₃/Ni systems, *J. Therm. Anal. Calorim.* 125 (2016) 1079–1086. doi:10.1007/s10973-016-5357-2.
- [44] H. Orui, R. Chiba, K. Nozawa, H. Arai, R. Kanno, High-temperature stability of alumina containing nickel–zirconia cermets for solid oxide fuel cell anodes, *J. Power Sources*. 238 (2013) 74–80. doi:10.1016/j.jpowsour.2013.03.056.

APPENDIX B: Effect of Hydrogen Concentration on the Mechanical Properties of Reduced Aluminum Titanate (Al_2TiO_5) Doped Ni-YSZ Solid Oxide Fuel Cell Anodes

What follows is a draft of a manuscript for publication. Please note that changes will be made before publication.

Effect of Hydrogen Concentration on the Mechanical Properties of Reduced Aluminum Titanate (Al_2TiO_5) Doped Ni-YSZ Solid Oxide Fuel Cell Anodes

Madisen McCleary, Roberta Amendola*

Montana State University, Mechanical & Industrial Engineering Department, 220

Roberts Hall Bozeman, MT 59718

*corresponding author: Roberta.amendola@montana.edu, 406-994-6296

Abstract:

Mechanical properties testing was performed on samples of Ni-YSZ anodes with 0-10 wt% ALT. Samples were reduced with either 5% H_2 – 95% N_2 or 100% H_2 . Mechanical strength results showed that ALT doping increased strength for both reduction conditions. It was found that the samples reduced in 100% H_2 had significantly lower strength when compared to those reduced in 5% H_2 – 95% N_2 . Weibull modulus values for the samples reduced in 100% H_2 were also lower than those reduced in 5% H_2 – 95% N_2 . Microstructural analyses showed the formation of two secondary phases: the partial reduction of NiAl_2O_4 and the Ti/YSZ framework. The reduction of NiAl_2O_4 is

faster for those samples reduced in 100% H₂ which leads to volume shrinkage and mechanical stress that lead to the low strength observed for these samples.

Introduction:

A solid oxide fuel cell (SOFC) is a renewable energy system where solid components electrochemically oxidize a fuel (mainly hydrogen or hydrocarbons) to produce electrical power and heat. In recent years, focus has shifted to investigation of materials choice for the SOFC components to increase power output and longevity of the SOFC. For SOFCs to be a viable option, materials must have a high power output to cost ratio and be easy to manufacture. Anode supported SOFCs have been given attention due to their ability to be operated at lower temperatures [1–7].

Due to the power limitations of a single SOFC, individual cells must be stacked in electrical series to produce sufficient amounts of electricity. To maximize the contact between cells, the SOFC stack is clamped with high pressures around 65 – 70 kPa [8,9]. For an anode supported geometry, the anode carries the mechanical load and provides the strength for the cell. Much data is available on the electrochemical properties of SOFCs, but little fundamental data exists on the thermo-mechanical properties. Due to the brittle nature of the ceramic materials in the SOFC, the reliability and robustness of the SOFC depends on the mechanical properties. These include the mechanical strength, the coefficient of thermal expansion, the elastic behavior and the fracture characteristics, among others. Brittle material failure is catastrophic and unpredictable and mechanical failure of the components could lead to lose of power from the cell. Therefore, it is

fundamental to study the mechanical properties of these ion conducting materials before use in SOFC stacks.

Ni-YSZ cermets are the most common anode materials due to the low cost to power ratio [10,11]. There is still much research into new material alternatives that are promising [12–20], but these compositions require more in-depth investigations before implementation into the SOFC stack. Mechanical properties of ceramic materials are extremely sensitive to changes in their composition and manufacturing process. Researchers have found that the addition of secondary phases can both improve the electrochemical performance along with mechanical strength due to the formation of new microstructures [5,6,21,22]. For ease of manufacturing, anode components are typically manufactured using a tape casting procedure with mechanical mixing of the powder into an aqueous slurry. Using this method, secondary phases can easily be added during the mixing process which would not involve extra manufacturing steps.

Previous research has shown that the addition of aluminum titanate (Al_2TiO_5 , ALT) or its constituents increases the mechanical strength of the Ni-YSZ anode by the formation of secondary phases [5,6,21,23–32]. Research has also observed that the addition of ALT stabilizes the anode and allows for slower degradation rates and increased power output. Previous research into ALT doping has shown large increases in the mechanical strength with doping levels up to 10 wt% ALT. The strength increase observed is due to the formation of two main secondary phases within the anode during sintering and subsequent reduction. It is well known that ALT at sintering temperatures will decompose to its constituents of Al_2O_3 and TiO_2 [33–37]. Al_2O_3 will react with NiO

to form NiAl_2O_4 [5,34,38–40] and TiO_2 will react with YSZ to destabilize the YSZ cubic crystal structure [24,25]. During reduction, the NiAl_2O_4 phase will go through partial reduction at high doping levels of ALT. NiAl_2O_4 has slow reaction kinetics and takes over 600 hours to fully reduce at 800°C [39,41]. It has been previously observed that reduction time increases with ALT doping [42]. Increased reduction time is detrimental to SOFC performance as the SOFC cannot produce full power until the anode is reduced. Studies were previously conducted on the reduction kinetics between anodes reduced in 5% H_2 – 95% N_2 versus 100% H_2 . It was found that the reduction time was significantly quicker with 100% H_2 . Knowing this, it would be preferable to use higher concentrations of hydrogen for electrochemical performance. This study aims to investigate the effects of hydrogen concentration on the mechanical performance of the ALT doped Ni-YSZ anode material to elucidate the effects of concentration on the microstructure and secondary phase formation within the anode.

Methods:

Nickel oxide (NiO) powder (4 μm , Alfa Aesar), 8 mol.% yttria stabilized zirconia (8YSZ) powder (300 nm, Tosoh) and aluminum titanate (Al_2TiO_5 , ALT) powder (25 nm, Sigma Aldrich) were used for sample manufacturing. Powders, in the ratio of 34 wt.% YSZ, 66 wt.% NiO and 0–10 wt.% ALT, were mechanically mixed for 24 hours with binder and deionized water. After mixing, the slurry was tape cast with a doctor blade thickness of 2 mm and allowed to dry.

Rectangular 6 mm x 40 mm samples were cut from the green tape using a rotary cutter. Thermolysis and partial sintering of the samples was performed using the following process: 1) ramp to 150°C at 2°C/min, 2) dwell for 2 hours, 3) ramp to 450°C at 0.5°C/min, 4) ramp to 1,100°C at 5°C/min, 5) dwell for 2 hours, 6) ramp to room temperature at 10°C/min in a box furnace (Thermolyne, 1300). Sintering was conducted with a heating/cooling rate of 5°C/min up to 1,500°C and a dwell time of 2 hours (Zircar, Hot Spot 110).

Reduction was performed in a tube furnace (Thermo Scientific, Lindberg Blue M) flowing either 5% H₂ - 95% N₂ gas or 100% H₂ gas at 800°C for a time sufficient to convert 97 wt.% of NiO into metallic nickel. The percentage reduction was evaluated with a Radwag XA 82/220.R2 microscale. Time required for the reduction process varied proportionally to the doping amount of ALT and concentration of hydrogen.

Un-doped and 1, 5 and 10 wt.% ALT doped batches of 30 samples reduced in either 5% H₂ – 95% N₂ or 100% H₂ were loaded at a rate of 0.2 mm/min in a three-point bending apparatus (Pasco Scientific 8236) as per ASTM C1161-13 standard [43]. Fracture strength, effective volume V_{eff} , scaled characteristic strength σ'_0 , Weibull modulus (m) with normalized upper and lower bounds, and porosity, by alcohol immersion method, were evaluated. Weibull statistics were conducted according to ASTM C1239-13 [44]. Fractographic analyses were performed using a Field emission scanning electron microscope (FE-SEM, Zeiss Ultra) on select samples.

Results and Discussion:

Mechanical Properties:

Table 1 summarizes the mechanical properties results for all the tested batches. It can be observed that the characteristic strength increases with ALT doping for both 5% H₂ – 95% N₂ and 100% H₂. The characteristic strength is calculated according to ASTM C1239-13 and is the value of the strength at a probability of survival of 1/e [44]. When comparing the data for the characteristic strength, it can be observed that the strength for the samples reduced in 100% H₂ was significantly lower for every doping level. The highest strength for the samples reduced in 5% H₂ – 95% N₂ was calculated for the 5 wt% ALT doped batch. For the samples reduced in 100% H₂, the highest strength was calculated for the batch with 10 wt% ALT doping. Discussion of the effective volume (V_{eff}) and the scaled characteristic strength can be found below.

Table 1: Mechanical properties of Ni-YSZ anodes doped with ALT reduced in 5% H₂-95% N₂ and 100% H₂

	0 wt% ALT	1 wt% ALT	5 wt% ALT	10 wt% ALT
Green Ni-YSZ-Reduced 5%H₂-95%N₂				
Characteristic Strength (MPa)	96	103	168	146
V_{eff} (mm ³)	0.28	0.32	0.27	0.35
Scaled Characteristic Strength (MPa)	82	87	142	127
Strength Increase (%)	N/A	6	73	54
Green Ni-YSZ-Reduced 100%H₂				
Characteristic Strength (MPa)	36	45	83	132
V_{eff} (mm ³)	0.87	1.35	1.28	0.41
Scaled Characteristic Strength (MPa)	35	50	91	113
Strength Increase (%)	N/A	42	160	223

Due to the nature of ceramic fracture, Weibull statistics must be employed to determine the mechanical properties of the material. The Weibull distribution assumes that the weakest flaw under tension determines the strength of the material. Due to the random distribution of flaws within each sample, the strength values among one batch of samples varies significantly. Figure 1 shows Weibull plots for the sample batches reduced in 5% H₂ – 95% N₂ (Figure 1a) and 100% H₂ (Figure 1b). The Weibull plots are used to determine the reliability of the sample batch to the Weibull distribution. The plot is created by conversion of the Weibull distribution (Equation 1) to the linear form (Equation 2).

$$p_s = \exp\left(-\frac{\sigma}{\sigma_0}\right)^m \quad (1)$$

$$\ln(\ln(1/p_s)) = m \ln(\sigma/\sigma_0) \quad (2)$$

Where p_s is the probability of survival for each sample, σ is the flexural strength of each sample (MPa), σ_0 is the characteristic strength (MPa), and m is the Weibull modulus.

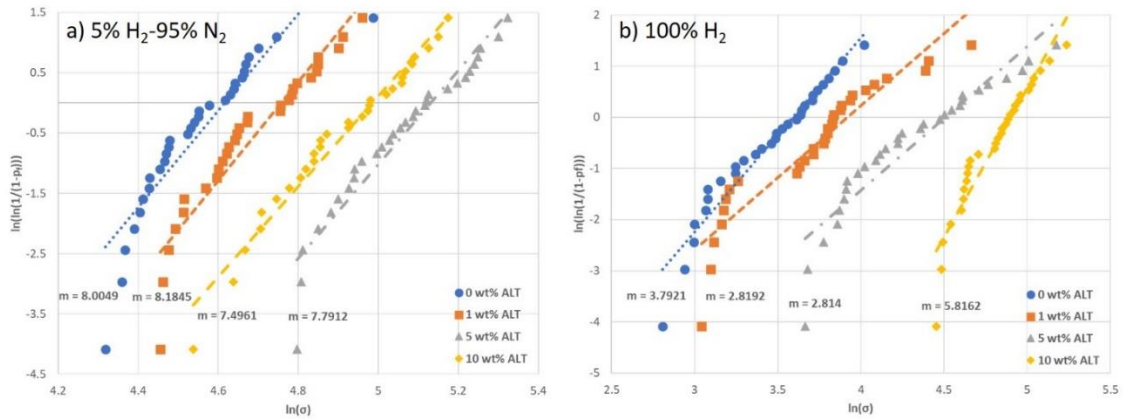


Figure 1: Weibull plots for Ni-YSZ anodes doped with ALT reduced in a) 5% H₂ - 95% N₂ and b) 100% H₂

If the sample batch well follows the Weibull distribution, then the data points should lie close to the linear trendline which corresponds to the Weibull modulus. It can be observed that for the samples reduced in 5% H₂ – 95% N₂ the data points lie closest to the trendline for the 5 wt% ALT doped anodes which exhibited the highest mechanical strength. Typically, the sample batches that follow the trendline closest are those that have the highest Weibull modulus. It can be observed that this is not the case for the 5% H₂ – 95% N₂ sample batches but it corresponds to the highest strength for the sample batches. For the 100% H₂ sample batches, the data points lie closest to the linear trendline for the 10 wt% ALT sample batch and this corresponds to the highest strength and Weibull modulus.

The Weibull modulus indicates the nature, severity and dispersion of flaws and is used for statistical comparison of the relative quality of two or more test data sets to predict the probability of failure [9,45,46]. A high Weibull modulus is desirable for all materials since it indicates an increased homogeneity in the flaw population and a more

predictable failure. On the contrary, a low Weibull modulus is indicative of a large spread within the group and a less predictable failure behavior. Table 2 shows the calculated Weibull modulus values. The normalized upper and lower bounds on the maximum likelihood estimate of the Weibull modulus (90% confidence interval) have been determined per ASTM C1239 – 13 for batches of 30 samples [47–49]. Comparing the two reduction conditions shows that the samples reduced in pure hydrogen have lower Weibull modulus values indicating a nonhomogeneous dispersion of flaws in the material. This would indicate a less reliable fracture strength. In comparison, the Weibull modulus values for the sample batches reduced in 5% H₂ – 95% N₂ are significantly higher and above the range for typical advanced ceramics of 5-7 [50].

Table 2: Weibull modulus and 90% confidence interval of Ni-YSZ anodes doped with ALT reduced in 5% H₂ - 95% N₂ and 100% H₂

	0 wt% ALT	1 wt% ALT	5 wt% ALT	10 wt% ALT
Green Ni-YSZ-Reduced 5%H₂-95%N₂				
Weibull Modulus	8.0	6.6	7.8	7.5
90% Confidence Interval	6.0 - 9.8	4.9 - 8.0	5.8 - 9.5	5.6 - 9.1
Green Ni-YSZ-Reduced 100%H₂				
Weibull Modulus	3.8	2.8	2.8	5.8
90% Confidence Interval	2.8 - 4.6	2.1 - 3.4	2.1 - 3.4	4.4 - 7.1

When using the Weibull distribution for determination of mechanical strength of brittle materials, it is assumed that the weakest flaw under tension determines the strength of the material. As each sample has different physical dimensions, the volume that is under tension is varied. If the volume under tension is larger than there is a higher probability of encountering a flaw which would lead to an apparently lower strength.

Conversely, a smaller volume under tension would have a lower likelihood of encountering a flaw and this would give an apparently high strength. Due to this variation from sample to sample, the volume under tension must be accounted for, for accurate comparison of the sample batches. The effective volume is used to calculate the stressed volume in each sample and can be found in Equation 3 [39,46,51–53]. After calculation of the effective volume, the characteristic strength for each batch can be calculated considering the average effective volume for the batch. All batches were scaled to the same effective volume of 1 mm³.

$$V_{eff} = \frac{lwh}{2(m+1)^2} \quad (3)$$

$$\sigma'_0 = \sigma_0 \left(\frac{V_{eff}}{1 \text{ mm}^3} \right)^{\frac{1}{m}} \quad (4)$$

For Equation 3 and 4, l is the length between support points (mm), w is the width of the sample (mm), h is the height of the sample (mm), m is the Weibull modulus, V_{eff} is the effective volume (mm³), σ_0 is the characteristic strength (MPa) and σ'_0 is the scaled characteristic strength (MPa).

It can be observed in Table 1 that the scaled characteristic strength for each reduction condition the same trends appear where the addition of ALT increases the overall strength of the material. The samples reduced in pure hydrogen have a significantly lower strength than similar samples reduced in 5% H₂ - 95% N₂. Further discussion of the differences in strength and Weibull modulus will be discussed below.

Table 3 shows the porosity measurements for the samples reduced with 5% H₂ – 95% N₂ and 100% H₂. It can be observed that the porosity measured for the samples reduced in 100% H₂ was higher than those reduced in 5% H₂ – 95% N₂. The largest difference in porosity can be observed for the 10 wt% ALT doped sample batch. It is known that porosity can have a large influence on the fracture strength of ceramic materials; so, it would seem that the fracture strengths should be close for the undoped sample batches and have a much larger spread for the 10 wt% ALT batches. This is not the case as there is a large difference in strength for the undoped sample batches but almost the same porosity. Therefore, open porosity must not be the only fracture for determining the fracture strength of these materials.

Table 3: Porosity of Ni-YSZ anodes doped with ALT reduced in 5% H₂-95% N₂ and 100% H₂

	0 wt% ALT	1 wt% ALT	5 wt% ALT	10 wt% ALT
Green Ni-YSZ-Reduced 5%H₂-95%N₂				
Porosity (%)	46	43	30	23
Green Ni-YSZ-Reduced 100%H₂				
Porosity (%)	47	48	33	31

Microstructural Analyses:

Field Emission Scanning Electron Microscopy (FE-SEM) was performed on samples' surface and cross sections. Figure 2 shows the surface microstructure of the Ni-YSZ samples with 0, 1, 5, and 10 wt% ALT reduced in 5% H₂ – 95% N₂. Figure 3 shows the microstructure of the samples reduced in 100% H₂. It can be observed that there is the formation of two new phases with the addition of ALT. The rough phase (circled in Figure 2c) has been previously identified as a phase of YSZ and TiO₂ [6,25]. The rough

phase appears in both microstructures at similar quantities for both reduction conditions. The rough phase is not visible for the 1 wt% ALT samples reduced in 100% H₂. This could be due to the low doping level not achieving uniform distribution of the phases across the surface. The small particle phase (squared in both Figure 2d and Figure 3c) has been previously identified as the partial reduction of NiAl₂O₄ into Ni-nanoparticles on a matrix of Al₂O₃ [25,54,55]. It can be observed that the small particle phase has a different structure depending on the reduction conditions. For the samples reduced in 5% H₂ – 95% N₂, the small particles are rather large and spread out when compared to the samples reduced in pure hydrogen where there is an abundance of very small particles in a tight cluster. The difference in phase structure could explain the differences in mechanical strength observed.

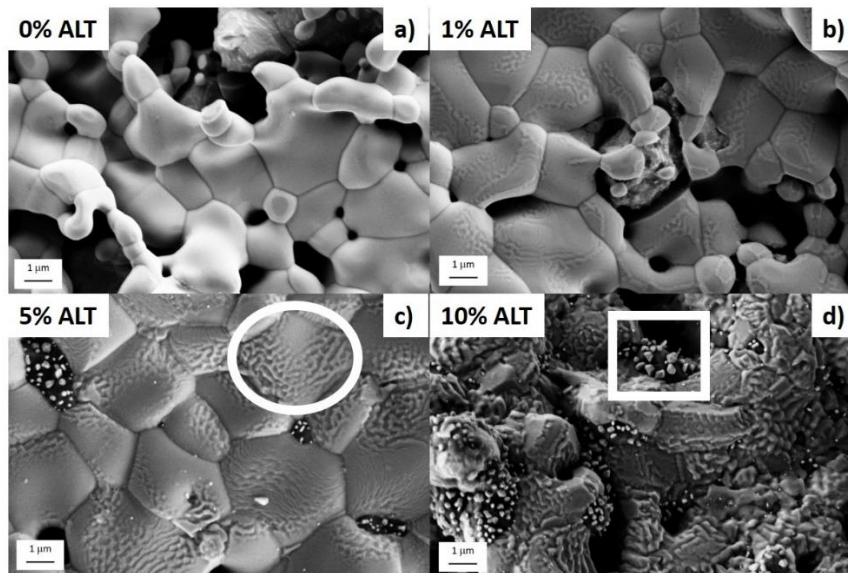


Figure 2: FE-SEM surface topography of Ni-YSZ doped with 0-10 wt% ALT a-d) reduced in 5% H₂ - 95% N₂

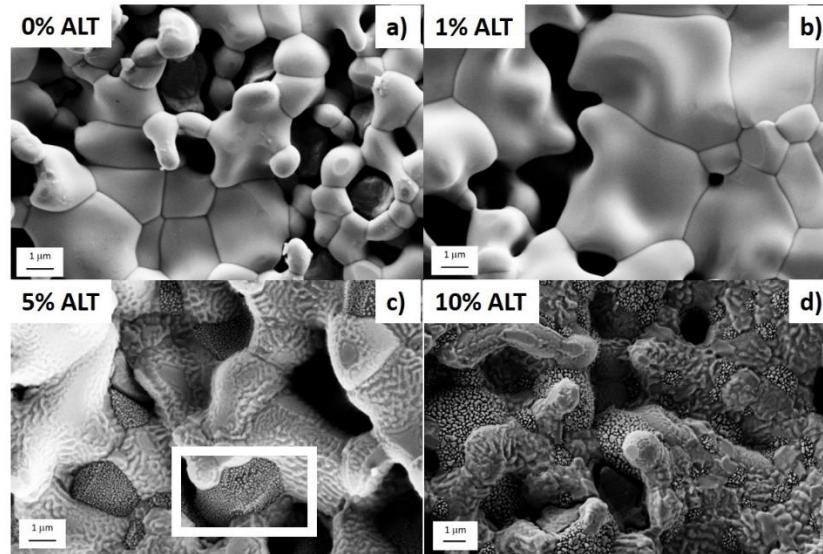


Figure 3: FE-SEM surface topography of Ni-YSZ doped with 0-10 wt% ALT a-d) reduced in 100% H₂

Observing the surface morphology, there is no change in the rough phase which has been previously observed for this material [25]. It is believed that the drastic decrease in strength is due to the unstable reduction of NiAl₂O₄. Previous research has shown that NiAl₂O₄ at 800°C in reducing atmosphere has different reaction kinetics depending on the concentration of hydrogen in the reducing gas [42]. Samples reduced in 100% H₂ have a reaction time on the order of 10 times faster [42]. The fast reduction kinetics in pure hydrogen could lead to unstable phase changes. Also, the strength of ceramic is dependent on the porosity distribution within the material [18,20,39,47,52] since the presence of one or more pores in the loaded volume will result in a more fragile material. The surface morphology confirms the higher porosity for the samples reduced in 100% H₂ which could lead to lower strength for this material but as discussed previously, porosity is not the only contributor to mechanical strength.

Previous research has also shown that the volume decrease during the reduction of NiAl_2O_4 is between 3 and 9% instead of the theoretical 18% indicating that the system, if given enough time, finds a mechanism to avoid generating large volume changes and relaxes the stresses associated with the reduction reaction [55]. For this case, the fast reduction in pure hydrogen does not allow for those volume change stresses to be released leading to high stressed areas in the material. This high stress from volume change will cause premature failure of the material.

Fractography was also performed on the samples to determine fracture characteristics depending on reduction conditions. Figures 4 and 5 shows the fracture surfaces for the samples reduced in 5% H_2 – 95% N_2 and 100% H_2 , respectively. It can be observed that the fracture surface of the undoped samples for both reduction methods has indications of intergranular fracture. Intergranular fracture occurs when the crack propagates around the grain along the grain boundaries. As grain boundaries are weak locations within the microstructure, this fracture path occurs at a lower energy and is usually indicative of a lower strength material. Intergranular fracture has previously been observed for these samples and porosity is thought to be the mechanism for failure. In Figure 4 c and d, it can be observed that the fracture mechanism has shifted to transgranular fracture as indicated by the sharp, flat planes in the fracture surface. Transgranular fracture is characterized by crack propagation through the grains of the material. This fracture path requires much higher energy and usually corresponds to a higher strength material. Transgranular fracture has been observed for higher amounts of ALT doping previously. It is believed that secondary phase formations determine the

strength of the material for ALT doping. It is typical for these materials to see a transition from intergranular to transgranular as observed for the samples reduced in 5% H₂ – 95% N₂. When observing the fracture characteristics for the samples reduced in 100% H₂, intergranular fracture is dominant for most doping amounts. The amount of transgranular fracture for the 5 and 10 wt% ALT is less than observed for the 5% H₂ – 95% N₂ sample batches. This dominance for intergranular fracture helps explain the decrease in strength observed for the samples reduced in 100% H₂.

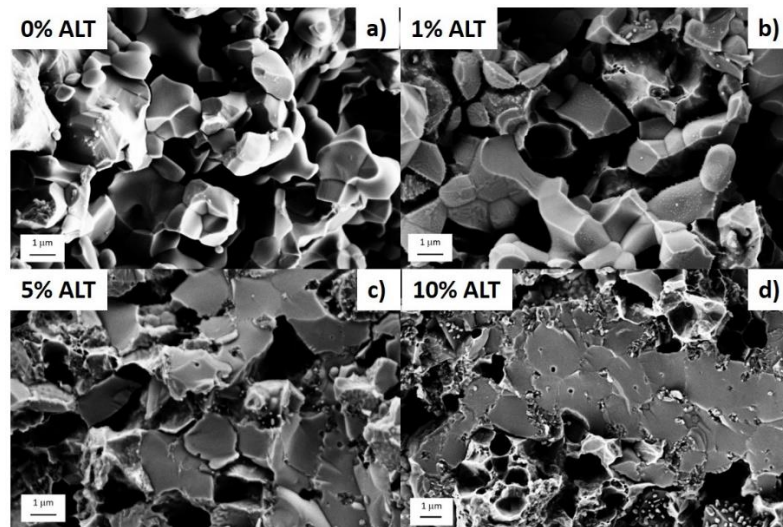


Figure 4: FE-SEM fracture surface morphology of Ni-YSZ doped with 0-10 wt% ALT a-d) reduced in 5% H₂ – 95% N₂

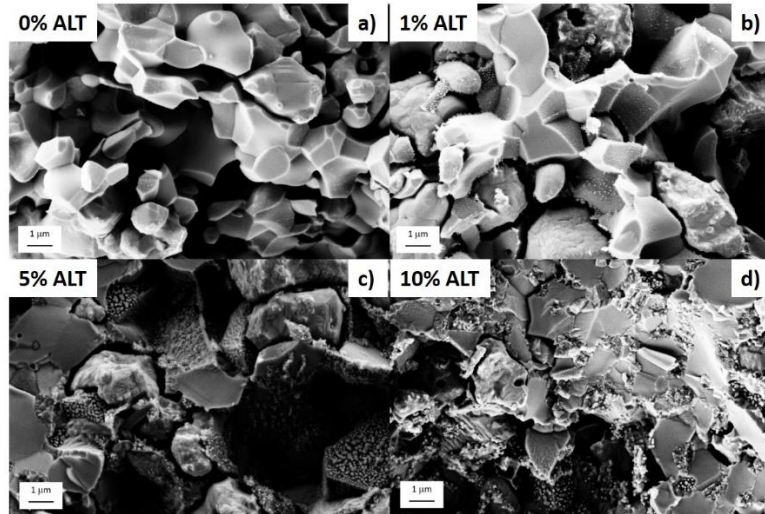


Figure 5: FE-SEM fracture surface morphology of Ni-YSZ doped with 0-10 wt% ALT a-d) reduced in 100% H₂

Conclusions:

Mechanical properties testing was performed on samples of Ni-YSZ anodes with 0-10 wt% ALT which were reduced with either of two different concentrations of hydrogen (5% and 100%). Mechanical strength results showed that ALT doping increase strength for both reduction conditions. It was found that the samples reduced in 100% H₂ had significantly lower strength when compared to those reduced in 5% H₂ – 95% N₂. Weibull modulus values for the samples reduced in 100% H₂ were also lower than those reduced in 5% H₂ – 95% N₂. Microstructural analyses showed the formation of two secondary phases: the partial reduction of NiAl₂O₄ and the Ti/YSZ framework. The partial reduction of NiAl₂O₄ was thought to be faster for those samples reduced in 100% H₂ which leads to volume shrinkage and mechanical stress that lead to the low strength observed for these samples.

References:

- [1] F. Zhao, A. V. Virkar, Dependence of polarization in anode-supported solid oxide fuel cells on various cell parameters, *J. Power Sources*. 141 (2005) 79–95. doi:10.1016/j.jpowsour.2004.08.057.
- [2] A.C. Müller, D. Herbristrit, E. Ivers-Tiffée, Development of a multilayer anode for solid oxide fuel cells, *Solid State Ionics*. 152–153 (2002) 537–542. doi:10.1016/S0167-2738(02)00357-0.
- [3] Z.R. Wang, J.Q. Qian, S.R. Wang, J.D. Cao, T.L. Wen, Improvement of anode-supported solid oxide fuel cells, *Solid State Ionics*. 179 (2008) 1593–1596. doi:10.1016/j.ssi.2008.03.022.
- [4] T. Setoguchi, K. Okamoto, K. Eguchi, H. Arai, Effects of anode material and fuel on anodic reaction of solid oxide fuel cells, *J. Electrochem. Soc.* 139 (1992) 2875–2880. doi:10.1149/1.2068998.
- [5] C.R. He, W.G. Wang, Alumina Doped Ni/YSZ Anode Materials for Solid Oxide Fuel Cells, *Fuel Cells*. 9 (2009) 630–635. doi:10.1002/fuce.200800152.
- [6] M. Mori, Y. Hiei, H. Itoh, G.A. Tompsett, N.M. Sammes, Evaluation of Ni and Ti-doped Y₂O₃ stabilized ZrO₂ cermet as an anode in high-temperature solid oxide fuel cells, *Solid State Ionics*. 160 (2003) 1–14. doi:10.1016/S0167-2738(03)00144-9.
- [7] M. Kleitz, F. Petitbon, Optimized SOFC electrode microstructure, *Solid State Ionics*. 92 (1996) 65–74. doi:10.1016/S0167-2738(96)00464-X.
- [8] T. Dey, D. Singdeo, M. Bose, R.N. Basu, P.C. Ghosh, Study of contact resistance at the electrode-interconnect interfaces in planar type Solid Oxide Fuel Cells, *J. Power Sources*. 233 (2013) 290–298. doi:10.1016/j.jpowsour.2013.01.111.
- [9] T. Dey, A. Dey, P.C. Ghosh, M. Bose, A.K. Mukhopadhyay, R.N. Basu, Influence of microstructure on nano-mechanical properties of single planar solid oxide fuel cell in pre- and post-reduced conditions, *Mater. Des.* (2014). doi:10.1016/j.matdes.2013.06.052.
- [10] M. Pihlatie, A. Kaiser, M. Mogensen, Mechanical properties of NiO/Ni–YSZ composites depending on temperature, porosity and redox cycling, *J. Eur. Ceram. Soc.* 29 (2009) 1657–1664. doi:10.1016/j.jeurceramsoc.2008.10.017.
- [11] N. Mahato, A. Banerjee, A. Gupta, S. Omar, K. Balani, Progress in material selection for solid oxide fuel cell technology: A review, *Prog. Mater. Sci.* 72 (2015) 141–337. doi:10.1016/j.pmatsci.2015.01.001.
- [12] J. Wei, G. Pećanac, J. Malzbender, Review of mechanical characterization methods for ceramics used in energy technologies, *Ceram. Int.* 40 (2014) 15371–15380. doi:10.1016/j.ceramint.2014.07.089.

- [13] G. Pećanac, S. Baumann, J. Malzbender, Mechanical properties and lifetime predictions for Ba_{0.5}Sr_{0.5}Co_{0.8}Fe_{0.2}O_{3-δ} membrane material, *J. Memb. Sci.* 385–386 (2011) 263–268. doi:10.1016/j.memsci.2011.10.005.
- [14] A. Atkinson, A. Selçuk, Mechanical behaviour of ceramic oxygen ion-conducting membranes, *Solid State Ionics*. 134 (2000) 59–66. doi:10.1016/S0167-2738(00)00714-1.
- [15] M. Lipińska-Chwałek, L. Kiesel, J. Malzbender, Mechanical properties of porous MgO substrates for membrane applications, *J. Eur. Ceram. Soc.* 34 (2014) 2519–2524. doi:10.1016/j.jeurceramsoc.2014.03.009.
- [16] B.X. Huang, V. Vasechko, Q.L. Ma, J. Malzbender, Thermo-mechanical properties of (Sr,Y)TiO₃ as anode material for solid oxide fuel cells, *J. Power Sources*. 206 (2012) 204–209. doi:10.1016/j.jpowsour.2012.01.137.
- [17] S. Giraud, J. Canel, Young's modulus of some SOFCs materials as a function of temperature, *J. Eur. Ceram. Soc.* 28 (2008) 77–83. doi:10.1016/j.jeurceramsoc.2007.05.009.
- [18] M. Radovic, E. Lara-Curzio, Mechanical properties of tape cast nickel-based anode materials for solid oxide fuel cells before and after reduction in hydrogen, *Acta Mater.* 52 (2004) 5747–5756. doi:10.1016/j.actamat.2004.08.023.
- [19] G. Pećanac, L. Kiesel, R. Kriegel, J. Malzbender, Comparison of thermo-mechanical characteristics of non-doped and 3 mol% B-site Zr-doped Ba_{0.5}Sr_{0.5}Co_{0.8}Fe_{0.2}O_{3-??}, *Ceram. Int.* 40 (2014) 1843–1850. doi:10.1016/j.ceramint.2013.07.086.
- [20] M. Radovic, E. Lara-curzio, Elastic Properties of Nickel-Based Anodes for Solid Oxide Fuel Cells as a Function of the Fraction of Reduced NiO, *J. Am. Ceram. Soc.* 87 (2004) 2242–2247. doi:10.1111/j.1151-2916.2004.tb07499.x.
- [21] Y. Ye, J. Li, H. Zhou, J. Chen, Microstructure and mechanical properties of yttria-stabilized ZrO₂/Al₂O₃ nanocomposite ceramics, *Ceram. Int.* 34 (2008) 1797–1803. doi:10.1016/j.ceramint.2007.06.005.
- [22] R. Kubrin, G. Blugan, J. Kuebler, Influence of cerium doping on mechanical properties of tetragonal scandium-stabilized zirconia, *J. Eur. Ceram. Soc.* 37 (2017) 1651–1656. doi:10.1016/j.jeurceramsoc.2016.11.038.
- [23] K. Swider, W. Worrell, Electronic Conduction Mechanism in Ytria- Stabilized Zirconia-Titania under Reducing Atmospheres, *J. Electrochem. Soc.* 143 (1996) 3706–3711. <http://jes.ecsdl.org/content/143/11/3706.short>.
- [24] D.R. Driscoll, B.W. Tokmakian, N.P. Johnson, C.D. Hunt, S.W. Sofie, Catalyst enhancing aluminum titanate for increasing strength of nickel-zirconia cermets, *Mater. Lett.* 209 (2017) 307–310. doi:10.1016/j.matlet.2017.08.035.
- [25] M. McCleary, R. Amendola, Effect of Aluminum Titanate

- (Al₂TiO₅) Doping on the Mechanical Performance of Solid Oxide Fuel Cell Ni-YSZ Anode, *Fuel Cells*. 17 (2017).
doi:10.1002/fuce.201700073.
- [26] S. Tekeli, The flexural strength, fracture toughness, hardness and densification behaviour of various amount of Al₂O₃-doped 8YSCZ/Al₂O₃ composites used as an electrolyte for solid oxide fuel cell, *Mater. Des.* 27 (2006) 230–235.
doi:10.1016/j.matdes.2004.10.011.
- [27] J.S. Lee, K.H. Choi, B.K. Ryu, B.C. Shin, I.S. Kim, Effects of gallia additions on sintering behavior of gadolinia-doped ceria, *Mater. Res. Bull.* 39 (2004) 2025–2033. doi:10.1016/j.materresbull.2004.07.022.
- [28] H. Xu, H. Yan, Z. Chen, The flexural strength and densification behavior of Al₂O₃-doped Ce_{0.8}Y_{0.2}O_{1.9} electrolyte composites, *Mater. Sci. Eng. A.* 447 (2007) 222–226. doi:10.1016/j.msea.2006.10.027.
- [29] N. Matsui, D. Kagaku, No Title, *J. Electrochem. Soc. Japan.* 58 (1990) 716.
- [30] S.S. Lion, W.L. Worrell, Electrical properties of novel mixed-conducting oxides, *Appl. Phys. A Solids Surfaces.* 49 (1989) 25–31. doi:10.1007/BF00615461.
- [31] Y.I. Kiyoshi Kobayashi, Yukiharu Kai, Shu Yamaguchi, Norihiko Fukatsu, Tsuyoshi Kawashima, K. Kobayashi, Y. Kai, S. Yamaguchi, N. Fukatsu, T. Kawashima, Y. Iguchi, Electronic conductivity measurements of 5 mol% TiO₂-doped YSZ by a d.c.-polarization technique, *Solid State Ionics.* 93 (1997) 193–199. doi:10.1016/S0167-2738(96)00534-6.
- [32] K. Kobayashi, K. Kato, T. Kawashima, S. Yamaguchi, Y. Iguchi, Total Electrical Conductivity Measurements of TiO₂ Doped YSZ Ceramics, *J. Ceram. Soc. Japan.* 106 (1998) 1073.
- [33] M. Nagano, S. Nagashima, H. Maeda, A. Kato, Sintering behavior of Al₂TiO₅ base ceramics and their thermal properties, *Ceram. Int.* 25 (1999) 681–687.
doi:10.1016/S0272-8842(98)00083-2.
- [34] D.R. Driscoll, M.D. McIntyre, M.M. Welander, S.W. Sofie, R.A. Walker, Enhancement of high temperature metallic catalysts: Aluminum titanate in the nickel-zirconia system, *Appl. Catal. A Gen.* 527 (2016) 36–44.
doi:10.1016/j.apcata.2016.08.020.
- [35] I.M. Low, D. Lawrence, R.I. Smith, Factors controlling the thermal stability of aluminum titanate ceramics in vacuum, *J. Am. Ceram. Soc.* 88 (2005) 2957–2961.
doi:10.1111/j.1551-2916.2005.00518.x.
- [36] G. Tilloca, Thermal stabilization of aluminium titanate and properties of aluminium titanate solid solutions, *J. Mater. Sci.* 26 (1991) 2809–2814.
doi:10.1007/BF00545574.
- [37] B. Freudenberg, A. Mocellin, Aluminum Titanate Formation by Solid-state

- Reaction of Fine Al₂O₃ and TiO₂ Powders, *J. Am. Ceram. Soc.* 70 (1987) 33–38.
- [38] C.H. Law, S.W. Sofie, Anchoring of Infiltrated Nickel Electro-Catalyst by Addition of Aluminum Titanate, *J. Electrochem. Soc.* 158 (2011) B1137–B1141. doi:10.1149/1.3610226.
- [39] B. Charlas, D.W. Ni, H.L. Frandsen, K. Brodersen, M. Chen, Mechanical Properties of Supports and Half-Cells for Solid Oxide Electrolysis Influenced by Alumina-Zirconia Composites, *Fuel Cells*. 17 (2017) 132–143. doi:10.1002/fuce.201600036.
- [40] J. Zygmuntowicz, P. Wiecińska, A. Miazga, K. Konopka, Characterization of composites containing NiAl₂O₄ spinel phase from Al₂O₃/NiO and Al₂O₃/Ni systems, *J. Therm. Anal. Calorim.* 125 (2016) 1079–1086. doi:10.1007/s10973-016-5357-2.
- [41] H. Orui, R. Chiba, K. Nozawa, H. Arai, R. Kanno, High-temperature stability of alumina containing nickel–zirconia cermets for solid oxide fuel cell anodes, *J. Power Sources*. 238 (2013) 74–80. doi:10.1016/j.jpowsour.2013.03.056.
- [42] M. McCleary, R. Amendola, Reduction kinetics of undoped and aluminum titanate (Al₂TiO₅) doped NiO-YSZ solid oxide fuel cell anodes, *Ceram. Int.* 44 (2018) 15557–15564. doi:10.1016/j.ceramint.2018.05.218.
- [43] ASTM C1161-18, Standard Test Method for Flexural Strength of Advanced Ceramics at Ambient Temperature, *ASTM Int.* (2018) 1–19. doi:10.1017/CBO9781107415324.004.
- [44] ASTM C1239-13, Standard Practice for Reporting Uniaxial Strength Data and Estimating Weibull Distribution Parameters for Advanced Ceramics, *ASTM Int.* (2013) 1–9. doi:10.1520/C1239-13.Scope.
- [45] H. Peterlik, Relationship of Strength and Defects of Ceramic Materials and Their Treatment by Weibull Theory, *J. Fo Ceram. Soc. Japan*. 109 (2001) 121–126. doi:10.1007/s13398-014-0173-7.2.
- [46] A. Nakajo, J. Kuebler, A. Faes, U.F. Vogt, H.J. Schindler, L.K. Chiang, S. Modena, J. Van Herle, T. Hocker, Compilation of mechanical properties for the structural analysis of solid oxide fuel cell stacks. Constitutive materials of anode-supported cells, *Ceram. Int.* 38 (2012) 3907–3927. doi:10.1016/j.ceramint.2012.01.043.
- [47] Z. Cui, Y. Huang, H. Liu, Predicting the mechanical properties of brittle porous materials with various porosity and pore sizes, *J. Mech. Behav. Biomed. Mater.* 71 (2017) 10–22. doi:10.1016/j.jmbbm.2017.02.014.
- [48] D. Wu, Y. Li, J. Zhang, L. Chang, D. Wu, Z. Fang, Y. Shi, Effects of the number of testing specimens and the estimation methods on the Weibull parameters of solid catalysts, *Chem. Eng. Sci.* 56 (2001) 7035–7044. doi:10.1016/S0009-

2509(01)00340-2.

- [49] A. Khalili, K. Kromp, Statistical properties of Weibull estimators, *J. Mater. Sci.* 26 (1991) 6741–6752.
- [50] J. Laurencin, G. Delette, F. Lefebvre-Joud, M. Dupeux, A numerical tool to estimate SOFC mechanical degradation: Case of the planar cell configuration, *J. Eur. Ceram. Soc.* 28 (2008) 1857–1869. doi:10.1016/j.jeurceramsoc.2007.12.025.
- [51] H. Fischer, W. Rentzsch, R. Marx, A modified size effect model for brittle nonmetallic materials, *Eng. Fract. Mech.* 69 (2002) 781–791. doi:10.1016/S0013-7944(01)00126-6.
- [52] H.L. Frandsen, T. Ramos, A. Faes, M. Pihlatie, K. Brodersen, Optimization of the strength of SOFC anode supports, *J. Eur. Ceram. Soc.* 32 (2012) 1041–1052. doi:10.1016/j.jeurceramsoc.2011.11.015.
- [53] F. Baratta, W. Matthews, Errors Associated with Flexure Testing of Brittle Materials, *U.S. Army Mater. Technol. Lab.* (1987) 16, 41–42.
- [54] R. Subramanian, E. Üstündağ, S.L. Sass, R. Dieckmann, In-situ formation of metal-ceramic microstructures by partial reduction reactions, *Solid State Ionics.* 75 (1995) 241–255. doi:10.1016/0167-2738(94)00148-L.
- [55] E. Üstündağ, Z. Zhang, M.L. Stocker, P. Rangaswamy, M.A.M. Bourke, J.A. Roberts, S. Subramanian, K.E. Sickafus, S.L. Sass, Influence of residual stresses on the evolution of microstructure during the partial reduction of NiAl₂O₄, *Mater. Sci. Eng. A.* 238 (1997) 50–65.

APPENDIX C: Effect of Doping Method on the Mechanical Properties of Aluminum Titanate (Al₂TiO₅) Doped Ni-YSZ Solid Oxide Fuel Cell Anodes

What follows is a draft of a manuscript for publication. Please note that changes will be made before publication.

Effect of Doping Method on the Mechanical Properties of Aluminum Titanate (Al₂TiO₅) Doped Ni-YSZ Solid Oxide Fuel Cell Anodes

Madisen McCleary, Roberta Amendola*, Zoe Benedict

Montana State University, Mechanical & Industrial Engineering Department, 220

Roberts Hall Bozeman, MT 59718

*corresponding author: Roberta.amendola@montana.edu, 406-994-6296

Abstract:

The mechanical properties of ALT doped Ni/YSZ anodes was tested using three-point bending. ALT doping was performed using one of two methods, infiltration or mechanical mixing. It was observed that ALT doping by either method increased the strength of the anode material when compared to the undoped anode. The sample batches with ALT doping by infiltration had slightly higher strengths when compared to the mechanical mixing method. However, the samples doped by infiltration had lower Weibull modulus values indicating a less reliable strength for the material. FE-SEM surface analyses confirmed the presence of secondary phases contributing to strength.

Fractography performed on the samples confirmed mechanical strength data by the presence of intergranular and transgranular fracture patterns.

Introduction:

A solid oxide fuel cell (SOFC) is a device that produces power through the electrochemical oxidation of a fuel (hydrogen or hydrocarbons). The only by-products when running pure hydrogen are water vapor, heat and electricity; therefore, the use of these cells can be incorporated into renewable energy systems. SOFCs have higher efficiencies than other types of fuel cells and much research has been done to increase longevity and slow degradation rate for these cells [1–3]. Research has mostly been focused on improved materials for each of the components (anode, cathode, and electrolyte) in terms of electrochemical output. Anode supported SOFCs have been given much attention in recent years due to their ability to operate at lower temperatures [4–10].

At this time, each individual cell (anode, electrolyte and cathode) can only produce a small amount of power; so, cells must be stacked in electrical series to produce enough power for societal needs. To maximize the power output between the cells, the stack is clamped with high pressures around 65 – 70 kPa [11,12]. Due to the anode supported design, the anode is the thickest component of the cell; therefore, it carries the mechanical load and provides strength to the cell and the stack. Even though much data is available regarding the electrochemical properties of the SOFC, little fundamental data is available regarding the mechanical performance of SOFC materials. SOFC components are composed of ceramic materials. Due to the brittle nature of the ceramic components, the reliability and strength of the anode materials depends critically on the mechanical

performance. Brittle materials fail with little to no strain and fracture occurs catastrophically and unpredictably. These fracture characteristics lead to the necessity to characterize SOFC materials before they are implemented into the SOFC stack.

The most commonly used anode materials are Ni/YSZ cermets due to the high performance to cost ratio [13,14]. Research is ongoing into new anode compositions, but much work is still needed before implementation into the SOFC stack [15–23]. Ceramic materials are sensitive to changes in their composition and manufacturing process. Mechanical properties can be drastically altered by small changes in chemistry and processing. Researchers have found that the addition of secondary phases through material doping can increase the mechanical performance of the cell through the formation of new microstructures and phases [8,9,24,25].

Previous research has shown that the addition of Al_2O_3 and TiO_2 can improve mechanical performance [8,9,24,26–30]. Research has also shown that the addition of aluminum titanate (Al_2TiO_5 , ALT) increases the mechanical properties of the Ni/YSZ anode material along with stabilization of the microstructure for increased electrochemical performance including increased power output and decreased degradation rates [31–35]. The addition of ALT to the Ni/YSZ anode material causes the formation of two new secondary phases that contribute to increased mechanical performance. During sintering, ALT decomposes to its constituents of Al_2O_3 and TiO_2 [32,36–39]. Al_2O_3 reacts with NiO to form NiAl_2O_4 [8,32,35,40,41]. TiO_2 will react with YSZ destabilizing its cubic crystal structure [42,43]. Subsequent reduction causes partial reduction of the NiAl_2O_4 phase to Ni nanoparticles atop an Al_2O_3 matrix [40,44].

Due to the sensitivity of the mechanical properties to changes in manufacturing process, different methods for secondary phase addition must be tested. Previous research on ALT doped Ni/YSZ anode materials was conducted on materials where ALT powder was added during tape cast slurry manufacturing. Using this process, ALT was homogeneously dispersed throughout the anode material. Another common doping procedure is infiltration [31,35]. Using this process, a solution of the doping materials is added after initial manufacturing. Typically, the solution is added after sintering of the ceramic material. Using this method, the ALT solution would be concentrated to the pores. Porosity in the anode is high due to the necessity for increased triple phase boundaries. Porosity acts as a stress concentrator within the anode and can cause premature failure of the ceramic [21,23,40,45,46]. Infiltration may allow for pore strengthening increasing the mechanical properties of the anode material. This study investigates the mechanical properties of ALT doped Ni/YSZ anodes by infiltration method in comparison to mechanically mixed anodes.

Methods:

Nickel oxide (NiO) powder (4 μm , Alfa Aesar), 8 mol.% yttria stabilized zirconia (8YSZ) powder (300 nm, Tosoh) and aluminum titanate (Al_2TiO_5 , ALT) powder (25 nm, Sigma Aldrich) were used for sample manufacturing. Powders, in the ratio of 34 wt.% YSZ, 66 wt.% NiO, were mechanically mixed for 24 hours with binder and deionized water. After mixing, the slurry was tape cast with a doctor blade thickness of 2 mm and allowed to dry.

Rectangular 6 mm x 40 mm samples were cut from the green tape using a rotary cutter. Thermolysis and partial sintering of the samples was performed using the following process: 1) ramp to 150°C at 2°C/min, 2) dwell for 2 hours, 3) ramp to 450°C at 0.5°C/min, 4) ramp to 1,100°C at 5°C/min, 5) dwell for 2 hours, 6) ramp to room temperature at 10°C/min in a box furnace (Thermolyne, 1300). After partial sintering, samples were infiltrated with an ALT solution. Aluminum nitrate and titanium lactate were combined in the proper ratios to form ALT. This solution was then soaked into the samples until the proper doping level was achieved (1, 5 or 10 wt% ALT). After infiltration, sintering was conducted with a heating/cooling rate of 5°C/min up to 1,500°C and a dwell time of 2 hours (Zircar, Hot Spot 110).

Reduction was performed in a tube furnace (Thermo Scientific, Lindberg Blue M) flowing 5% H₂ - 95% N₂ gas at 800°C for a time sufficient to convert 97 wt.% of NiO into metallic nickel. The percentage reduction was evaluated with a Radwag XA 82/220.R2 microscale. Time required for the reduction process varied proportionally to the doping amount of ALT. Un-doped and 1, 5 and 10 wt.% ALT doped batches of 30 samples were loaded at a rate of 0.2 mm/min in a three-point bending apparatus (Pasco Scientific 8236) as per ASTM C1161-13 standard [47]. Fracture strength, effective volume V_{eff} , scaled characteristic strength σ'_0 , Weibull modulus (m) with normalized upper and lower bounds, and porosity, by alcohol immersion method, were evaluated. Weibull statistics were evaluated according to ASTM C1239-13 [48]. Fractographic analyses were performed using a Field emission scanning electron microscope (FE-SEM, Zeiss Ultra) on select samples.

Results and Discussion:

Mechanical Properties:

Table 1 summarizes the results for all the tested batches. It can be observed that the characteristic strengths calculated are similar for 1 wt% ALT doping and higher for the infiltration process for the 5 and 10 wt% ALT doped sample batches. The characteristic strength is calculated according to ASTM C1239-13 and is the value of the flexural strength at a probability of survival of $1/e$ [48]. For both infiltration methods, the mechanical strength was highest for 5 wt% ALT doping. This has been previously observed due to the residual stresses at 10 wt% ALT doping. The formation of the secondary phases (discussed further below) has an accompanying volume change and these volume change stresses are beneficial at lower doping amounts but detrimental at high doping amounts. Discussion of the effective volume (V_{eff}) and the scaled characteristic strength can be found below.

Table 1: Mechanical properties of Ni-YSZ anodes doped with ALT reduced in 5% H₂-95% N₂ and 100% H₂

	0 wt% ALT	1 wt% ALT	5 wt% ALT	10 wt% ALT
Infiltration				
Characteristic Strength (MPa)	N/A	121	185	171
V_{eff} (mm ³)	N/A	0.65	0.10	0.24
Scaled Characteristic Strength (MPa)	N/A	110	141	131
Strength Increase (%)	N/A	34	71	60
Mechanically Mixed				
Characteristic Strength (MPa)	96	115	168	146
V_{eff} (mm ³)	0.28	0.32	0.27	0.35
Scaled Characteristic Strength (MPa)	82	87	142	127
Strength Increase (%)	N/A	6	73	54

The unpredictable nature of brittle fracture of ceramics materials leads to a necessity for statistical analyses of mechanical properties data. Weibull statistics are typically used for advanced ceramic materials as laid out in ASTM C1239-13 [48]. Weibull statistics employs the weakest link theory where the weakest flaw under tension determines the strength of the material. Flaws are randomly distributed throughout the anode material and each sample will have a different flaw distribution. These flaws could be due to manufacturing process or microstructural features such as porosity. Figure 1 shows the Weibull plot for the sample batches. The Weibull plot is used to evaluate the reliability of the sample batch. The plots are created by manipulating the Weibull equation (Equation 1) into its linear form (Equation 2).

$$p_s = \exp\left(-\frac{\sigma}{\sigma_0}\right)^m \quad (1)$$

$$\ln(\ln(1/p_s)) = m \ln(\sigma/\sigma_0) \quad (2)$$

Where p_s is the probability of survival for each sample, σ is the flexural strength of each sample (MPa), σ_0 is the characteristic strength (MPa), and m is the Weibull modulus.

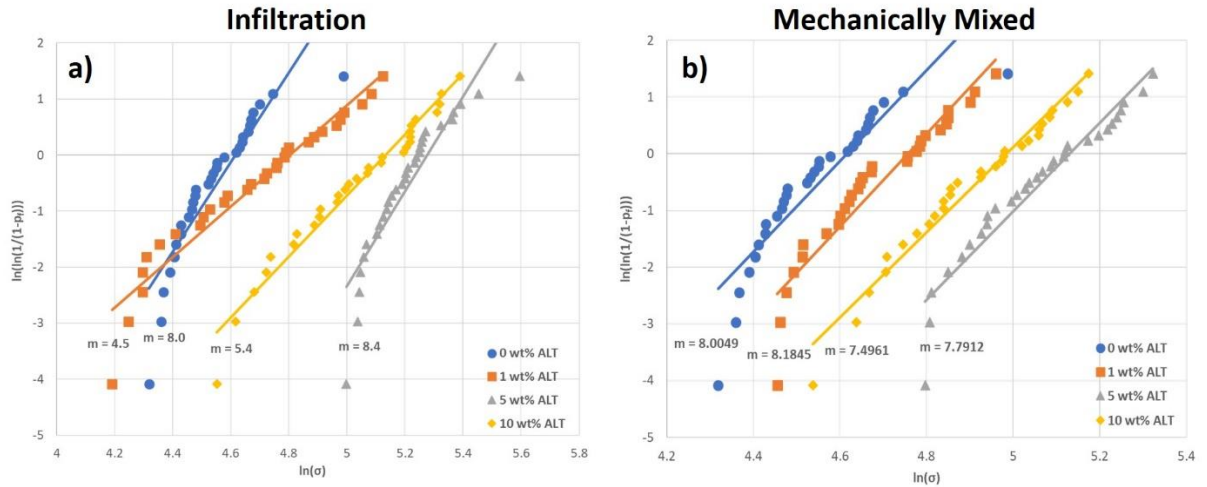


Figure 1: Weibull plots for Ni-YSZ anodes doped with ALT by a) infiltration and b) mechanically mixed methods

For the Weibull plots, each data point represents an individual sample from the batch and each linear trendline corresponds to a specific batch of 30 samples. If the data well follow the Weibull distribution then the data points should lie close to the linear trendline. It can be said that those batches that well follow the Weibull distribution are more reliable in terms of fracture characteristics. It can be observed that for the sample batches using infiltration method, the 5 wt% ALT doped anodes follow the linear trendline and are the batch with the highest strength and highest Weibull modulus. Comparing to the samples that were mechanically mixed, the 10 wt% ALT sample batch most closely follows the linear trendline and corresponds to neither the highest strength nor highest Weibull modulus. Usually, as with the infiltrated samples, the highest strength and Weibull modulus corresponds to the sample batch that closely followed the linear trendline. Due to the unpredictable fracture characteristics of brittle materials, this

is not always the case and many different variables must be considered when discussing mechanical strength.

The Weibull distribution has two factors that affect the shape of the distribution. When using this method, the characteristic strength and the Weibull modulus determine the distribution. The characteristic strength has previously been discussed. The Weibull modulus for the context of advanced ceramics mechanical properties indicates the nature, severity and dispersion of flaws within the material. This value is used to compare two or more sets of data in prediction of the failure properties [49–51]. When using the Weibull modulus for the purposes of ceramics characteristics, a high Weibull modulus is favorable as it is indicative of a homogeneous flaw population with more predictable fracture characteristics. A low Weibull modulus usually corresponds to a less homogeneous flaw population with a less predictable fracture strength. In Table 2, the Weibull modulus values are shown with the normalized upper and lower bounds (90% confidence interval) as outlined in ASTM C1239-13 [52–54]. It can be observed in Table 2 that the Weibull modulus trend is similar for both doping methods with a decrease in Weibull modulus for 1 and 10 wt% ALT doping. The variation in Weibull modulus values is larger for the infiltrated sample batches which could lead to less predictable fracture strength for this doping method. The typical range of Weibull modulus values for these materials are 5 – 7 [55]. It can be observed that the Weibull modulus values are inside and above the range for the mechanically mixed sample batches. For the sample batches with infiltration method, the Weibull modulus value for the 1 wt% ALT doped sample batch falls outside of the range with the 10 wt% ALT sample batch at the low end

of the range. These large variations in Weibull modulus values for the infiltrated sample batches will be further discussed below.

Table 2: Weibull modulus and 90% confidence interval of Ni-YSZ anodes doped with ALT by infiltration or mechanical mixing

	0 wt% ALT	1 wt% ALT	5 wt% ALT	10 wt% ALT
Infiltration				
Weibull Modulus	N/A	4.5	8.4	5.4
90% Confidence Interval	N/A	3.4 - 5.5	6.3 - 10.3	4.1 - 6.6
Mechanically Mixed				
Weibull Modulus	8.0	6.6	7.8	7.5
90% Confidence Interval	6.0 - 9.8	4.9 - 8.0	5.8 - 9.5	5.6 - 9.1

The Weibull distribution assumes that the weakest flaw under tension determines the strength of the material. Depending on the individual size of each sample tested, the volume under tension will be different. These variations in sample size can give a false impression of the mechanical strength by flaw distributions. When there is a larger volume tested then there is a higher probability of encountering a flaw that is detrimental to the material which would give an apparently low strength. The converse is also true, where a smaller tested volume has a lower probability of encountering a flaw giving an apparently high strength. Due to these variations, the volume under tension, the effective volume, must be considered for accurate comparison of the sample batches. The effective volume is calculated using Equation 3 for samples fractured using three-point bending [40,46,56–58]. After calculation of the effective volume, the characteristic strength can be scaled to the same effective volume, 1 mm³, using Equation 4.

$$V_{eff} = \frac{lwh}{2(m+1)^2} \quad (3)$$

$$\sigma'_0 = \sigma_0 \left(\frac{V_{eff}}{1 \text{ mm}^3} \right)^{\frac{1}{m}} \quad (4)$$

For Equation 3 and 4, l is the length between support points (mm), w is the width of the sample (mm), h is the height of the sample (mm), m is the Weibull modulus, V_{eff} is the effective volume (mm^3), σ_0 is the characteristic strength (MPa) and σ'_0 is the scaled characteristic strength (MPa).

When observing the scaled characteristic strength data in Table 1, similar trends are present where the highest strength for both doping methods can be seen at 5 wt% ALT doping. When comparing the strength for the different methods, it can be observed that the characteristic strength values are very similar with the infiltrated samples showing slightly higher strengths. Also, both methods for ALT doping showed increased strength when compared to the undoped sample batch.

Table 3 shows the porosity for the sample batches. The strength of ceramic is dependent on the porosity distribution within the material [21,23,40,45,46] since the presence of one or more pores in the loaded volume will result in a more fragile material. It can be observed that the porosity for the infiltrated samples is similar for the 1 wt% ALT doped sample batch. With high doping amounts, it can be observed that the porosity is higher for the infiltrated sample batches when compared to the samples using mechanical mixing method. ALT acts as a sintering aid within the Ni/YSZ anode [31,32,35]. Due to the different methods for ALT doping, ALT could increase sintering with the mechanically mixed samples leading to less porosity for the material. A decrease

in porosity should lead to increased strength for the mechanically mixed sample batches due to less pores to act as stress concentrators within the material. This is not the case as the infiltrated samples have a higher strength. The higher strength could be due to the infiltration process concentrating ALT to the pores of the material.

Table 3: Porosity of Ni-YSZ anodes doped with ALT using infiltration and mechanical mixing methods

	0 wt% ALT	1 wt% ALT	5 wt% ALT	10 wt% ALT
Infiltration				
Porosity (%)	N/A	43	34	32
Mechanically Mixed				
Porosity (%)	46	43	30	23

Microstructural Analyses:

Field Emission Scanning Electron Microscopy (FE-SEM) was performed on select samples' surface and cross sections. Figure 2 shows the surface microstructure of the Ni-YSZ samples with 0, 1, 5, and 10 wt% ALT by mechanical mixing method. Figure 3 shows the microstructure of the samples doped with ALT by infiltration. It can be observed that there is the formation of two secondary phases that have been previously identified. The rough phase (circled in Figure 2c) has been previously found to be the destabilization of YSZ due to TiO₂ doping [9,59]. The rough phase appears after 1 wt% ALT doping for the mechanically mixed sample batch, but it is not visible for the infiltrated samples. This is common due to the low doping amount of ALT. The rough phase will be widely dispersed leading to low amounts of the rough phase to be identified using FE-SEM. The second phase present has been previously termed the small particle phase (boxed in Figure 2d) and is the partial reduction of NiAl₂O₄ to Ni nanoparticles

atop an Al_2O_3 matrix [59–61]. The small particle phase can be identified in the sample batches with high doping levels of ALT.

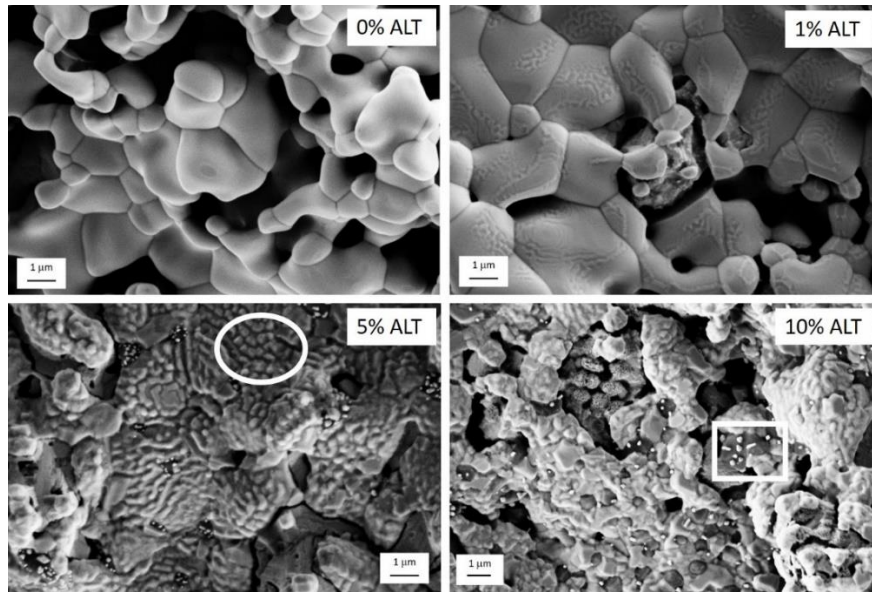


Figure 2: FE-SEM surface topography of Ni-YSZ doped with ALT by mechanical mixing method

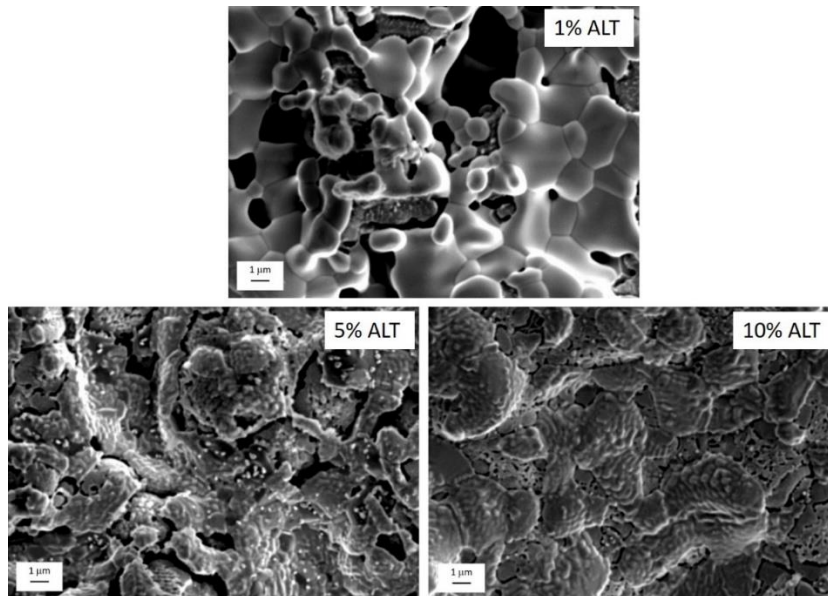


Figure 3: FE-SEM surface topography of Ni-YSZ doped with ALT by infiltration method

Fractography was also performed on the samples to determine fracture characteristics depending on doping method. Figures 4 and 5 shows the fracture surfaces for the samples doped by mechanical mixing and infiltration, respectively. There are two common fracture paths that can be identified for ceramic materials. Intergranular fracture is characterized by a fracture path along the grain boundaries of the material. As grain boundaries are weak locations within the material, the fracture usually occurs at low energy indicating a weaker material. Transgranular fracture is characterized by fracture through the grains of the material. Much more energy is needed to fracture through the grains and indicates a much stronger material. When observing the FE-SEM fractography, intergranular fracture is dominant for the undoped and 1 wt% ALT doped samples for the mechanical mixing method. The presence of intergranular fracture confirms the lower strength observed for these sample batches. For the infiltrated sample batch with 1 wt% ALT doping, the fracture appears to be transgranular confirming the higher strength observed when compared to the mechanical mixing method. For the 5 and 10 wt% ALT doped samples, the mechanical mixing method shows transgranular fracture confirming the increase in strength observed with higher doping of ALT. For the 5 and 10 wt% ALT doped sample batches using infiltration, it can be observed that transgranular fracture is also present confirming the increase in strength observed.

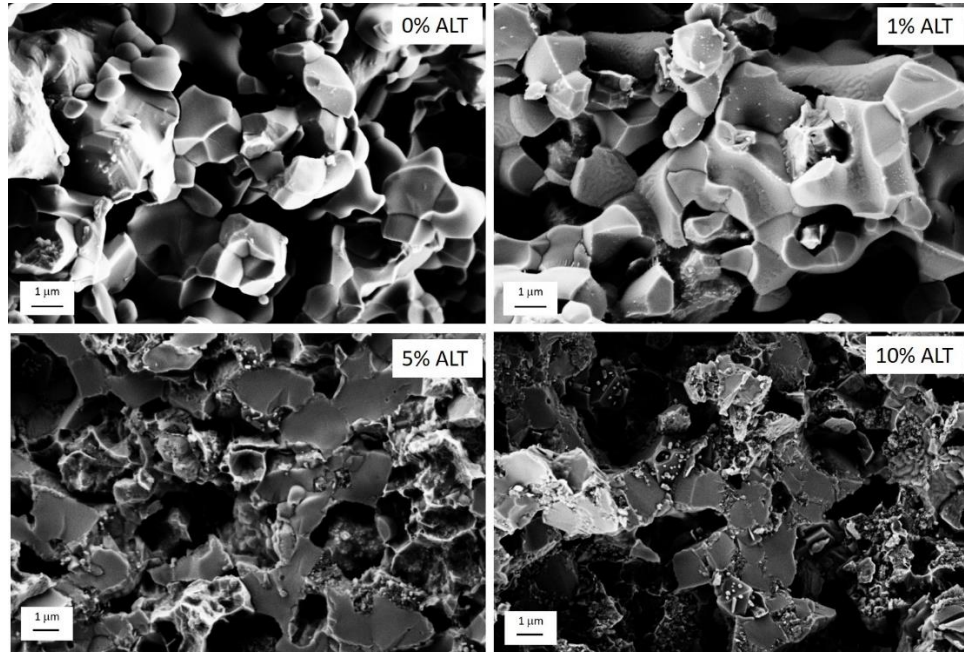


Figure 4: FE-SEM fracture surface morphology of Ni-YSZ doped with ALT by mechanical mixing method

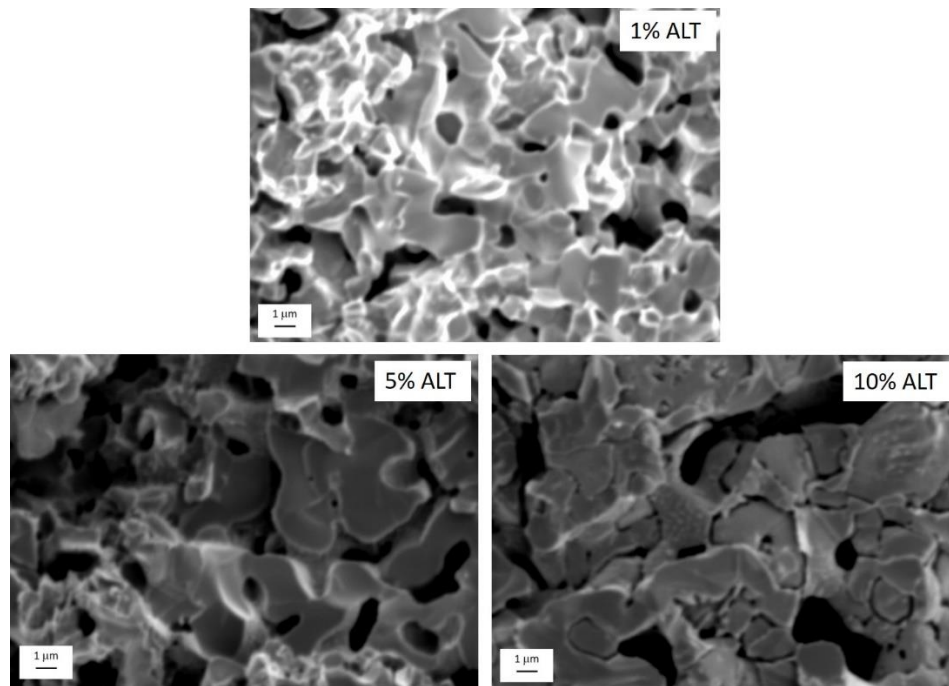


Figure 5: FE-SEM fracture surface morphology of Ni-YSZ doped with ALT by infiltration method

Conclusions:

The mechanical properties of ALT doped Ni/YSZ anodes were tested comparing two different doping methods, mechanical mixing and infiltration. Sample batches of 30 were fracture using three-point bending and fractography was performed on select samples. ALT doping was up to 10 wt% for both doping methods. It was observed that ALT doping by either method increased the strength of the anode when compared to undoped samples. Both methods had similar mechanical strength values with infiltration showing slightly higher strengths. The Weibull modulus for the infiltrated samples was lower than for mechanical mixing showing less reliability for the infiltrated samples. Fractography confirmed transgranular fracture for high doping levels of ALT and confirmed strength results calculated.

References:

- [1] a Atkinson, S. Barnett, R.J. Gorte, J.T.S. Irvine, a J. McEvoy, M. Mogensen, S.C. Singhal, J. Vohs, Advanced anodes for high-temperature fuel cells., *Nat. Mater.* 3 (2004) 17–27. doi:10.1038/nmat1040.
- [2] S.. Singhal, Advances in solid oxide fuel cell technology, *Solid State Ionics.* 135 (2000) 305–313. doi:10.1016/S0167-2738(00)00452-5.
- [3] J. Wu, X. Liu, Recent development of SOFC metallic interconnect, *J. Mater. Sci. Technol.* 26 (2010) 293–305. doi:10.1016/S1005-0302(10)60049-7.
- [4] F. Zhao, A. V. Virkar, Dependence of polarization in anode-supported solid oxide fuel cells on various cell parameters, *J. Power Sources.* 141 (2005) 79–95. doi:10.1016/j.jpowsour.2004.08.057.
- [5] A.C. Müller, D. Herbstritt, E. Ivers-Tiffée, Development of a multilayer anode for solid oxide fuel cells, *Solid State Ionics.* 152–153 (2002) 537–542. doi:10.1016/S0167-2738(02)00357-0.
- [6] Z.R. Wang, J.Q. Qian, S.R. Wang, J.D. Cao, T.L. Wen, Improvement of anode-supported solid oxide fuel cells, *Solid State Ionics.* 179 (2008) 1593–1596. doi:10.1016/j.ssi.2008.03.022.
- [7] T. Setoguchi, K. Okamoto, K. Eguchi, H. Arai, Effects of anode material and fuel on anodic reaction of solid oxide fuel cells, *J. Electrochem. Soc.* 139 (1992) 2875–2880. doi:10.1149/1.2068998.
- [8] C.R. He, W.G. Wang, Alumina Doped Ni/YSZ Anode Materials for Solid Oxide Fuel Cells, *Fuel Cells.* 9 (2009) 630–635. doi:10.1002/fuce.200800152.
- [9] M. Mori, Y. Hiei, H. Itoh, G.A. Tompsett, N.M. Sammes, Evaluation of Ni and Ti-doped Y2O3 stabilized ZrO2 cermet as an anode in high-temperature solid oxide fuel cells, *Solid State Ionics.* 160 (2003) 1–14. doi:10.1016/S0167-2738(03)00144-9.
- [10] M. Kleitz, F. Petitbon, Optimized SOFC electrode microstructure, *Solid State Ionics.* 92 (1996) 65–74. doi:10.1016/S0167-2738(96)00464-X.
- [11] T. Dey, D. Singdeo, M. Bose, R.N. Basu, P.C. Ghosh, Study of contact resistance at the electrode-interconnect interfaces in planar type Solid Oxide Fuel Cells, *J. Power Sources.* 233 (2013) 290–298. doi:10.1016/j.jpowsour.2013.01.111.
- [12] T. Dey, A. Dey, P.C. Ghosh, M. Bose, A.K. Mukhopadhyay, R.N. Basu, Influence of microstructure on nano-mechanical properties of single planar solid oxide fuel cell in pre- and post-reduced conditions, *Mater. Des.* (2014).

doi:10.1016/j.matdes.2013.06.052.

- [13] M. Pihlatie, A. Kaiser, M. Mogensen, Mechanical properties of NiO/Ni–YSZ composites depending on temperature, porosity and redox cycling, *J. Eur. Ceram. Soc.* 29 (2009) 1657–1664. doi:10.1016/j.jeurceramsoc.2008.10.017.
- [14] N. Mahato, A. Banerjee, A. Gupta, S. Omar, K. Balani, Progress in material selection for solid oxide fuel cell technology: A review, *Prog. Mater. Sci.* 72 (2015) 141–337. doi:10.1016/j.pmatsci.2015.01.001.
- [15] J. Wei, G. Pećanac, J. Malzbender, Review of mechanical characterization methods for ceramics used in energy technologies, *Ceram. Int.* 40 (2014) 15371–15380. doi:10.1016/j.ceramint.2014.07.089.
- [16] G. Pećanac, S. Baumann, J. Malzbender, Mechanical properties and lifetime predictions for Ba_{0.5}Sr_{0.5}Co_{0.8}Fe_{0.2}O_{3-δ} membrane material, *J. Memb. Sci.* 385–386 (2011) 263–268. doi:10.1016/j.memsci.2011.10.005.
- [17] A. Atkinson, A. Selçuk, Mechanical behaviour of ceramic oxygen ion-conducting membranes, *Solid State Ionics.* 134 (2000) 59–66. doi:10.1016/S0167-2738(00)00714-1.
- [18] M. Lipińska-Chwałek, L. Kiesel, J. Malzbender, Mechanical properties of porous MgO substrates for membrane applications, *J. Eur. Ceram. Soc.* 34 (2014) 2519–2524. doi:10.1016/j.jeurceramsoc.2014.03.009.
- [19] B.X. Huang, V. Vasechko, Q.L. Ma, J. Malzbender, Thermo-mechanical properties of (Sr,Y)TiO₃ as anode material for solid oxide fuel cells, *J. Power Sources.* 206 (2012) 204–209. doi:10.1016/j.jpowsour.2012.01.137.
- [20] S. Giraud, J. Canel, Young's modulus of some SOFCs materials as a function of temperature, *J. Eur. Ceram. Soc.* 28 (2008) 77–83. doi:10.1016/j.jeurceramsoc.2007.05.009.
- [21] M. Radovic, E. Lara-Curzio, Mechanical properties of tape cast nickel-based anode materials for solid oxide fuel cells before and after reduction in hydrogen, *Acta Mater.* 52 (2004) 5747–5756. doi:10.1016/j.actamat.2004.08.023.
- [22] G. Pećanac, L. Kiesel, R. Kriegel, J. Malzbender, Comparison of thermo-mechanical characteristics of non-doped and 3 mol% B-site Zr-doped Ba_{0.5}Sr_{0.5}Co_{0.8}Fe_{0.2}O_{3-??}, *Ceram. Int.* 40 (2014) 1843–1850. doi:10.1016/j.ceramint.2013.07.086.
- [23] M. Radovic, E. Lara-curzio, Elastic Properties of Nickel-Based Anodes for Solid Oxide Fuel Cells as a Function of the Fraction of Reduced NiO, *J. Am. Ceram. Soc.* 87 (2004) 2242–2247. doi:10.1111/j.1151-2916.2004.tb07499.x.

- [24] Y. Ye, J. Li, H. Zhou, J. Chen, Microstructure and mechanical properties of yttria-stabilized ZrO₂/Al₂O₃ nanocomposite ceramics, *Ceram. Int.* 34 (2008) 1797–1803. doi:10.1016/j.ceramint.2007.06.005.
- [25] R. Kubrin, G. Blugan, J. Kuebler, Influence of cerium doping on mechanical properties of tetragonal scandium-stabilized zirconia, *J. Eur. Ceram. Soc.* 37 (2017) 1651–1656. doi:10.1016/j.jeurceramsoc.2016.11.038.
- [26] K. Swider, W. Worrell, Electronic Conduction Mechanism in Yttria-Stabilized Zirconia-Titania under Reducing Atmospheres, *J. Electrochem. Soc.* 143 (1996) 3706–3711. <http://jes.ecsdl.org/content/143/11/3706.short>.
- [27] S. Tekeli, The flexural strength, fracture toughness, hardness and densification behaviour of various amount of Al₂O₃-doped 8YSCZ/Al₂O₃ composites used as an electrolyte for solid oxide fuel cell, *Mater. Des.* 27 (2006) 230–235. doi:10.1016/j.matdes.2004.10.011.
- [28] J.S. Lee, K.H. Choi, B.K. Ryu, B.C. Shin, I.S. Kim, Effects of gallia additions on sintering behavior of gadolinia-doped ceria, *Mater. Res. Bull.* 39 (2004) 2025–2033. doi:10.1016/j.materresbull.2004.07.022.
- [29] H. Xu, H. Yan, Z. Chen, The flexural strength and densification behavior of Al₂O₃-doped Ce_{0.8}Y_{0.2}O_{1.9} electrolyte composites, *Mater. Sci. Eng. A.* 447 (2007) 222–226. doi:10.1016/j.msea.2006.10.027.
- [30] K. Kobayashi, K. Kato, T. Kawashima, S. Yamaguchi, Y. Iguchi, Total Electrical Conductivity Measurements of TiO₂ Doped YSZ Ceramics, *J. Ceram. Soc. Japan.* 106 (1998) 1073.
- [31] D. Driscoll, C. Hunt, J. Muretta, S.W. Sofie, Thermally Stabilized Nickel Electro-Catalyst Introduced by Infiltration for High Temperature Electrochemical Energy Conversion, *ECS Trans.* 53 (2013) 63–72. doi:10.1149/05309.0063ecst.
- [32] D.R. Driscoll, M.D. McIntyre, M.M. Welander, S.W. Sofie, R.A. Walker, Enhancement of high temperature metallic catalysts: Aluminum titanate in the nickel-zirconia system, *Appl. Catal. A Gen.* 527 (2016) 36–44. doi:10.1016/j.apcata.2016.08.020.
- [33] M.M. Welander, M.S. Zachariasen, S.W. Sofie, R.A. Walker, Enhancing Ni-YSZ Anode Resilience to Environmental Redox Stress with Aluminum Titanate Secondary Phases, *ACS Appl. Energy Mater.* 1 (2018) 6295–6302. doi:10.1021/acsaem.8b01288.
- [34] M.M. Welander, M.S. Zachariasen, C.D. Hunt, S.W. Sofie, R.A. Walker, Operando Studies of Redox Resilience in ALT Enhanced NiO-YSZ SOFC Anodes, *J. Electrochem. Soc.* 165 (2018) F152–F157. doi:10.1149/2.0531803jes.

- [35] C.H. Law, S.W. Sofie, Anchoring of Infiltrated Nickel Electro-Catalyst by Addition of Aluminum Titanate, *J. Electrochem. Soc.* 158 (2011) B1137–B1141. doi:10.1149/1.3610226.
- [36] M. Nagano, S. Nagashima, H. Maeda, A. Kato, Sintering behavior of Al₂TiO₅ base ceramics and their thermal properties, *Ceram. Int.* 25 (1999) 681–687. doi:10.1016/S0272-8842(98)00083-2.
- [37] I.M. Low, D. Lawrence, R.I. Smith, Factors controlling the thermal stability of aluminum titanate ceramics in vacuum, *J. Am. Ceram. Soc.* 88 (2005) 2957–2961. doi:10.1111/j.1551-2916.2005.00518.x.
- [38] G. Tilloca, Thermal stabilization of aluminium titanate and properties of aluminium titanate solid solutions, *J. Mater. Sci.* 26 (1991) 2809–2814. doi:10.1007/BF00545574.
- [39] B. Freudenberg, A. Mocellin, Aluminum Titanate Formation by Solid-state Reaction of Fine Al₂O₃ and TiO₂ Powders, *J. Am. Ceram. Soc.* 70 (1987) 33–38.
- [40] B. Charlas, D.W. Ni, H.L. Frandsen, K. Brodersen, M. Chen, Mechanical Properties of Supports and Half-Cells for Solid Oxide Electrolysis Influenced by Alumina-Zirconia Composites, *Fuel Cells.* 17 (2017) 132–143. doi:10.1002/fuce.201600036.
- [41] J. Zygmuntowicz, P. Wiecińska, A. Miazga, K. Konopka, Characterization of composites containing NiAl₂O₄ spinel phase from Al₂O₃/NiO and Al₂O₃/Ni systems, *J. Therm. Anal. Calorim.* 125 (2016) 1079–1086. doi:10.1007/s10973-016-5357-2.
- [42] D.R. Driscoll, B.W. Tokmakian, N.P. Johnson, C.D. Hunt, S.W. Sofie, Catalyst enhancing aluminum titanate for increasing strength of nickel-zirconia cermets, *Mater. Lett.* 209 (2017) 307–310. doi:10.1016/j.matlet.2017.08.035.
- [43] M. Mcleary, R. Amendola, Effect of Aluminum Titanate (Al₂TiO₅) Doping on the Mechanical Performance of Solid Oxide Fuel Cell Ni-YSZ Anode, *Fuel Cells.* (2017) 862–868. doi:10.1002/fuce.201700073.
- [44] H. Orui, R. Chiba, K. Nozawa, H. Arai, R. Kanno, High-temperature stability of alumina containing nickel–zirconia cermets for solid oxide fuel cell anodes, *J. Power Sources.* 238 (2013) 74–80. doi:10.1016/j.jpowsour.2013.03.056.
- [45] Z. Cui, Y. Huang, H. Liu, Predicting the mechanical properties of brittle porous materials with various porosity and pore sizes, *J. Mech. Behav. Biomed. Mater.* 71 (2017) 10–22. doi:10.1016/j.jmbbm.2017.02.014.

- [46] H.L. Frandsen, T. Ramos, A. Faes, M. Pihlatie, K. Brodersen, Optimization of the strength of SOFC anode supports, *J. Eur. Ceram. Soc.* 32 (2012) 1041–1052. doi:10.1016/j.jeurceramsoc.2011.11.015.
- [47] ASTM C1161-18, Standard Test Method for Flexural Strength of Advanced Ceramics at Ambient Temperature, *ASTM Int.* (2018) 1–19. doi:10.1017/CBO9781107415324.004.
- [48] ASTM C1239-13, Standard Practice for Reporting Uniaxial Strength Data and Estimating Weibull Distribution Parameters for Advanced Ceramics, *ASTM Int.* (2013) 1–9. doi:10.1520/C1239-13.Scope.
- [49] T. Dey, A. Dey, P.C. Ghosh, M. Bose, A.K. Mukhopadhyay, R.N. Basu, Influence of microstructure on nano-mechanical properties of single planar solid oxide fuel cell in pre- and post-reduced conditions, *Mater. Des.* 53 (2014) 182–191. doi:10.1016/j.matdes.2013.06.052.
- [50] H. Peterlik, Relationship of Strength and Defects of Ceramic Materials and Their Treatment by Weibull Theory, *J. Fo Ceram. Soc. Japan.* 109 (2001) 121–126. doi:10.1007/s13398-014-0173-7.2.
- [51] A. Nakajo, J. Kuebler, A. Faes, U.F. Vogt, H.J. Schindler, L.K. Chiang, S. Modena, J. Van Herle, T. Hocker, Compilation of mechanical properties for the structural analysis of solid oxide fuel cell stacks. Constitutive materials of anode-supported cells, *Ceram. Int.* 38 (2012) 3907–3927. doi:10.1016/j.ceramint.2012.01.043.
- [52] Z. Cui, Y. Huang, H. Liu, Predicting the mechanical properties of brittle porous materials with various porosity and pore sizes, *J. Mech. Behav. Biomed. Mater.* 71 (2017) 10–22. doi:10.1016/j.jmbbm.2017.02.014.
- [53] D. Wu, Y. Li, J. Zhang, L. Chang, D. Wu, Z. Fang, Y. Shi, Effects of the number of testing specimens and the estimation methods on the Weibull parameters of solid catalysts, *Chem. Eng. Sci.* 56 (2001) 7035–7044. doi:10.1016/S0009-2509(01)00340-2.
- [54] A. Khalili, K. Kromp, Statistical properties of Weibull estimators, *J. Mater. Sci.* 26 (1991) 6741–6752.
- [55] J. Laurencin, G. Delette, F. Lefebvre-Joud, M. Dupeux, A numerical tool to estimate SOFC mechanical degradation: Case of the planar cell configuration, *J. Eur. Ceram. Soc.* 28 (2008) 1857–1869. doi:10.1016/j.jeurceramsoc.2007.12.025.
- [56] A. Nakajo, J. Kuebler, A. Faes, U.F. Vogt, H.J. Schindler, L.K. Chiang, S. Modena, J. Van Herle, T. Hocker, Compilation of mechanical properties for the structural analysis of solid oxide fuel cell stacks. Constitutive materials of anode-

supported cells, *Ceram. Int.* 38 (2012) 3907–3927.
doi:10.1016/j.ceramint.2012.01.043.

- [57] H. Fischer, W. Rentzsch, R. Marx, A modified size effect model for brittle nonmetallic materials, *Eng. Fract. Mech.* 69 (2002) 781–791. doi:10.1016/S0013-7944(01)00126-6.
- [58] F. Baratta, W. Matthews, Errors Associated with Flexure Testing of Brittle Materials, *U.S. Army Mater. Technol. Lab.* (1987) 16, 41–42.
- [59] M. McCleary, R. Amendola, Effect of Aluminum Titanate (Al_2TiO_5) Doping on the Mechanical Performance of Solid Oxide Fuel Cell Ni-YSZ Anode, *Fuel Cells*. 17 (2017). doi:10.1002/fuce.201700073.
- [60] R. Subramanian, E. Üstündağ, S.L. Sass, R. Dieckmann, In-situ formation of metal-ceramic microstructures by partial reduction reactions, *Solid State Ionics*. 75 (1995) 241–255. doi:10.1016/0167-2738(94)00148-L.
- [61] E. Üstündağ, Z. Zhang, M.L. Stocker, P. Rangaswamy, M.A.M. Bourke, J.A. Roberts, S. Subramanian, K.E. Sickafus, S.L. Sass, Influence of residual stresses on the evolution of microstructure during the partial reduction of NiAl_2O_4 , *Mater. Sci. Eng. A*. 238 (1997) 50–65.